The influence of warps on the vertical structure of galactic discs

Tigran Khachaturyants

Declaration

Type of Award: Doctor of Philosophy

School: Natural Sciences

I declare that while registered as a candidate for the research degree, I have not been a registered candidate or enrolled student for another award of the University or other academic or professional institution.

I declare that no material contained in the thesis has been used in any other submission for an academic award and is solely my own work.

No proof-reading service was used in the compilation of this thesis.

Tigran Khachaturyants

Abstract

Since their discovery in disc galaxies, including the Milky Way, warps have been the subject of extensive debate regarding their origin and role in galactic evolution. Cosmological simulations have shown that galactic warps represent the misaligned inflow of gas onto the disc. In this thesis, I study the consequences of misaligned gas inflow on the vertical structure of discs in a suite of Milky Way N-body+SPH simulations.

As the misaligned cold gas accretes onto the disc, there is ample opportunity for star formation to occur in the warp, which has been shown previously in N-body+SPH simulations. The relatively recent discovery of young stellar populations (Cepheids) in the Galactic warp supports this hypothesis as it indicates ongoing star formation. I demonstrate that star formation does occur in the misaligned gas inflows and that the formed warp populations settle and populate the thick disc. These warp populations have near-circular orbits and are, therefore, capable of reaching the Solar neighbourhood via radial migration. Additionally, I am able to show that warp stars have unique chemical and dynamical properties that make them stand out above in-situ stars in chemical and action spaces. After defining the regions in these spaces where the warp star purity is above 80%, I apply them to an observational sample in the Solar annulus and produce the first sample of warp star candidates in the Milky Way.

I demonstrate that misaligned cold gas can excite well defined prograde and retrograde bending waves with higher amplitudes than those excited in an unwarped

model. One of the key results of my analysis is the persistence of prograde $m = 1$ bending waves in the warped model, which according to the WKB approximation, are located in the forbidden region and are expected to dissipate. The same prograde bending waves appear to be less coherent in the unwarped model. I find that the prograde $m = 1$ bending waves are coupled with the $m = 2$ density waves, most likely brought on by the coincidence between the forbidden WKB bending and allowed WKB density regions. The results of this analysis demonstrate that the accretion of misaligned gas is capable of exciting and injecting significant power into both prograde and retrograde $m = 1$ bending waves. The lack of such a perturbing force in the unwarped model leads to the natural decay and weaker amplitudes of the prograde and retrograde bending waves, respectively.

I find positive slopes in the $L_z - \langle v_z \rangle$ relation of simulated Solar neighbourhood samples in both warped and unwarped models. However, only the slope in the warped model reaches values as large as observed in the Solar neighbourhood. The cause of the positive slope is seen as the result of bending waves passing through the Solar neighbourhood which can explain the difference in slopes between the two models. I determine that warps are a vital component in the study of the disc's vertical structure and evolution and can provide tools to uncover the evolutionary history of the Milky Way.

Contents

List of Tables

List of Figures

Acknowledgements

First and foremost, I would like to thank my supervisor, Professor Victor P. Debattista, for his immeasurable patience, wisdom, and guidance as I progressed through my PhD at the University of Central Lancashire. I would also like to thank Dr Mark Norris, Dr Joseph Caruana, Dr Eugene Vasiliev, Dr Payel Das, and Alcione Mora for their feedback and advice.

I am also grateful to my colleagues and collaborators Dr Leandro Beraldo e Silva, Dr João Amarante, and Steven Gough-Kelly for their feedback, advice, and lengthy conversations on galactic dynamics and the difficulties of programming. To João and Steven especially, thank you for your useful comments regarding this thesis on such short notice.

Finally, I would like to thank Professor Anatoly Zasov and Professor Irina Astashova for their guidance and support throughout the years.

Dedication

To my loving family, without whom I would have avoided the vastness of space. Your patience and boundless support is the fuel for my passion and without them, I can't imagine getting this far. To my younger brothers, without whom I would have probably finished this thesis sooner, although interrupting my studies to play games was invaluable respite that I truly cherished. To my dearest friends, Leni, Pratyush, Sarah, Chase, Shaun, and Rachel you provided endless moral support in spite of my prolonged absence and lack of communication, and I am truly thankful for that. Your patience is a virtue and I plan to return it tenfold.

Chapter 1

Introduction

1.1 Galactic structure

Galaxies were first accurately identified and catalogued in the eighteenth century by Charles Messier. However, their origin was not well understood, and they were assumed to be part of the Milky Way (MW). Immanuel Kant suggested that some of the nebulae might be separate and complete *island universes*, similar to the MW. The evidence to support Kant's ideas was beyond the capabilities of the telescopes of that time, but as the technology improved, a more coherent picture began to form. In the 1920's, Edwin Hubble was able to measure the distances to these 'nebulae' and confirmed that they were, in fact, galaxies, distant gravitationally bound stellar structures, separate from the MW. Hubble suggested four broad classes which the observed galaxies could be placed into based on their optical appearance (Hubble 1926). This classification is known as the Hubble sequence and is presented in Figure 1.1. The left half of the Hubble sequence contains the elliptical class of galaxies, which are characterised by their elliptical isophotes. Ellipticals are further divided into subgroups based on the shape of their isophotes: from circular, E0, to elliptical, E7. Figure 1.2 shows an example of two elliptical galaxies with minimum (left) and maximum (right) ellipticity values. Elliptical galaxies do not have well defined outer
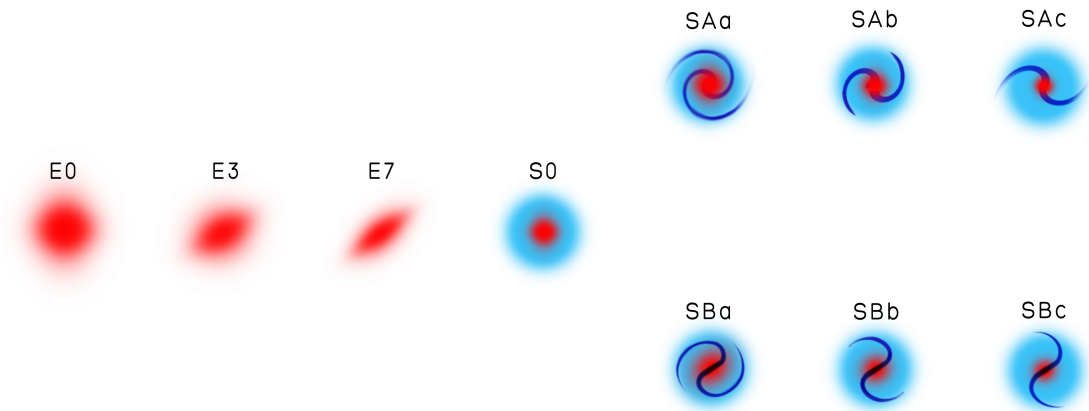
Figure 1.1: The Hubble sequence classification of galaxies (Graham 2019).
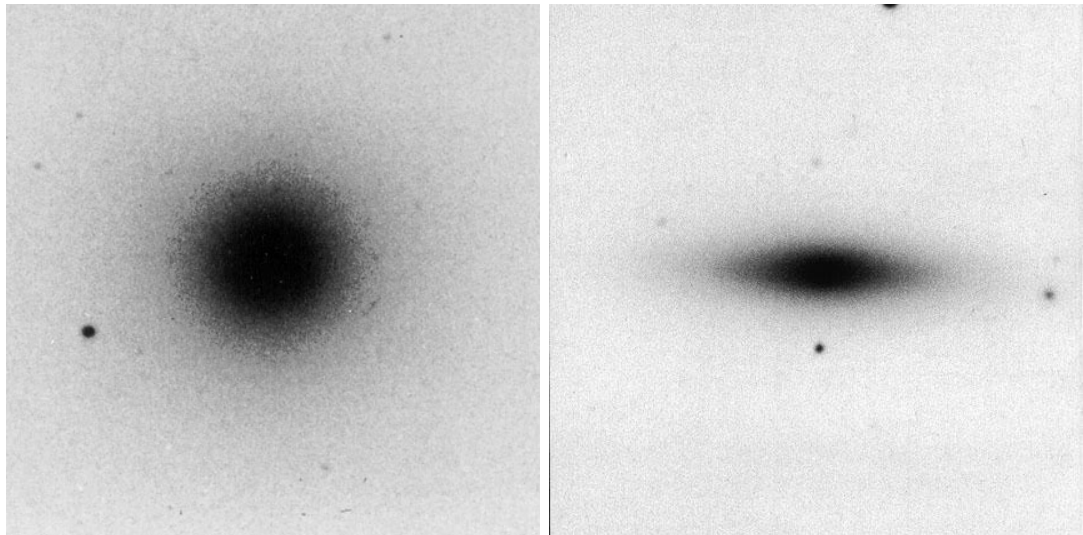
Figure 1.2: Optical images of NGC 1379 (left) and NGC 4623 (right) elliptical galaxies (Sandage & Bedke 1994). These galaxies are examples of the minimum and maximum ellipticity values which make up the E0 and E7 subgroups.

edges, so their surface brightness profiles smoothly decrease with radius. The size of ellipticals is commonly defined by the effective radius, R_e, which is the isophote radius that contains half of the galaxy's total luminosity. Most elliptical galaxies are deprived of recent star formation, commonly referred to as 'red and dead' (Faber & Gallagher 1976). However, there are instances of 'blue' ellipticals, *i.e.* with ongoing star formation (George 2017). The current understanding of how elliptical galaxies form is through galaxy mergers (de Zeeuw & Franx 1991; González-García et al. 2009), though historically they were mistakenly assumed to be the early stage of galactic evolution, hence their 'early-type' denomination.

Galaxies with an ellipticity greater than that of E7 galaxies but lack any spiral features are referred to as lenticulars (S0). Lenticular galaxies are located in the centre of the Hubble sequence and, similar to ellipticals, were referred to as 'early-type' in the past. This label was attributed due to the incorrect assumption that S0 galaxies were a transition state between elliptical and spiral galaxies. Lenticulars are usually observed in clusters (Dressler 1980) and become less frequent at increasing redshifts (Dressler et al. 1997; Couch et al. 1998; Postman et al. 2005), implying that the environment plays a role in the formation of S0 galaxies. A class that is not present in the Hubble sequence are the irregular galaxies (Im), which do not have a well-defined shape. Irregular galaxies are characterised as small and faint systems (see Gallagher & Hunter 1984, for a review on irregular galaxies), with notable examples being the Large and Small Magellanic Clouds.

On the right side of the Hubble sequence is the spiral class of galaxies, characterised by their disc-shaped structure and the presence of spiral arms. This class is subdivided based on the presence (SB) or absence (SA) of a central bar component; an example of both barred (top) and unbarred (bottom) galaxies is presented in Figure 1.3. Barred galaxies are more common in the local universe with two out of three spiral galaxies being barred (Buta et al. 2015). The nearest examples of spiral

Figure 1.3: Top: NGC 1300, an SB(rs)bc barred spiral galaxy. Credit: NASA, ESA, and The Hubble Heritage Team (STScI/AURA) Acknowledgment: P. Knezek (WIYN). Bottom: M63, an SAbc unbarred spiral galaxy with flocculent spiral arms. Credit: ESO.

class galaxies are the MW and Andromeda galaxies (M31), both belonging to the barred subclass, with the MW having a rotating bar that extends up to ~ 5 kpc (Wegg et al. 2015). A further subdivision of the spiral galaxy class is based on the tightness of the spiral arms. Unbarred (bared) galaxies are broken up into three subclasses from tightly to loosely wound, SA(B)a and SA(B)c, respectively.

Spiral galaxies are observed to have a dense central component that is thicker than the disc, referred to as the bulge. Bulges are not unique to the spiral galaxy class, with the bulge decreasing in size and luminosity when moving from ellipticals to loosely wound spirals in the Hubble sequence (Wyse et al. 1997). Bulges are divided into classical and pseudobulges. Classical bulges are spherical in structure, dynamically hot, and speculated to have formed via hierarchical merging (Renzini 1999; Martinez-Valpuesta & Athanassoula 2008). Pseudobulges are more box-like in shape, have disc-like kinematics, and have been theorised to form via secular processes (e.g. see Kormendy & Kennicutt 2004, for review on the formation of pseudobulges). A type of pseudobulge that is commonly observed in spiral galaxies, including our own (e.g. Weiland et al. 1994; Binney et al. 1997; López-Corredoira et al. 2005), is the boxy peanut-shaped (B/P) bulge (Erwin & Debattista 2017). N-body simulations have demonstrated that violent vertical instabilities in newly formed bars (buckling instability) produce B/P bulges (e.g. Raha et al. 1991a; Merritt & Sellwood 1994; Debattista et al. 2004), which were later confirmed in two external galaxies with ongoing buckling instabilities (Erwin & Debattista 2016).

De Vaucouleurs further extended the Hubble sequence to include barred (S0B) and unbarred (S0A) lenticular galaxies along with weakly barred spiral galaxies (SAB). De Vaucoulerus also added more characterisation to the spiral structure to include diffuse spirals and further subdivisions in the tightness of the spiral arms. Surveys of galactic structure in the local universe have found that spiral galaxies

make up more than half of the observed galaxies while elliptical and lenticular galaxies make up a third of the extragalactic surveys (Loveday 1996; Cappellari et al. 2011; Willett et al. 2013). Irregular and merging galaxies cumulatively make up around 10% of the observed extragalactic sources (Loveday 1996). Galactic structure has been shown to be influenced by the environment (e.g. Dressler 1980), with early and late-type galaxies being more dominant in high-density (cluster) and low-density regions, respectively.

1.2   Spiral galaxies

The differences between spiral and elliptical galaxies are very apparent, with early-types having a spheroidal and diffuse structure and late-types having a main disc with diverse substructure. The formation of elliptical galaxies is assumed to be solely via major mergers of two or more disc galaxies, but this raises the question on how disc galaxies themselves form. In the ΛCDM cosmological paradigm, the halos of disc galaxies like our own (e.g. see Helmi 2020, for review) and M31 (Ibata et al. 2005; Escala et al. 2020) form through hierarchical assembly, i.e. through mergers. It is assumed that the mergers involved are primarily minor in nature.

The ΛCDM model can also describe the fundamental building blocks of galactic formation. Initially, the hot gas in the dark matter halo can radiatively cool and pool in the potential well. This protogalaxy is formed by a fraction of the total gas mass in the halo, but it contains most of the available angular momentum (van den Bosch et al. 2001). The gas cools and settles onto near-circular orbits, forming a rapidly rotating disc. The resulting surface density of the disc will increase, which will trigger star formation (Kennicutt 1998). With dense gas being located closer to the centre, due to its lower angular momentum, star formation is initially centrally concentrated. Star formation then proceeds in gas with higher angular momentum, which leads to a larger stellar disc at later times, a process that is referred to as

inside-out formation (Kepner 1999; Nelson et al. 2012; Patel et al. 2013). The inside-out process can produce a radial age gradient as stars in the centre are the first to form; such a radial decrease in the average stellar age has been observed in external galaxies (Bell & de Jong 2000; MacArthur et al. 2004; Williams et al. 2009; Dale et al. 2016; Frankel et al. 2019). However, other mechanisms can affect the resulting age profiles, such as radial migration, discussed later in this section.

Most of the stellar mass in spiral galaxies is concentrated in the galactic disc. The surface density profile, $\Sigma(R)$, of the stellar disc can be described using an exponential profile,

$$\Sigma(R) = \Sigma_0 e^{-R/h_R} \tag{1.1}$$

where Σ_0 is the central surface density and h_R is the scale length, defined as the radius at which the density decreases by a factor of e. The vertical structure of disc galaxies is usually broken into two separate components referred to as the thin and thick discs. The thin disc is characterised by stellar populations that are on average younger and, consequently, more metal-rich than those found in the thick disc. These disc components are commonly referred to as geometrically thin and thick, as the disc can also be separated into components by chemistry alone (Hayden et al. 2017). The vertical density profile of the disc similarly follows an exponential law,

$$\rho(R, z) = \rho(R, 0)e^{-|z|/h_z(R)} \tag{1.2}$$

where z is the height from the midplane, $\rho(R, 0)$ and $h_z(R)$ are the midplane density and the vertical scale height at radius R, respectively. The scale height also depends on the stellar population, with younger stars having smaller scale heights (Binney & Tremaine 2008a). Studies of the MW's radial and vertical density profiles have produced a scale length of $h_R = 2.5 \pm 0.4$kpc for the thin disc (Bland-Hawthorn &

rotation

trailing arms   leading arms
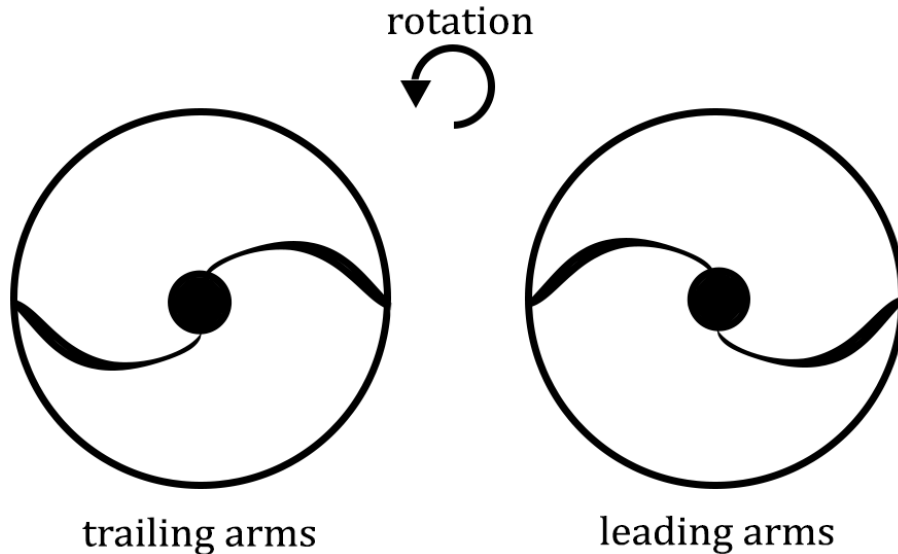
Figure 1.4: Visualisation of trailing (left) and leading (right) spiral arms, classified by their orientation relative to the direction of rotation of the galaxy (top middle).

Gerhard 2016) and scale heights of $h_z \simeq 300$pc and $h_z \simeq 900$pc for the thin and thick discs (Bland-Hawthorn & Gerhard 2016; Jurić et al. 2008), respectively.

1.2.1   Spiral formation

Observations have shown that the majority of spiral arms are trailing, i.e. pointed in a counterrotating direction relative to the disc (Fig 1.4, left), while leading spirals (Fig 1.4, right) only make up a fraction of spirals (Buta et al. 2003). In galactic dynamics, the formation of spirals remains a challenging area of research with many outstanding questions on their evolution and transient nature.

Similar to the initial classification of galaxies, spirals are separated into different groups based on their direct observations. The most abundant spiral type is the two-arm spiral which is characterised by two symmetric arms. In surveys of external galaxies, such as the Sloan Digital Sky Survey (SDSS, York et al. 2000) and the Galaxy Zoo 2 project (Willett et al. 2013), two-arm spirals were found in $\sim 60\%$ and $\sim 80\%$ of galaxies, respectively. Two-arm spirals are often present only at

the inner radii and then split into multiple spirals on the outskirts of the disc, but there are galaxies where the two-arm spiral spans the entire disc (Elmegreen & Elmegreen 1982; Grosbøl et al. 2004). Early classifications were focused on the visible spectrum, but two-arm spirals are also observed in near-infrared light, while in the optical band, the disc presents multiple, short, and discontinuous spiral arms (flocculent) (Block & Wainscoat 1991; Thornley & Mundy 1997). This implies that the spiral affects the entire disc, not just the young populations (visible spectrum). The current spiral arm classification is completed with flocculent and multi-armed spirals, which are less frequent than two-arm spirals (Elmegreen 1990). There are rare cases of single-armed spirals in the universe (de Vaucouleurs et al. 1991), but any successful spiral formation theory must be able to explain and recreate the observed spiral phenomena.

The rotation curves observed in disc galaxies have shown that stars in the inner regions of the disc have shorter orbital periods than those in the outer regions. Therefore, if spiral arms were material structures, they would naturally wind up in a few galactic rotations (Wilczynski 1896). However, the abundance of spirals in disc galaxies implies that spiral arms must be long-lived or transient in nature. The first breakthrough came from Lin & Shu (1964, 1966) who proposed that the observed spirals were actually density waves propagating through the galactic disc and rigidly rotating at a set frequency, referred to as the pattern speed (Ω_p). Density waves would not be affected by differential rotation as they move through the matter in the disc. The density wave theory also addressed the increased star formation in the spirals as the gas would be compressed with the approach of the density wave, thereby inducing star formation. Later work by Schweizer (1976) supported the density wave theory as red (old) and star-forming (young) spiral arms were observed to be at similar locations. Red spirals were observed to be more diffuse, which Schweizer (1976) suggested was caused by the eventual smoothing of newly

formed stars in the spiral, while the star forming edge of the spiral would be bright and well defined.

Further advancement in the field of spiral formation came from the discovery of the swing amplification mechanism (Toomre 1981), a process in which perturbations in the disc are amplified and then sheared into spiral patterns via differential rotation. The amplification happens when the epicyclic motion of a star matches that of the spiral pattern. To measure how susceptible a disc is to perturbations, Toomre (1964) defined the Q parameter, which acts as a critical threshold, beyond which the disc is stable against axisymmetric perturbations. The Toomre Q parameter is defined as

$$Q \equiv \frac{\sigma_R \kappa}{3.36 G \Sigma} \tag{1.3}$$

where σ_R is the radial velocity dispersion, κ is the epicyclic frequency, and Σ is the surface mass density. For $Q > 1$, the disc is stable to axisymmetric perturbations, while for $Q < 1$, the disc becomes vastly unstable against gravitational collapse and is generally not realised in galaxies. Swing amplification is significant up to $Q \lesssim 2$ (Binney & Tremaine 2008a). Galaxies with large radial velocity dispersions are considered radially 'hot' and will not be susceptible to axisymmetric perturbations, while the opposite is true for radially 'cold' galaxies. Initially, it can seem that spiral density waves are bound to dissipate with time as they will inevitably heat the disc and prevent any further excitation, but that is not always the case. With the presence of any cooling mechanism in the disc, density waves have the capacity to continuously reappear as new spirals (Sellwood & Carlberg 1984). Sellwood & Lin (1989) observed in their N-body simulations that spiral patterns change the particle distribution in such a way that a new dynamical instability can arise. This change manifests as a "groove" in the phase space density distribution at a particular angular momentum, and it, in turn, drives a new instability, referred to as a *groove mode*. With all these mechanisms in play, a picture of transient spiral formation

begins to form in which spirals can be long-lived, affect the disc structure, naturally dissipate, and then give rise to new spiral waves.

The transient nature of spirals plays a significant role in the galactic disc; Sellwood & Binney (2002a) described a mechanism that can redistribute stars from different parts of the disc, named radial migration. Transient spirals can have a wide range of Ω_p throughout the disc (Sellwood & Carlberg 1984; Roškar et al. 2012), and where Ω_p matches the circular frequency of the disc is referred to as the corotation radius. Stars trapped at the corotation radius can experience changes to their galactocentric radius while the eccentricity of their orbit remains mostly unaffected, *i.e.* a star can remain on a near-circular orbit while experiencing changes in its angular momentum. If spirals were long-lived, then the star would experience these changes in perpetuity, but the transient nature of spirals means stars can escape the corotation radius with a net change to their angular momentum. As a result, radial migration can lead to a large redistribution of stars without changes to their radial actions and, therefore, orbital eccentricity, which means the disc will not experience any radial heating.

To explain how the scattering occurs without affecting the orbital eccentricity, we obtain the relationship between the angular momentum changes induced by the spiral and the associated changes in the random velocities of stars. In a rotating frame of a steady spiral perturbation, neither the specific energy, E, or vertical angular momentum, L, are conserved. However, the following combination, known as Jacobi's integral, E_J (Sellwood & Binney 2002a), is conserved:

$$E_J = E - \Omega_p L \tag{1.4}$$

where Ω_p is the pattern speed of the spiral perturbation. From this, we see that the relation between the changes in angular momentum and energy is

$$\Delta E = \Omega_p \Delta L \tag{1.5}$$

A fraction of the energy increment, ΔE, represents the changes in circular motion while the remainder represents changes in random motion. By defining J_R as any parameter that quantifies radial kinetic energy, we obtain

$$dE = \frac{\partial E}{\partial J_R}dJ_R + \frac{\partial E}{\partial L}dL \qquad (1.6)$$

Sellwood & Binney (2002a) showed that if J_R is chosen to be the "radial action", then the partial derivatives in Equation 1.6 become the angular frequencies of a star's radial and azimuthal motions, ω_R and Ω, respectively. Substituting these frequencies into Equation 1.6 and then combining the result with Equation 1.5 gives

$$\Delta J_R = \frac{\Omega_p - \Omega}{\omega_R}\Delta L \qquad (1.7)$$

We observe that for stars at corotation, *i.e.* $\Omega = \Omega_p$, changes in L do not cause changes in J_R, while for stars outside this resonance they do. The classical Lindblad diagram in Figure 1.5 illustrates the physical origin of this relation. The solid line is indicative of circular orbits in a disk galaxy model with a flat rotation curve. The white region in the upper left half of the diagram is occupied by eccentric orbits, while the grey shaded region shows inaccessible orbits. The distance from the curve of circular orbits is a measure of J_R, so a higher radial action indicates a more eccentric orbit. Equation 1.5 shows that stars are scattered along the lines of constant slope, Ω_p, which at corotation (annotated) is also the tangent to the curve of circular orbits. We observe that stars that are corotating with the wave do not experience any changes in J_R to first order when they are scattered. However, scattering that occurs at near or non-circular orbits results in energy being exchanged.

Radial migration complicates our understanding of the evolutionary history of galaxies, including the picture of inside-out formation, since every annulus is now assumed not to be evolving in isolation. The scale of this effect was measured in a MW-like simulation (Roškar et al. 2008a) and shown to cause an upturn in the age profile as older stars radially migrated to the outer disc. In essence, radial
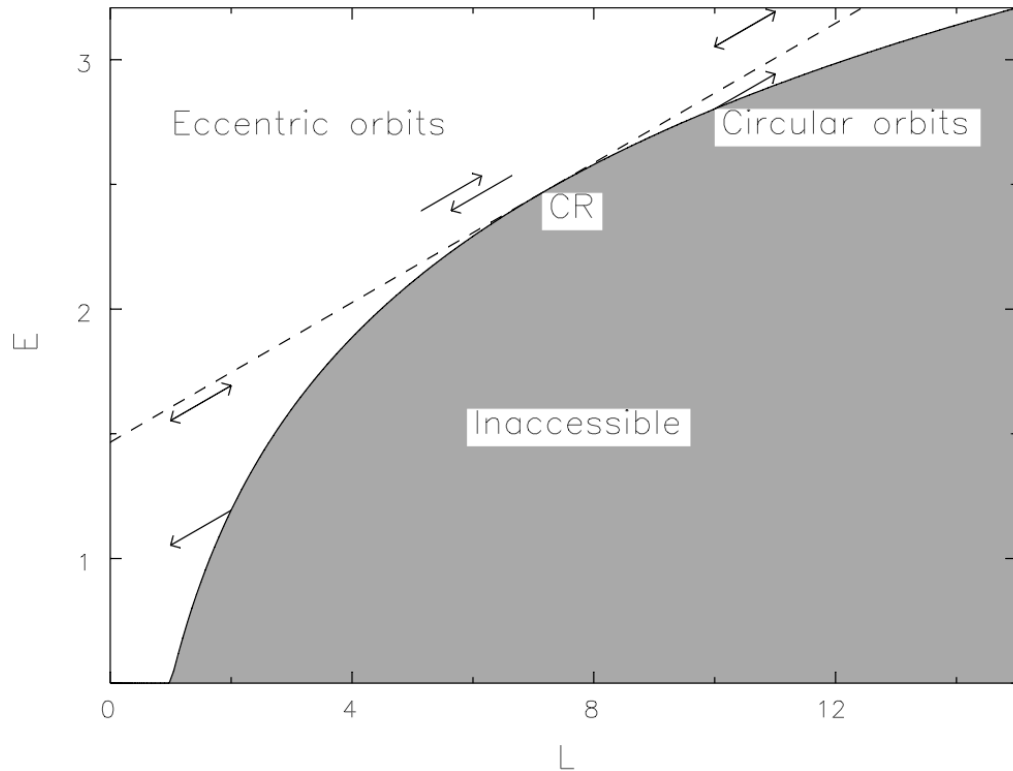
Figure 1.5: Classical Lindblad diagram from Sellwood & Binney (2002a) that shows the relation between L and E. The solid curve indicates circular orbits while eccentric orbits fill the region above it. The arrows indicate a number of possible scatterings of stars by a steadily rotating wave which has a pattern speed (dashed line) equal to the slope of the tangent at corotation (CR).

migration is a random walk as stars continuously experience a push and pull at the corotation radius, leading to older stars having more time to migrate outwards. This age upturn was also later confirmed through observations in the MW (Frankel et al. 2020) and external galaxies (Yoachim et al. 2010; Radburn-Smith et al. 2012; Willett et al. 2013).

1.3   Warps

When viewing external galaxies edge on, their optically visible disc is usually remarkably flat. However, a peculiar substructure has been long observed in their HI distribution. This substructure is observed on the outer edges of the disc and deviates from the midplane symmetry as it extends away from the midplane; this is a galactic warp. Warps can also be detected in less edge-on and even face-on galaxies through the kinematic analysis of the HI distribution (e.g. Shostak & van der Kruit 1984). Two major types of warps have been identified through observations and subsequently named based on their geometric shape: the S-shaped and U-shaped warps. Warps that extend in opposite directions on either side of the disc are the aptly named S-shaped warps. These warps are commonly referred to as *integral warps* due to their resemblance to the integral symbol. The edge-on galaxy NGC 4013 (Zschaechner & Rand 2015) in Figure 1.6 is a clear example of such a warped galaxy with the composite colour image (top) presenting a flat disc, while the HI map (bottom) shows a distinct S-shape warp. Warps that extend in the same direction away from the midplane are the U-shaped warps. Outside of the two main types, Sanchez-Saavedra et al. (2003) introduced a third warp type where the disc is only affected from one side, forming an L-shaped warp.

García-Ruiz et al. (2002b) demonstrated that 20 out of 26 external galaxies in the WHISP survey are warped. Most of these warps are S-shaped, while only two are U-shaped and observed in galaxies that are strongly interacting with nearby
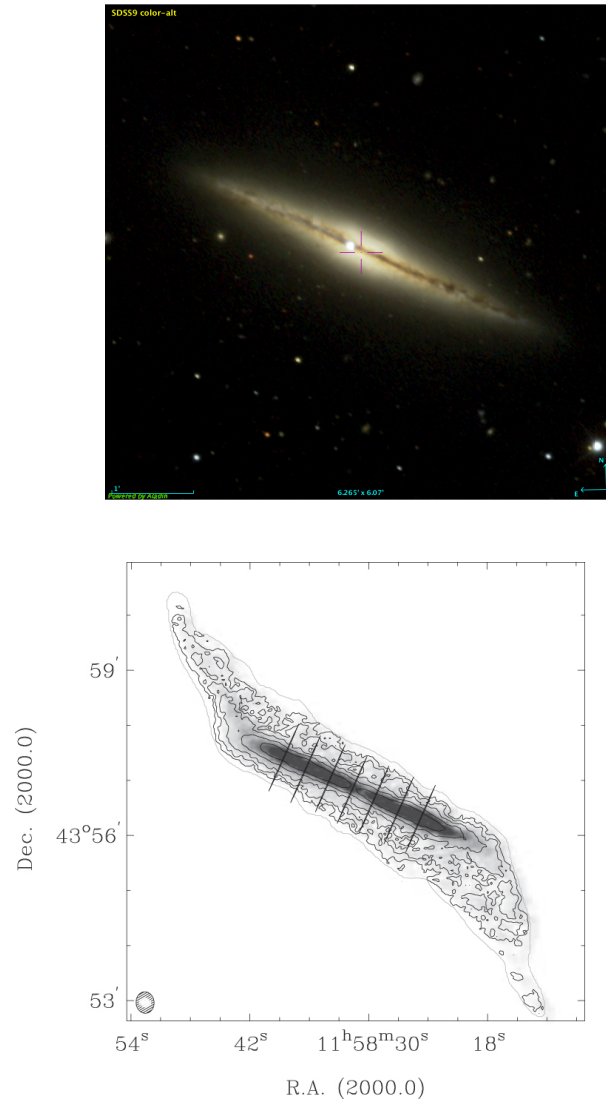
Figure 1.6: Top: composite colour image from SDSS (York et al. 2000, retrieved via Aladin sky atlas, https://aladin.u-strasbg.fr) of NGC 4013 which shows a flat optical disc. Bottom: The HI zeroth-moment map of NGC 4013 Zschaechner & Rand (2015). The outer regions of the edge-on galaxy are clearly warped.

companions. Additionally, García-Ruiz et al. (2002b) noted a possible environmental dependence in warps as galaxies in their sample had larger and more asymmetric warps in rich environments than in poor environments. However, due to the overall ubiquity of warps in their sample, García-Ruiz et al. (2002b) did not consider interactions with the environment as the sole origin of warps in disc galaxies. Ann & Park (2006) analysed the disc morphologies of 385 edge-on galaxies and demonstrated that 73% of galaxies in their sample had warps: 51% S-shaped and 22% U-shaped. Ann & Park (2006) observed a higher frequency of warps in poor environments rather than in rich ones, somewhat consistent with the findings of García-Ruiz et al. (2002b).

Warping has also been observed in the stellar discs of external galaxies, although their amplitude is smaller than the ones found in HI (Ann & Park 2006). There are rare cases of strong warping in stellar discs that come close to matching the HI warp, but in those cases the galaxies are interacting, e.g. Mkn 305 and Mkn 306 (Kollatschny & Dietrich 1990). Stellar warps could be the result of tidal interactions warping the outer stellar disc or of the gas in HI warps forming stars and, therefore, a stellar warp. In external galaxies, star formation has only been inferred and not directly observed: UV-bright stellar complexes were located far outside the optical disc (e.g. Zaritsky & Christlein 2007a; Herbert-Fort et al. 2010a) where warps are usually observed and in one case these complexes were associated with the HI warp (Thilker et al. 2005a).

The MW was the first warped galaxy to be observed. The warp was observed in the HI gas using 21-cm hydrogen-line observations by both Burke (1957) and Kerr (1957a) who independently discovered a ~ 300pc maximum deviation of the galactic plane at $R \sim 12$kpc. Warping was later observed in the outer optical (Arp 1964) and HI (Newton & Emerson 1977) discs of M31. The stellar disc of the MW was initially discovered to be warped in the red clump (RC) stars (López-Corredoira

et al. 2002a). López-Corredoira et al. (2002a) compared the amplitudes of the HI (Burton 1988) and RC warps and found that they were coincident in both orientation and maximum amplitude. Similar to the HI, the RC warp was measured for both ends of the warp, referred to as the south and north sides for the warp below and above the plane, respectively. The maximum displacement for the south side was measured to be $|z| \sim 1.5$kpc at a radius of $R = 14$kpc, while the north side only matched the HI warp up to $R = 13$kpc. Chen et al. (2019b) used more updated HI data than López-Corredoira et al. (2002a) (Levine et al. 2006a) and, in their case, the RC warp did not match the gas warp, which they assumed was due to the sampling incompleteness of the RC stars. The warp in the MW was also traced in pulsars (Yusifov 2004) and dust (Drimmel & Spergel 2001), however, both samples could not match the amplitude of the HI warp, either due to large uncertainties (pulsars) or a different amplitude (dust).

More recently, with the release of the *Wide-field Infrared Survey Explorer* (*WISE*) catalogue of periodic variables, Chen et al. (2019b) compiled a sample of classical Cepheids and observed that they trace the Galactic warp. Classical Cepheids are a type of young variable star, making the Chen et al. (2019b) result a significant breakthrough in the study of warps as it implied the presence of recent star formation in the warp. When compared to the previous warp tracers (dust, pulsars, RC) Cepheids are a closer match to the HI warp, further implying that there may be ongoing star formation in the gas warp.

The structure of the warp can be modelled as a series of concentric rings with increasing inclination, as shown in Figure 1.7. The imaginary line that marks the intersection between the concentric rings and the midplane is called the line of nodes (LON, red dashed line). This method is referred to as the "tilted ring model", and it is a vital tool in the study of galactic warps. The tilted-ring model can uncover warps in more face-on galaxies when applied to the HI velocity field (e.g. Rogstad
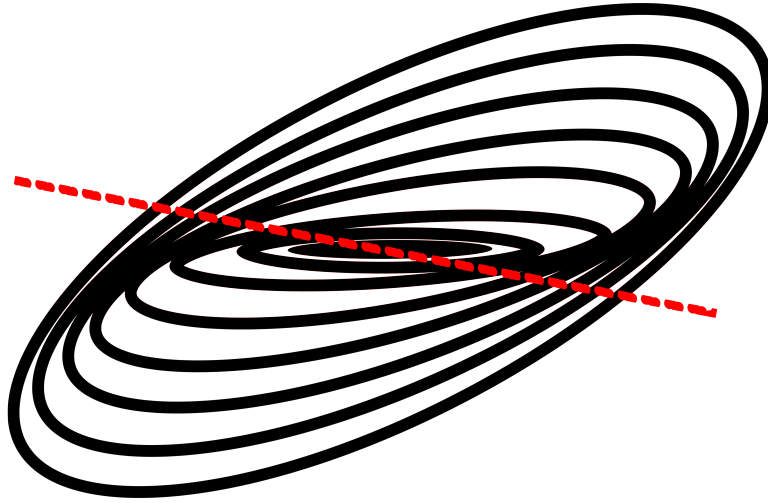
Figure 1.7: The tilted ring model for the warp. The red dashed line is the line of nodes (LON), which indicates the intersection between the rings and the midplane.

et al. 1974; Bosma 1981a,b).

By deconstructing the HI data of 12 external galaxies into tilted rings and analysing their properties, Briggs (1990a) was able to establish three rules for warp behaviour:

1. The warp is detected between the isophotal radii at which the B-band surface brightness is 25 and 26.5 mag/arcsecond^2, referred to as R_{25} and R_{Ho}, respectively.

2. The LON is straight within R_{Ho}

3. Outside of R_{Ho}, the LON lies along a loosely wound, leading spiral

The first rule was a key discovery in the study of warp formation as it determined that gas warps are located beyond the optical region of a galaxy. The second Briggs rule could only be confirmed recently in the Milky Way with the exquisite data from Chen et al. (2019b) and the Gaia Collaboration et al. (2018a), as previous

studies were not able to test it due to large uncertainties in the data (Burton 1988; Drimmel & Spergel 2001; López-Corredoira et al. 2002a). By assuming that the LON does not vary with R, Chen et al. (2019b) were able to determine the mean galactocentric azimuth of the LON with relatively low uncertainties and a final value of $\phi = 17.5° \pm 1.0°$ (formal errors) $\pm 3.0°$ (systematic errors).

1.3.1 Cause of the warp

The cause of galactic warps is still a highly contested question, with extensive work being done in numerical simulations. Many mechanisms of warp formation have been proposed (see the reviews of Binney 1992; Sellwood 2013), but it is uncertain which of them is more prevalent or what combination of them is more likely to form warps, but two of the mechanisms we touch upon have an environmental dependency.

Tidal interactions

One of the leading hypotheses on how warps form, especially in the MW, is via satellite interaction. There are many possible culprits that could have had a tidal interaction strong enough to induce the Galactic warp we observe today. The two key perturbers in the MW are the currently infalling Large Magellanic Cloud (LMC, Weinberg & Blitz 2006; Kalberla et al. 2007a; Laporte et al. 2018a,d; Petersen & Peñarrubia 2021) and the Sagittarius dwarf galaxy (Bailin 2003; Purcell et al. 2011a; Gómez et al. 2013a) which is in the process of being accreted.

The recent detection of the MW reflex motion due to LMC's infall (Petersen & Peñarrubia 2021) indicated that the gravitational perturbations induced by the LMC are paramount in the dynamical models of the MW. However, the scenario in which the LMC-induced perturbation forms the Galactic warp has gone through many changes. The LMC was initially considered to be too far ($\sim 50\mathrm{kpc}$) and not massive enough ($\sim 2\%$ of the MW mass) to induce the observed warp (e.g. Hunter

& Toomre 1969a). Further studies showed that both Magellanic clouds could cause a wake in the dark matter halo (Weinberg 1995). García-Ruiz et al. (2002a) used N-body+ring models to account for the wake in the dark matter halo, however, they could not produce satisfactory results even when their satellite had a bound mass larger than the highest LMC estimate ($\sim 1.5 \times 10^{10} M_\odot$, Schommer et al. 1992). In addition to the inflated mass, the resulting LON in García-Ruiz et al. (2002a) was also tightly wound, with the growing warp pattern being smeared and losing coherence. Using the perturbative method developed in Weiland et al. (1994), Weinberg & Blitz (2006) demonstrated that the resulting tidal field of an LMC-like satellite with a bound mass $\sim 2 \times 10^{10} M_\odot$ could induce a warp matching the one observed in the MW.

More recently, with the improved measurements of the LMC's proper motion (Kallivayalil et al. 2006, 2013) and the use of N-body simulations with hydrodynamics, Laporte et al. (2018d) were able to match the phase and the antisymmetrical shape of the MW warp. However, Laporte et al. (2018d) still had quantitative discrepancies with the MW warp, including much higher bound mass estimates for the LMC ($0.3 - 2.5 \times 10^{11} M_\odot$), and height deficits of $\Delta Z = 0.7$ kpc at both $R = 16$ kpc and $R = 22$ kpc. A significant limitation of the LMC warp formation scenario is the uncertainty in the mass estimate of its key perturber. However, using the dynamical timing argument (method of estimating the total mass in the Local Group), Peñarrubia et al. (2016) have indicated that the total mass of the LMC may have been greatly underestimated ($\sim 0.25 \times 10^{12} M_\odot$).

The relatively recent ($\sim 0.4 - 1$ Gyr) and close ($R \sim 20$ kpc) passage of the Sagittarius dwarf galaxy (Sgr) through the MW disc makes it a suitable candidate for the perturbing source that could give rise to the Galactic warp. Unlike the LMC, Sgr has passed through the Galactic disc numerous times, is closer than the LMC, and has a mass range between $\sim 10^8 - 10^9$ M$_\odot$ (Ibata et al. 1997; Ibata &

Razoumov 1998a), making it a more likely candidate as the key perturber. Laporte et al. (2018d) performed similar experiments in their simulations but with a Sgr-like satellite mass of $10^{11}M_\odot$ and observed that the warp amplitudes were similar to those produced with the heavy LMC model. However, Laporte et al. (2018d) also observed that the warp in the Sgr scenario was generally out of phase with the observed HI warp. Additionally, Laporte et al. (2018d) demonstrated that the Fourier decomposition of the $\langle z \rangle$ distribution in the disc produced higher-order Fourier modes. These higher-order modes are most likely due to the numerous approaches of the Sgr-like satellite. As a result, both satellites provide a significant perturbing force that induces warps in the simulated discs, though they do not successfully match the profile of the Galactic warp.

Disc-halo interaction

Self-consistent N-body simulations (e.g. Debattista & Sellwood 1999) have shown that galactic discs embedded in a rotating halo develop a warp via dynamical friction when the angular momentum of the disc and halo are misaligned. The simulations in Debattista & Sellwood (1999) are purely N-body with the gas substituted by an HI component modelled as a sheet of test particles. The resulting warps mimic Briggs' rules of warp behaviour as the LON traces out a leading spiral relative to the inner disc and lasts longest in the HI component. Ideta et al. (2000) and Jeon et al. (2009) were able to recreate these results by producing S-type warps in a variety of misaligned halos. The misalignments described in this mechanism are expected in hierarchical models of galaxy formation (Quinn & Binney 1992) and therefore can account for the high fraction of warps in the universe. Evidence of this mechanism is harder to confirm through observations. However, the tilted ring analysis of the HI velocity field in NGC 5055 (Battaglia et al. 2006) provided some support as the inner flat and outer warped HI discs have different kinematic centres and systemic

velocities. Battaglia et al. (2006) suggested that these differences could have been brought on by a halo with a different orientation and offset with respect to the disc.

Gas accretion

The formation of spiral galaxies occurs with the pooling of cold gas in the potential well of the dark matter halo, but, as noted previously, the resulting disc only contains a fraction of the total gas. Inside the virial radius of the dark matter halo, there is gas that comprises the circumgalactic medium (CGM). The CGM of the MW has been extensively studied, and a hot gas ($T \sim 10^6$K) component has been discovered through the stellar spectra of distant stars (Spitzer 1956). This component was named the hot gas corona, and since then, it had been observed in external galaxies ranging from ellipticals to spirals (e.g. Bregman & Lloyd-Davies 2007; Putman et al. 2012; Tumlinson et al. 2017). The hot gas corona is a key component of the CGM, however, there are also colder components within the halo's virial radius. The total mass of the cool gas ($T \lesssim 10^5$) contained in the CGM of the MW has been estimated to be $M_{\mathrm{g,cool}} \sim 9 \times 10^{10} \mathrm{M_\odot}$ (Tumlinson et al. 2011, 2017; Prochaska et al. 2017), while the mass of the hot gas corona ($T \gtrsim 10^6 K$), has been estimated to be $M_{\mathrm{g,hot}} \sim 1.5 \times 10^{10} \mathrm{M_\odot}$ (Anderson & Bregman 2010).

The gas in the hot gas corona is ionised and, therefore, capable of cooling via Bremsstrahlung radiation ("braking radiation"), and as the gas cools, it sinks to lower radii. In a scenario where the angular momentum of the hot gas corona is misaligned with the galactic disc, the gas can reach the disc misaligned and, therefore, form a galactic warp. This has been proposed to be one of the many possible causes of galactic warps (e.g. Roškar et al. 2010a). Cold gas accretion has been inferred in external galaxies through observation of large HI complexes on the outskirts of the disc (Sancisi et al. 2008a) and partially inferred in the MW (Richter 2017; Fox et al. 2019; Qu et al. 2020). The gas accretion scenario can address some

of the issues in contemporary theories of warp formation. Firstly, misaligned gas accretion can address the persistence of warps in disc galaxies as it is continuous rather than episodic. Secondly, gas accretion can also address the near-constant star formation rate in the Solar Neighbourhood (Binney et al. 2000a; Twarog 1980a) as the Galactic gas reserve is continuously refilled.

Roškar et al. (2010a) studied warps that formed via gas accretion in a fully cosmological simulation of a MW-like galaxy with a hot gas corona that has its angular momentum misaligned with that of the disc. One of the more striking results from Roškar et al. (2010a) are the stellar populations forming in the warp throughout the simulation's evolution, referred to as warp stars. The warp stars in their simulation form in the misaligned accreting gas and settle into the geometric thick disc of the galaxy. If such tracer populations were detected in the MW disc, they could indirectly confirm that the Galactic warp formed via accreting misaligned gas.

1.4   Chemical evolution

The study of galactic chemical evolution takes into account the formation of chemical elements and their redistribution. Early stellar populations form in the primordial gas of galactic discs, and through their evolution they fuse hydrogen and helium into heavier elements (Burbidge et al. 1957). The fusion products are then redistributed back into the interstellar medium (ISM). Redistribution occurs in the form of stellar winds throughout a star's lifetime and as a supernova at the end of their evolution. Both processes change the ISM by injecting it with energy and enriching it with metals, the latter being incorporated in future stellar populations. This metal enrichment proceeds with each new stellar population, increasing the metal content of the ISM and of future stars. Metal enrichment does not occur in isolation as different factors affect the enrichment rate, including the frequency of supernovae explosions

(Adams et al. 2013), the galactic inflow and outflow rates (Lu et al. 2015), and the initial mass distribution (Fontanot et al. 2017). Stars fuse heavier elements in their cores, while their surface metallicity, which is observable, is indicative of the ISM at the time of formation. By observing the metallicity of stellar populations and the state of the ISM in the MW, a chemical evolution model can be constructed, putting further constraints on the evolutionary history of our Galaxy.

One of the earliest chemical evolution models is the Simple Model (van den Bergh 1962; Schmidt 1963; Tinsley 1980) where the key assumptions are that the system is isolated (no gas outflows or inflows) and the gas is well mixed (instantaneous recycling) at all times. These assumptions are inconsistent with the formation and evolution of galactic systems, and the resulting stellar populations show discrepancies with observations. The Simple Model has a strong shortage of metal-poor stars, known as the G-dwarf problem (Searle & Sargent 1972; Pagel & Patchett 1975; Haywood 2001), and it does not produce enough K-dwarfs (Casuso & Beckman 2004) and M-dwarfs (Woolf & West 2012). These inconsistencies are resolved by allowing gas infall into the system (Tinsley 1975; Hartwick 1976; Tinsley 1977). The simulations used in this thesis avoid the issues of the Simple Model by approximating the cosmological context in which real galaxies form (see Section 1.6.2). As a result, the galaxies analysed within this thesis produce metallicity distributions similar to those observed in the MW (e.g. APOGEE, Abolfathi et al. 2018; GALAH, Buder et al. 2020)

1.4.1 Chemical space

One of the more important diagnostics in the chemical evolution of galaxies is the relative production of chemical elements. Elemental abundances can help infer different properties of stellar populations, including their evolutionary history and origin. An abundance relationship that is used throughout this thesis is between the iron

abundance ([Fe/H]) and the enhancement of α-elements (O, Mg, Si, S, Ca, and Ti), referred to as *chemical space*. Enhancement is defined as the fractional abundance of α-elements versus iron, [α/Fe]. The presence of α-elements plays an important role in the study of chemical evolution. Most α-elements are produced in massive short-lived stars which collapse as Type II supernovae (SNII), while a substantial source of Fe in galaxies is from Type Ia supernovae (SNIa) which are longer-lived sources.

Another important diagnostic is the age-metallicity relation (AMR). AMRs show the relationship between the age and metallicity of stellar populations and, in a closed model, it is expected to exhibit a negative trend with older populations being metal-poor and younger populations being more metal-rich. In the MW, the AMR is surprisingly flat and broad in shape, even when accounting for the large uncertainties in the estimation of stellar ages (Casagrande et al. 2016). The current explanation for the flatness of the Galactic AMR is the contamination of annuli by stars of different metallicities radially migrating into the region.

Trends in chemical space

Different stellar populations can be identified in chemical space. The distribution of stars in chemical space ([Fe/H]-[α/Fe] plane), shows two distinct stellar populations in the Solar Neighbourhood (e.g., Reddy et al. 2006; Adibekyan et al. 2012; Nidever et al. 2014; Snaith et al. 2015). The first track has near-solar [α/Fe] values across a large range of metallicities. The second track has high-[α/Fe] (α-rich) values at low metallicity until [Fe/H] ~ -0.5, after which [α/Fe] experiences a downturn as a function of the metallicity until it reaches and merges with the solar-[α/Fe] track at [Fe/H] ~ 0.2 (Hayden et al. 2015). The delayed onset of SNIa is the likely cause of the downturn in the α-rich track as, prior to the downturn, SNII are the primary source of metals in the ISM. After the downturn, SNIa begin to contribute metals,
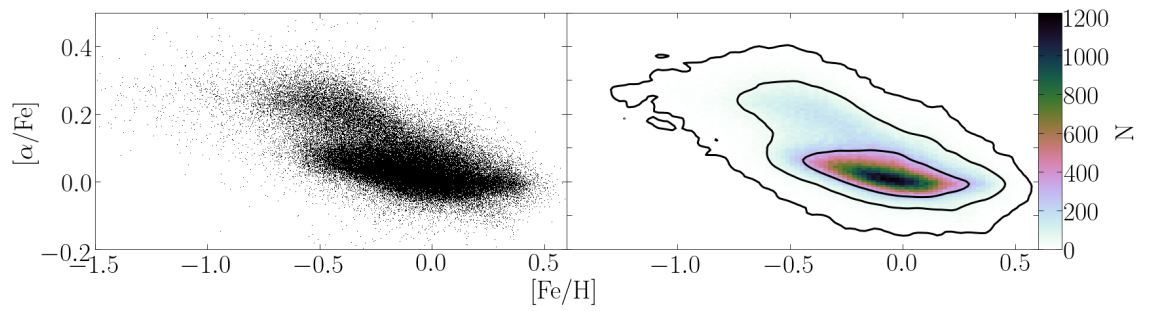
Figure 1.8: The observed [Fe/H] versus [α/Fe] distribution for stars in the solar neighbourhood ($1/\varpi < 3\,\text{kpc}$) from the combined GALAH-APOGEE catalogue (Nandakumar et al. 2020). The left panel is down-sampled and shows only 20% of the observed data points. The right panel shows the number density distribution of the entire sample in the Solar neighbourhood, with contours denoting 1, 2, 3 σ of the overall densities. There are two sequences in the distribution of stars in the [Fe/H]-[α/Fe] plane, one at Solar-[α/Fe] abundances, and the other at high-[α/Fe] abundances.

enriching the ISM primarily in iron peak elements and, consequently, lowering the $[\alpha/\text{Fe}]$ ratio. Figure 1.8 shows the chemical space in the Solar Neighbourhood, which demonstrates the two populations.

The vertical scale-height of the α-rich population has been measured to be much larger than that of the Solar-$[\alpha/\text{Fe}]$ stars (e.g., Bovy et al. 2012a,b,c; Hayden et al. 2015), indicating that they belong to thick disc. The α-rich (thick disc) sequence was found to be similar over a radial range of $5 < \text{R/kpc} < 11$ (Nidever et al. 2014). The general properties that are observed in these thick disc populations are their shorter radial scale-lengths, larger vertical scale-heights, and hotter kinematics than most stars in the Solar neighbourhood (Cheng et al. 2012; Anders et al. 2014). However, some thick-disc stars have been observed to have Solar-$[\alpha/\text{Fe}]$ abundances and very high metallicities (e.g., Adibekyan et al. 2012; Nidever et al. 2014; Snaith et al. 2015). Additionally, a separate metal-poor and α-rich population was recently observed in the chemical space of the Solar neighbourhood, hypothesised to be the result of past merger events (Helmi et al. 2018; Grand et al. 2020).

Warp contamination

The various mechanisms of warp formation described in Section 1.3.1 can have different potential effects on the chemical space of the galactic disc. In the context of chemical evolution, one mechanism of particular interest is the accretion of gas from the CGM. The gas in the CGM is not pristine due to stellar feedback blowing contaminated gas into the corona, however, the CGM is overall metal-poor. Thus, one can assume that the warp populations described in Roškar et al. (2010a) form in the metal-poor accreting gas and, as a result, are expected to occupy the low metallicity and low-α region of chemical space.

CHAPTER 1

1.5 *Gaia*

The launch of the *Gaia* space observatory in late 2013 has impacted the study of the MW with high-resolution astrometric measurements of over 1.8 billion sources. Prior to the launch of the *Gaia* mission (Gaia Collaboration et al. 2016c), reliable stellar kinematics were limited to the Solar neighbourhood (Holmberg et al. 2009) and large scale catalogues had limited resolution (e.g. Hipparcos, Robin et al. 2012). In this section, we will describe the current and upcoming data releases of the *Gaia* mission.

The first data release (DR1, Gaia Collaboration et al. 2016a) delivered astrometric data for 1.1 billion sources. However, the data in DR1 had systematic errors (Lindegren et al. 2016) and did not have full 6D coordinates due to the absence of radial velocity measurements. The second *Gaia* data release (DR2, Gaia Collaboration et al. 2018a), provided data for 1.3 billion sources with a more reliable method of verifying the accuracy of the astrometric solution (Lindegren et al. 2018) and radial velocity measurements for 7 million sources (RV sample, Soubiran et al. 2018). The radial velocities were computed from the spectra of a stellar subset with magnitudes brighter than $G = 12$ using the narrow Gaia Radial Velocity Spectrometer (RVS, Cropper et al. 2018; Sartoretti et al. 2018).

The early instalment of the third *Gaia* data release (eDR3, Gaia Collaboration et al. 2020; Fabricius et al. 2020), increased the total number of observed sources to an unprecedented ~ 1.8 billion. The parallaxes, proper motions, and the $(G_{\mathrm{BP}} - G_{\mathrm{RP}})$ colour were measured for 1.5 billion of those sources. *Gaia* eDR3 shows a significant improvement over DR2, with the systematic errors in the astrometry being suppressed by $30\% - 40\%$ for the parallaxes and by a factor ~ 2.5 for the proper motions (Gaia Collaboration et al. 2020). The full third data release, *Gaia* DR3, will add radial velocities, spectra, light curves, and other parameters for a large subset of the sources (Fabricius et al. 2020).

CHAPTER 1

One of the main challenges in astrometric catalogues are the distance estimates, a challenge also present in *Gaia*. The distance to a source can be estimated by measuring the parallax, ϖ, and taking its inverse, known as the parallax distance, $d_p \equiv 1/\varpi$. The majority of stars in the *Gaia* releases are distant and faint, which results in large ϖ uncertainties, making parallax distances unreliable. Bailer-Jones et al. (2018) demonstrated that the precision of the *Gaia* parallax distances is greatly reduced and becomes increasingly biased beyond a few kpc. Ting & Rix (2019) later confirmed this drop in precision by cross-matching *Gaia* DR2 with a red clump sample from APOGEE (Ting et al. 2018) which are standard candles that can provide accurate photometric distances across the MW. Ting & Rix (2019) showed a strong divergence between the photometric and parallax distances at larger heliocentric distances, d, with a median difference of ~ 0.6 kpc at $d = 4$ kpc between them.

By estimating the stellar distances using a probabilistic approach, it is possible to reduce these uncertainties. Bailer-Jones et al. (2020) estimated the stellar distances using a prior constructed from a three-dimensional model of our Galaxy, which included interstellar extinction and *Gaia*'s variable magnitude limit. They provided two distance estimates: the first estimate is based purely on the parallax, and the other accounts for the parallax, colour, and magnitude of a star (photogeometric distance). Bailer-Jones et al. (2020) found that the photogeometric estimate had higher accuracy and precision for stars with poor parallaxes (faint). Lastly, Schönrich et al. (2019) derived Bayesian distances for all the stars in the RV sample of *Gaia* DR2 and used the method from Schönrich et al. (2012) to validate the resulting distances. As a result of their work, Schönrich et al. (2019) produced a sample of $\sim 7 \times 10^6$ stars with unbiased distances and, therefore, more reliable 6D coordinates in the Galactocentric frame.

The utility of the *Gaia* data is enhanced when cross-matched with ground-based spectroscopic surveys. The combination of astrometric and spectroscopic (e.g. radial

velocities and chemical abundances) data creates a robust framework to study the evolutionary history of the MW. The unprecedented scale of the *Gaia* project is reflected in the planning of contemporary ground-based spectroscopic surveys, as one of their aims is complementing the available and upcoming astrometric data. Cross-matches have and are being performed with surveys such as APOGEE (Majewski et al. 2017), GALAH (Buder et al. 2020; De Silva et al. 2015), GAIA-ESO (Gilmore et al. 2012), and RAVE (Steinmetz et al. 2006; Casey et al. 2017; Kunder et al. 2017) which have been publishing datasets alongside the *Gaia* releases. As the *Gaia* mission operates and accumulates data, with the full DR3 release planned for 2022, future spectroscopic surveys such as the Milky Way Mapper (Kollmeier et al. 2017) and MOONS (Cirasuolo et al. 2012) will continue to complement the Gaia data.

1.5.1   Selected results from *Gaia*

Results from the *Gaia* DR1 and DR2 releases have been extensive and revolutionary in the field of Galactic astronomy (see the reviews of Helmi 2020; Brown 2021). In this section, we will describe selected results from *Gaia* in the Solar neighbourhood that relate to the work done in this thesis, particularly the vertical disc structure and chemodynamics.

Using the *Gaia* DR1 catalogue, Schönrich & Dehnen (2018b) were able to derive the azimuthal, v_φ, and vertical, v_z, velocities for $\sim 1.8 \times 10^5$ stars that were situated along narrow cones in the centre and anti-centre directions. As a result of their kinematic analysis, Schönrich & Dehnen (2018b) found a linear increase in the mean v_z, $\langle v_z \rangle$, distribution versus the vertical angular momentum, L_z and v_φ. This increase was later confirmed in Huang et al. (2018b) who used a cross-match of DR1 with a spectroscopic survey which provided 6D coordinates for $\sim 1.2 \times 10^5$ stars. This increase is considered to be the imprint of the MW warp on the local stellar kinematics. A more peculiar result was the presence of a wave-like pattern in the

$\langle v_z \rangle$ distribution in both the centre and anti-centre directions, possibly caused by a winding warp or a bending wave.

Using the *Gaia* DR2 catalogue, Antoja et al. (2018) selected $\sim 10^6$ stars in the Solar annulus with full 6D coordinates, and discovered a spiral in the vertical phase-space (z-v_z plane). The presence of this phase-space spiral is indicative of ongoing vertical phase mixing in the Solar Neighbourhood in response to vertical perturbations. The source of the perturbations is a subject of debate, however, a widely accepted scenario is that the perturbation was caused by bending waves propagating through the MW disc. A popular hypothesis is that bending waves were excited by the recent passage of the Sgr (Ibata & Razoumov 1998a; Dehnen 1998a; Laporte et al. 2019a) which was brought up in Section 1.3.1 as a possible cause of the MW warp. The accretion of misaligned cooling gas is another potential cause of warps (Section 1.3.1) and a potential source of bending waves in galactic discs (Gómez et al. 2017). With an irregular accretion rate, the gas can continuously perturb the disc, giving rise to bending waves.

In observational astronomy, stellar age is a parameter primarily estimated via stellar models (Soderblom 2010) and it is vital in the study of Galactic archaeology. Stellar ages are prone to large uncertainties when estimated with most models, but there are exceptions such as age estimates from asteroseismology that, in the best case scenario, are accurate to $\sim 10\%$ (Soderblom 2010). Asteroseismology further constrains the widely used stellar models using the oscillation modes detected in stellar photometry. However, the requirement of high-quality photometry over a long time baseline and the inherent limitations in the stellar models make it unsuitable for *Gaia*. A method that is widely used in modern astrophysics and has been successfully applied to the *Gaia* cross-matches is isochrone fitting. Isochrones are curves of constant age in the Hertzsprung-Russell diagram (HRD) that are calculated by fitting evolutionary models of main-sequence stars to the observed HRD.

The uncertainties from isochrone age estimates are, on average, very large ranging from 20% to 50% (Jørgensen & Lindegren 2005), but by constraining the stellar models with more observable parameters, the accuracy can be improved. Sanders & Das (2018a) calculated the distance, age, and mass estimates for ~ 3 million stars from the cross-match of *Gaia* DR2 and six spectroscopic surveys; we refer to this dataset as SD18. The estimates were produced using a Bayesian framework that characterised the probability density function of the three parameters using photometric, spectroscopic and astrometric data. The ages in SD18 are estimated to be accurate to $15\% - 20\%$ for giant stars and $20\% - 30\%$ for turn-off stars. A dataset of this scale, though relatively small when compared to the entire *Gaia* dataset, becomes a valuable tool in studying stellar populations based on their kinematics, chemistry, and age.

1.6 Simulations

Numerical simulations are essential in the study of secular and chemical processes in galaxies and can be broadly characterised by the phenomena that they account for in their models. A widely used type of simulation, due to its relatively low computational cost, is one that only accounts for the gravitational interactions between particles, referred to as N-body. The other broad group of simulations are hydrodynamical, which, in addition to gravitation, account for the hydrodynamical processes that take place in gas (e.g. star formation, feedback, chemical enrichment). The inclusion of hydrodynamics significantly increases the computational costs of simulations, however, it provides further insight into many evolutionary processes that occur in galaxies.

1.6.1 N-body simulations

The first N-body simulation was carried out by Holmberg (1941) using a set-up of 37 lightbulbs to model the tidal deformations of two merging spiral galaxies. The computational limitations of the time prevented any significant progress in the use of N-body simulations, but with the development of faster computers, N-body simulations would become more commonplace. Using variable time-steps, von Hoerner (1960) was able to limit the number of force computations and successfully ran the first fully computational N-body simulation with $N = 16$ particles. In the span of a decade, the particle counts in such simulations would increase by factors of ~ 5 (Aarseth 1963) and ~ 20 (Peebles 1970) and with further advances in computer technology and calculation methods, current N-body simulations can reach particle counts of $N \sim 10^{12}$ (Potter et al. 2017).

Variable timesteps significantly reduced the computation times in simulations, however, older simulations (e.g. von Hoerner 1960) with N particles were performed using direct integration between individual particle pairs, increasing the computations as N^2. To reach the particle counts and running times of modern simulations, the methods of approximating gravitational calculations had to improve. The tree algorithm, first implemented in Appel (1985) and further developed by Barnes & Hut (1986), is a popular method used in modern simulations. The main principle of the tree algorithm is the construction of an *octree*, a recursive sub-division of space into eight equal octants until each spatial cube, referred to as a *leaf*, contains a single particle. Upon construction, the code will begin traversing the octree and evaluating at each stage if the following criterion is satisfied

$$l/D < \theta \tag{1.8}$$

where l is the size of the cell, D is the distance between the particle and cell's centre of mass (COM), and θ is a dimensionless parameter that controls the accuracy, referred to as the *opening angle*. The opening angle is commonly set to be $\theta \sim 1$,

and when the condition in Eq. 1.8 is satisfied, the particles are merged into a pseudo-particle that inherits the cell's COM. When the condition is not satisfied, the cell is further opened up into sub-cells, and the process is repeated. The traversing method accounts for both densely and loosely distributed particles, thereby significantly reducing the number of calculations needed to integrate the system. Compared to the direct integration methods, the number of calculations in tree code simulations with N particles scales as $N \log(N)$, a significant improvement.

The advances in computing power and tree code methods improved the scale of N-body simulations, but their resolution, when compared to real astrophysical systems, is significantly limited. As a result, particles are usually modelled with larger masses, e.g. the particles found in the models used in this thesis have a mass range of $\sim 10^5 - 10^6 \mathrm{M}_\odot$, but these high masses lead to unphysical interactions between particles. Close encounters between massive particles require shorter time-steps, thereby making time integration more expensive. Massive particles can also experience large-angle scatterings and the formation of bound particle pairs. These issues can be circumvented by representing the particles as extended masses, i.e. smoothing their potentials instead of having them interact as point sources. This potential smoothing will soften the interactions between massive particles when close encounters occur. A common smoothing potential that is used in modern simulations is the Plummer sphere:

$$\Phi(r) = \frac{1}{\sqrt{r^2 + \epsilon^2}} \tag{1.9}$$

where r is the separation between the particles and ϵ is a constant generally referred to as the *smoothing length*. White (1979) derived the minimum smoothing length required to avoid unrealistic scattering between particles:

$$\epsilon \sim \frac{G\mu}{\sigma^2} \tag{1.10}$$

where μ and σ are the mean mass and velocity dispersion. There is no clear upper limit for the smoothing length, but as ϵ increases, there will be further loss of spatial resolution in the simulations. A typical value set for the smoothing length in cosmological simulations is $2 - 4\%$ of the mean inter-particle distance.

1.6.2 Smoothed particle hydrodynamics

N-body simulations only model the gravitational interactions between particles and are a useful tool in the study of large-scale structures (DM halos), the dynamics of stellar discs, and dense stellar systems (clusters). The inclusion of gas hydrodynamics will more accurately simulate the structural and chemical evolution of galaxies. Smoothed particle hydrodynamics (SPH) account for the hydrodynamical processes by partitioning the gas into particles and following the motions of the particles with a Lagrangian approach. The use of a Lagrangian approach makes the SPH method especially useful in the study of galactic discs as it conserves angular momentum. This method was originally introduced by Lucy (1977), and Gingold & Monaghan (1977) and has been widely used in galactic simulations since then (e.g Monaghan 1992, 1997, 2005; Springel 2005; Rosswog 2009; Roškar et al. 2010a). Every gas particle in SPH is assigned a smoothing length, h, such that a set number of particles (neighbours), N_{smooth}, is contained within $2h$. The simulations used throughout this thesis use the SPH method with the recommended value of $N_{\text{smooth}} = 32$ (Stinson et al. 2006a).

Hydrodynamical processes that occur in the gas can be accounted for in N-body+SPH simulations, including the formation of stars and their effect on the ISM. Stellar particles form when gas particles have their number density exceed a set value (star formation threshold), their temperature is below a certain threshold, and the gas is part of a converging flow. A formed star inherits the chemical composition and set mass fraction of the parent gas particle. The resulting star particles experience

evolutionary processes such as stellar winds, Type Ia, and Type II supernovae, all resulting in the redistribution of gas and injection of energy into the ISM. These processes provide a feedback mechanism in galactic simulations.

Leftover gas is blown into the ISM via stellar winds, while the supernovae redistribute the now enriched gas and inject their energy into the ISM. The supernovae energy is of the order $\sim 10^{50}$erg and is powerful enough to heat the surrounding gas to temperatures of $T \gtrsim 10^6$K, *i.e.* hot enough to be ejected from the galactic disc (Dekel & Silk 1986). Supernovae regulate star formation by heating the surrounding gas and preventing it from collapsing into new stars (Silk 2003). As the star particles represent entire stellar populations and the supernovae are very short-lived processes, supernovae cannot be modelled directly in simulations without the use of sub-grid methods. One of the currently accepted methods is the one prescribed by Stinson et al. (2006a) which uses the blastwave approximation (Chevalier 1974; McKee & Ostriker 1977) to calculate the maximum blast radius within which gas cooling is temporarily suppressed. The supernova phase sets the timescale of the cooling and, realistically, should be of the same order as the Sedov phase, during which gas cannot cool efficiently. This phase is estimated to last for $\sim 10^{-6}$Gyr (Padmanabhan 2001), which is far below the temporal resolution of our simulations. We, therefore, use a cooling time equivalent to the snowplough phase of the supernova during which the excess thermal energy is radiated away, and the momentum of the blastwave is conserved (McKee & Ostriker 1977; Cioffi et al. 1988).

1.7 Context for this thesis

The origin of galactic warps continues to be a subject of debate with numerous hypotheses being investigated both theoretically and in simulations (Sellwood 2013). A topic that has not been studied as extensively is the role a warp has on galactic structure, more specifically a warp formed via gas accretion (e.g. Roškar et al. 2010a;

CHAPTER 1

Gómez et al. 2017). The recent discovery of the *Gaia* phase-space spiral (Antoja et al. 2018) indicates that the MW disc is being perturbed. Some sources that are hypothesised to be the source of this perturbation are also potential causes of the Galactic warp (Ibata & Razoumov 1998a; Dehnen 1998a; Laporte et al. 2018d, 2019a). Gómez et al. (2017) used fully cosmological simulations to show that all prevalent warp forming mechanisms can create complex vertical substructures, but the gas accretion scenario produced bending waves in the youngest populations and cold gas only. These results could imply that the perturbing force of accreting gas is only strong enough to affect younger midplane stars. In this thesis, we look at isolated N-body+SPH simulations and quantify the impact misaligned accreting gas has on the disc.

Using N-body+SPH simulations, Roškar et al. (2010a) were able to show that stars born in the warp populate the geometric thick disc, which is indicative of a vertically hot population. Additionally, the medium in which warp stars form, *i.e.* metal-poor accreting gas, implies that warp stars could occupy a unique region of chemical space. With the discovery of young stellar populations in the Galactic warp (Chen et al. 2019b), an important question is raised regarding warp stars settling into the disc and how distinct they are given the current observations. By studying the chemical space of N-body+SPH simulations, we will investigate how warp stars in the Solar Neighbourhood differ from other stellar populations in chemical, dynamical and kinematic properties. After defining these properties, we will test how likely warp stars are to be observed in the *Gaia* catalogue and produce a sample of warp star candidates. With available ages for the warp star candidates (Sanders & Das 2018a) this thesis will attempt to give an age estimate for the Galactic warp and determine if it is a long-lived structure.

Chapter 2

Simulations considered

In this chapter, we describe the simulations used throughout this thesis which are grouped into two categories: warped and unwarped. As described in Chapter 1.6, our simulations use the SPH method. This thesis considers one unwarped model, UM, and four warped models, WM1 through WM4. The following sections will describe the general setup and initial conditions for the models, following with their differentiating parameters, and ending on our pre-processing procedures.

2.1 Warped models

The warped models were produced via the method of Debattista et al. (2015), which constructs triaxial dark matter models with gas angular momentum misaligned with the principal axes of the halo. The resulting misalignment mirrors that found in cosmological simulations (van den Bosch et al. 2002a; Roškar et al. 2010a; Gómez et al. 2017; Earp et al. 2019). Aumer & White (2013) have shown that inserting a rotating gas corona into a non-spherical dark matter halo leads to a substantial loss of gas angular momentum. Therefore, this approach already includes adiabatic gas while merging haloes to produce a non-spherical system. We merge two identical spherical Navarro–Frenk–White (NFW) (Navarro et al. 1996) dark matter haloes,

each of which has a co-spatial gas corona comprising 10 per cent of the total mass.

Each dark matter halo has a mass $M_{200} = 8.7 \times 10^{11}\,\mathrm{M_\odot}$ and virial radius $r_{200} \simeq 200\,\mathrm{kpc}$. The gas is in pressure equilibrium within the global potential. Gas velocities are initialised to give a spin parameter of $\lambda = 0.16$ (Bullock et al. 2001), with specific angular momentum $j \propto R$, where R is the cylindrical radius. Both the dark matter halo and the gas corona are comprised of 10^6 particles. Gas particles initially have masses $1.4 \times 10^5\,\mathrm{M_\odot}$ with the softening dependant on the warped model, with $\epsilon = 20\,\mathrm{pc}$ in WM1-2, and $\epsilon = 50\,\mathrm{pc}$ in WM3-4. The dark matter for all models comes in two mass flavours ($10^6\,\mathrm{M_\odot}$ and $3.6 \times 10^6\,\mathrm{M_\odot}$ inside and outside 200 kpc, respectively) and $\epsilon = 100\,\mathrm{pc}$.

The two halos are placed 500 kpc apart and approach each other head-on at $100\,\mathrm{km\,s^{-1}}$. If the direction of the separation vector (and the relative velocity) is the x-axis, we tilt one of the halos about the y-axis so that the final system will be prolate with long axis along the x-axis and a gas angular momentum tilted with respect to the axes of the halo. The setup of the merging haloes is part of the initial conditions, so it does not count towards the time elapsed in the models, which starts with the initiation of star formation.

Each model is evolved using the N-body+SPH code GASOLINE (Wadsley et al. 2004) with a base time-step dependant on the model with $\delta t = 10\,\mathrm{Myr}$ for WM1 and $\delta t = 100\,\mathrm{Myr}$ for WM2-4. For individual particles, the base time-step is refined such that each particle satisfies the condition $\delta t = \delta t/2^n < \eta\sqrt{\epsilon/a_g}$, where a_g is the acceleration at the particle's current position, with $\eta = 0.175$, and the opening angle of the tree code calculation set to $\theta = 0.7$. The WM1-2 models are evolved for 12 Gyr while WM3-4 are only evolved for 10 Gyr.

The result of this setup is a dark matter halo that has $r_{200} = 238\,\mathrm{kpc}$ and $M_{200} = 1.6 \times 10^{12}\,\mathrm{M_\odot}$, and gas with $\lambda = 0.11$. At this point ($t = 0\,\mathrm{Gyr}$) we turn on gas cooling, star formation, and stellar feedback using the blastwave prescriptions

of Stinson et al. (2006b). Gas particles form stars with a 10% efficiency if a gas particle has temperature $T < 15,000$ K, is part of a converging flow, and its number density exceeds a model-dependant value. The density thresholds are $n > 1$ cm^{-3} (medium threshold) in the WM1-2 models, $n > 0.1$ cm^{-3} (low threshold) in WM3, and $n > 100$ cm^{-3} (high threshold) in WM4.

Star particles form with an initial mass of 1/3 that of the initial gas particle masses, which at our resolution corresponds to 4.6×10^4 M$_\odot$. The softening of the star particles is also dependant on the warped model, with $\epsilon = 20$ pc in WM1-2, and $\epsilon = 50$ pc in WM3-4. Once the mass of a gas particle drops below 1/5 of its initial mass, the remaining mass is distributed amongst the nearest neighbouring gas particles, leading to a decreasing number of gas particles. Each star particle represents an entire stellar population with a Miller–Scalo (Miller & Scalo 1979) initial mass function. The evolution of star particles includes asymptotic giant branch stellar winds and feedback from Type II and Type Ia supernovae, with their energy injected into the interstellar medium (ISM). Each supernova releases 10^{50} erg into the ISM. The time-step of gas particles also satisfies the condition $\delta t_{gas} = h\eta_{courant}/[(1+\alpha)c + \beta\mu_{max}]$, where h is the SPH smoothing length, $\eta_{courant} = 0.4$, $\alpha = 1$ is the shear coefficient, $\beta = 2$ is the viscosity coefficient and μ_{max} is described in Wadsley et al. (2004). The SPH kernel uses the 32 nearest neighbours. In models WM1-2 gas cooling takes into account the gas metallicity using the prescriptions of Shen et al. (2010); in order to prevent the cooling from dropping below our resolution, we set a pressure floor on gas particles of $p_{floor} = 3G\epsilon^2\rho^2$, where G is Newton's gravitational constant, and ρ is the gas particle's density (Agertz et al. 2009).

Model name	WM1	WM2	WM3	WM4	UM
Final timestep [Gyr]	12	12	10	10	12
δt [Myr]	10	100	100	100	5
M_{200} [10^{11} M$_\odot$]	8.7	8.7	8.7	8.7	10
$\epsilon_{\text{star}}/\epsilon_{\text{gas}}/\epsilon_{\text{dm}}$ [pc]	20/20/100	20/20/100	50/50/100	50/50/100	50/50/100
Metal line cooling	on	on	off	off	off
Star formation efficiency [%]	10	10	10	10	5
Star formation threshold [cm^{-3}]	1	1	0.1	100	0.1
Supernova feedback [10^{50} erg]	1	1	1	1	8

Table 2.1: Varying parameters of the considered models.

2.2 Unwarped model

The UM model is the M1 simulation described in Fiteni et al. (2021). The model is similar to the spherical models we start with in the warped models, except it has a single NFW dark matter halo with a virial radius of $r_{200} \simeq 200$ kpc, a virial mass of $M_{200} = 10^{12}$ M$_\odot$ and a gas angular spin of $\lambda = 0.065$ (Bullock et al. 2001). Feedback via supernova explosions again employs the blastwave prescription (Stinson et al. 2006b). The feedback from supernovae is set to 8×10^{50} erg per supernova, which is higher than in the warped models. Similar to models WM3-4, the cooling does not account for the gas metallicity and the softening parameters are $\epsilon = 50$pc for gas and star particles and $\epsilon = 100$ pc for dark matter. Star formation efficiency in the UM model is set to 5% with a density threshold of $n >$0.1 cm^{-3} (low threshold). The UM model is also evolved using the N-body+SPH code GASOLINE for 12 Gyr and with the same tree code setup as in the WM1-4 models, however, we use a base time-step of $\delta t = 5$ Myr. Finally, Table 2.2 shows the parameters that vary between all of the models used throughout this thesis.

2.3 Simulation pre-processing

The simulation snapshots of each model are processed through our custom PYTHON library suite that utilises functions from the PYNBODY library. The suite centres the galactic disc and then rotates it into the (x, y) plane based on the angular momentum of the inner stellar disc, defined by $r \leq 5$ kpc. For the warped models we compute the angular momentum of the misaligned cold gas ($T_{gas} < 50,000$K) at the outer edge of the galactic disc ($15 \leq R/\,\text{kpc} \leq 20$) to determine the orientation of the gas warp. Each snapshot is rotated by the cylindrical angle of the warp's angular momentum, φ_L, so that the warp's major axis is on the x-axis and, consequently, the line of nodes is on the y-axis. The UM model has no warp therefore we do not preform any reorientation based on the gas. The disc of each model is finally rotated $180°$ about the y-axis to match the sense of rotation and warp orientation of the Milky Way (Chen et al. 2019a). As a result of these rotations, the south side of the gas warp (below the mid-plane) is along the positive x-axis. This orientation is implied throughout this thesis.

The rotation curves of all five models at their respective final timesteps (see Table 2.2) are presented in Figure 2.1. The potentials in each model were interpolated using the AGAMA software library (Vasiliev 2019) with a single multipole approximation for the stellar, gas, and dark particles combined. Rotation curves of the approximated potentials are presented in Figure 2.1 as dashed red lines. Similar to the Milky Way, the rotation curves of all five models are relatively flat, though some models (WM1, WM2, and UM) have a higher stellar density in the centre and therefore a spike in the rotation curve at ~ 1 kpc.
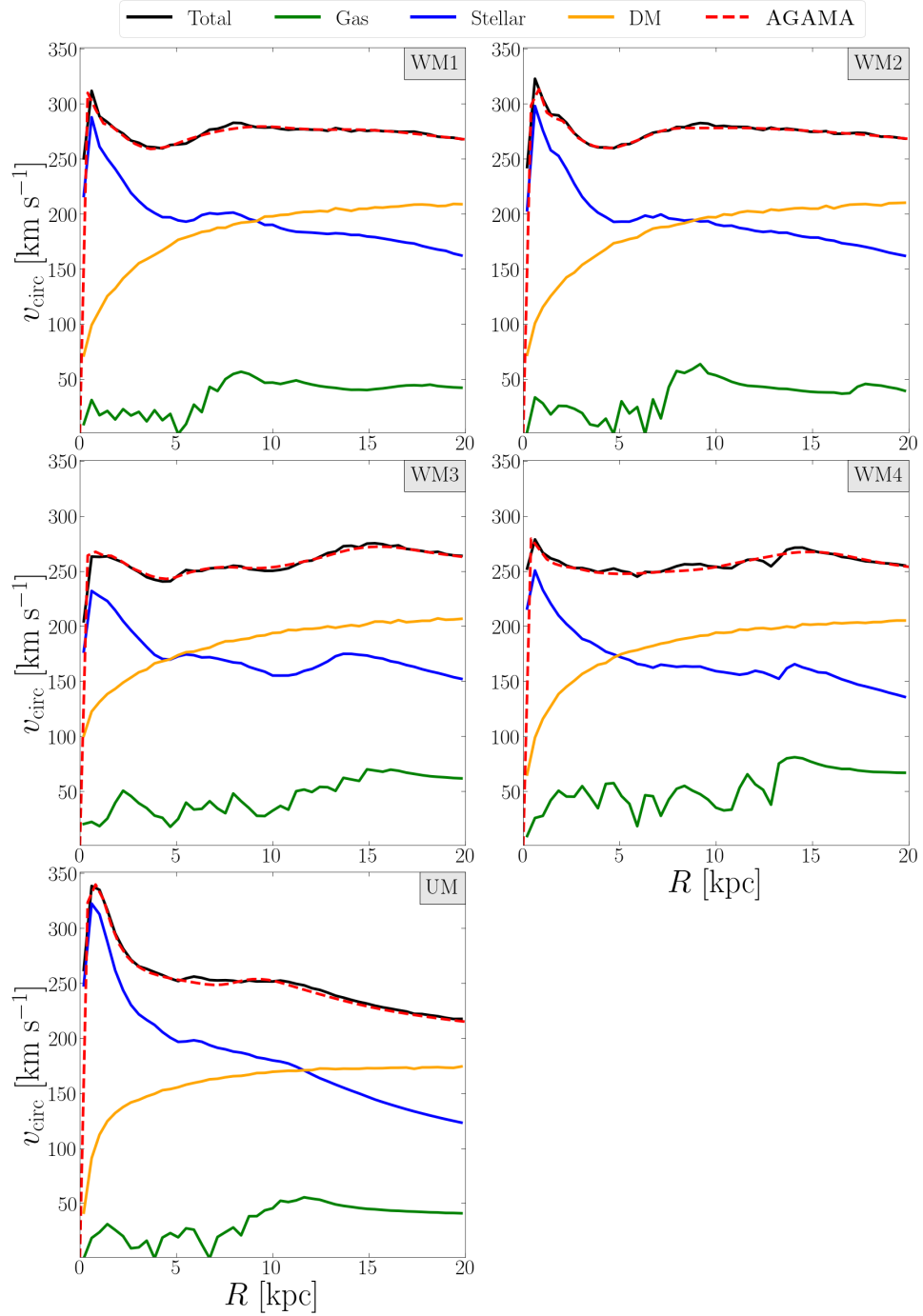
Figure 2.1: Rotation curves of all five models at their respective final timesteps (see Table 2.2), with each model indicated in the upper right corner. Solid lines represent the rotation curves of each galactic component along with a total rotation curve, while the interpolated total potential (computed with AGAMA, Vasiliev 2019) is represented by the dashed red lines.

Chapter 3

Warp star settling

This chapter is based on a paper submitted to MNRAS as Tigran Khachaturyants, Leandro Beraldo e Silva, Victor P. Debattista. The warped simulation used throughout this chapter is the WM2 model.

3.1 Abstract

In recent years star formation has been discovered in the Milky Way's warp. These stars formed in the warp (warp stars) must eventually settle into the plane of the disc. We use an N-body+smooth particle hydrodynamics model of a warped galaxy to study how warp stars settle into the disc. By following warp stars in angular momentum space, we show that they first tilt to partially align with the main disc in a time scale of $\sim 1\,\mathrm{Gyr}$. Then, once differential precession halts this process, they phase mix into an axisymmetric distribution on a time scale of $\sim 6\,\mathrm{Gyr}$. The warp stars end up populating the geometric thick disc. Because the warp in our simulation is growing, the warp stars settle to a distribution with a negative vertical age gradient as younger stars settle further from the mid-plane. While vertically extended, warp star orbits are still nearly circular and they are therefore subject to radial migration. As a result warp stars can be found throughout the disc. The

density distribution of a given population of warp stars evolves from a torus to an increasingly centrally filled-in density distribution.

3.2 Introduction

Warps are common features in most disc galaxies, as observed in their HI gas (Sancisi 1976; Bosma 1991; García-Ruiz et al. 2002c) and, to a lesser extent, in their stars (Reshetnikov et al. 2002). In the Milky Way (MW), a warp in the HI has long been known (Kerr 1957b; Weaver & Williams 1974; Levine et al. 2006b; Kalberla et al. 2007b), while a stellar warp, traced by red clump (RC) stars, has been observed more recently (López-Corredoira et al. 2002b). The maximum amplitude of the RC and HI warps in the MW are not only coincident in their orientation but also in their amplitude, reaching vertical displacements $|z| \sim 1.5\,\mathrm{kpc}$ at $R = 14\,\mathrm{kpc}$ and galactocentric azimuth $\phi \approx 85°$ on the south side (below the mid-plane), while on the north side (above the mid-plane) the coincidence holds up to $R \leq 13\,\mathrm{kpc}$ (López-Corredoira et al. 2002b).

The cause of warping in galactic discs is still not definitively established, with several mechanisms proposed (see the reviews of Binney 1992; Kuijken & Garcia-Ruiz 2001; Sellwood 2013). These include tidal interactions, direct gas accretion, and disc-halo interactions. In the MW, tidal interaction with the Large Magellanic Cloud (LMC) and the Sagittarius dwarf galaxy (Sgr) have been considered possible sources of the warping (Weinberg 1998; Jiang & Binney 1999; Bailin 2003; Purcell et al. 2011b; Gómez et al. 2013b; Laporte et al. 2018b). Alternatively, misaligned cold gas accretion has been proposed (Ostriker & Binney 1989a) and found in simulations, particularly in MW-like models (Roškar et al. 2010a; Gómez et al. 2017). This scenario could explain the persistence of warps as gas is continuously accreted on to the outskirts of discs. Evidence of cold gas accretion has been inferred in external galaxies via large complexes of HI at the outskirts of spiral galaxies (Fraternali &

Binney 2008; Sancisi et al. 2008b; Westmeier et al. 2011; Zschaechner et al. 2015). In the case of the MW, the gas accretion scenario not only provides an explanation for the origin of the warp but also for the near-constant star formation rate in the Solar neighbourhood (Twarog 1980b; Binney et al. 2000b). Nonetheless, direct observational evidence for continuous accretion of gas is still lacking.

Using data from Gaia-DR2 (Gaia Collaboration et al. 2018b) and from the *Wide-field Infrared Survey Explorer* (*WISE*) catalogue of periodic variables (Chen et al. 2018a), Chen et al. (2019a) compiled a sample of classical Cepheids, finding that the Galactic warp is also traced by these stars. This implies that stars are forming in-situ in the warp. Understanding where these stars end up can shed light on the formation and evolution of the warp, and consequently on the evolution of the MW as a whole. Of all the warp tracers Chen et al. (2019a) considered (including dust, pulsars, RC stars), they found that the Hɪ gas and Cepheids are the most similar in their distributions, implying that the Cepheids have to form in-situ in the warp. Evidence of star formation on the outskirts of galactic discs has also been inferred in external galaxies via UV-bright stellar complexes (Thilker et al. 2005b; Zaritsky & Christlein 2007b; Herbert-Fort et al. 2010b; Mondal et al. 2019). The UV-bright stellar complexes were observed far outside the optical discs where warps are usually observed, and in one case (Thilker et al. 2005b) these complexes were associated with the warped Hɪ disc.

Roškar et al. (2010a) presented a fully cosmological simulation of a Milky Way-like galaxy in which its hot gaseous corona has angular momentum misaligned with that of the disc. The gas cools and sinks toward the stellar disc, forming a warp. Stars formed in this warp settle into the disc and populate the geometric thick disc (see Figure 13 in Roškar et al. 2010a). In this paper, we use a warped N-body+SPH (Smooth Particle Hydrodynamics) simulation to investigate, in further detail, the settling of stars formed in the gas accreting along a warp.

The paper is organised as follows: In Section 3.3 we describe the evolution and extent of the gas warp and in Section 3.4 describe how stars formed in the warp (hereafter, 'warp stars') are defined in the simulation. In Section 3.5 we analyse different warp populations separated by their time of formation and track the changes of their angular momenta throughout the simulation's evolution. In Section 3.6 we turn our attention to the resulting density distribution of warp stars in the disc. In Section 3.7 we present our conclusions, before ending with a summary of our results.

3.3 Warp evolution

The extent of the simulation's gas warp is shown in the top row of Figure 3.1 where we present the edge-on column density of cold gas at 2 Gyr (left) and 12 Gyr (right). In the span of 10 Gyr the warp grows significantly in radial extent, and becomes more inclined relative to the disc. To quantify the inclination and orientation of the warp, for each component (stars and cold gas), we measure the spherical angles θ_L (polar) and ϕ_L (azimuthal) between their angular momenta, measured within spherical annuli, and the inner stellar disc. As the angular momentum vector of the stellar disc has been realigned along the z-axis for all times, θ_L and ϕ_L are simply:

$$\phi_L = \arctan(L_y/L_x), \tag{3.1}$$

and

$$\theta_L = \arccos(L_z/|L|), \tag{3.2}$$

where L_x, L_y, L_z, and $|L|$ are the three Cartesian components and magnitude of the angular momentum, respectively. In the bottom row of Figure 3.1 we present Briggs figures (Briggs 1990a) for the stellar (black) and cold gas (red) discs at 2 Gyr (left) and 12 Gyr (right), where the triangle (square) marker represents $R = 10$ kpc ($R = 20$ kpc). Briggs figures are cylindrical polar plots where θ_L and ϕ_L are represented by the polar r and ϕ coordinates, respectively. The θ_L and ϕ_L angles are
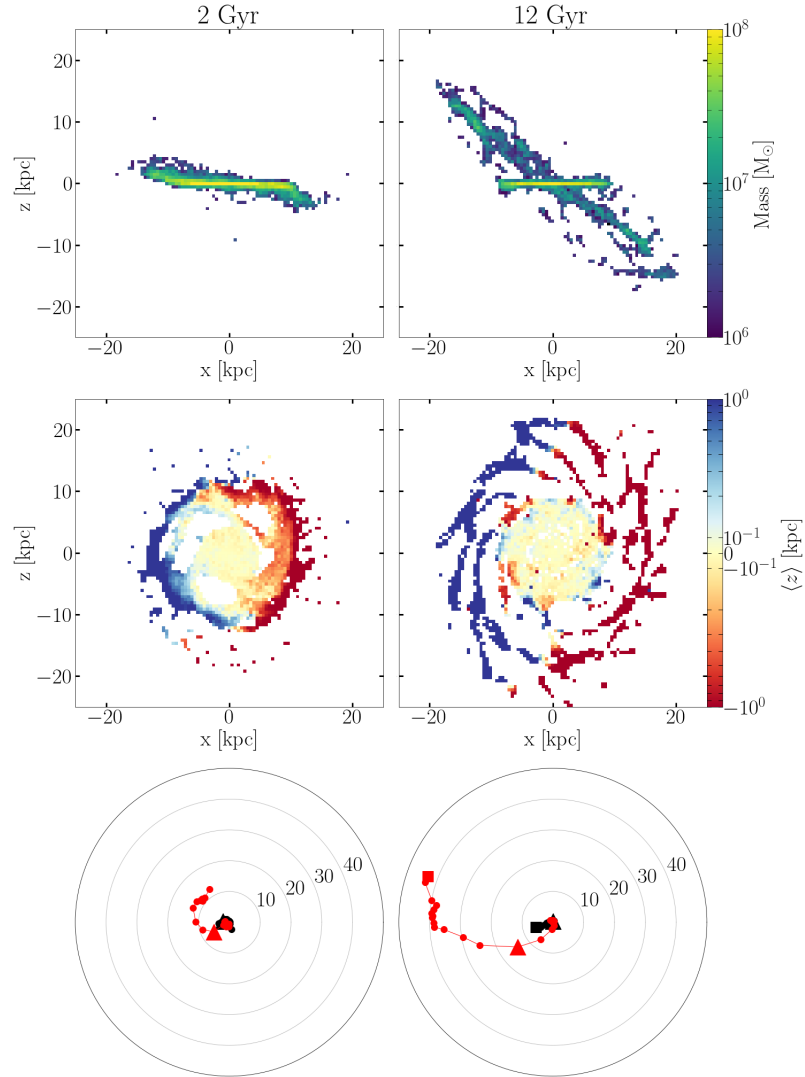
Figure 3.1: The structure of the gas warp at 2 Gyr (left column) and 12 Gyr (right column). Top row: The edge-on column density distribution of cold gas (T$\leq 50,000$ K) in the simulation. In the span of 10 Gyr, the gas warp can be traced to larger R (from $R \sim 13$ kpc to $R \sim 20$ kpc) and $|z|$ (from $|z| \sim 5$ kpc up to $|z| \sim 20$ kpc). Middle row: the face-on mean height, $\langle z \rangle$, distribution of cold gas (T$\leq 50,000$ K) in the simulation. Bottom row: The Briggs figures for the cold gas (red) and stellar (black) discs. There are two distinct markers that show values at $R = 10$ kpc (star marker) and at $R = 20$ kpc (square marker). The Briggs figures show that the gas disc becomes significantly more warped between the two times, while the stellar disc is initially slightly warped ($\theta_L \sim 2°$ at $R = 10$ kpc) and becomes even less so by the end ($\theta_L \sim 0.3°$ at $R = 10$ kpc).
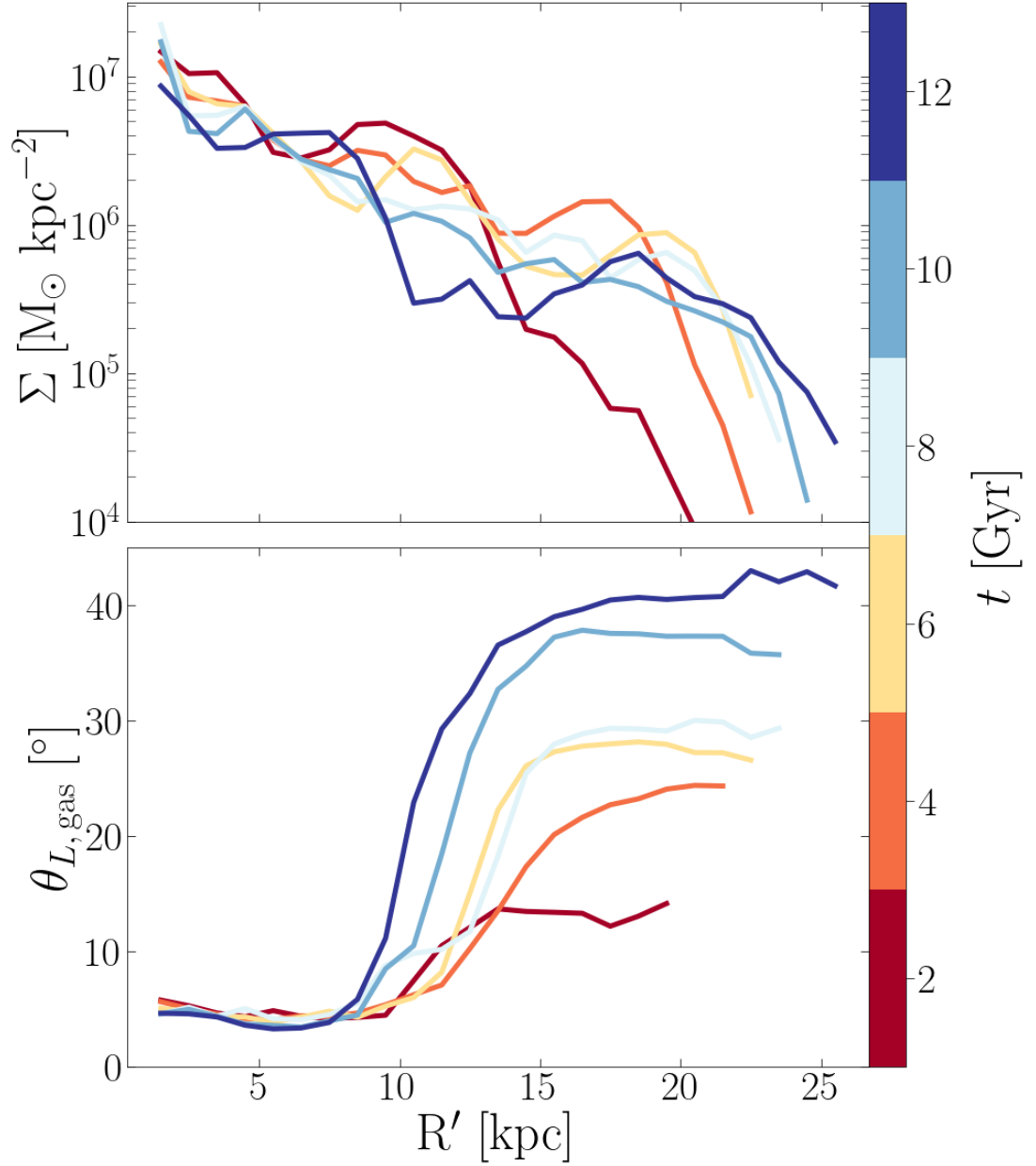
Figure 3.2: Profiles of the surface density, Σ, (top) and $\theta_{L,\mathrm{gas}}$ (bottom) in the cold gas at different times (colour), where R' is defined as the cylindrical radius in the cold gas plane at each annulus. The gas warp grows horizontally and becomes more inclined with time.

calculated for the mean angular momentum vector in each bin of a cylindrical grid with $0 \leq R/\text{kpc} \leq 20\,\text{kpc}$ and $\Delta R = 1\,\text{kpc}$. The cold gas warp grows significantly over the 10 Gyr interval, while the stellar warp decreases in extent, and then flattens over the same time interval. In Figure 3.2 we show the profiles of the surface density, Σ, (top) and of $\theta_{L,\,\text{gas}}$ (bottom) for the cold gas disc at different times (colour), where R' is defined as the cylindrical radius in the cold gas plane at each annulus. Over the model's evolution, the inclination of the cold gas warp beyond 10 kpc increases by a factor ~ 4, reaching $\theta_L \sim 40°$. The warp also grows in mass and size as the Σ profile increases beyond 15 kpc and reaches $R' \sim 25\,\text{kpc}$ by the end of the simulation.

3.4 Defining warp stars

We record the phase-space coordinates and time at formation, t_{form}, for every star in the simulation. The phase-space coordinates need to be centred and reoriented relative to the disc at their respective t_{form}. Using our PYTHON library suite, we create an interpolating function that takes into account the centre of mass and angular momentum vector of the galactic disc at each 100 Myr saved snapshot. We calculate the location of the centre of mass and orientation of the galactic disc for each star by interpolating to their individual t_{form}. This procedure gives the formation location in galaxy centred coordinates, and the inclination of the star's angular momentum at formation relative to that of the galactic disc (θ_{form}).

To identify warp stars (*i.e.* stars born in the warp), we use θ_{form} and the cylindrical formation radius, R_{form}. We plot the distribution of all stars in this space, which we will refer to as the *formation space*. In Figure 3.3 we present the distribution of the mean time of formation, $\langle t_{\text{form}} \rangle$, (top) and the mean absolute height of formation, $\langle |z_{\text{form}}| \rangle$, (bottom) in the formation space. The "tail-like" region at $R_{\text{form}} > 10\,\text{kpc}$ (outlined by a red square) is comprised of stars that formed at relatively high $|z_{\text{form}}|$,
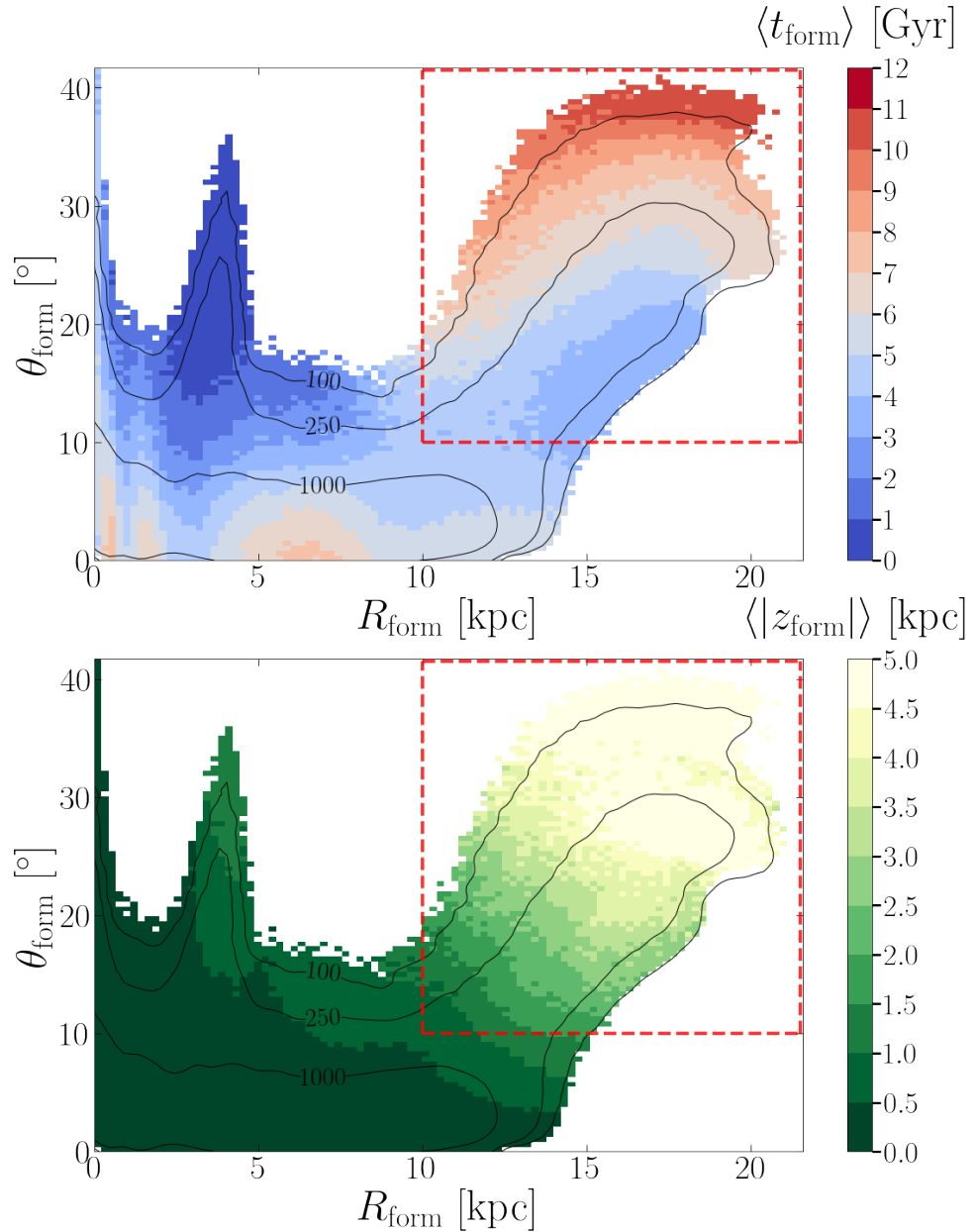
Figure 3.3: The distribution of stars in the R_{form}-θ_{form} space (formation space), coloured by the mean time of formation (top) and by the mean absolute formation height, $\langle |z_{\mathrm{form}}| \rangle$, (bottom). The black lines show the number counts in the formation space for both panels. We define stars formed in the warp as those with $\theta_{\mathrm{form}} \geq 10°$ and $R_{\mathrm{form}} \geq 10\,\mathrm{kpc}$, the "tail-like" region outlined by the red square. A population of stars that was formed in an early, transient warp at low radii ($R_{\mathrm{form}} \leq 7\,\mathrm{kpc}$) and high inclinations relative to the disc ($\theta_{\mathrm{form}} \geq 10°$) is not included in our warp star population.

which increases with t_{form}. These stars are formed throughout the model's evolution starting from 2 Gyr and lasting till the end of the simulation, at 12 Gyr. This population is highly inclined ($\theta_{\mathrm{form}} > 10°$) and is formed on the outskirts of the disc; thus we define the primary warp population as stars with $R_{\mathrm{form}} \geq 10 \,\mathrm{kpc}$ and $\theta_{\mathrm{form}} \geq 10°$. There are $\sim 6 \times 10^5$ warp stars in the simulation and they comprise 13% of all stars. The other significant populations that we observe are the in-situ main disc population ($R_{\mathrm{form}} \leq 10 \,\mathrm{kpc}$ and $\theta_{\mathrm{form}} \leq 10°$), and a "hump-like" region containing an old warp population ($2 \leq R_{\mathrm{form}}/\,\mathrm{kpc} \leq 5$ and $\theta_{\mathrm{form}} \geq 15°$). This early warp population derives from a short-lived warp epoch when the model is still settling, and we therefore do not include it in our analysis of the warp. Neglecting this population does not change any of the following results.

3.5 Dynamical evolution of warp populations

We study how warp stars settle into the disc by considering mono-age populations. Our goal is to unravel the mechanisms by which they settle and reach equilibrium within the main disc, the timescale for settling, and the (evolving) density distribution they settle to.

3.5.1 Overall evolution

Figure 3.4 presents the mass distribution in Briggs figures for 4 representative mono-age warp populations (columns) at various times after their formation, denoted by δt. The Briggs figures provide a clear picture of how warp stars start out heavily inclined relative to the disc (outer regions in the diagrams) and end up phase mixing into a homogeneous distribution. All populations form along the gas warp, indicated by the solid red lines in the first row. The gas warp traces a leading spiral shape (the sense of disc rotation in these figures is clockwise), which is one of the characteristics
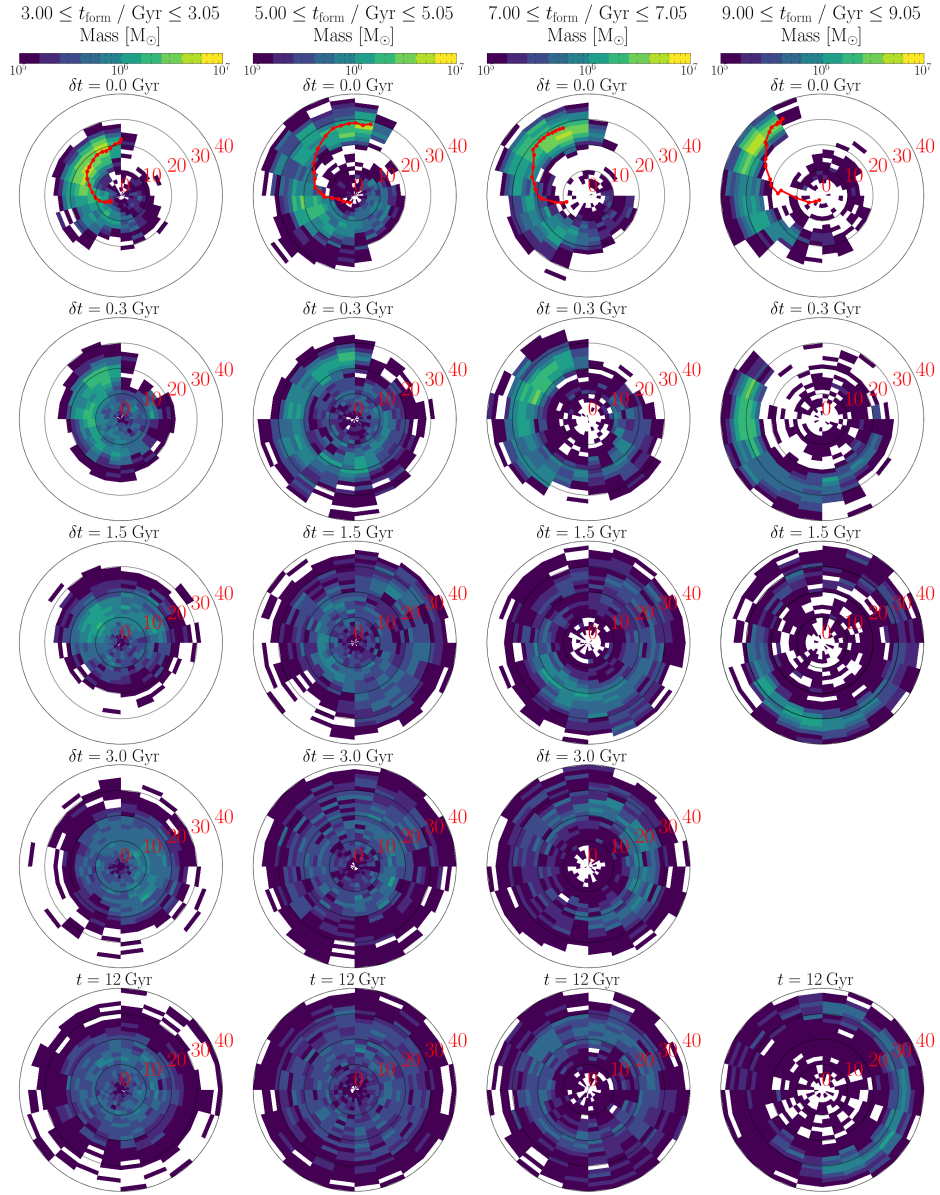
Figure 3.4: Mass distribution in Briggs figures for 4 mono-age warp populations. The populations are formed over 50 Myr intervals (top of each column) with each row representing later times, δt The bottom row shows the populations at the end of the simulation, at $t = 12$ Gyr. At $\delta t = 0$ Myr (first row), the red line represents the Briggs figure of the gas warp at the formation of each population. Some stars appear to start out with $\theta_L < 10°$, but this is due to them drifting already during the first 50 Myr. In the two left columns, the initial $m = 1$ LON spiral distributions phase mix into uniform distributions by the end of the simulation, whereas in the right two columns phase mixing is incomplete at $t = 12$ Gyr.

of gas warps (Briggs 1990a)[1]. Warp stars formed at different times have different ranges of θ_L, with the earlier-forming population ($t_{\mathrm{form}} = 3\,\mathrm{Gyr}$) centred on $\theta_L = 20°$ and the later ($t_{\mathrm{form}} = 9\,\mathrm{Gyr}$) centred on $\theta_L = 35°$. The phase mixing of warp stars in ϕ_L is already visible $300\,\mathrm{Myr}$ after formation for all 4 mono-age populations, as the spiral structure winds up. This winding represents the differential precession of different annuli within the warp. The higher the initial θ_L of the population (θ_{form}), the slower is precession of the population and the longer is the time required for the LON spiral to wind up. For instance, considering $\delta t = 1.5\,\mathrm{Gyr}$, the population formed at $t \simeq 3\,\mathrm{Gyr}$ is well on its way to being uniform in ϕ_L, but there is less of a wrap for increasingly later-forming populations. By the end of the simulation, the later-forming populations have still not fully phase-mixed in ϕ_L, as evident by the horseshoe distribution for the population formed at $\sim 9\,\mathrm{Gyr}$. The phase mixing indicates that the warp populations settle into nearly-axisymmetric discs or tori – see Sec. 3.5.3. They remain relatively thick, as can be seen by the large θ_L values of most of the stars, corresponding to stars which avoid having an angular momentum directed along the z-axis.

A weaker evolution that can be discerned from the Briggs figures is a rapid early decline in the values of θ_L. This is easiest to see directly for the population formed at $3\,\mathrm{Gyr}$, but is present to different extents in all 4 populations. This process represents a tilting of each warp population.

Lastly, the Briggs figures show that there is a tendency for some stars to move to larger θ_L. In Sec. 3.5.4 we demonstrate that this is caused by stars migrating to smaller radii, while preserving their vertical motions so that the net orbital plane of each star becomes more tilted.

---

[1]We remind the reader that this is a spiral in the orientation of the angular momentum vector of different shells. In coordinate space this represents a winding of the intersection of each annulus with the main plane of the galaxy, *i.e.* the spiral can be thought of as the radial locus of the line-of-nodes (LON). For this reason, we will refer to this spiral as the LON spiral.
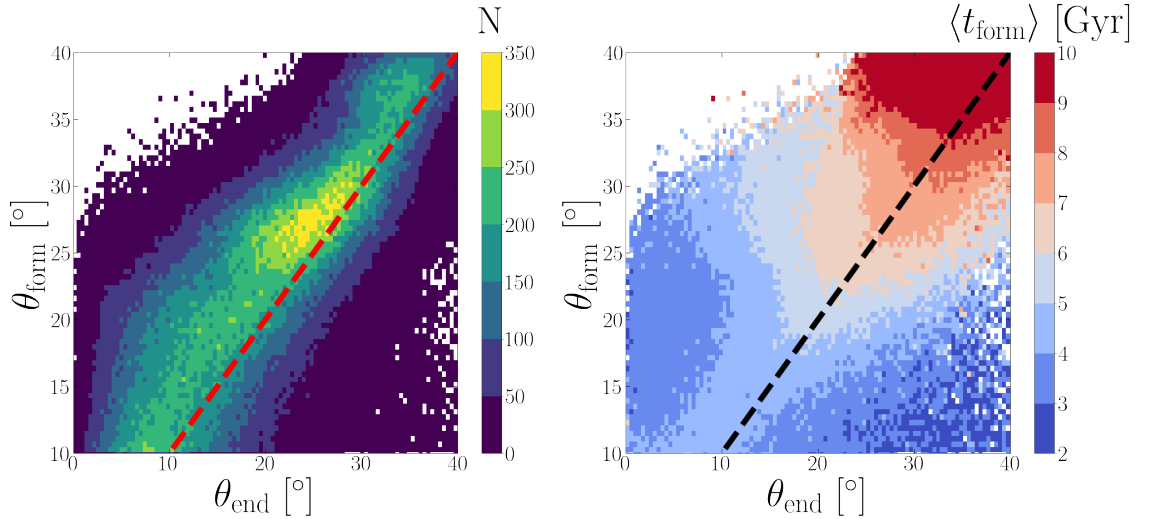
Figure 3.5: Distribution of θ_{form} versus θ_L at the end of the simulation, θ_{end}, for individual warp stars formed before 10 Gyr coloured by the number (left) and the mean time of formation (right). The diagonal dashed line indicates $\theta_{\mathrm{form}} = \theta_{\mathrm{end}}$.

In the following subsections we study in greater detail the tilting of warp populations, their phase mixing and finally their radial migration.

3.5.2 Orbital tilting

Figure 3.4 suggested that warp populations reach lower θ_L as they realign with the galactic disc, which we refer to as tilting. We now study the tilting of mono-age warp populations in more detail. We start by showing that tilting is indeed taking place by comparing θ_L of all warp particles at formation (θ_{form}) and at the end of the simulation (θ_{end}). Figure 3.5 presents the distribution of warp stars in the ($\theta_{\mathrm{end}}, \theta_{\mathrm{form}}$) space. The diagonal lines in both panels indicate $\theta_{\mathrm{form}} = \theta_{\mathrm{end}}$. Warp stars experience some degree of tilting, with $\sim 72\%$ of warp stars located above the $\theta_{\mathrm{form}} = \theta_{\mathrm{end}}$ line. The right panel of Figure 3.5 shows the distribution of average time of formation, $\langle t_{\mathrm{form}} \rangle$ in the ($\theta_{\mathrm{end}}, \theta_{\mathrm{form}}$) space. All warp stars, regardless of t_{form}, undergo some tilting, with the median tilt being $med(\theta_{\mathrm{end}} - \theta_{\mathrm{form}}) = -3.5°$.
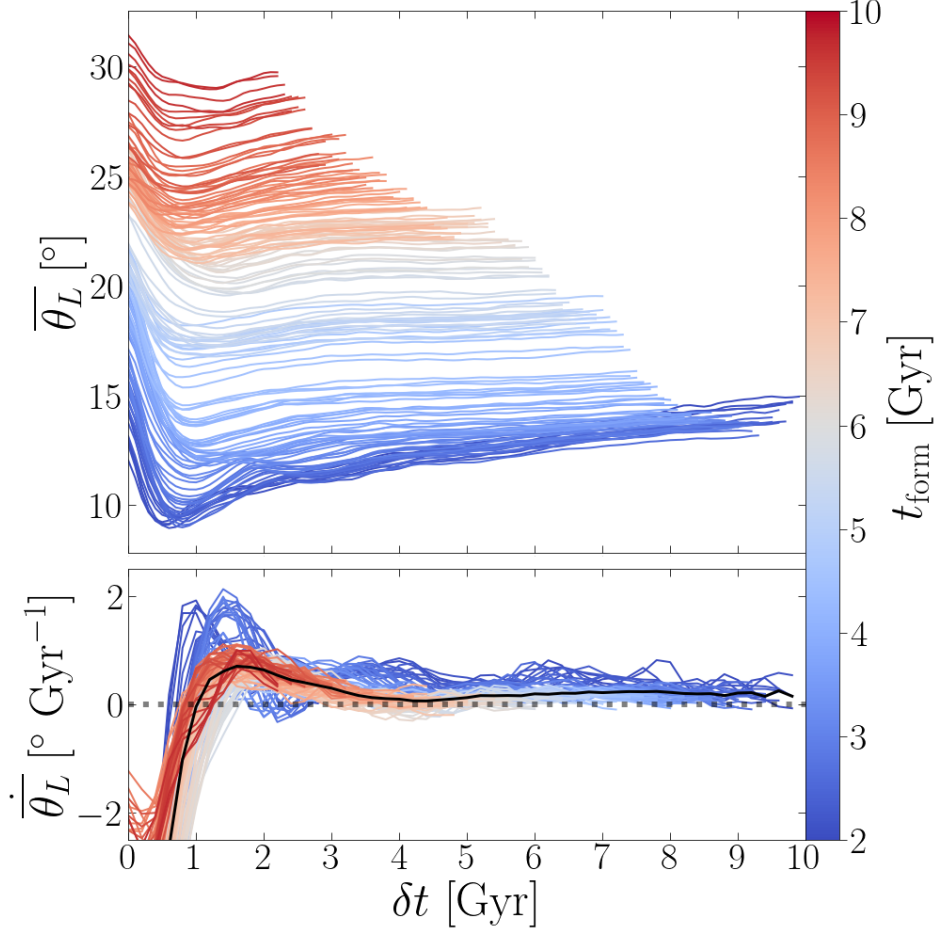
Figure 3.6: Top: evolution of the population-averaged θ_L, $\overline{\theta_L}$, of all mono-age warp populations formed in the simulation before $t_{\text{form}} \leq 10\,\text{Gyr}$, where δt is defined as the time since a population's formation. Each curve is coloured by t_{form}. A 1D Gaussian filter with a mask size of $w = 0.5\,\text{Gyr}$ and standard deviation of $\sigma = 0.1\,\text{Gyr}$ is applied to the evolution at each δt. Bottom: evolution of the rate of change of $\overline{\theta_L}$, $\dot{\overline{\theta_L}}$, for the same mono-age warp populations. The rates of change are calculated from the smoothed evolution curves. The solid black line represents the median rate of change between all mono-age populations which has a tilting time of $\tau_{\text{tilt}} \sim 0.9\,\text{Gyr}$. The dotted horizontal line indicates $\dot{\overline{\theta_L}} = 0°\,\text{Gyr}^{-1}$.

The top panel of Figure 3.6 presents the evolution of the average θ_L, $\overline{\theta_L}$, for all mono-age warp populations formed during $2 \leq t_{\mathrm{form}}/\,\mathrm{Gyr} \leq 10$, in bins of $\Delta t_{\mathrm{form}} = 50\,\mathrm{Myr}$. The average is taken over all star particles of a given population. All warp populations experience a rapid drop in $\overline{\theta_L}$ by $\delta t \sim 1\,\mathrm{Gyr}$, followed by a smaller and gentler rise. The decrease in $\overline{\theta_L}$ varies from $\sim 5°$ for the oldest population to about half that for younger populations. The bottom panel shows the rate of change of $\overline{\theta_L}$, $\dot{\overline{\theta_L}}$, for the same populations. The horizontal dotted line represents $\dot{\overline{\theta_L}} = 0°\,\mathrm{Gyr}^{-1}$. We observe that $\dot{\overline{\theta_L}}$ starts out negative for all populations and quickly plateaus at a nearly constant value of $\dot{\overline{\theta_L}} \sim 0.5\,\mathrm{deg}\,\mathrm{Gyr}^{-1}$. The initial negative tilt rate is due to the bulk tilting warp populations experience as they settle into the disc. This is produced by the torquing from the main disc and persists so long as the warp populations remain more or less coherent before differential precession destroys a relatively coherent plane for each population. The Briggs figures of Figure 3.4 show that, for a wide range of t_{form}, by $\delta t = 300\,\mathrm{Myr}$ the warp populations have precessed differentially enough that the innermost populations are then tilted in the opposite sense as the outermost ones ($\delta\phi \sim 180°$). At this point the global tilting of a population becomes less efficient and their evolution is dominated by precession, which we study in Section 3.5.3.

Figure 3.7 shows the evolution and rate of change of the average $|z|$, $\overline{|z|}$, for the same mono-age populations, likewise averaged over all particles in a stellar population. The evolution of $\overline{|z|}$ is shown in the top panel; all of the warp populations plateau after just $1\,\mathrm{Gyr}$. The rate of change of $\overline{|z|}$, $\dot{\overline{|z|}}$, shown in the bottom panel, starts out mostly negative and quickly decreases to $0\,\mathrm{kpc}\,\mathrm{Gyr}^{-1}$ in less than $1\,\mathrm{Gyr}$, a timescale similar to that in the first part of the $\dot{\overline{\theta_L}}$ evolution. As with the evolution of $\overline{\theta_L}$, we note a correlation between the age of the population and $\overline{|z|}$, with younger populations being formed further away from the mid-plane, and also settling to a thicker distribution.
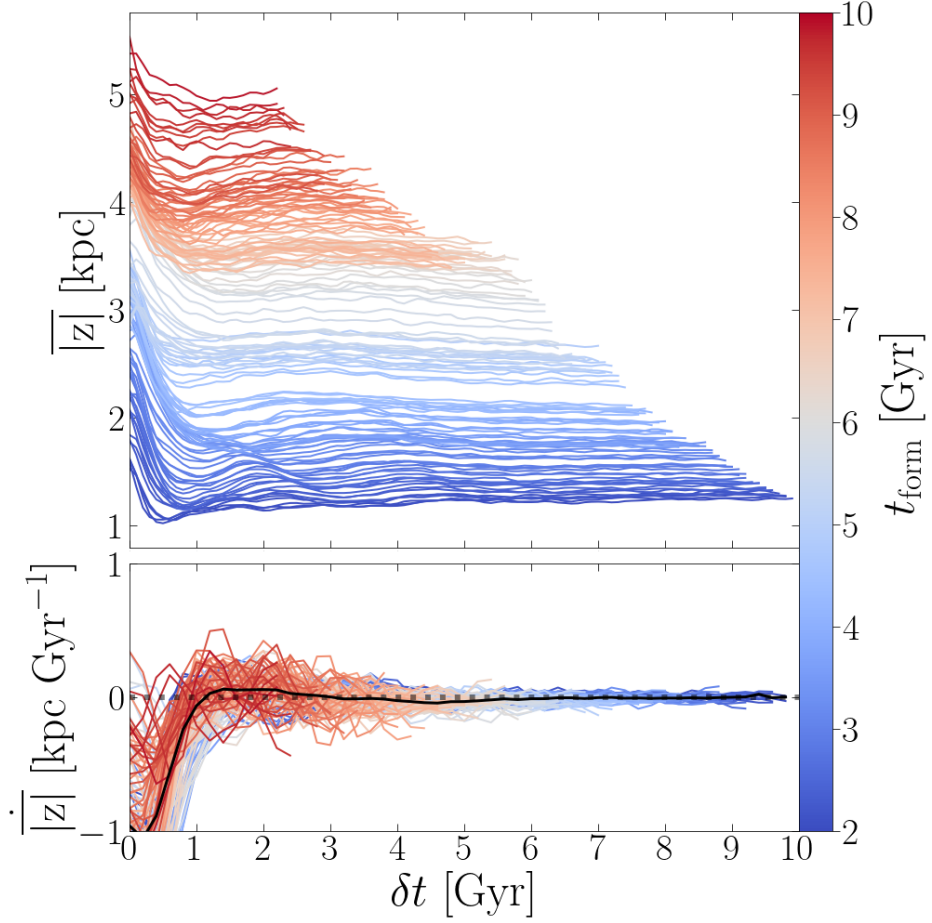
Figure 3.7: Top: evolution of the population-averaged absolute z, $\overline{|z|}$ of different mono-age warp populations before $t_{\mathrm{form}} \leq 10\,\mathrm{Gyr}$, where δt is defined as the time since a population's formation. Each curve is coloured by t_{form}. A 1D Gaussian filter with a mask size of $w = 0.5\,\mathrm{Gyr}$ and standard deviation of $\sigma = 0.1\,\mathrm{Gyr}$ is applied to the evolution at each δt. For each population the value of $\overline{|z|}$ starts to flatten after $\delta t \sim 1\,\mathrm{Gyr}$, reaching a stable configuration. The value of $\overline{|z|}$ for each population increases with t_{form} as older populations form at higher $|z|$, similar to how older populations form at higher θ_{form} (Figure 3.3). Bottom: evolution of the $\overline{|z|}$ rate of change, $\dot{\overline{|z|}}$, for the same mono-age warp populations. The rates of change are calculated from the smoothed evolution curves. A rapid decrease in $\dot{\overline{|z|}}$ happens during the first 1 Gyr and then settles about $\dot{\overline{|z|}} = 0\,\mathrm{kpc\,Gyr^{-1}}$ (dashed horizontal line). The solid black line represents the median rate of change between all mono-age populations; this has a tilting time of $\tau_{\mathrm{tilt}} \sim 1\,\mathrm{Gyr}$.

Given the similarity in the evolution of $\overline{\dot{\theta}_L}$ and $\overline{\dot{|z|}}$, we measure a timescale for the bulk tilting of warp populations. In order to measure the tilting times, τ_{tilt}, for both $\overline{\theta_L}$ and $\overline{|z|}$ we set as a criterion the first time the rate of change reaches values of $\overline{\dot{\theta}_L} \geq 0° \, \mathrm{Gyr}^{-1}$ and $\overline{\dot{|z|}} \geq 0 \, \mathrm{kpc} \, \mathrm{Gyr}^{-1}$, respectively. We find that $\sim 50\%$ of mono-age warp populations experience bulk tilting by $\delta t = 1 \, \mathrm{Gyr}$ when the criterion is applied to both $\overline{\dot{\theta}_L}$ and $\overline{\dot{|z|}}$. In both cases the longest tilting time is $\tau_{\mathrm{tilt}} \sim 1.8 \, \mathrm{Gyr}$.

3.5.3   Phase mixing

The Briggs figures of mono-age warp populations in Figure 3.4 show that their LON spirals wind up. This winding drives a phase mixing so that eventually no trace of a warp remains and a warp population becomes axisymmetric. In this Section we study the phase mixing using the $m = 1$ Fourier amplitude, the total angular momentum, and the entropy of each mono-age population.

Winding of the LON spiral

The distributions of angular momenta in Figure 3.4 for each mono-age warp population traces an $m = 1$ Fourier spiral in angular momentum space at formation. By measuring the amplitude of the Fourier $m = 1$, A_1, in the angular momentum space as in the Briggs figures we can follow the phase mixing of each population. In the top panel of Figure 3.8 we plot the evolution of A_1 for all mono-age warp populations. The peak A_1 for each warp population is at formation, and rapidly declines during the first 1 Gyr. The decline in most warp populations is not monotonic, with the oldest warp populations having multiple peaks of decreasing amplitude lasting up to $\delta t = 5 \, \mathrm{Gyr}$ after which the decrease is smoother. For younger populations A_1 declines more smoothly, though still not monotonically. However, populations with $t_{\mathrm{form}} \geq 9.5 \, \mathrm{Gyr}$ exhibit a similar second peak as in the older populations. The bottom panel shows the rate of change of A_1, $\dot{A}_1$, for the same populations, with
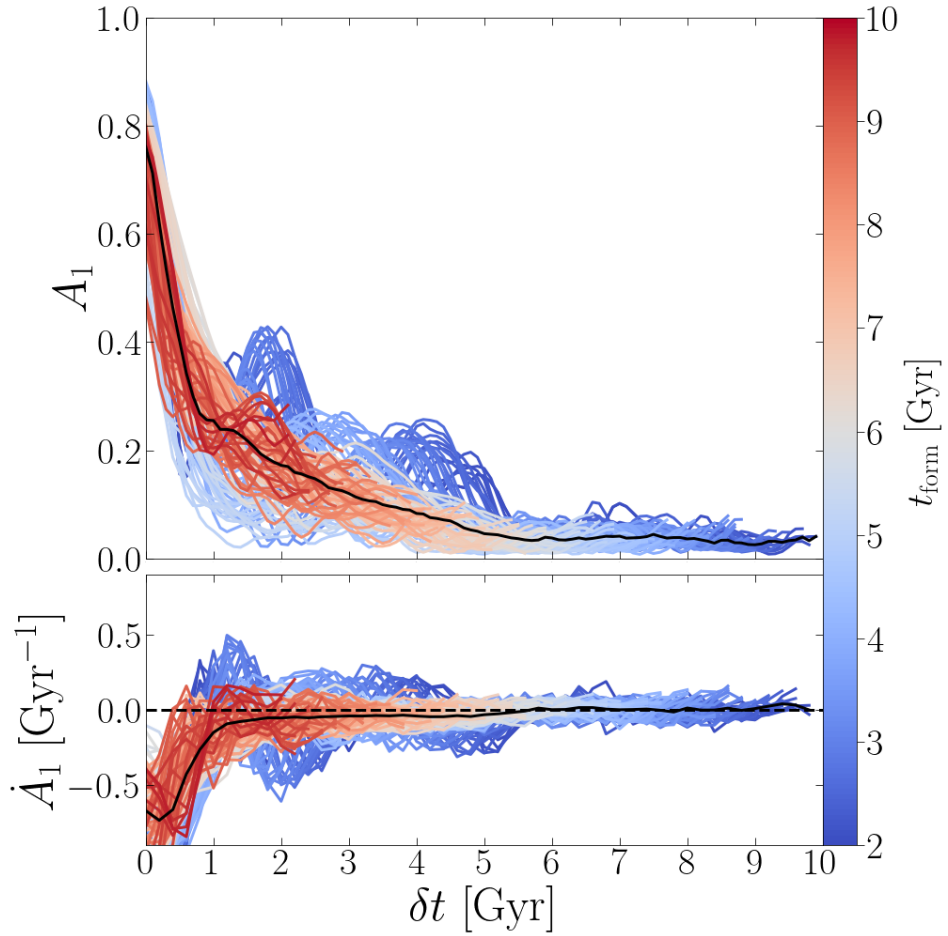
Figure 3.8: Top: Evolution of the A_1 amplitude for all mono-age warp populations formed in the simulation before $t_{\mathrm{form}} \leq 10\,\mathrm{Gyr}$, where δt is defined as the times since a population's formation. Each curve is coloured by t_{form}. A 1D Gaussian filter with a mask size of $w = 0.5\,\mathrm{Gyr}$ and standard deviation of $\sigma = 0.1\,\mathrm{Gyr}$ is applied to the evolution at each δt. The black solid line is the median value of A_1 between all mono-age populations. Bottom: evolution of the rate of change of A_1, $\dot{A}_1$, for the same mono-age warp populations. The rates of change are calculated from the smoothed evolution curves. The solid black line represents the median rate of change between all mono-age populations. The dotted horizontal line indicates $\dot{A}_1 = 0\,\mathrm{Gyr}^{-1}$.

$\dot{A}_1 = 0\,\mathrm{Gyr}^{-1}$ indicated by a dashed horizontal line. For all mono-age populations a significant oscillation in $\dot{A}_1$ is observed. The median curves of A_1 and $\dot{A}_1$ across all mono-age populations are shown as solid black lines in the top and bottom panels of Figure 3.8, respectively.

Fitting an exponential decay to A_1 as a function of time leads to exponential times $0.9 < \tau/\,\mathrm{Gyr} < 2.3$. The phase mixing timescales, τ_{pm}, can be estimated by taking the median of the time derivatives between all mono-age populations and measuring when it reaches $0\,\mathrm{Gyr}^{-1}$. In the bottom panel of Figure 3.8 the median of the time derivative reaches the zero-line around $\tau_{\mathrm{pm}} \sim 6\,\mathrm{Gyr}$, a timescale that is longer than the tilting times computed in Section 3.5.2.

Phase mixing from the average angular momentum vector

The uniform distribution ϕ_L in the Briggs figures (Figure 3.4) of settled populations implies that if the angular momentum of each warp population were vector-averaged over all stars then the resulting mean angular momentum would be along the z axis, with inclination $\theta = 0°$. Thus by analysing the evolution of the inclination of the average angular momentum vector, we can further gauge the phase mixing timescale. In the top panel of Figure 3.9 we present the evolution of the inclination of the average angular momentum, $\theta_{\bar{L}}$, for mono-age populations. The evolution of $\theta_{\bar{L}}$ shows that warp populations with $t_{\mathrm{form}} \geq 6\,\mathrm{Gyr}$ do not reach $\sim 0°$, indicating that they are still phase mixing, in agreement with Figure 3.4. Older populations with $t_{\mathrm{form}} < 6\,\mathrm{Gyr}$ settle to $\theta_{\bar{L}} = 0°$ on different timescales, with the oldest population presenting the similar multiple peaks as in Figure 3.8. In the bottom panel, the evolution of the rate of change, $\dot{\theta}_{\bar{L}}$, shows that the phase mixing process is much more rapid for the older populations but then $\theta_{\bar{L}}$ rises again at $\sim 2\,\mathrm{Gyr}$ and then oscillates about $\dot{\theta}_{\bar{L}} = 0°\,\mathrm{Gyr}^{-1}$. Younger populations show a slower and smoother increase towards $\dot{\theta}_{\bar{L}} = 0°\,\mathrm{Gyr}^{-1}$ in their rate of change. The median curves for $\theta_{\bar{L}}$
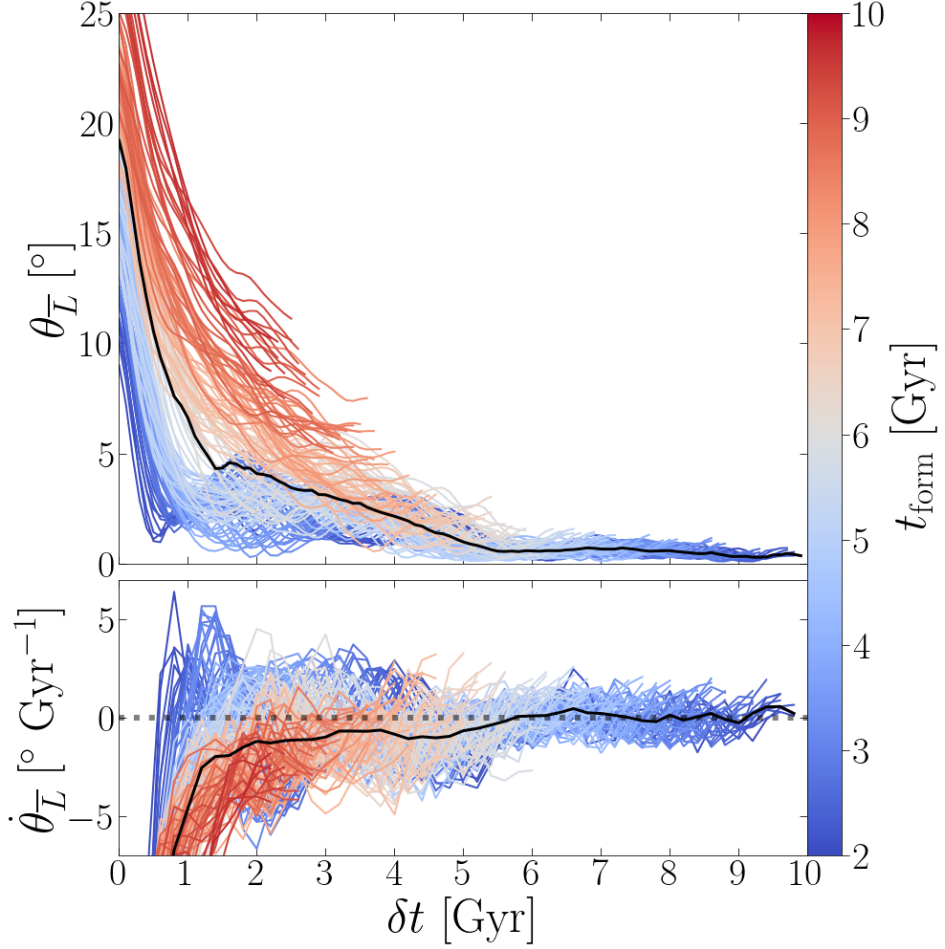
Figure 3.9: Top: evolution of the population-averaged angular momentum incli-
nation, $\theta_{\bar{L}}$, for all mono-age warp populations formed in the simulation before
$t_{\mathrm{form}} \leq 10\,\mathrm{Gyr}$, where δt is defined as the time since a population's formation. Each
curve is coloured by t_{form}. A 1D Gaussian filter with a mask size of $w = 0.5\,\mathrm{Gyr}$
and standard deviation of $\sigma = 0.1\,\mathrm{Gyr}$ is applied to the evolution at each δt. The
black solid line is the median value of $\theta_{\bar{L}}$ between all mono-age populations. Bottom:
evolution of the rate of change of $\theta_{\bar{L}}$, $\dot{\theta}_{\bar{L}}$, for the same mono-age warp populations.
The rates of change are calculated from the smoothed evolution curves. The solid
black line represents the median rate of change between all mono-age populations.
The dotted horizontal line indicates $\dot{\theta}_{\bar{L}} = 0° \, \mathrm{Gyr}^{-1}$.

and $\dot{\theta}_{\bar{L}}$ between all mono-age populations are shown as solid black lines in the top and bottom panels of Figure 3.9, respectively.

Based on the $\theta_{\bar{L}}$ evolution we estimate the phase mixing time, τ_{pm}, using the method described in Section 3.5.3, i.e. when the median of the time derivatives reaches $0°\,\mathrm{Gyr}^{-1}$. In the bottom panel of Figure 3.9 the median of the time derivatives reaches the zero-line around $\tau_{\mathrm{pm}} \sim 6\,\mathrm{Gyr}$. This timescale is again longer than the tilting times computed in Section 3.5.2.

Entropy-based phase mixing timescale

Lastly, we also characterise the phase mixing process using a non-parametric entropy estimator. The entropy definition we adopt is:

$$S = - \int f(\phi_L) \ln f(\phi_L) \, \mathrm{d}\phi_L, \qquad (3.3)$$

where $f(\phi_L)$ is the probability density function. This functional form is chosen primarily because of its desirable mathematical properties, including that it can be estimated as

$$\hat{S} = -\frac{1}{N} \sum_{i=1}^{N} \ln \hat{f}_i, \qquad (3.4)$$

where the sum runs over the warp stars of a given population and $\hat{f}_i$ is the estimate of $f(\phi_L)$ for each star particle. Eq. 3.4 converges to Eq. 3.3 if $\hat{f}_i$ is calculated with specific recipes (see Beraldo e Silva et al. 2019b,a, and references therein). Here we adopt the Nearest Neighbour method, where in one dimension the distribution is estimated as:

$$\hat{f}_i = \frac{1}{2(N-1)e^\gamma D_{in}}, \qquad (3.5)$$

where $\gamma \simeq 0.577$ is the Euler-Mascheroni constant and D_{in} is the distance of particle i to its nearest neighbour (see Biau & Devroye 2015; Beraldo e Silva et al. 2019b,a, for more general expressions). Since $-\pi \leq \phi_L \leq \pi$, for a fully-mixed population
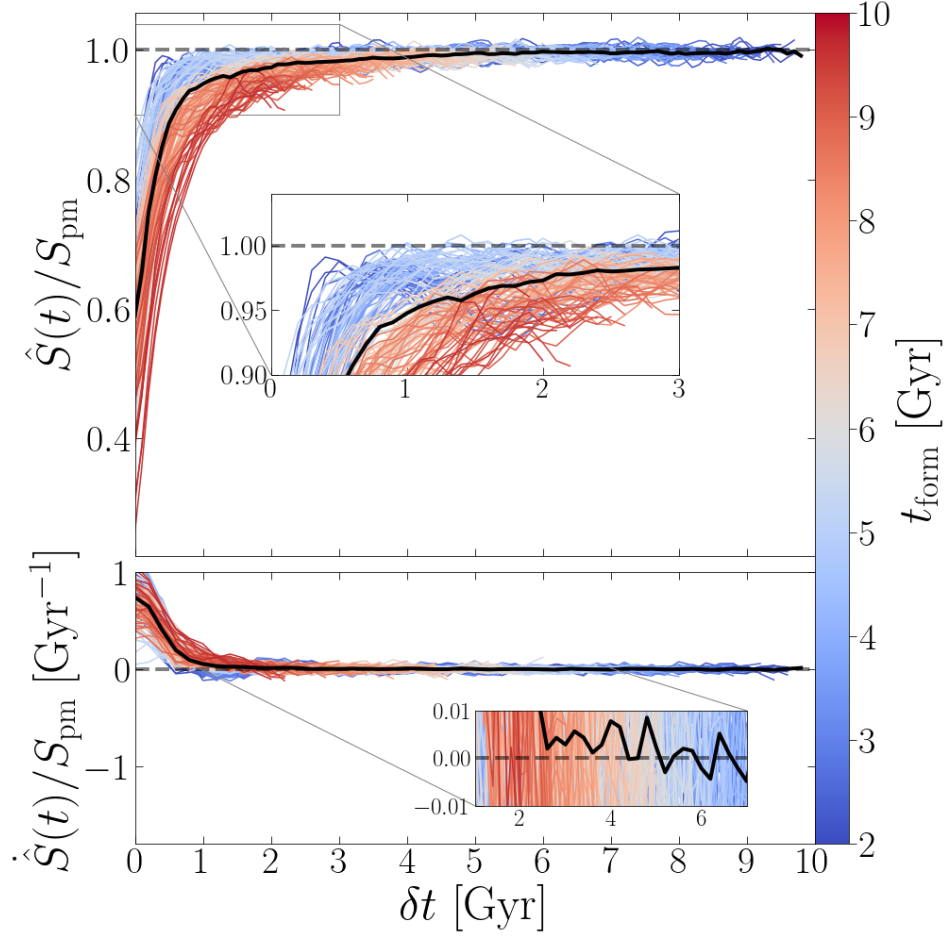
Figure 3.10: Top: evolution of the entropy estimate, $\hat{S}(t)$, normalised by S_{pm} for all mono-age warp populations formed in the simulation before $t_{\mathrm{form}} \leq 10\,\mathrm{Gyr}$, where δt is defined as the time since a population's formation. Each curve is coloured by t_{form}. A 1D Gaussian filter with a mask size of $w = 0.5\,\mathrm{Gyr}$ and standard deviation of $\sigma = 0.1\,\mathrm{Gyr}$ is applied to each population. The black solid line is the median value of $\hat{S}(t)$ between all mono-age populations. The dotted horizontal line indicates $\hat{S}(t)/S_{\mathrm{pm}} = 1$. The inset shows an expanded version of the region indicated by the rectangle at top left. Bottom: evolution of the rate of change of $\hat{S}(t)$, $\dot{\hat{S}}(t)$, normalised by S_{pm} for the same mono-age warp populations. The rates of change are calculated from the smoothed evolution curves. The black solid line is the median rate of change between all mono-age populations. The dotted horizontal line indicates $\dot{\hat{S}}(t) = 0$. The inset shows an expanded version of the region around the zero-line.

the phase-mixed distribution is $f_{\mathrm{pm}} = 1/(2\pi)$, and from Eq. 3.3, the phase-mixed entropy is $S_{\mathrm{pm}} = \ln(2\pi)$.

We use Eqs. 3.4-3.5 to estimate the entropy of the same mono-age warp populations defined before at different times. The entropy evolution, normalised by the phase-mixed value S_{pm}, is shown in the top panel of Figure 3.10, colour-coded by the formation times. All mono-age warp populations show a rapid increase in entropy, on a time-scale of $\delta t \sim 1\,\mathrm{Gyr}$, after which the system asymptotically evolves to the phase-mixed state, on a longer time-scale. Populations born after $t_{\mathrm{form}} \gtrsim 6\,\mathrm{Gyr}$ do not have time to completely phase-mix, in good agreement with the Briggs figures in Figure 3.4. Young populations are born with smaller entropies, which is a result of the larger radius at which they are forming, resulting in a narrower range of ϕ_L values. The median curves for $\hat{S}/S_{pm}$ and $\dot{\hat{S}}/S_{pm}$ across all mono-age populations are shown as solid black lines in the top and bottom panels of Figure 3.10, respectively.

We estimate the phase mixing timescale using the same method described in Section 3.5.3, i.e. when the median of the time derivatives reaches $0\,\mathrm{Gyr}^{-1}$. Though the median of the time derivatives fluctuates as it approaches the zero-line (see bottom inset), we estimate that $\tau_{\mathrm{pm}} \sim 5 - 6\,\mathrm{Gyr}$. This phase mixing timescale is in agreement with the results from Sections 3.5.3 & 3.5.3, reaffirming that phase mixing continues long after the tilting has concluded.

3.5.4 Inward migration of warp populations

In our definition, a warp population must have formed at $r > 10\,\mathrm{kpc}$. Figure 3.6 showed that $\overline{\dot{\theta}_L}$ at $\delta t \gtrsim 2\,\mathrm{Gyr}$ for many warp populations is positive, at $\sim 0.5°$. A naive interpretation of this result is that the warp populations continue to heat vertically after they settle. Aside from the fact that thick populations do not heat vertically easily since they spend most of their time away from the thin disc, where

most of the perturbers that can heat them reside, Figure 3.7 contradicts this inter-pretation, because it shows that $\overline{|z|}$ is not increasing at the same time. A different interpretation is therefore needed. Here we show that warp populations migrate inwards; with $\overline{|z|}$ constant, the inward migration must result in an increasing θ_L and a positive $\overline{\dot{\theta}_L}$.

Figure 3.11 considers the evolution and rate of change of the population-averaged vertical angular momentum, $\overline{L_z}$. The evolution of $\overline{L_z}$ (top panel) shows an increase in the first 1 Gyr for all populations with $t_{\mathrm{form}} > 4.5$ Gyr, while older populations show a decrease. These changes subsequently slow down significantly as all populations plateau with only a weak negative gradient. The rate of change, $\overline{\dot{L}_z}$, (bottom panel) shows that after $\delta t \sim 1$ Gyr all populations have a negative $\overline{\dot{L}_z}$, though there is an initial spike for populations with $t_{\mathrm{form}} \geq 4.5$ Gyr. The solid black line indicates the median between all rates of change. The vertical angular momentum correlates with t_{form} of the warp populations, because of the growing radius of the warp. The initial spike in younger populations is related to the growing warp as younger populations have larger θ_{form} and due to the projection of L_z, even small tilts translate to larger changes in L_z. Older populations form in a younger, shallower warp and do not experience the same initial spike. In spite of this difference, all warp populations have comparable values of $\overline{\dot{L}_z}$ for $\delta t > 1$ Gyr. The net decrease in vertical angular momentum of warp populations well after they formed represents either a radial heating of each population, or an inward migration.

We therefore analyse how the radial positions of the warp populations change with time. We use the spherical radius, rather than the cylindrical one, since the disc is warped. Figure 3.12 presents the evolution of the population-averaged spherical radius, $\overline{r}$, for the mono-age warp populations. The top panel shows the evolution of $\overline{r}$, which clearly decreases at all times for all populations. This change implies that the decrease of the angular momentum of warp stars is accompanied by a net
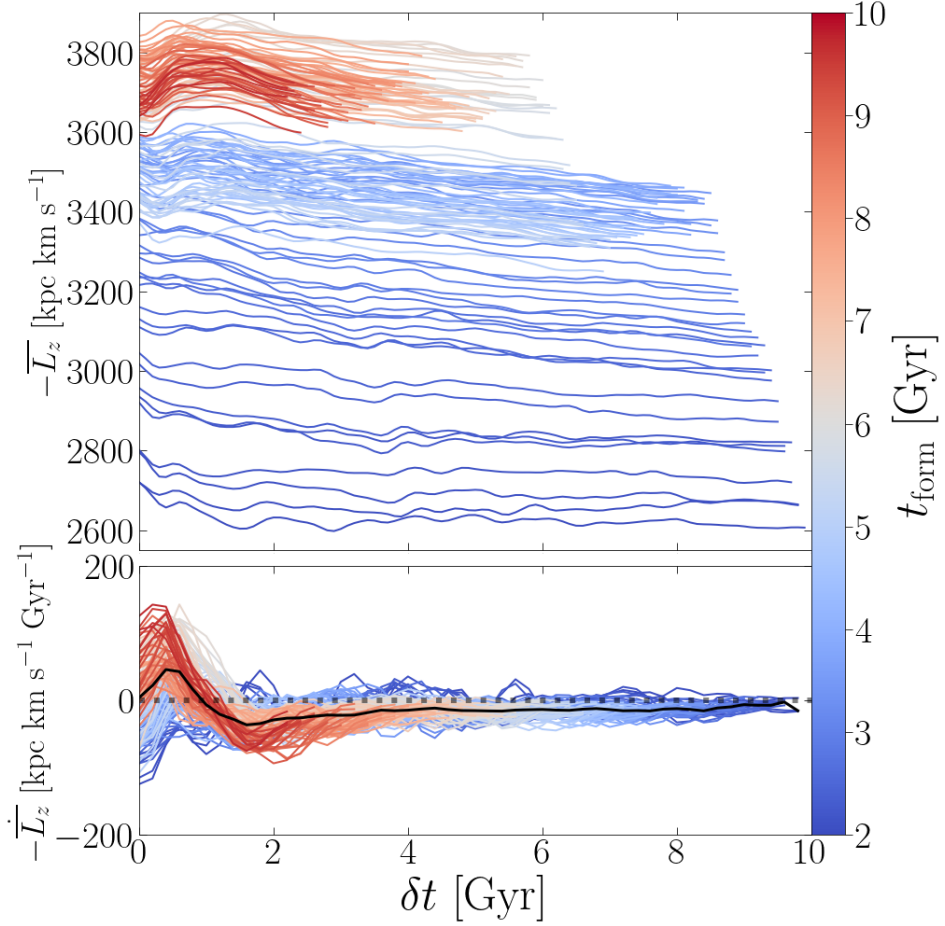
Figure 3.11: Top: evolution of the population-averaged vertical angular momentum, $\overline{L_z}$, for different mono-age warp populations in the simulation, where δt is defined as the time since a population's formation. Each curve is coloured by t_{form}. A 1D Gaussian filter with a mask size of $w = 0.5\,\text{Gyr}$ and standard deviation of $\sigma = 0.1\,\text{Gyr}$ is applied to the evolution at each δt. Most of the change in the vertical angular momentum happens during the first 1 Gyr after which they decline slowly or remain flat. Bottom: evolution of the $\overline{L_z}$ rate of change, $\dot{\overline{L_z}}$, for the same mono-age warp populations. The rates of change are calculated from the smoothed evolution curves. The solid black line represents the median rate of change between all mono-age populations. We observe that $\overline{L_z}$ is continuously decreasing as the rate of change remains mostly below $\dot{\overline{L_z}} = 0\,\text{kpc}\,\text{km}\,\text{s}^{-1}\,\text{Gyr}^{-1}$ (dashed horizontal line).
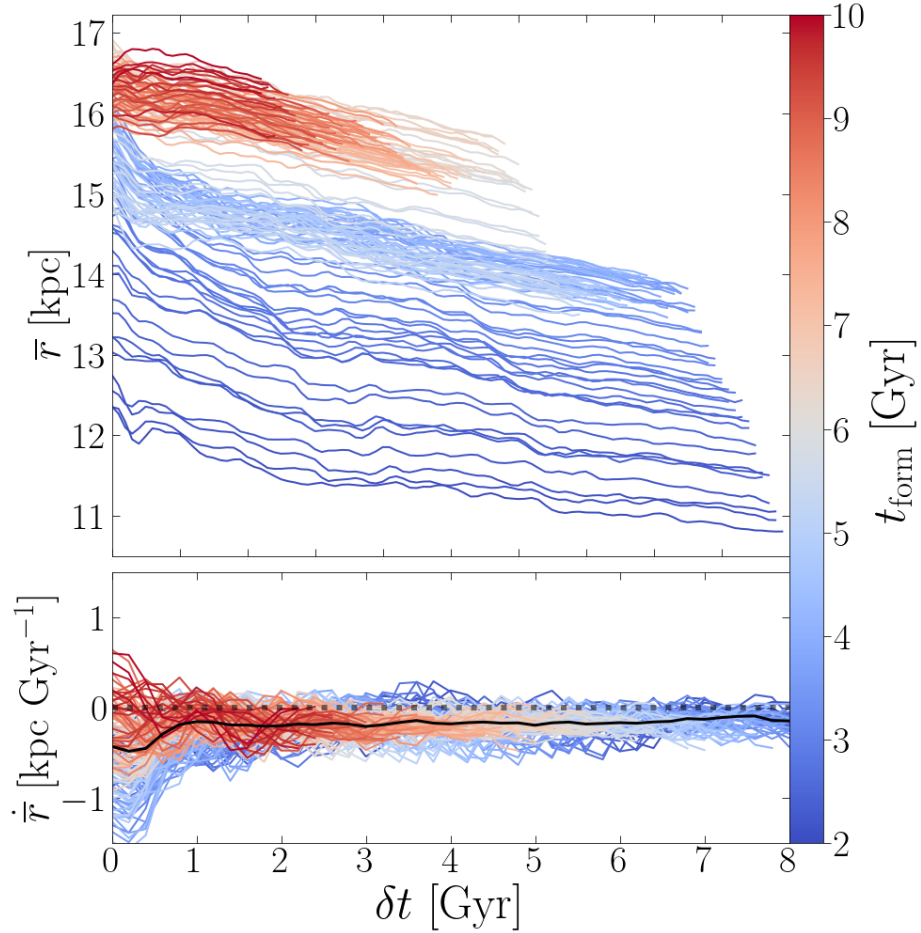
Figure 3.12: Top: evolution of the population-averaged spherical radius, $\bar{r}$, of different mono-age warp populations, where δt is defined as the time since a population's formation. Each curve is coloured by t_{form}. A 1D Gaussian filter with a mask size of $w = 0.5\,\text{Gyr}$ and standard deviation of $\sigma = 0.1\,\text{Gyr}$ is applied to the evolution at each δt. The decrease of $\bar{r}$ is different for all populations and is strongest for $t_{\text{form}} \sim 3\,\text{Gyr}$ at 15% with the weakest decrease for $t_{\text{form}} > 6\,\text{Gyr}$ at 5%. Bottom: evolution of the $\bar{r}$ rate of change, $\dot{\bar{r}}$, for the same mono-age warp populations. The rates of change are calculated from the smoothed evolution curves. The solid black line represents the median rate of change between all mono-age populations. A consistently negative $\dot{\bar{r}} < 0\,\text{kpc}\,\text{Gyr}^{-1}$ is observed (dashed horizontal line), with the exception of a few transient positive values for the oldest population. This is indicative of continuous inward migration for all warp populations, regardless of their t_{form}.
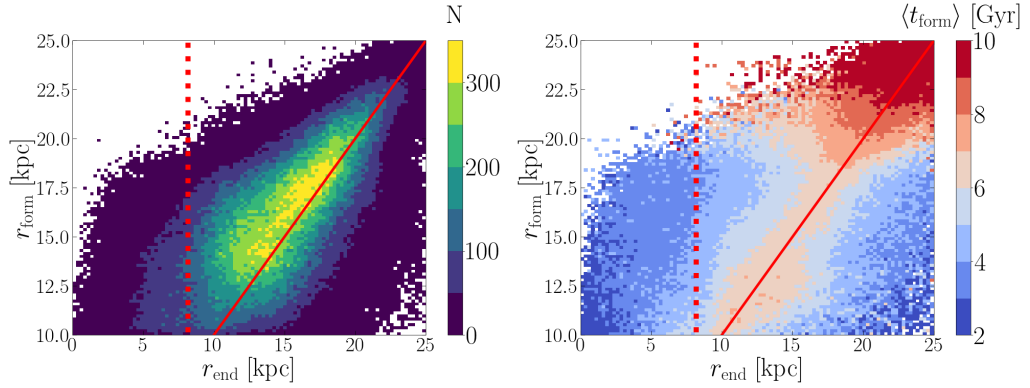
Figure 3.13: Distribution of spherical formation radius, r_{form}, versus the spherical radius at the end of the simulation, r_{end}, for warp stars coloured by the number (left) and by the mean time of formation, t_{form} (right). The diagonal solid line indicates $r_{\mathrm{form}} = r_{\mathrm{end}}$. Stars that are below the $r_{\mathrm{form}} = r_{\mathrm{end}}$ line comprise 1/3 of the total warp star sample. The vertical dotted line indicates the location of the Solar annulus. Warp stars born after $t_{\mathrm{form}} \gtrsim 6\,\mathrm{Gyr}$ do not have enough time to migrate into the Solar annulus.

radial movement inwards, and continues well after the population tilting has ended. The decrease of $\bar{r}$ is continuous for all populations which we confirm by plotting the rate of change for $\bar{r}$, $\dot{\bar{r}}$, (bottom panel) which is predominantly negative after $\delta t = 1\,\mathrm{Gyr}$. The net inward movement of warp populations is a result of the fact that, by definition, they form only at large radii ($\geq 10\,\mathrm{kpc}$).

In Figure 3.13 we consider the relation between the formation radius, r_{form}, and the final radial position, r_{end}, for all warp stars. The left panel shows that 66% of warp stars move inwards. This movement inwards happens regardless of t_{form} (right panel), with older populations experiencing the strongest inward movement (extending to $r_{\mathrm{form}} - r_{\mathrm{end}} \sim 15\,\mathrm{kpc}$). This could indicate migration by spiral churning where the migration is characterised by a random walk (Sellwood & Binney 2002b). A radial gradient of decreasing age is established in the inner disc, with warp stars at the smallest radius being the oldest ones. This is the mirror image of

the usual outwardly increasing age gradient for stars formed within the main disc and migrating outwards (Roškar et al. 2008b; Beraldo e Silva et al. 2020a). We note that the oldest populations also move outwards, which also hints at migration via spiral churning.

Finally, we explore whether the warp populations are on highly eccentric orbits, or nearly circular ones. We integrate the orbits of settled warp stars in the interpolated potential derived using AGAMA (see Chapter 2.3). The initial conditions of the warp stars are set to their 6D coordinates at the end of the simulation at 12 Gyr. Because the youngest warp stars may not have had enough time to tilt into the disc, we limit our analysis to warp stars with $t_{\mathrm{form}} \leq 10\,\mathrm{Gyr}$. After integrating each warp star for 10 orbital periods, we use the maximum and minimum cylindrical radii along the orbit to calculate the orbital eccentricities:

$$e = \frac{R_{max} - R_{min}}{R_{max} + R_{min}} \tag{3.6}$$

Figure 3.14 presents the 2D histogram of orbital eccentricities plotted versus t_{form}. This distribution shows that a large fraction of warp stars have $0.1 \leq e \leq 0.4$. The lines indicate the median (red solid), mean (red dashed), and the 16th and 84th percentiles (black annotated) of the eccentricity in each t_{form} bin; a weak decline of the mean eccentricity from 0.3 for the oldest population to 0.2 for the youngest is evident. These nearly circular orbits indicate that the radial migration is driven by spiral churning (Sellwood & Binney 2002b; Roškar et al. 2012) rather than by heating. The decreasing mean angular momentum amplitude is purely a result of the unbalanced distribution of formation radii of warp stars.

3.6   Resulting disc structure

The dynamical evolution of warp populations explored in Section 3.5 showed that as soon as warp stars form they begin rapidly tilting and then phase mixing in the
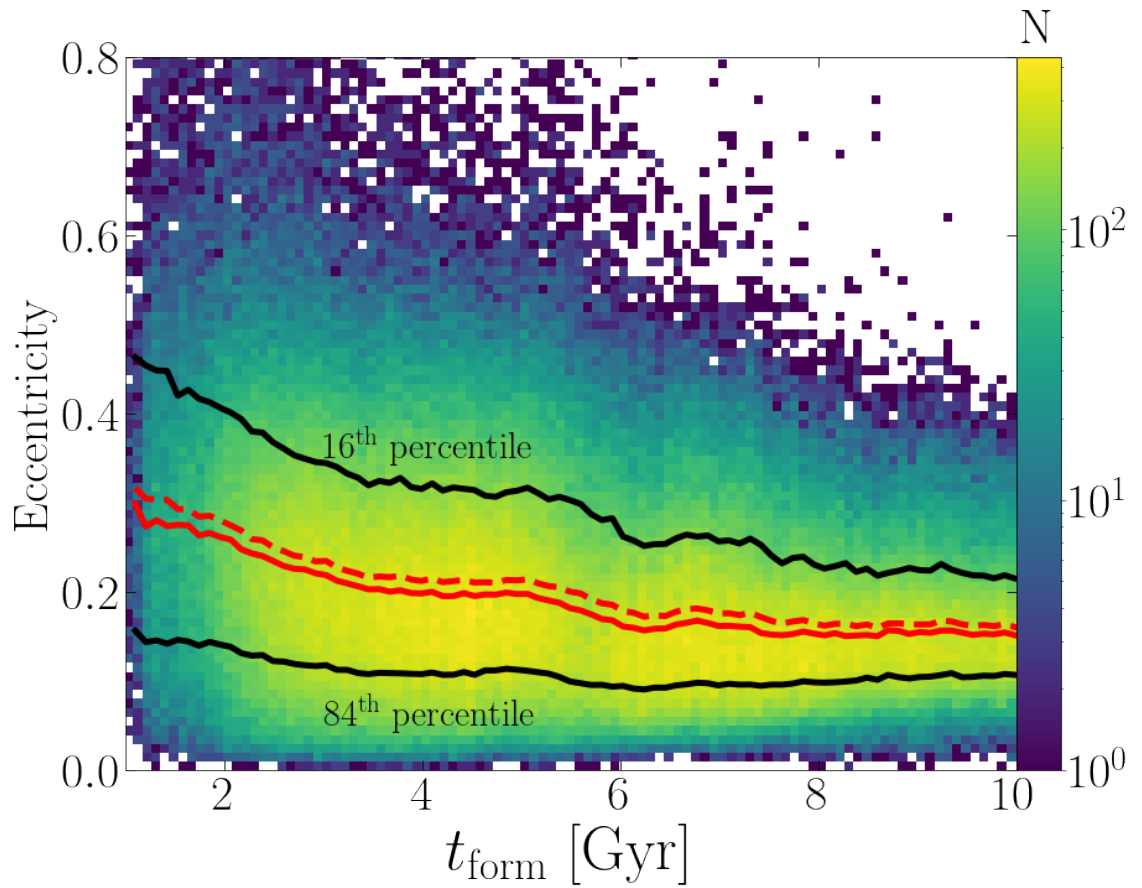
Figure 3.14: Eccentricities of warp stars versus t_{form}. The lines indicate the median (red solid), mean (red dashed), and the 16th and 84th percentiles (black annotated) of the eccentricity for each t_{form} bin. The younger warp stars having slightly more circular orbits. In general most orbits are fairly close to circular.
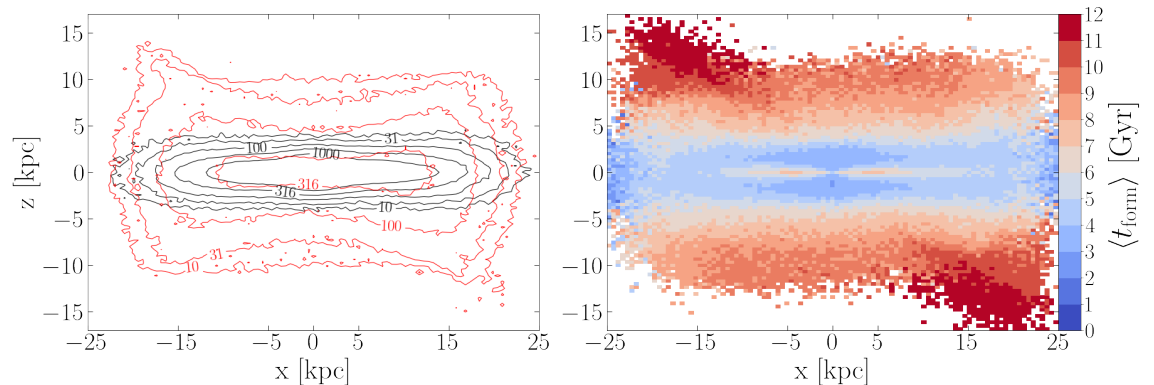
Figure 3.15: Edge-on views of the simulation at 12 Gyr. Left column: number density contour plots of the warp (red contours) and main disc (black contours) populations. Warp stars occupy higher $|z|$ than stars formed in the disc and outnumber disc stars by a factor of 10 starting from at $|z| \sim 4\,\mathrm{kpc}$. Right column: distribution of the mean formation time, $\langle t_{\mathrm{form}} \rangle$ for all stars formed throughout the simulation. There is a vertical gradient in $\langle t_{\mathrm{form}} \rangle$ and a young warp population that traces the gas warp starting from $|z| \geq 5\,\mathrm{kpc}$.

galactic disc. These processes are accompanied by the slow but continuous inward (and outward) migration of the warp populations. We now explore the resulting disc structure of settled warp populations.

Figure 3.15 presents the edge-on distributions of warp and in-situ stars at $t = 12\,\mathrm{Gyr}$. In the left panel, the contours show the number density distribution of warp (red) and in-situ (black) stars. Warp stars occupy the geometric thick disc with visible flaring at $|x| \geq 15\,\mathrm{kpc}$ and a maximum vertical extent of $|z| \leq 10\,\mathrm{kpc}$. In the right column is the edge-on distribution of $\langle t_{\mathrm{form}} \rangle$ for all the stars formed throughout the simulation. Starting from $|z| \geq 5\,\mathrm{kpc}$, newly formed warp stars can be observed tracing the gas warp, the major axis of which is along the x-axis (Chapter 2.3).

We now analyse in detail the resulting density distributions of stars formed in the

warp, selecting the ones currently located at $2 < R/\,\mathrm{kpc} < 25$ and $0 < |z|/\,\mathrm{kpc} < 15$. We define 30 broad mono-age populations (bin width $\Delta t_{\mathrm{form}} = 250\,\mathrm{Myr}$) in the interval $2 < t_{\mathrm{form}}/\,\mathrm{Gyr} < 9.5$, where the lower limit is chosen to avoid the stars formed in the early chaotic transient warp, and the upper limit chosen such that the youngest population considered has had enough time to settle. For each of these mono-age populations, we simultaneously fit the radial surface number density profile, $\Sigma(R)$, and the vertical number density profile, $\xi(z|R)$.

The radial profile $\Sigma(R)$ is modelled with a skew-normal distribution (Azzalini 1985), which we found to be the best functional form after comparison with different models (see e.g. Bovy et al. 2016; Beraldo e Silva et al. 2020a). In this model, the profile is given by

$$\Sigma(R|\mu_R, h_R, \alpha) = \frac{1}{A}\phi(R|\mu_R, h_R)\Phi(\alpha R|\mu_R, h_R), \tag{3.7}$$

where $\phi(x|\mu, h)$ is the normal (Gaussian) distribution with location μ and scale h, $\Phi(x)$ is its cumulative distribution function and A is determined by the normalization condition

$$\int_{R_{\mathrm{min}}}^{R_{\mathrm{max}}} \Sigma(R)2\pi R\,\mathrm{d}R = 1. \tag{3.8}$$

The parameter α controls the skewness: the Gaussian distribution is recovered as a particular case when $\alpha = 0$. Note that $-\infty < \alpha < \infty$, while the real skewness can be obtained from α and ranges from -1 to 1. Note also that μ_R and h_R are close to, but not exactly, the position of the peak, R_{peak}, and the dispersion σ_R, respectively, which are also obtained by simple formulae from the parameters α, μ_R and h_R (see Azzalini 1985).

The vertical density profiles $\xi(z|R)$ are modelled with the so-called generalised normal distribution (Nadarajah 2005):

$$\xi(z|R, \mu_z, h_z, \beta) = \frac{1}{B}\exp\left[-\left|\frac{|z| - \mu_z}{h_z}\right|^\beta\right], \tag{3.9}$$

where β controls the kurtosis ($\beta = 2$ for the Gaussian) and B is obtained by imposing the condition

$$\int_{z_{\min}}^{z_{\max}} \xi(z|R)\,\mathrm{d}z = 1. \tag{3.10}$$

In the above expressions, all three parameters β, μ_z and h_z depend on R in a non-trivial way. After some experimentation we determined that each of these parameters needs to be modelled as a third-order polynomial in radius R. The position of the peak in $|z|$ is directly given by $z_{\mathrm{peak}} = \mu_z$. Finally, the total number density profile is written as

$$\nu(R, z|\theta) = \Sigma(R|\theta)\xi(z|R, \theta), \tag{3.11}$$

where θ is the set of parameters. For each mono-age population, we first fit this model maximizing the log-likelihood

$$\ln \mathcal{L}(\theta) = \sum_i \ln\left[\nu(R_i, z_i|\theta)\right] \tag{3.12}$$

with a variant of Powell's method, which is a conjugate direction method (Powell 1964; Press et al. 1992). Then, we use this first fitting result as input to MCMC-sample the posterior distribution function with the EMCEE package (Foreman-Mackey et al. 2013), assuming flat priors for all parameters. Best fit parameters and uncertainties are estimated with the median and the 16 and 84 percentiles of the parameter samples, respectively.

For illustrative purposes, in Figures 3.16 and 3.17 we slice some of these populations into cylindrical shells, determining the surface number density profile $\Sigma(R)$ (left panels) and, for each shell, the vertical number density profiles $\xi(z|R)$ (right panels). In Figures 3.16 and 3.17, each row represents a different mono-age population, with the formation times indicated. The best fit models are represented by dashed lines.
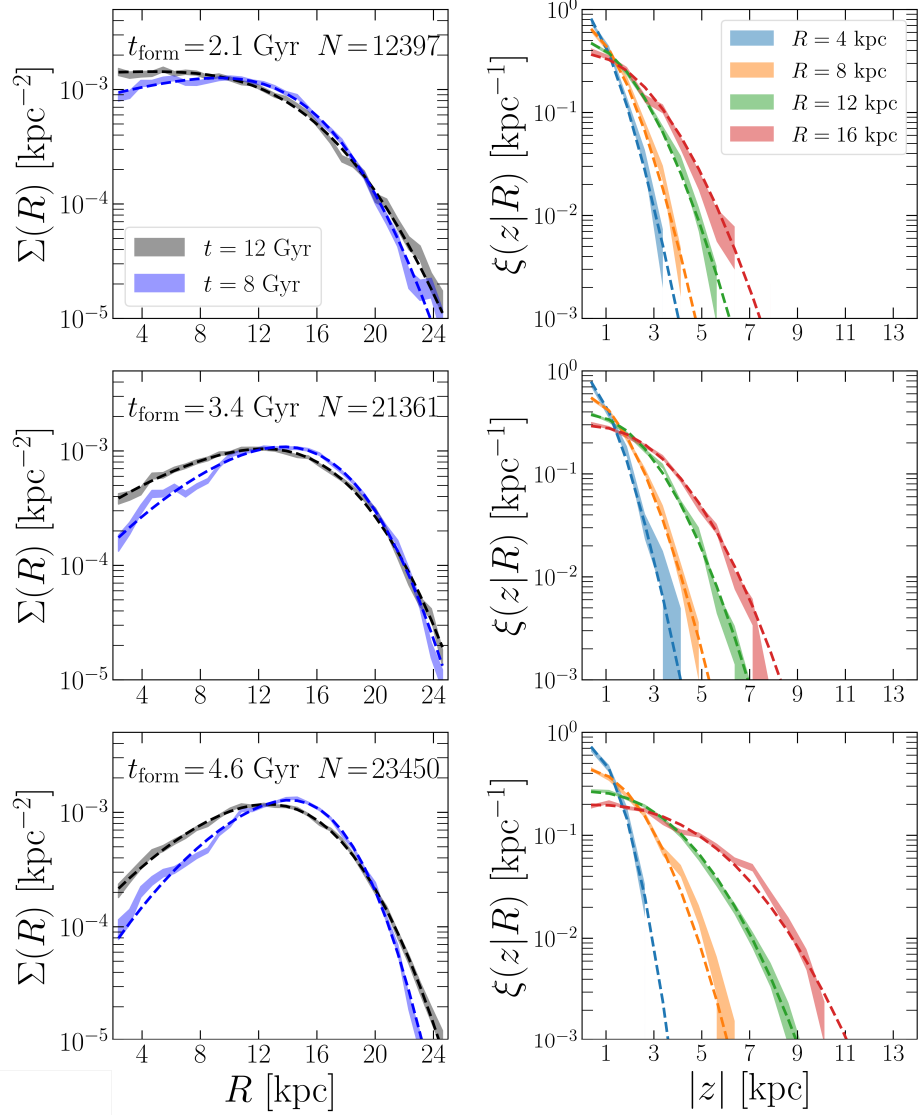
Figure 3.16: Left: radial density profiles for old ($t_{\mathrm{form}} < 5\,\mathrm{Gyr}$) mono-age populations (rows), with formation times indicated. Black (blue) curves show the profiles at $t = 12\,\mathrm{Gyr}$ ($t = 8\,\mathrm{Gyr}$), which are well described by skew-normal distributions (dashed lines). Due to inward migration, older populations are progressively negatively-skewed, peaking at smaller radii, and all populations evolve significantly over the last 4 Gyr (compare black and blue curves within each panel). Right: vertical profiles for different radii (colours) at $t = 12\,\mathrm{Gyr}$. The profiles are well described by generalized normal distributions (dashed lines), and get more flattened and thicker for larger R and larger t_{form} (Figure 3.17)
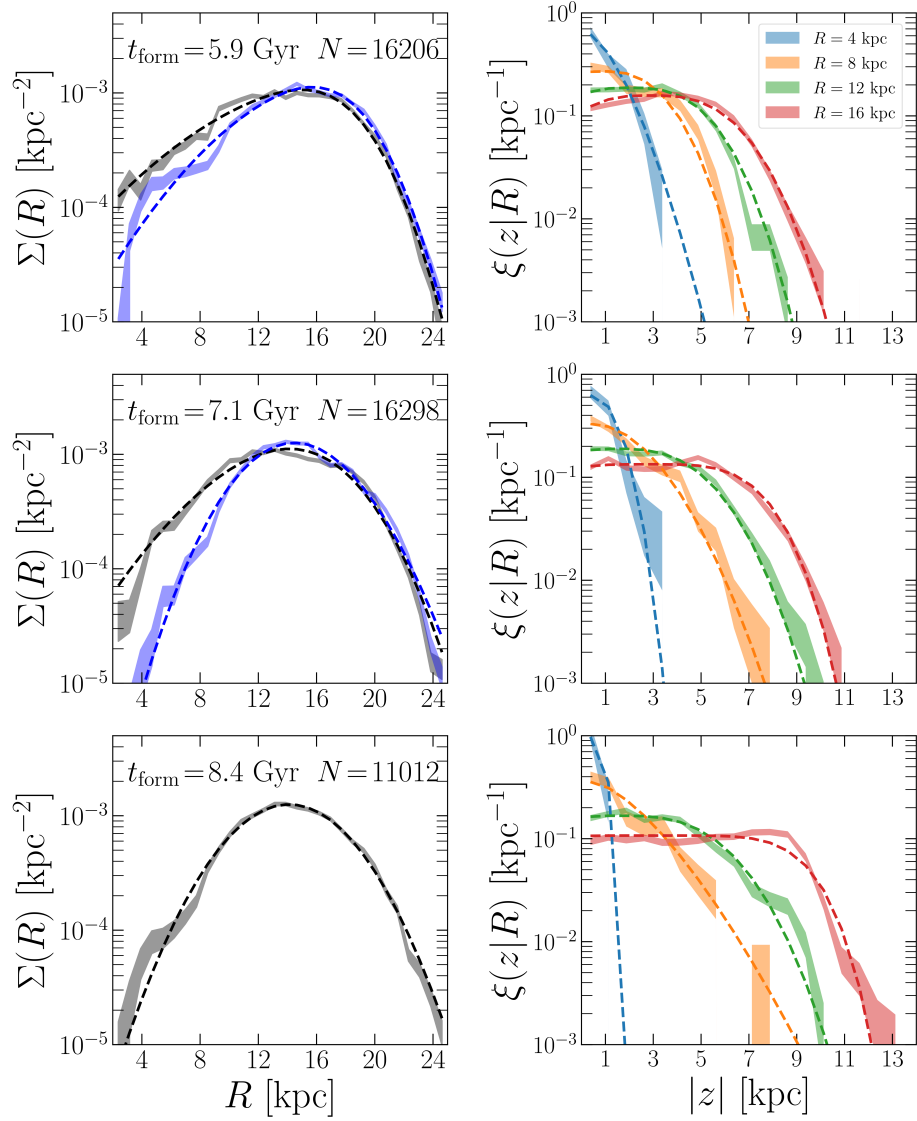
Figure 3.17: Same as Figure 3.16 younger populations ($t_{\mathrm{form}} > 5\,\mathrm{Gyr}$). Younger populations have approximately Gaussian profiles peaking at $R_{\mathrm{peak}} \approx 15\,\mathrm{kpc}$.

3.6.1 Radial density profiles

The black shaded curves in the left column of Figures 3.16 and 3.17 show $\Sigma(R)$, with Poisson uncertainties, at the final snapshot ($t = 12\,\mathrm{Gyr}$). For young populations (Figure 3.17), $\Sigma(R)$ is peaked at $R_{\mathrm{peak}} \approx 14\,\mathrm{kpc}$ and is approximately symmetric around this peak. Older populations (Figure 3.16) get increasingly centrally concentrated, with R_{peak} moving to lower values and $\Sigma(R)$ becoming increasingly skewed. In order to confirm that this is the consequence of a continuous evolution (as opposed to rather different initial conditions of different mono-age populations), we also show the profiles of the same populations, calculated at $t = 8\,\mathrm{Gyr}$ (blue shaded curves). The apparent time evolution from the bottom to the top panels is confirmed within each panel, with each mono-age population (including the oldest one at the top of Figure 3.16) becoming more centrally concentrated over the 4 Gyr between $t = 8\,\mathrm{Gyr}$ and $t = 12\,\mathrm{Gyr}$, indicating the effect of continuous inward migration.

The best fit models (dashed lines) in the left column of Figures 3.16 and 3.17, show a good agreement with the empirical profiles. In Figure 3.18, we show the best fit parameters as a function of the formation time (black shaded curves, evaluated at $t = 12\,\mathrm{Gyr}$). Instead of α, μ_R and h_R, we show the derived quantities representing the skewness, the peak position, R_{peak}, and the dispersion of the radial coordinate, σ_R. The skewness (left panel) shows a clear trend, decreasing from ≈ 0 for the youngest populations (large t_{form}) to ~ -1 for the oldest ones (small t_{form}), consistent with the strong change of slope of the inner part of $\Sigma(R)$ observed in Figures 3.16 and 3.17. The position of the density peak is shown in the central panel. It decreases mildly from $R_{\mathrm{peak}} \approx 14\,\mathrm{kpc}$ for the youngest populations to $R_{\mathrm{peak}} \approx 12\,\mathrm{kpc}$ for $t_{\mathrm{form}} \approx 4\,\mathrm{Gyr}$, after which it strongly decreases (from right to left) to $R_{\mathrm{peak}} \approx 4\,\mathrm{kpc}$ for the oldest populations. This strong decrease seems to be associated with the inner slope of $\Sigma(R)$ becoming close to zero for small t_{form} (see Figures 3.16 and
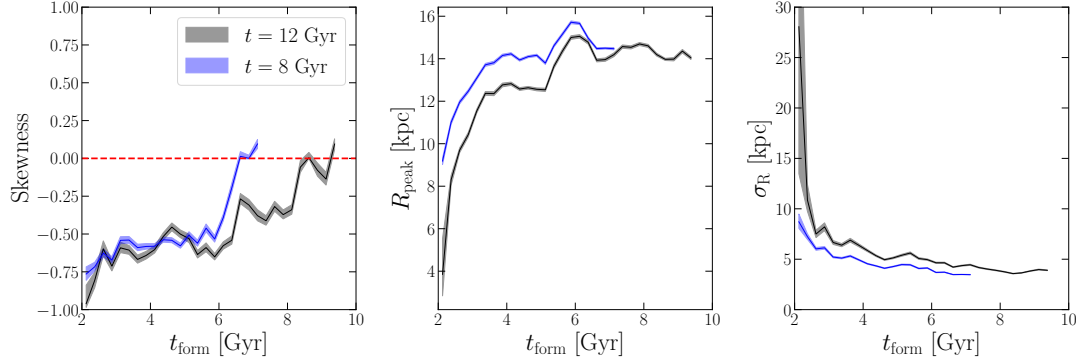
Figure 3.18: Derived quantities from the best fit models of the radial density profiles for different mono-age populations, evaluated at $t = 12\,\mathrm{Gyr}$ (black) and $t = 8\,\mathrm{Gyr}$ (blue). The skewness (left panel) is approximately zero for young populations (large t_{form}) and gets progressively more negatively-skewed for older populations (small t_{form}). The central panel shows that the profiles peak at $R_{\mathrm{peak}} \approx 14\,\mathrm{Gyr}$ for $t_{\mathrm{form}} \gtrsim 5\,\mathrm{kpc}$, and drops quickly to $R_{\mathrm{peak}} \approx 4\,\mathrm{kpc}$ at $t_{\mathrm{form}} \approx 2\,\mathrm{Gyr}$. The dispersion (right panel) is $\sigma_R \approx 5\,\mathrm{kpc}$ for $t_{\mathrm{form}} \gtrsim 5\,\mathrm{Gyr}$ and increases rapidly for $t_{\mathrm{form}} \lesssim 5\,\mathrm{Gyr}$.

3.17), in which case a small change in this slope can imply large changes in the peak position. Finally, the radial dispersion (right-hand panel) is $\sigma_R \approx 5\,\mathrm{kpc}$ for $t_{\mathrm{form}} \gtrsim 5\,\mathrm{Gyr}$, and increases rapidly for older populations, which is correlated with the behaviour of R_{peak} just mentioned (a strictly horizontal inner $\Sigma(R)$ would imply an infinite dispersion).

As in Figures 3.16 and 3.17, blue shaded curves represent the best fit models of the same mono-age populations, evaluated at $t = 8\,\mathrm{Gyr}$. All parameters follow similar trends with t_{form}. Comparison of the black and blue curves shows that the profiles become more negatively skewed, more centrally concentrated and with larger dispersion over the last 4 Gyr of evolution. Interestingly, for both $t = 8\,\mathrm{Gyr}$ and $t = 12\,\mathrm{Gyr}$, the skewness is ~ 0 for those populations with $t_{\mathrm{form}} \sim t$, *i.e.* for the youngest populations at each snapshot. This suggests that all mono-age populations are formed with (or quickly evolve to) a Gaussian radial density profile, subsequently

evolving towards negatively skewed distributions associated with inward migration. It is also interesting to note that, at $t = 8\,\mathrm{Gyr}$, R_{peak} and σ_R do not show the strong gradients near $t_{\mathrm{form}} \approx 2\,\mathrm{Gyr}$ observed at $t = 12\,\mathrm{Gyr}$. Comparison with the top-left panel of Figure 3.16 suggests that this is associated with the fact that, at $t = 8\,\mathrm{Gyr}$, the oldest populations did not have enough time to achieve a nearly-uniform inner radial density profile.

3.6.2 Vertical density profiles

The right panels in Figures 3.16 and 3.17 show the vertical number density profiles $\xi(z|R)$, with Poisson uncertainties, within cylindrical shells of width $2\,\mathrm{kpc}$ at different radii (colours), for each mono-age population (t_{form} indicated in the left panels), evaluated at $t = 12\,\mathrm{Gyr}$. As a general trend, the vertical profiles get flatter and thicker, both as a function of R (for a fixed t_{form}) and as a function of t_{form} (for a fixed R). The dashed lines represent the best fit models and we observe a good agreement with the empirical profiles for all radii and formation times.

Figure 3.19 shows the best fit values and uncertainties of parameters β, z_{peak} and h_z (see Eq. 3.9) as functions of radius, for the same formation times shown in Figures 3.16 and 3.17. As mentioned above, the radial variation of each of these parameters is modelled as a third-order polynomial, resulting in a total of 12 parameters. The left panel shows the parameter β. The horizontal line at $\beta = 2$ represents a Gaussian distribution and we see that no mono-age population has $\xi(z|R)$ compatible with a Gaussian for all radii. The oldest population ($t_{\mathrm{form}} \approx 2.1\,\mathrm{Gyr}$) is the only one for which β increases monotonically as a function of radius, being compatible with a Gaussian for $R \gtrsim 16\,\mathrm{kpc}$, while $\xi(z|R)$ is more spiky than the Gaussian for $R \lesssim 16\,\mathrm{kpc}$. For all the other populations, β depends non-trivially on radius. However, despite this complexity, broadly speaking in the range $8 \lesssim R/\,\mathrm{kpc} \lesssim 20$, the parameter β increases as a function of R (for a fixed t_{form}) and as a function
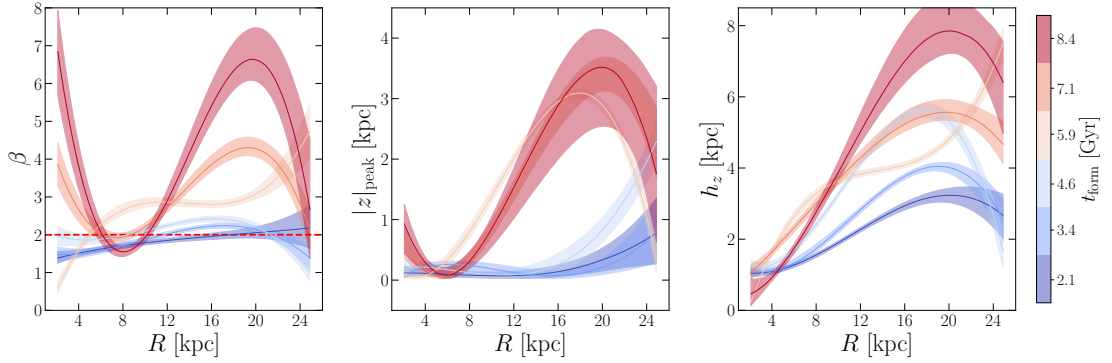
Figure 3.19: Best fit parameters of the vertical density profiles using Eq. 3.9 for different mono-age populations, colour-coded by the formation time. All quantities have complex radial dependencies, but are simpler if we consider the restricted interval $8 \lesssim R/\,\mathrm{kpc} \lesssim 20$, where, broadly speaking, all quantities increase monotonically with radius for most populations. The β parameter (left panel) of no population is compatible with a Gaussian (horizontal dashed line) for all radii, while young populations (yellow) are highly non-Gaussian. The central panel shows the peak location, which seems to split into two groups: old populations ($t_{\mathrm{form}} \lesssim 5\,\mathrm{Gyr}$) peak near the plane ($0 \lesssim z_{\mathrm{peak}} \lesssim 1$), while for younger populations z_{peak} increases rapidly with radius, achieving $z_{\mathrm{peak}} \approx 4\,\mathrm{kpc}$. The right panel shows that, broadly speaking, the scale parameter h_z increases with radius (flaring profiles), with younger populations flaring more than the older ones.

of t_{form} (for a fixed R). The location of the peak, shown in the central panel, also has non-trivial dependencies on R, if we take into account all the radial interval. In the restricted interval $8 \lesssim R/\,\mathrm{kpc} \lesssim 20$, we note two main groups, with the three oldest populations peaking at small $|z|$, with $0 \lesssim z_{\mathrm{peak}}/\,\mathrm{kpc} \lesssim 1$, while for the three youngest populations z_{peak} increases fast with radius, achieving $z_{\mathrm{peak}} \approx 4\,\mathrm{kpc}$. This suggests some abrupt change in the final $\langle|z|\rangle$ for stars formed at $t_{\mathrm{form}} \approx 5\,\mathrm{Gyr}$. Finally, the scale parameter h_z is shown in the right panel. Once more, despite the complex radial dependence, if we restrict to the interval $8 \lesssim R/\,\mathrm{kpc} \lesssim 20$, we note an approximately monotonic increase with R, *i.e.* flaring vertical profiles, with younger populations flaring more than the old ones.

In summary, stars formed in the warp make their way into the disc and settle into radial density profiles which can be described as skew-normal distributions (Azzalini 1985), with young stars approximately described by Gaussians peaking at a radius close to where the warp reaches its peak tilt, and which evolve to increasingly negatively skewed distributions and smaller R_{peak} for older populations. The vertical density profiles are well described by the generalized normal distribution (Nadarajah 2005), and become flatter and thicker, both as a function of R and of t_{form}.

3.7 Discussion

We have studied the dynamical evolution of stars formed in the warp of an N-body+SPH simulation. We showed that the warp populations experience a rapid tilting, becoming more aligned with the disc (Figures 3.5 & 3.6). The extent by which warp stars can tilt into the main plane is limited by the speed with which differential precession disrupts a coherent warped plane. Warp populations in the simulation tilt by $\lesssim 5°$. Once they have tilted, warp stars continue to experience differential precession, which drives phase mixing, a slower process that continues much longer. After settling the warp stars populate the geometric thick disc (Figure 3.15), in good

agreement with the results of Roškar et al. (2010a), who showed that the warp stars in their cosmological simulation end up populating a geometric thick disc.

In Figures 3.12 and 3.13 we found that the average radial positions of the warp stars are constantly decreasing even after settling. This decrease in the average radius is partly due to the fact that no warp stars, by our definition, are formed inside 10 kpc, which means that there is a net inward migration of warp stars. This decrease by itself is not evidence of radial migration, since the stars might be reaching smaller radii via heating. Stars need to be on near-circular orbits to migrate radially via spiral churning (Sellwood & Binney 2002b; Roškar et al. 2012). We found that all warp populations have low eccentricities after they settle into the disc, making them susceptible to spiral churning which drives radial migration. Though warp stars populate the geometric thick disc and have higher $|z|$, that does not exclude them from radial migration since thick disc stars can migrate (Solway et al. 2012; Mikkola et al. 2020; Beraldo e Silva et al. 2020b).

The fiducial simulation presented here was run with a low gas density threshold for star formation in order that stars could form in the warp. To confirm that the settling process is not unique to this simulation we performed the same analysis as in Section 3.5 on five other simulations. Some of the key differences between the simulations are their star formation thresholds (low and high) and the longevity of the gas warp (short or long-lasting). In these supplemental simulations settling of warp stars is still observed in all mono-age populations, but the resulting thick disc in each simulation varies in thickness and t_{form} gradients for warp stars. The vertical age gradient shown in Section 3.6.2 is present in some of the supplemental simulations with a trend where a growing warp leads to a stronger age positive gradient. In cases where star formation in the warp is less favourable (high threshold) or the warp is short-lived, we generally find a near-zero or negative age gradient. The difference in the vertical gradients therefore comes as a result of how the warp in each simulation

evolved. Growing warps form newer stars at increasingly higher θ_L and $|z|$ which settle into the thick disc at higher $|z|$, forming a positive vertical gradient. Lastly, there are differences in the tilting and phase mixing timescales along with the extent of the subsequent radial migration depending on the warp extent, but in all cases we find that warp stars settle onto near-circular orbits. The settling, phase mixing, and migration of stars that we have focused on here therefore can be considered to be generic of stars formed in a warp, while the details of the density distributions on which the warp stars settle (thickness, age gradients, etc) are specific to the evolution of the specific warp in which they form.

3.7.1 Consequences for the Milky Way

With the discovery of young stars (e.g. Cepheids) tracing the HI Galactic warp (Chen et al. 2019a) in the Milky Way, an important question to consider is whether these warp populations can eventually be found in the Solar Neighbourhood. The warp stars in our simulation form at increasingly large radii, and in any case are all formed outside $R = 10$ kpc, and therefore, in order to observe them in the Solar Neighbourhood, these stars must migrate radially. In Section 3.5.4 we have shown that warp stars migrate inwards to quite small radii via spiral churning. We conclude that stars forming in the Milky Way's warp can indeed be found in the Solar Neighbourhood, and populating the thick disc. The age range of warp stars at the Solar annulus of our fiducial simulation shows that due to the diffusive nature of migration, the only young warp stars that can be observed are those born closest to the Solar annulus (see right panel of Figure 3.13). Young warp stars born further in the warp experience rapid tilting, but do not have enough time to migrate to the Solar Neighbourhood, unlike older populations which are observed throughout the disc.

Since the detailed history of the warp in our model is unlikely to match that of

the Milky Way's warp, we refrain from more direct comparisons of our model to the Milky Way.

3.7.2 Summary

We have selected populations of stars formed in the warp of an N-body+SPH simulation. We identified warp populations, by measuring the inclination of the angular momentum of each star, θ_L, and analysed their dynamical evolution. In summary, we have shown that:

- Most warp stars tilt to become more aligned with the galactic disc by $\sim 5°$. Orbital tilting is evident from the mean tilt of the angular momenta, $\overline{\theta_L}$, and the mean absolute height above the mid-plane, $\overline{|z|}$, of mono-age warp populations, which experience rapid declines during the first $\sim 1\,\mathrm{Gyr}$ before becoming roughly constant. Using the $\overline{\theta_L}$ and $\overline{|z|}$ rates of change, we found tilting times ranging from $0.25\,\mathrm{Gyr}$ to $1.75\,\mathrm{Gyr}$.

- Mono-age warp populations phase-mix in angular momentum space via differential precession at different rates. Stars are completely homogeneous in the distribution of the angular momentum azimuthal angle ϕ_L after $6\,\mathrm{Gyr}$.

- The time derivative of the vertical angular momentum, L_z, along with that of the radial positions is negative after $1\,\mathrm{Gyr}$ for all warp populations and both decrease until the end of the simulation. This is suggestive of inward radial migration of warp populations.

- We found that almost all warp stars that have settled are on close to circular orbits, with mean eccentricities ranging from 0.2 to 0.3 for all settled warp populations. These low eccentricities indicate that warp stars are able to migrate to the inner disc via spiral churning.

CHAPTER 3

- A detailed modelling of the density distribution of settled warp stars finds that their initial torus-shaped density distribution is slowly filled in as warp stars migrate to smaller radii. Because the warp in the model grows with time, the warp populations settle to increasingly thicker tori/discs.

- A settled mono-age warp population is radially flaring. In our model the flaring increases with the formation time of the population, an indication of the growing warp.

Chapter 4

Bending waves caused by galactic warps

This chapter is based on a paper in preparation as Tigran Khachaturyants, Leandro Beraldo e Silva, Victor P. Debattista1, Kathryne J. Daniel. The simulations used throughout this chapter are the WM1 (warped) and UM (unwarped) models.

4.1 Abstract

GAIA has shown clear evidence of bending waves in the vertical kinematics of stars in the Solar Neighbourhood. We use a simulation of a warped galaxy to show that if the Milky Way warp was formed and is supported via gas accretion then the irregular infall of gas could give rise to bending waves. The propagation of these bending waves seems to result in a correlation between the mean vertical velocity and the angular momentum, similar to that observed in the Solar neighbourhood. The bending waves propagate across the entire disc in the span of $\sim 400\,\mathrm{Myr}$ and stellar populations of all ages are affected by them, though the effect is more distinct in younger stars. In an unwarped simulation, the effect of bending waves is significantly weaker than those excited by the accreting gas and they appear to be

a superposition of other weaker sources. We observe positive slopes in the L_z vs v_z relation for simulated Solar neighbourhoods in both simulations, possibly as a result of the bending waves. However, only the warped simulation has slopes of similar or higher values than measured in the Milky Way. A spectral analysis of the density and vertical displacement in both warped and unwarped simulations shows good agreement with the WKB approximation with both models containing slow and long-lasting retrograde bending waves in their discs. The fast prograde bending waves are present in the warped simulation throughout its evolution while in the unwarped case they decay in the span of $\sim 1\,\mathrm{Gyr}$. This difference is likely due to the continuous re-excitement by the accretion of cold gas in the warped simulation. The presence of a long-lasting warp gives rise to more prograde bending waves as the disc is being continuously perturbed which counteracts the natural dissipation via differential rotation. Warps are, therefore, a vital component in the study of the disc's vertical structure and evolution. In conclusion, warps produced by accretion of misaligned gas provide a natural rejuvenation mechanism for prograde bending waves that may be currently observed in the Milky Way.

4.2   Introduction

Using the Tycho-GAIA DR1 Astrometric Solution (TGAS) dataset (Gaia Collaboration et al. 2016d,b), Schönrich & Dehnen (2018a) found a linear increase in the mean vertical velocity, $\langle v_z \rangle$, with the azimuthal velocity, v_ϕ, angular momentum, L_z, and guiding radius, R_g, of stars in the Solar Neighbourhood. Since the line of nodes of the Galactic warp is only $\sim 17.5°$ ahead of the Sun (Chen et al. 2019a), this linear increase is potentially the warp's direct imprint on the local stellar kinematics. Because the TGAS dataset lacks radial velocity measurements, Schönrich & Dehnen (2018a) used only stars along narrow cones in the centre and anti-centre directions, for which the radial velocity is not required to obtain v_z and v_ϕ. Schönrich & Dehnen

(2018a) also noted the presence of a wave-like pattern imprinted on the overall $\langle v_z \rangle$ distribution, towards both the centre and anti-centre directions. A smooth, monotonic warp would not present such a signal; instead Schönrich & Dehnen (2018a) obtained a good fit with a simple sinusoidal wave, as might be produced by a winding warp or by a bending wave. Subsequently, this pattern in $\langle v_z \rangle$ was replicated by Huang et al. (2018a) using a $\sim 10^5$-star sample from the LAMOST-TGAS data. Unlike the TGAS sample, LAMOST-TGAS has full 6D phase space measurements, which allowed Huang et al. (2018a) to replicate the wavelike pattern in $\langle v_z \rangle$ versus L_z and versus v_ϕ in the entire Solar Neighbourhood (SN). With the release of GAIA DR2 the linear increase and wave-like pattern in $\langle v_z \rangle$ were again confirmed by Friske & Schönrich (2019).

Subsequently, GAIA DR2 discovered a phase-space spiral in the (z, v_z) plane (Antoja et al. 2018). Antoja et al. (2018) selected $\sim 9 \times 10^5$ stars in the Solar annulus of GAIA DR2 RVS, a sample containing the full 6D phase-space coordinates (Gaia Collaboration et al. 2018c), and projected them onto the (z, v_z) plane. The result was a spiral with one complete wrap, with a trailing tail reaching up to $\sim 700 \, \mathrm{pc}$ and $\sim 40 \, \mathrm{km \, s^{-1}}$ in $|z|$ and $|v_z|$, respectively. The presence of this phase-space spiral indicates that the SN is undergoing vertical phase mixing as a result of vertical perturbations (Antoja et al. 2018). The *Gaia* phase-space spiral was dissected by Li & Shen (2020), who showed it is weaker for stars on radially hotter orbits.

The cause of these vertical perturbations in the SN remains uncertain. In general, vertical perturbations in galactic discs propagate as bending waves (Hunter & Toomre 1969b; Merritt & Sellwood 1994; Sellwood 1996; Sellwood et al. 1998; Kazantzidis et al. 2009; Chequers et al. 2018; Khoperskov et al. 2019; Darling & Widrow 2019; Bland-Hawthorn et al. 2019) with many possible causes. Widrow et al. (2012) presented evidence for a wave-like perturbation in the Galactic disc in the form of the Galactic North-South asymmetry, speculating it could have come

about via satellite interaction. Feldmann & Spolyar (2014) used a high-resolution numerical simulation to study the interactions of dark matter substructure with the disc and observed that subhalo interactions resulted in distinct and coherent variations in the vertical velocities of disc stars. Gómez et al. (2017) presented multiple high-resolution cosmological simulations of individual Milky Way-sized galaxies that develop significant vertical bending waves via satellite interactions.

The Sagittarius dwarf galaxy (Sgr) is the most frequently invoked external cause of vertical excitation of the Milky Way's disc (Ibata & Razoumov 1998b; Dehnen 1998b; Laporte et al. 2019b), due to its relatively recent ($\sim 0.4 - 1$ Gyr) passage through the disc and an orbit that is perpendicular to the Galactic plane (Ibata & Razoumov 1998b; Laporte et al. 2019b). Sgr has also been suggested to be the cause of the bending wave observed by Schönrich & Dehnen (2018a) and Huang et al. (2018a). The analysis of the phase-space spiral lead Antoja et al. (2018) to infer that the Galactic disc was perturbed in the past $300 - 900$ Myr, which matches current estimates of a pericentric passage by Sgr. Li & Shen (2020) presented further support for the Sgr scenario with a vertically perturbed test particle simulation. They estimated that the perturbation should have happened at least 500 Myr ago to observe the *Gaia* phase-space spiral in its current form. However, other simulations have shown inconsistencies in the Sgr scenario. Binney & Schönrich (2018) produced a phase-space spiral in a SN population extracted from a distribution function fitted to GAIA DR2 RVS and estimated that the spiral formed 400 ± 150 Myr ago. While their time scale estimate is in some agreement with Antoja et al. (2018)'s results, the mass and duration of the interaction required to produce similar phase-space spirals were significantly higher and faster, respectively. In a pure N-body simulation Bland-Hawthorn & Tepper-García (2021) have shown that the current mass estimate of the Sgr dwarf is too low to excite the phase spiral. Instead Bland-Hawthorn & Tepper-García (2021) suggested that the interaction had to have happened $1 - 2$ Gyr

ago with the Sgr dwarf losing mass at a high rate. Additionally, Bennett & Bovy (2021) used one-dimensional (vertical) models of satellite-disc interaction and were unable to reproduce the observed asymmetry in the vertical number counts for any plausible combination of Sgr and Milky-Way properties.

On the other hand, Chequers et al. (2018) showed that isolated galaxies can also self-excite bending waves. Their N-body simulations of isolated galaxies naturally develop bending waves not just when the halo is clumpy but also when it is smooth. The bending waves in both kinds of simulations have a similar morphology and frequencies, but differ in amplitude, with the clumpy halo exciting waves of higher amplitudes. In the smooth halo models, the bending waves were likely seeded by the random noise of the halo and bulge particle distributions (Chequers & Widrow 2017). In the clumpy halo models, instead, the subhalos imprint local perturbations on the disc which then shear into bending waves. Buckling of a galactic bar also induces bending waves in the disc. Khoperskov et al. (2019) presented a high resolution N-body simulation that developed a bar which then buckled, i.e. it suffered a vertical bending instability of the bar (Raha et al. 1991b; Sellwood & Merritt 1994). The resulting bending waves propagate outward in the disc and remain coherent for a long time, with the phase-space spirals still being distinguishable 3 Gyr after the bar buckles. However, it is unclear whether the Milky Way's bar could have buckled this recently without scattering too many relatively young stars into the bulge (Debattista et al. 2019a).

An alternative mechanism for generating vertical bending waves comes from the observation that, in galaxy formation simulations, gas reaches the disc with a misaligned angular momentum (Binney & May 1986; Ostriker & Binney 1989b; van den Bosch et al. 2002b; Roškar et al. 2010b; Velliscig et al. 2015; Stevens et al. 2017; Earp et al. 2019), regardless of whether it settles to the disc via hot or cold modes. Such angular momentum misalignments cause long-lived warps, as opposed

to the transient warps excited by interactions (Ostriker & Binney 1989c; Roškar et al. 2010b; Aumer et al. 2013). These warps provide another mechanism by which the disc may be vertically excited, as shown by Gómez et al. (2017), who found that some of their cosmological simulations had prominent vertical bends in discs which have not recently interacted with a satellite. They argued that these bends are most prominent in the youngest stellar populations ($< 2\,\mathrm{Gyr}$) and cold gas, and almost absent in the oldest stars.

The Milky Way's Hᴵ disc has long been known to be warped (Kerr 1957b; Weaver & Williams 1974; Levine et al. 2006c), with the warp reaching $\geq 4\,\mathrm{kpc}$ above the midplane at $R = 25\,\mathrm{kpc}$. A warp has also been observed in the stellar component of the Galactic disc (Efremov et al. 1981; Reed 1996; López-Corredoira et al. 2014). Recently, with the help of the *WISE* catalogue of periodic variable stars (Chen et al. 2018b), the stellar warp has also been mapped in greater detail in the young stellar populations (Chen et al. 2019a).

This paper uses N-body+SPH (Smooth Particle Hydrodynamics) simulations to explore a scenario in which bending waves are induced by gas accreting along a warp. The paper is organised as follows: the evolution of the warp is described in Section 4.3. In Section 4.4 we analyse the bending waves that develop in both the warped and unwarped simulations, comparing and contrasting them. In Section 4.5 we discuss the results of this paper. Lastly we summarise our results in Section 4.6.

4.3   Warp evolution

The top row of Fig. 4.1 presents edge-on views of stars (colour) and the cool ($T_g \leq 5 \times 10^4$ K) gas (red contours) between $t = 3\,\mathrm{Gyr}$ and $12\,\mathrm{Gyr}$. Throughout the evolution of the warped model, gas is accreted onto the disc along an integral-shaped warp. By $12\,\mathrm{Gyr}$ the gas warp extends up to $15\,\mathrm{kpc}$ above the plane at $R \sim 20\,\mathrm{kpc}$. Because of our re-orientation of the disc, the major axis of the warp is
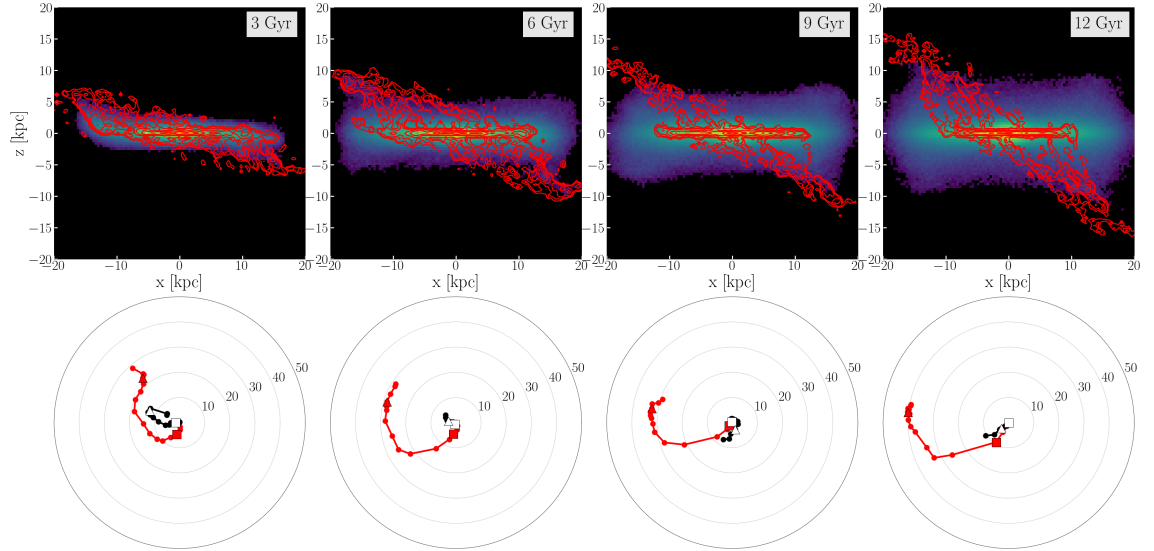
Figure 4.1: Top row: edge-on views of the stellar and cold gas (T$\leq 50,000$ K) distributions at four times in the evolution of the warped model. The colour represents the stellar surface density, while the red contours represent the cold gas column density. The times are labelled at the top-right in each panel. A warp is present throughout the evolution of the warped model. The simulation is rotated so that the major axis of the warp is along the x-axis. The warp reaches heights $|z| \sim 15$ kpc over this evolution. Bottom row: Briggs figures for the warped model showing the evolution of the stellar (black) and cool gas (red) warps at the same times. Markers represent annuli with $\Delta R = 1$ kpc, equally spaced from 5 to 20 kpc, with the square and triangle markers indicating annuli at 10 kpc and 20 kpc, respectively. The stellar disc is somewhat warped at $t = 3$ Gyr but becomes flatter throughout its evolution.

.
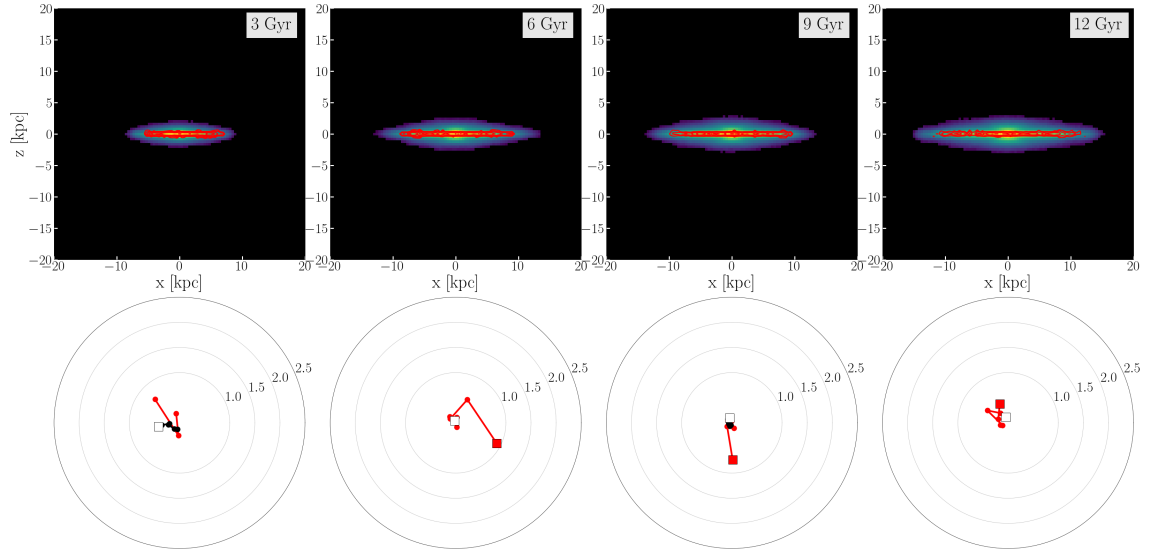
Figure 4.2: Similar to Fig. 4.1 but for the unwarped model. In contrast to the warped model, there are no warps in either the gaseous or stellar components in the edge-on distributions. The Briggs figures have a reduced scale with max $\theta = 2.5°$ set as the upper limit, so even though we see some changes at different radii, both gas and stellar discs are quite flat throughout the model's evolution.

.

along the x-axis and reaches a peak negative value along the $x > 0$ side; in reality
viewed from an inertial frame the disc is tilting slowly and continuously during this
time (Binney & May 1986; Ostriker & Binney 1989b; Debattista et al. 2015; Earp
et al. 2017, 2019) but we subtract this tilting.

In order to study the evolution of the warp, we construct Briggs figures (Briggs
1990b) for the warped and unwarped models. A Briggs figure represents warping
by means of the spherical angles, ϕ_J and θ_J, between the total angular momenta of
concentric annuli and the z-axis. These are then plotted as the radial, ρ (for θ_J),
and angular, ψ, (for ϕ_J) variables of a 2D polar plot. Because we reorient the discs
into the (x, y) plane based on the angular momentum of the inner disc stars before
we perform any analysis, the inner disc is at the centre of the Briggs figures, $i.e.$ it
has angular momentum along the z-axis. The bottom row of Fig. 4.1 shows Briggs
figures for the warped model at the same time intervals. The figure presents the
stars (in black) and the cool gas (in red) separately. The stellar and gaseous discs
are divided into annuli of width $\Delta R = 2$ kpc, and then we calculate the total angular
momentum of particles in each annulus. A warp is present in the gas component
throughout the evolution of the warped model. The warp grows slowly with time;
by 12 Gyr it extends to almost $40°$. The warp traces a leading spiral relative to the
sense of rotation of the disc, in agreement with Briggs's third rule of warp behaviour
(Briggs 1990b). On the other hand, the stellar component loses its large-scale warp
after 6 Gyr, and only a small warp remains.

In contrast, a similar analysis on the unwarped model does not reveal any disc
warping. In the top row of Fig. 4.2 the edge-on views of the unwarped model present
no stellar (colour) or gaseous (red contours) warps at any point in time. The bottom
row of Fig. 4.2 shows similar Briggs figures as in Fig. 4.1 but with significantly
smaller θ_L upper limits to underline the lack of warping in the unwarped model. We
observe no warping in the stellar component at all times and only minor tilting at

$R = 10\,\mathrm{kpc}$ at 6 and 9 Gyr for the gaseous component.'

Fig. 4.3 presents cold gas and stellar profiles for both models at $t = 10\,\mathrm{Gyr}$ in the surface density (top panel) and their inclination (bottom panel). The unwarped model experiences drops in surface density and inclination at the edge ($10\,\mathrm{kpc}$). In the warped model we observe a slower decline in the surface density with a weak increase in inclination ($\sim 15°$), caused by newly ($\leq 2\,\mathrm{Gyr}$) formed warp stars

4.4   Bending waves

4.4.1   The presence of vertical bends

Fig. 4.4 shows the stellar face-on distributions of the average height, $\langle z \rangle$ (top), and the average vertical velocity, $\langle v_z \rangle$ (bottom), in the warped (left) and unwarped (right) models. The distributions highlight the presence of large-scale bends (coherent blue and red structures) in the disc. The warped model exhibits bends with amplitudes of $\sim 100\,\mathrm{pc}$ and $\sim 3\,\mathrm{km\,s^{-1}}$ $\langle z \rangle$ and $\langle v_z \rangle$, respectively, that reach far inside the disc down to $R \simeq 2\,\mathrm{kpc}$. In agreement with Chequers et al. (2018), bends are also observed in the unwarped model, but are noticeably weaker, with amplitudes of $\sim 25\,\mathrm{pc}$ and $\sim 1\,\mathrm{km\,s^{-1}}$, respectively. The bends in the unwarped model also reach far inside the disc reaching the very centre. At first impression, the structure of the bends in both models do not appear to have any distinct shape and wavelength, requiring a more in-depth spectral analysis of the surface $\langle z \rangle$ distributions to probe for bending waves.

4.4.2   Spectral analysis of bending waves

In a cold, initially unperturbed axisymmetric, razor-thin disc rotating with an angular rotation curve $\Omega(R)$, bending waves with wavelengths smaller than the disc
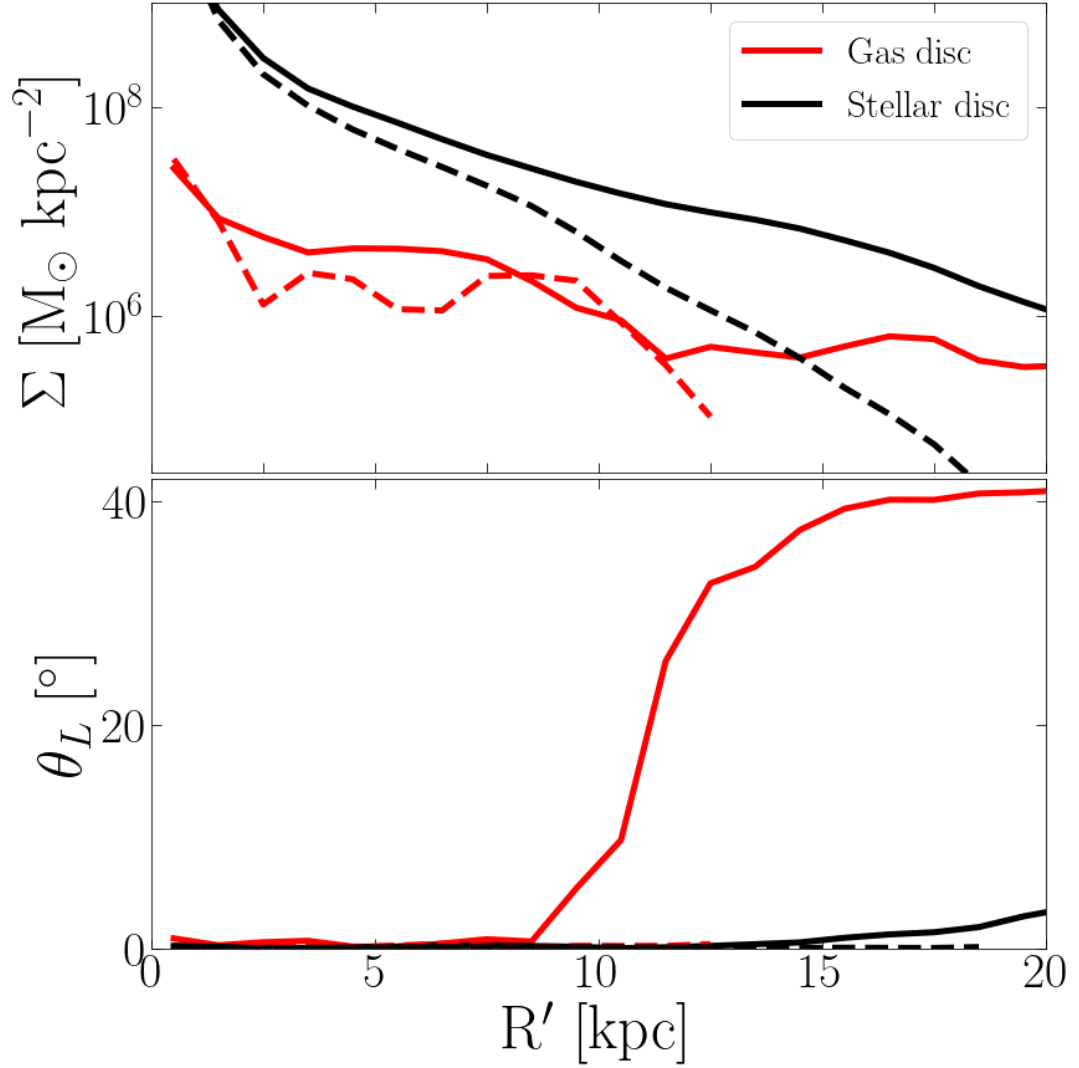
Figure 4.3: Profiles of the surface density, Σ, (top) and $\theta_{L,\,\mathrm{gas}}$ (bottom) in the warped (solid lines) and unwarped (dashed lines) models at $t = 12\,\mathrm{Gyr}$. The profiles are shown for both the cold gas (red) and stellar (black) discs, where R' is defined as the cylindrical radius in the cold gas and stellar planes at each annulus. Only bins with $\Sigma \geq 7 \times 10^6\,\mathrm{M_\odot}$ are shown.
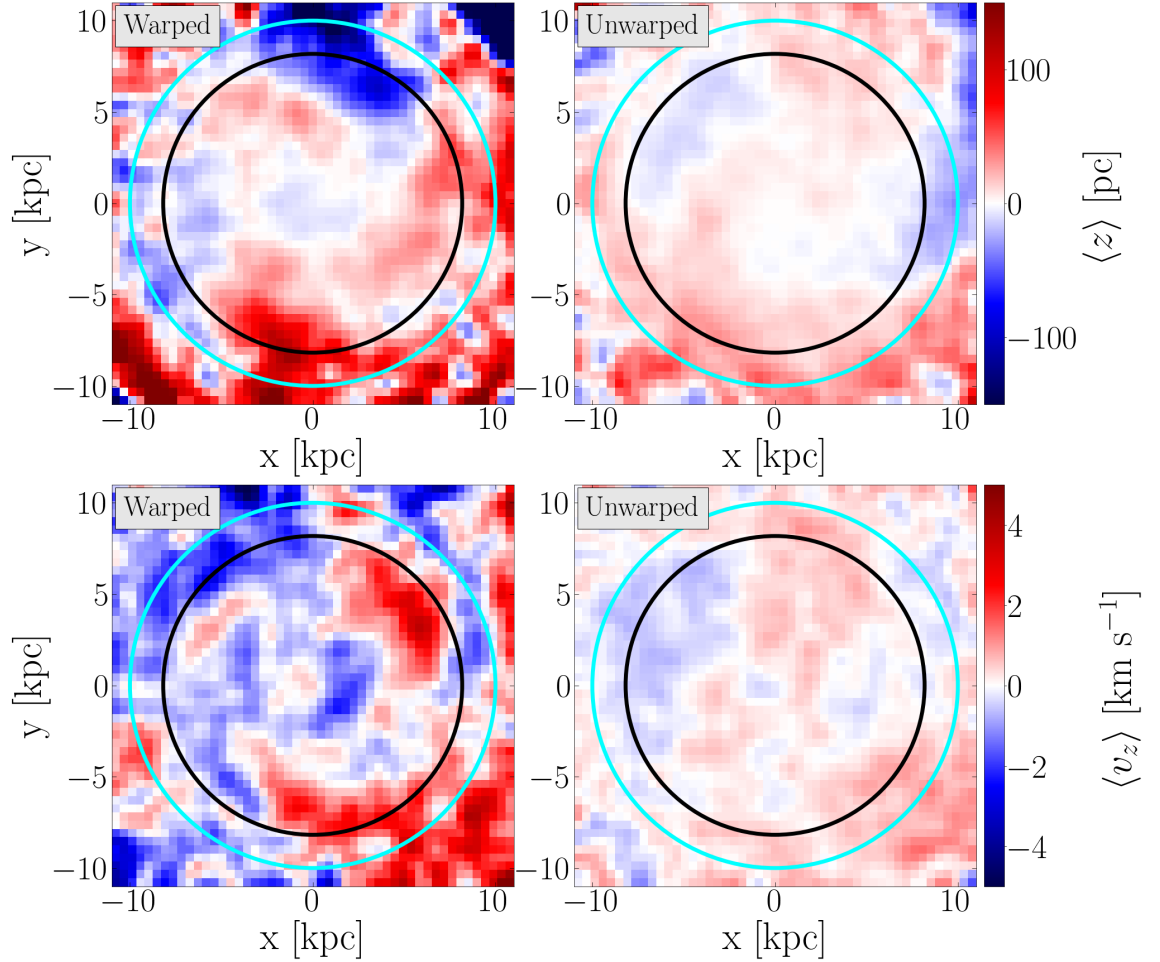
Figure 4.4: Face-on distributions of the stellar mean height, $\langle z \rangle$ (top), and mean vertical velocity, $\langle v_z \rangle$ (bottom), for the warped (left) and unwarped (right) simulations at $t = 11.7$ Gyr. A Gaussian filter has been applied to the colour distribution in each panel with a standard deviation of the Gaussian kernel set to $\sigma = 1$ pixel $= 450 \times 450$ pc. The solid black and cyan circles represent the Solar annulus, $R = 8.18$ kpc, and $R = 10$ kpc, respectively.

scale length (*i.e.* in the WKB approximation) satisfy the dispersion relation

$$m^2 \left[\Omega_p - \Omega(R)\right]^2 - 2\pi G\Sigma(R)|k| - \nu_h^2 = 0, \tag{4.1}$$

where $\omega = m\Omega_p$ is the wave frequency, Ω_p is the associated pattern speed, $\Sigma(R)$ is the disc surface density, k is the wave number and ν_h is the frequency of vertical oscillation due to the halo potential (Hunter & Toomre 1969b; Sparke & Casertano 1988; Binney & Tremaine 2008b; Sellwood 2013). For a given rotation curve $\Omega(R)$, these waves can only propagate in regions provided they satisfy the condition

$$m^2 \left[\Omega_{\mathrm{p}} - \Omega(R)\right]^2 \geq \nu_h^2, \tag{4.2}$$

which defines, for $m = 1$, a "forbidden" region, $\Omega - \nu_h < \Omega_p < \Omega + \nu_h$, where WKB bending waves cannot propagate (e.g. Nelson & Tremaine 1995). This is analogous to the allowed region for the propagation of density waves in cold discs, defined by

$$m^2 \left[\Omega_{\mathrm{p}} - \Omega(R)\right]^2 \leq \kappa^2, \tag{4.3}$$

where κ is the epyciclic frequency of radial oscillation – see Binney & Tremaine (2008b).

The dispersion relation of Eq. 4.1 implies that bending waves can manifest as either a "fast" prograde wave, with $\Omega_{\mathrm{p}} = \Omega + \sqrt{2\pi G\Sigma|k| + \nu_h^2}/m$, or a "slow" retrogade wave, with $\Omega_{\mathrm{p}} = \Omega - \sqrt{2\pi G\Sigma|k| + \nu_h^2}/m$. Due to differential precession, the "fast" component is expected to phase-mix rapidly and hence decay, while the "slow" retrograde wave is expected to be long-lived.

In order to investigate in detail the propagation of bending waves in our models, in this section, we employ the spectral analysis technique of Sellwood & Athanassoula (1986), using a code based on that of Roškar et al. (2012). This allows us to recover the spatial distribution and temporal evolution of pattern speeds. The code is applied to both the unwarped and the warped simulations, first for the density distribution and then for the vertical distribution.

CHAPTER 4

At each snapshot, we start by selecting star particles in concentric annular bins. In each annulus, we first expand the azimuthal angular dependence of the normalised mass distribution in a Fourier series

$$\mu(R, \phi) = 1 + \sum_{m=1}^{\infty} c_m(R) e^{-im\phi}, \tag{4.4}$$

with

$$c_m(R) = \frac{1}{M(R)} \sum_{p=1}^{N} m_p e^{im\phi_p}, \tag{4.5}$$

where the sum runs over particles inside the annulus, m_p and ϕ_p are the mass and azimuth of particle p, respectively, and $M(R)$ is the total mass within the annulus. We calculate the coefficients $c_m(R)$ for every snapshot in a given time interval (hereafter baseline) and then perform a discrete Fourier transform of this time series as

$$C_{m,k}(R) = \sum_{j=0}^{S-1} c_m(R, t_j) w_j e^{2\pi ijk/S}, \tag{4.6}$$

with $k = -S/2, ..., S/2$, where S is the number of snapshots in the baseline. The associated frequencies are given by

$$\Omega_k = \frac{2\pi}{m} \frac{k}{S\Delta t}, \tag{4.7}$$

where Δt is the time between snapshots, and we adopt the Gaussian window function

$$w(j) = e^{-(j-S/2)^2/(S/4)^2}. \tag{4.8}$$

Finally, the power spectrum is computed as

$$P(R, \Omega_k) = \frac{1}{W} |C_{m,k}(R)|^2, \tag{4.9}$$

where

$$W = S \sum_{j=0}^{S-1} w_j^2. \tag{4.10}$$

We perform this calculation for a time baseline $S\Delta t = 1$ Gyr, resulting in a resolution $\Delta\Omega = 2\pi/m \ \mathrm{km\,s^{-1}\,kpc^{-1}}$ – see Eq. 4.7. We repeat this calculation for several time baselines.

CHAPTER 4

In order to analyse the bending signal, similarly to Eq. 4.5 we define

$$\gamma_m(R) = \frac{1}{M(R)} \sum_{p=1}^{N} z_p m_p e^{im\phi_p}, \qquad (4.11)$$

where z_p is the vertical height of particle p, and use Eqs. 4.6-4.9 *mutatis mutandis.* Note that now $\gamma_m(R)$ is given in kpc and the associated power spectrum is given in kpc^2.

For the analysis in this section, in order to compare results with the analytic expressions of the WKB approximation, we also compute the frequencies of circular motion $\Omega(R)$ and radial oscillation $\kappa(R)$ produced by the total potential and the frequency of vertical oscillation produced by the halo $\nu_h(R)$, using AGAMA (Vasiliev 2019). These frequencies are computed in the middle of each 1 Gyr baseline.

Unwarped simulation

The two left-hand columns of Fig. 4.5 show, for the unwarped simulation, the power spectra obtained for $m = 1$ and $m = 2$ density perturbations (as indicated in the titles) in the (Ω, R) plane at different times (rows), from 5 Gyr to 12 Gyr. The $m = 2$ density signal shows multiple pattern speeds at all times, covering a large radial extent and revealing the presence of multiple spiral density waves. The thick dashed white lines show the rotation curves, $\Omega(R)$, at the different times, while the thin dashed white lines show the inner and outer Lindblad resonances $\Omega \pm \kappa/m$. The white shaded regions above and below these lines represent the forbidden regions for propagation of density waves, as predicted by the WKB approximation – see Eq. 4.3. Most clearly for $m = 2$, the power tends to lie in the allowed region, in good agreement with the WKB approximation.

The panels at the right of each of these spectrograms show the total power, i.e. the radially-integrated power spectra (in log scale); prominent peaks for $m = 2$ can be immediately distinguished. These peaks are used to estimate the pattern speed values, and are identified via an iterative scheme similar to that of Roškar

et al. (2012): we first identify the most prominent peak, fit a Gaussian function to it and subtract this Gaussian contribution from the total power. Then, we identify the next most prominent peak and repeat the process, identifying the pattern speed value and power for a maximum of four peaks in total in the interval $-100 \lesssim \Omega/\,\mathrm{km\,s^{-1}\,kpc^{-1}} \lesssim 100$ (horizontal lines, with length representing the power after the Gaussian subtraction of peaks previously identified). The $m = 1$ density signal shows some significant power, but the pattern speed peaks are not as prominent as those for $m = 2$, which is expected since spirals are normally two-armed. It is interesting to note an apparent correlation between an $m = 1$ peak at $\Omega_p \approx 25$ $\mathrm{km\,s^{-1}\,kpc^{-1}}$ with an $m = 2$ peak at the same pattern speed, which suggests imperfectly bisymmetric spiral arms.

Fig. 4.6 (left panels) shows the identified $m = 1$ (top) and $m = 2$ (bottom) density pattern speeds for several 1 Gyr-baselines, with colours representing the ratio R_{peak}/R_{CR}, where R_{peak} is the radius where the power spectrum peaks for a given pattern speed and R_{CR} is the co-rotation radius. Density signals with pattern speeds peaking inside (outside) co-rotation are blue (red). The area of each point is proportional to the total power in Fig. 4.5, and the prominent peaks for the $m = 2$ signal translate into larger markers for $m = 2$, in comparison to $m = 1$. Focusing on $m = 2$, this figure clearly shows the simultaneous presence of multiple pattern speeds. The neutral colours ($R_{\mathrm{peak}}/R_{CR} \approx 1$) show that these pattern speeds tend to peak along the rotation curve $\Omega(R)$, i.e. in the region allowed by the dispersion relation of Eq. 4.1, as anticipated in Fig. 4.5. The higher pattern speeds, at $60 - 75\,\mathrm{km\,s^{-1}\,kpc^{-1}}$, located inside co-rotation (blue points) and decreasing in time are due to the presence of a slowing bar (see Fiteni et al. 2021). The other two prominent pattern speeds can be attributed to the propagation of spiral density waves. It is interesting to note that in this simulation, and for the time interval analysed, the pattern speeds show some evolution, changing values, power amplitude and peaking

both inside and outside co-rotation, but not very vigorously transient behaviour. The strongest pattern is at $\Omega \approx 20 - 25\,\mathrm{km\,s^{-1}\,kpc^{-1}}$. As shown in Roškar et al. (2012), what is transient about these spirals is not necessarily their frequency, with some modes seemingly preferred, but their amplitude, which continuously varies. We cannot exclude the possibility that certain modes are continuously being re-excited, most likely with random relative phases.

The power spectra for the $m = 1$ and $m = 2$ bending signal in the unwarped simulation are shown in the two right-hand columns of Fig. 4.5 (as indicated in the titles). The panels to the right of these spectrograms again show the radially-integrated power spectra (strong and pale blue) with the peaks identified in the same way as before. The white thick dashed lines again show the rotation curve $\Omega(R)$, while the shaded white areas between $\Omega \pm \nu_h/m$ represent the forbidden regions for bending waves – see Eq. 4.2. Focusing on $m = 1$, the most noticeable feature in these spectra is the ubiquitous presence of a slow retrograde pattern at $-15 \lesssim \Omega/\,\mathrm{km\,s^{-1}\,kpc^{-1}} \lesssim -10$ and extending from $R = 5\,\mathrm{kpc}$ to $15\,\mathrm{kpc}$. For some snapshots, we also detect a fast prograde motion at $\Omega \approx 50\,\mathrm{km\,s^{-1}\,kpc^{-1}}$, which generally has much lower power than the slow retrograde pattern.

The right-hand panels of Fig. 4.6 show the time evolution of the pattern speeds identified for the bending signals $m = 1$ (top) and $m = 2$ (bottom) - note that the scale for area of the points is $8\times$ that of the density waves. Focusing again on $m = 1$, we confirm the ubiquitous presence of the slow retrograde mode, while a fast prograde pattern at $\Omega \approx 50\,\mathrm{km\,s^{-1}\,kpc^{-1}}$ is barely noticeable and only detected in a few snapshots. This seems in accordance with the theoretical expectation that, no matter how the bending perturbation is produced, the associated slow retrograde wave is long-lived, while the fast prograde wave decays quickly.

Interestingly, a "slow" bending $m = 1$ prograde pattern, at $\Omega \approx 20-25\,\mathrm{km\,s^{-1}\,kpc^{-1}}$ is detected at virtually all snapshots, located inside the forbidden region for bending
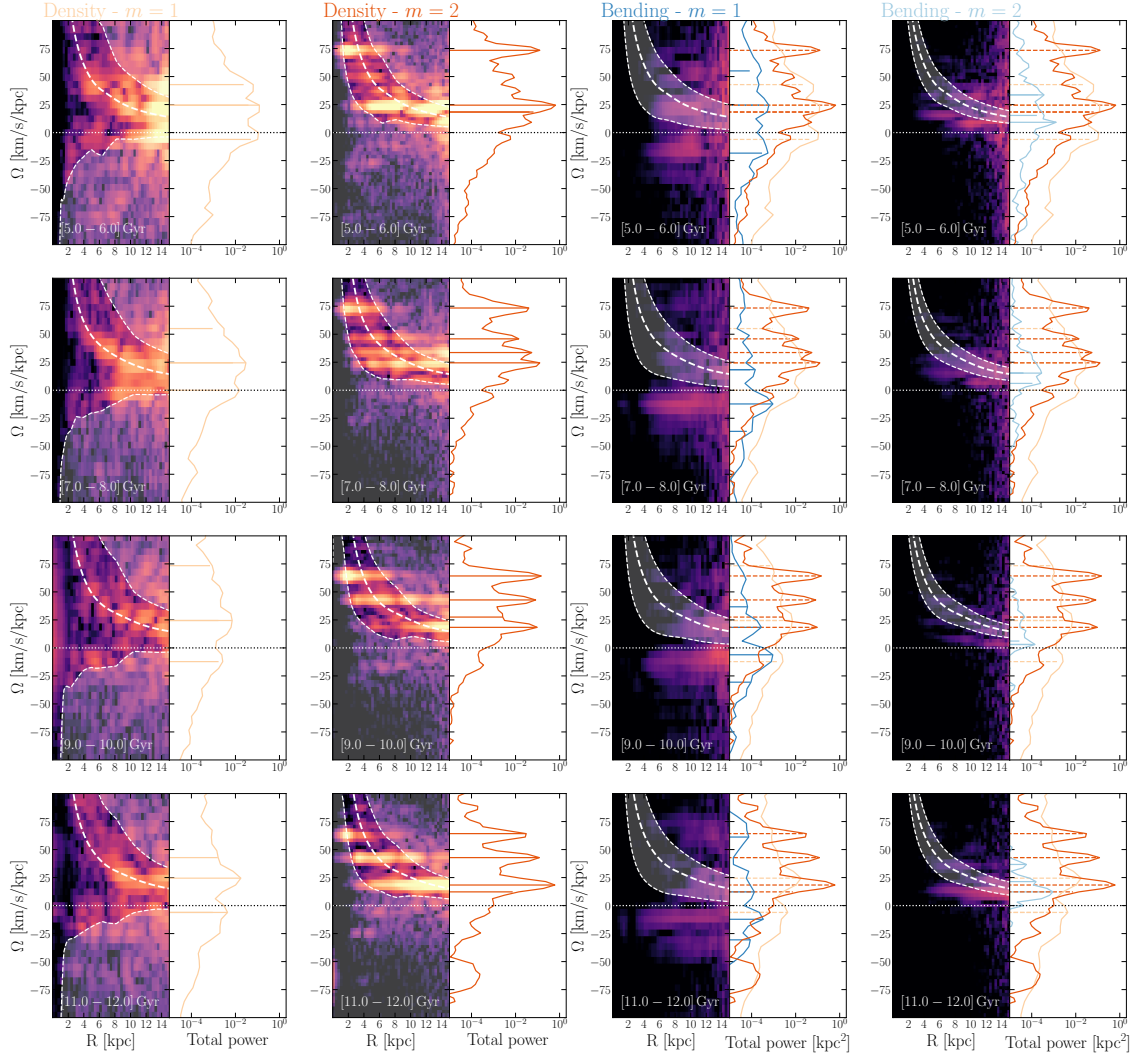
Figure 4.5: Power spectra for perturbations in the unwarped simulation at several time-intervals (rows). The first two columns show the power spectra for $m = 1$ and $m = 2$ density (bar+spiral) perturbations, with the radius-integrated power shown to the right of the spectrograms. The thick and thin white dashed lines show $\Omega(R)$ and $\Omega \pm \kappa/m$, respectively, and the lightly shaded white areas represent the "forbidden" regions for WKB density waves. The power concentrates along $\Omega(R)$, avoiding the forbidden region. The two right-hand columns show the power spectra for $m = 1$ and $m = 2$ bending perturbations. The thick and thin white dashed lines show $\Omega(R)$ and $\Omega \pm \nu_h/m$, and the white shaded areas represent the forbidden regions for WKB bending waves. For $m = 1$, the expected long-lived slow retrograde motion is clearly visible, while the fast prograde pattern is weak.

waves – see Fig. 4.5. Over-plot in the two right-hand total power panels of Fig. 4.5 are the total power curves for the $m = 1$ and $m = 2$ density signals (pale and strong orange, respectively), as shown in the two left-hand columns. This slow $m = 1$ pattern speed lies close to the aforementioned correlated $m = 1$ and $m = 2$ density peaks seemingly associated with an asymmetric two-armed spiral density wave. This may suggest a possible coupling of density and bending waves. We discuss this issue further in Sec. 4.5.

Warped simulation

Fig. 4.7 shows the power spectra for the warped simulation (in this simulation we stored outputs at high cadence already from 2 Gyr, which permits us to perform spectral analysis from this point), with the same scheme of density and bending $m = 1$ and $m = 2$ signals as in Fig. 4.5. As in the unwarped model, the $m = 2$ density signal exhibits multiple pattern speeds present simultaneously, covering a large radial extent. The pattern speeds are not as sharply defined as in the unwarped simulation, which might be due to the perturbation from the warp. Alternatively, this could be because the warped model is thicker: at 12 Gyr and between $0 \geq R/\,\mathrm{kpc} \geq 10$ the discs of the warped and unwarped models have root-mean-square z, of 0.8 kpc and 0.5 kpc, respectively. Once more, we note that the pattern speeds tend to occupy the allowed region of WKB density waves.

The left-hand panels of Fig. 4.8 show the time evolution of the pattern speeds identified in Fig. 4.7 for the $m = 1$ (top) and $m = 2$ (bottom) density signal. In this simulation, there is no hint of a bar, and essentially all identified $m = 2$ pattern speeds peak inside co-rotation (blue points). The longer time interval explored in this simulation provides a better appreciation of the transient character of the spirals.

The right hand panels of Fig. 4.7 show the spectrograms for the bending signals.
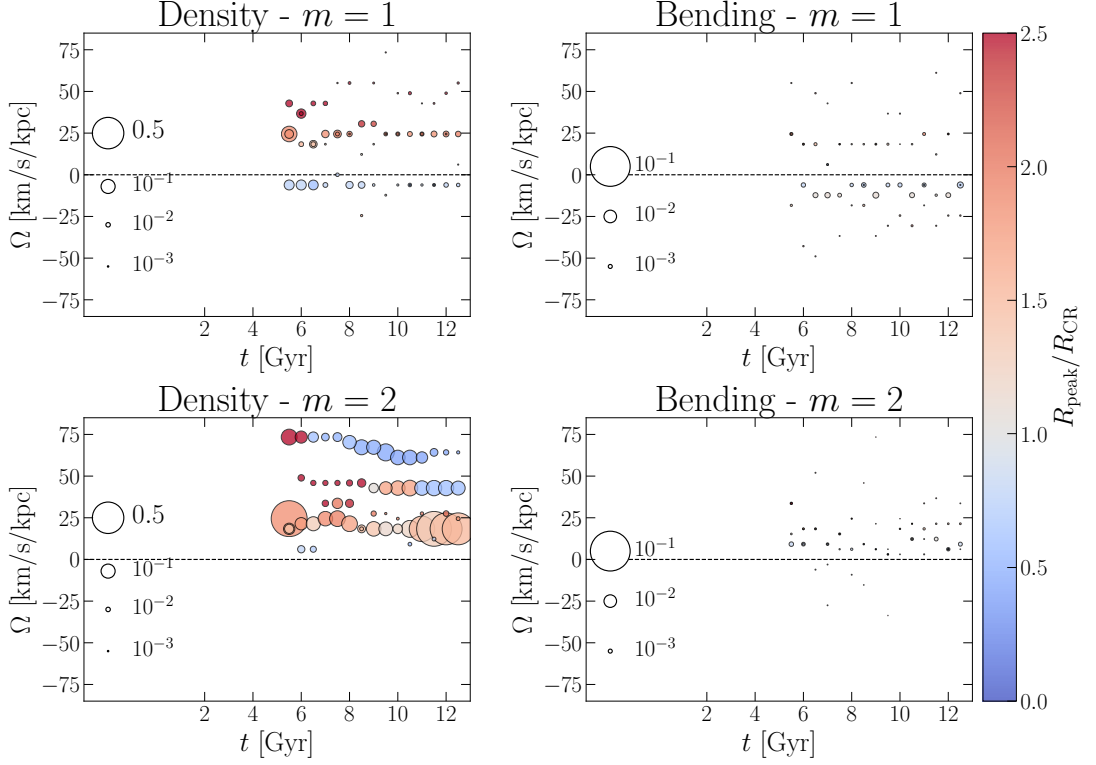
Figure 4.6: Pattern speeds identified in Fig. 4.5, for the $m = 1$ (top) and $m = 2$ (bottom) density (left) and bending signals (right). Point areas are proportional to the radially-integrated power, with scale in the right-hand plots $8\times$ larger than in the left-hand panels. Colours indicate the ratio of the radius where the pattern speed peaks to the co-rotation radius. For the $m = 2$ density signal, the high pattern speeds (upper points) generally lie inside co-rotation and decrease with time, suggestive of a slowing bar. The other two discernible patterns are associated with spiral density waves, with the strongest one at $\Omega \approx 20 - 25 \, \mathrm{km \, s^{-1} \, kpc^{-1}}$. The $m = 1$ bending plot shows the ubiquitous presence of a slow retrograde pattern (at $-15 \leq \Omega / \, \mathrm{km \, s^{-1} \, kpc^{-1}} \leq -10$) and (at some times) a very weak fast prograde signal at $\Omega \approx 50 \, \mathrm{km \, s^{-1} \, kpc^{-1}}$.
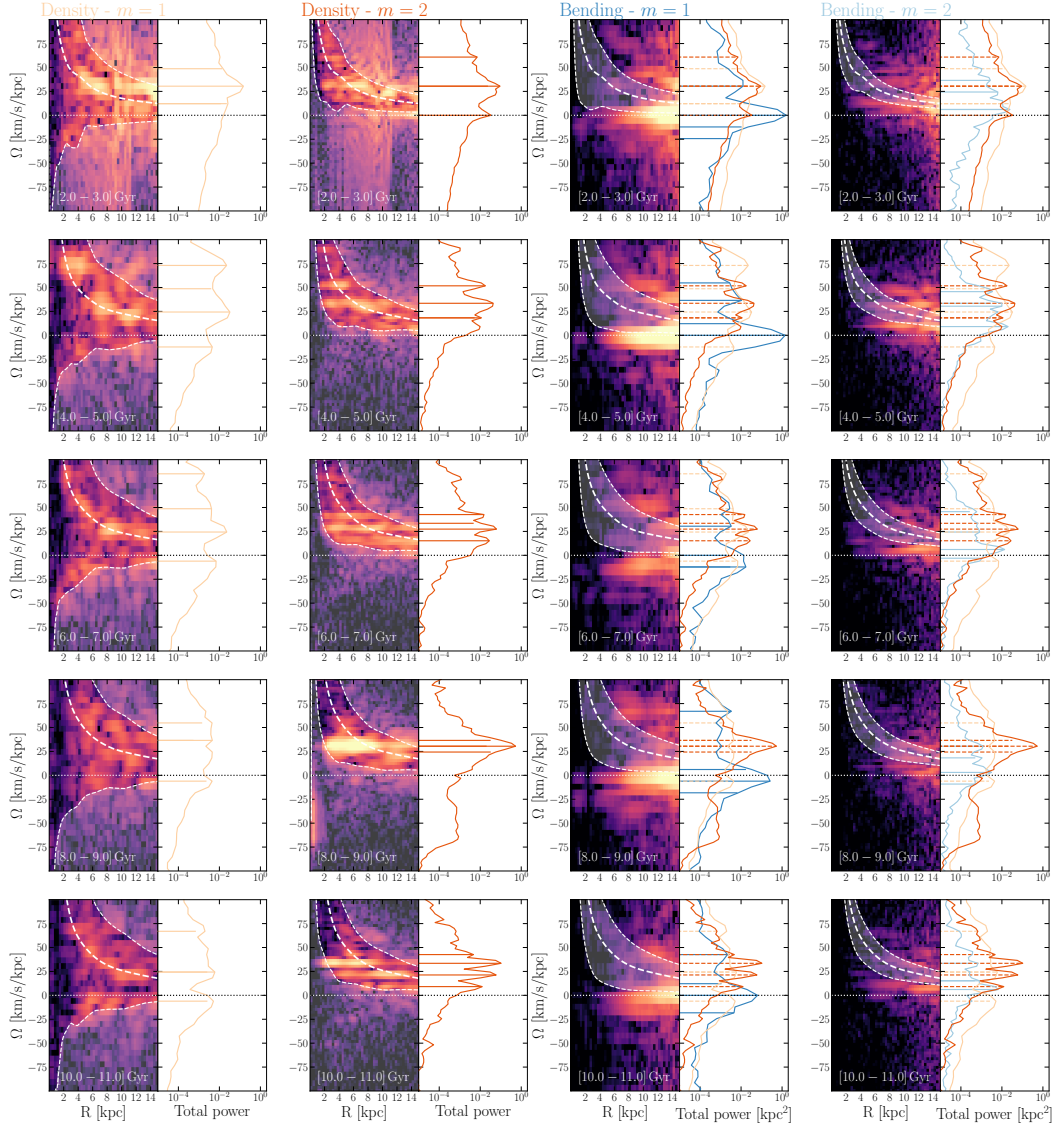
Figure 4.7: Similar to Fig. 4.5, showing the power spectra at different times (rows) for the $m = 1$ and $m = 2$ density (left) and bending (right) perturbations in the warped simulation. The $m = 2$ density panels show the simultaneous presence of various pattern speeds in the region allowed for WKB density waves. In the $m = 1$ bending panels, the most noticeable difference with respect to Fig. 4.5 is the strong peak at $\Omega \approx 0 \, \mathrm{km \, s^{-1} \, kpc^{-1}}$, which is a trivial manifestation of the warp. As in the unwarped simulation, a slow retrograde motion is detected in the $m = 1$ bending plot. Significant $m = 1$ bending power is present for large Ω at large radii, i.e. a fast prograde motion avoiding the forbidden region for WKB bending waves, and peaking at $25 \leq \Omega / \, \mathrm{km \, s^{-1} \, kpc^{-1}} \leq 50$.

The bending $m = 1$ waves exhibit a prominent peak at $\Omega = 0\,\mathrm{km\,s^{-1}\,kpc^{-1}}$ for almost all snapshots, which is the trivial signal of the warp itself. This peak is so prominent that it can visually hide nearby peaks, which our iterative peak finding and Gaussian subtraction scheme allows us to detect (solid blue horizontal lines). The $m = 1$ peak due to the slow retrograde motion ($\Omega \approx -15\,\mathrm{km\,s^{-1}\,kpc^{-1}}$) is detected at almost all time-intervals. Additionally, significant power in fast prograde waves is now observed, at large radii, and peaking at $25 \leq \Omega/\,\mathrm{km\,s^{-1}\,kpc^{-1}} \leq 50$.

The right-hand panels of Fig. 4.8 show the time evolution of the pattern speeds identified in Fig. 4.7 for the $m = 1$ (top) and $m = 2$ (bottom) bending signals. For better viewing, we suppress the $m = 1$ points with power $> 10^{-1}\,\mathrm{kpc^2}$, which are all located at $\Omega \approx 0\,\mathrm{km\,s^{-1}\,kpc^{-1}}$ and represent the warp (the large blue point near $\Omega \approx 0\,\mathrm{km\,s^{-1}\,kpc^{-1}}$ has a slightly lower power so avoids the cut). As in the unwarped simulation (see Fig. 4.6), we can see the ubiquitous presence of a slow retrograde $m = 1$ motion in the warped simulation, with substantially more power than in that model.

The main difference between the warped and the unwarped models is the presence of a strong, fast prograde motion in the $m = 1$ bending signal, at $25 \lesssim \Omega/\,\mathrm{km\,s^{-1}\,kpc^{-1}} \lesssim 50$ in the warped system. The strong red colours show that this pattern peaks at large radii, thus avoiding the forbidden region of WKB bending waves. Although these points decrease in size over time, they are present at all times. This is due to the long-lived nature of the warp in this simulation. While fast prograde bending waves are expected to decay quickly, the warp continuously perturbs the disc, re-exciting these waves.

As we did in the unwarped simulation, in the right columns of Fig. 4.7, we also over-plot the total power curves of the $m = 1$ (pale orange) and $m = 2$ (strong orange) seen in the left-hand columns. Neglecting the warp's stationary signature, an apparent correlation of the bending waves with the density signals is again present,
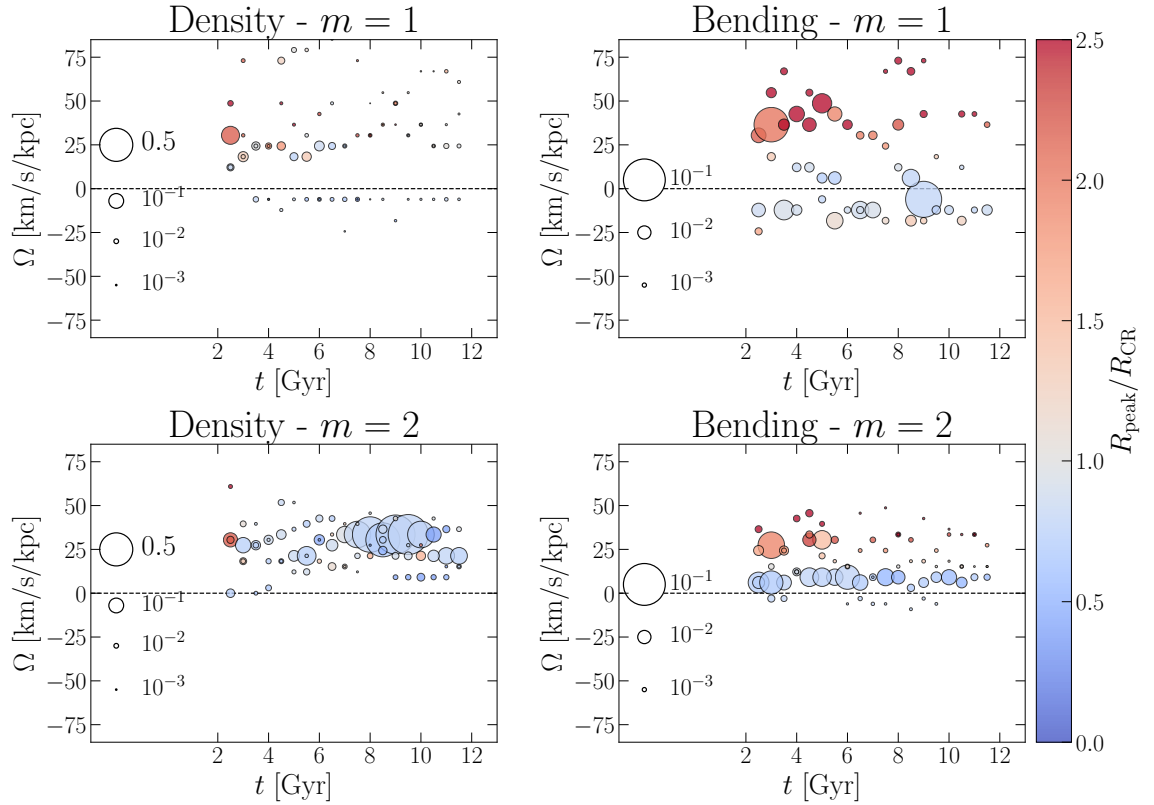
Figure 4.8: Time evolution of the pattern speeds identified in Fig. 4.7, for the warped simulation. The $m = 2$ density panel reveals a more transient evolution of the pattern speeds, in comparison to the unwarped simulation. In the $m = 1$ bending panel, we suppress points with power $> 10^{-1}\,\mathrm{kpc}^2$, which all lie at $\Omega \approx 0\,\mathrm{km\,s^{-1}\,kpc^{-1}}$ and represent a trivial manifestation of the warp (the large blue point has slightly less power and evaded the cut). As in the unwarped simulation (Fig. 4.6), a persistent slow retrograde $m = 1$ bending signal is detected. Unlike the unwarped simulation, a fast $m = 1$ bending prograde motion ($25 \leq \Omega / \mathrm{km\,s^{-1}\,kpc^{-1}} \leq 50$) is detected at large radii (red) with substantial power.

especially for the peak at $\Omega_p \approx 25$ km s^{-1} kpc^{-1}, which often penetrates into the forbidden region. We discuss this pattern speed overlap in Sec. 4.5.

The main conclusion from the analysis in this section is that slow retrograde bending waves are present in both the unwarped and the warped models, throughout their evolution. On the other hand, only in the warped model are significant fast prograde bending waves detected, which must be persistently re-excited by the warp.

4.4.3   The source of the vertical perturbations

In the previous section we demonstrated the presence of bending waves in both the warped and unwarped simulations, although with different properties. Bending waves in simulations of unwarped isolated galaxies were already reported by Chequers & Widrow (2017), who suggested shot noise in the dark matter halo as a source mechanism. The origin of bending waves in our unwarped simulation is discussed in Sec. 4.5; Here we focus on the main source of vertical perturbation in the warped simulation. In the WKB approximation prograde bending waves are expected to dissipate rapidly and therefore be weak, as indeed we find in the unwarped simulation. However, in the warped model the consistent power in the prograde bending waves indicates that the disc in the warped model is continuously being vertically excited.

The top panel of Fig. 4.9 shows the evolution of the mass flux of cool gas $(T < 50,000K)$ through a spherical shell with radius and thickness of $R = 15$ kpc and $\Delta R = 0.2$ kpc, respectively. The flux of cool gas varies substantially, with long term inflow modulated by rapid variations. Similar to the analysis in Section 4.4.2, we apply a discrete Fourier transform to the evolution of the mass flux over 1 Gyr baselines to derive the characteristic timescales of the variations. The bottom panel of Fig. 4.9 shows the resulting frequencies of the mass flux. Most of the frequencies cluster between 0 and 20 kpc km s^{-1}, and reaching to 40 kpc km s^{-1}. These
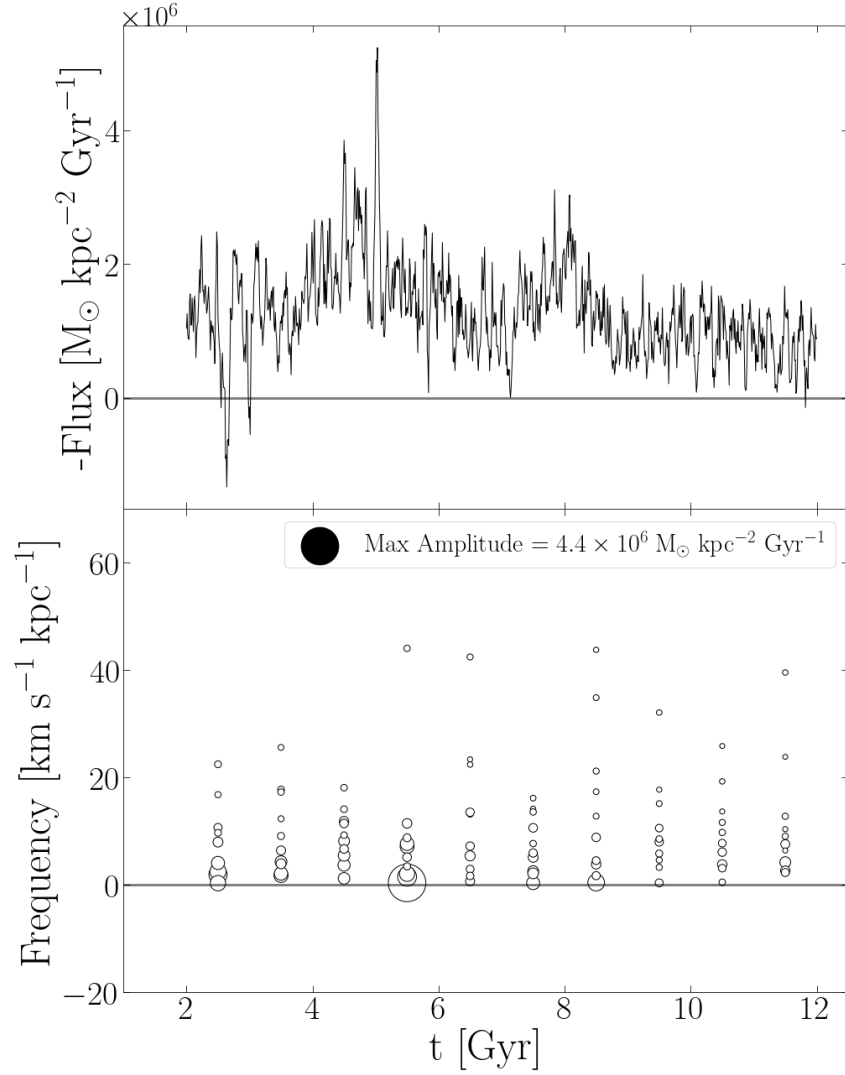
Figure 4.9: Top: evolution of the mass flux of cold gas (T < 50,000K) through a spherical shell with $R = 15\,\mathrm{kpc}$ and $\Delta R = 0.2\,\mathrm{kpc}$. Bottom: frequencies derived from a discrete Fourier transform of the mass flux on 1 Gyr baselines. The marker size indicates the frequency amplitude with the value of the maximum amplitude and respective marker size shown in the legend.

results show that the disc is continuously perturbed by the irregularly accreting gas with a maximum amplitude of $4.4 \times 10^6 \, \mathrm{M_\odot} \, \mathrm{kpc}^{-2} \, \mathrm{Gyr}^{-1}$. These frequencies substantially overlap the frequencies of the bending waves, indicating a favourable spectrum of perturbations for exciting the bending waves. We propose, therefore, that the irregular inflow of gas from the warp onto the disc is the source of the vertical perturbations which are responsible for exciting the bending waves in the warped model.

4.4.4 Vertical kinematics in the Solar Neighbourhood

In Fig. 4.4 the vertical bends are accompanied by non-zero $\langle v_z \rangle$. Schönrich & Dehnen (2018a) and Huang et al. (2018a) observed an increase in $\langle v_z \rangle$ with angular momentum $|L_z|$, which they speculated was due to either an extension of the warp, or to a bending wave. We test whether such a signal can arise in our models.

Fig. 4.10 examines a simulated SN sample in the warped model at 11.4 Gyr, with plots similar to those of Schönrich & Dehnen (2018a) and Huang et al. (2018a). Three panels plot $\langle v_z \rangle$ versus L_z (top right), versus azimuthal velocity, v_ϕ (bottom right), and versus cylindrical and guiding radii, R and R_g (bottom left, the latter computed using AGAMA, Vasiliev 2019). With the improved mapping of the Milky Way's warp, the Sun's position relative to it is now clearer: the Sun is $\sim 17.5°$ behind the ascending node of the warp (Chen et al. 2019a). Our sample is contained within a sphere of radius 2 kpc at $R = 8.18 \, \mathrm{kpc}$ and azimuth of $\phi_w = 72.5°$, where ϕ_w is the azimuthal angle along the direction of rotation measured from the negative major axis of the warp. The location of our sample is indicated in the top left panel of Fig. 4.10, on top of a face-on map of $\langle v_z \rangle$. Although all of the binned $\langle v_z \rangle$ variations have relatively larger errors (despite our bins being large compared with Schönrich & Dehnen (2018a) and Huang et al. (2018a)), we observe a general increase of $\langle v_z \rangle$ with $-L_z$ along with underlying wiggles, as in the Milky Way. Following Schönrich
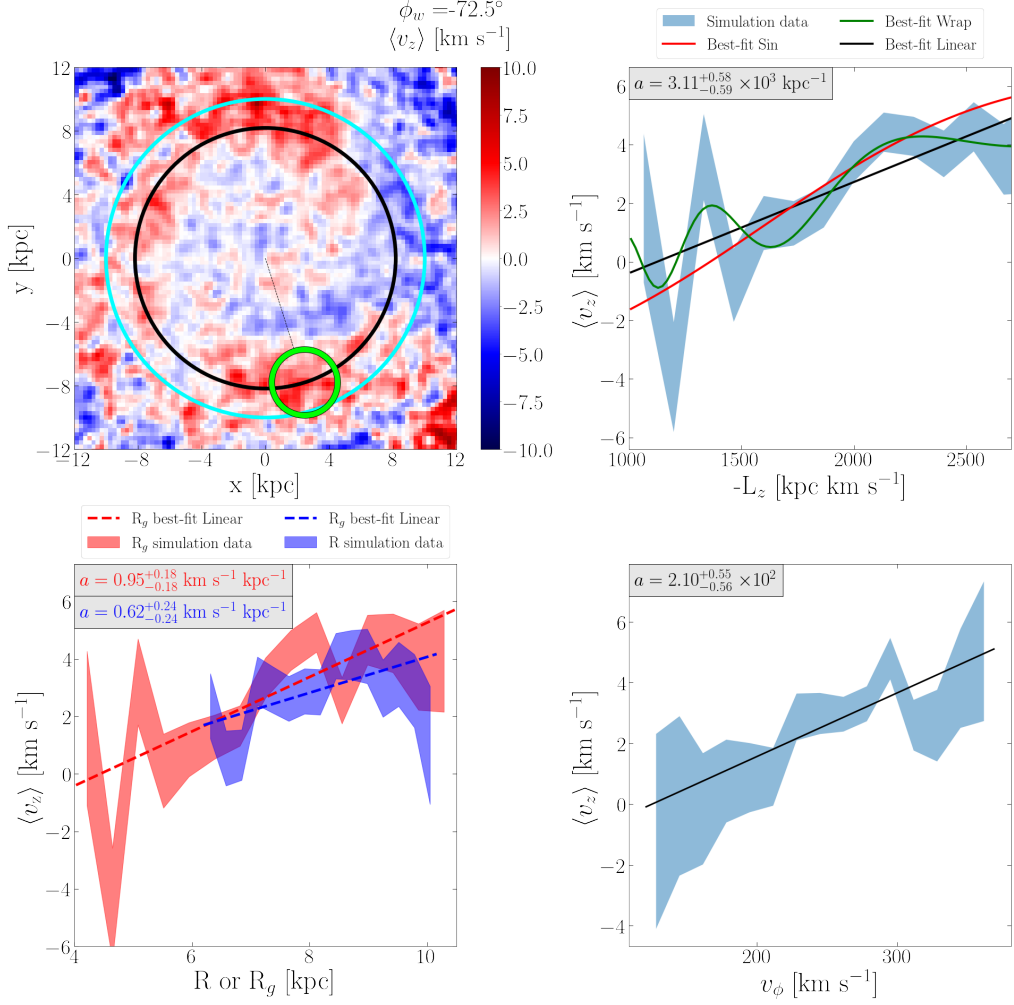
Figure 4.10: Top left: face-on $\langle v_z \rangle$ distribution of stars in the warped model at 11.4 Gyr. The green circle indicates the SN sample with its ϕ_w displayed above the colour bar. The solid black and cyan circles represent $R = 8.18$ kpc and $R = 10$ kpc, respectively. A Gaussian filter is applied to the colour distribution with a standard deviation $\sigma = 1$ pixel $= 260 \times 260$ pc. Right: binned distributions in the SN sample of $\langle v_z \rangle$ as functions of L_z (top) and v_ϕ (bottom). The solid lines indicate different model fits: linear (black), sinusoidal (red), and wrapping (green) (see Eqn. 4.12 - 4.14). Bottom left: binned distributions of $\langle v_z \rangle$ as functions of cylindrical radius, R (blue) and guiding radius, R_g, (red) in the SN sample. Each distribution has a linear fit (dashed lines). The slopes of all linear fits are shown in the top left corners of the respective panels. The shaded regions show the standard deviation of v_z in each bin.

CHAPTER 4

& Dehnen (2018a), we fit a variety of functions to the $\langle v_z \rangle$ versus L_z distribution:

$$\langle v_z \rangle = b + aL_z', \tag{4.12}$$

$$\langle v_z \rangle = b + aL_z' + A\sin(2\pi L_z'/c + d), \tag{4.13}$$

and

$$\langle v_z \rangle = b + aL_z' + A\sin(2\pi c/L_z + d), \tag{4.14}$$

where $L_z' = L_z - 1600\,\mathrm{kpc\,km\,s^{-1}}$ in the Milky Way, and a, b, c, d, A are fitting parameters. For the warped model we set $L_z' = L_z - 2000\,\mathrm{kpc\,km\,s^{-1}}$ based on the mean value of L_z at $R = 8.18\,\mathrm{kpc}$, but note that in the fit of Eqn. 4.12 the slope is independent of this pivot point. The best fit parameters for Eqns. 4.12 - 4.14 are listed in Table 4.1 where we see that our linear fit is of the same scale as the one measured in the Milky Way, which has $a = 3.11 \pm 0.70 \times 10^3\,\mathrm{kpc}$ (Huang et al. 2018a). The fits to Eqns. 4.13 - 4.14 present larger uncertainties and deviations from the values of Schönrich & Dehnen (2018a), however, the larger bins make it difficult to detect any higher frequency variations in $\langle v_z \rangle$. Thus we only fit simple linear functions to the other $\langle v_z \rangle$ distributions (v_ϕ, R, and R_g), the slopes of which are presented in the top left corner of the respective panels, and we note that they are also of the same order as those measured in the SN (Schönrich & Dehnen 2018a).

Schönrich & Dehnen (2018a) argued that one possible interpretation of the non-vanishing slope of the $\langle v_z \rangle$-L_z relation is that the stellar disc is warped at the Solar cylinder. The slope of the relation in this scenario would vary smoothly with azimuth as $\cos(\phi_w + \phi_c)$ (where ϕ_c is some constant), which we can check in our model. In Fig. 4.11 we plot the slope, a, of the linear fit of Eqn. 4.12 as a function of ϕ_w, the azimuthal angle at which the sample is selected. This relation is plotted for a number of snapshots, with a time interval $\delta t = 20\,\mathrm{Myr}$ to show the short-term changes in the slope. For this measurement we use 12 samples that consist of 2 kpc spheres. The spheres are equally spaced in azimuth to avoid overlapping the samples. The
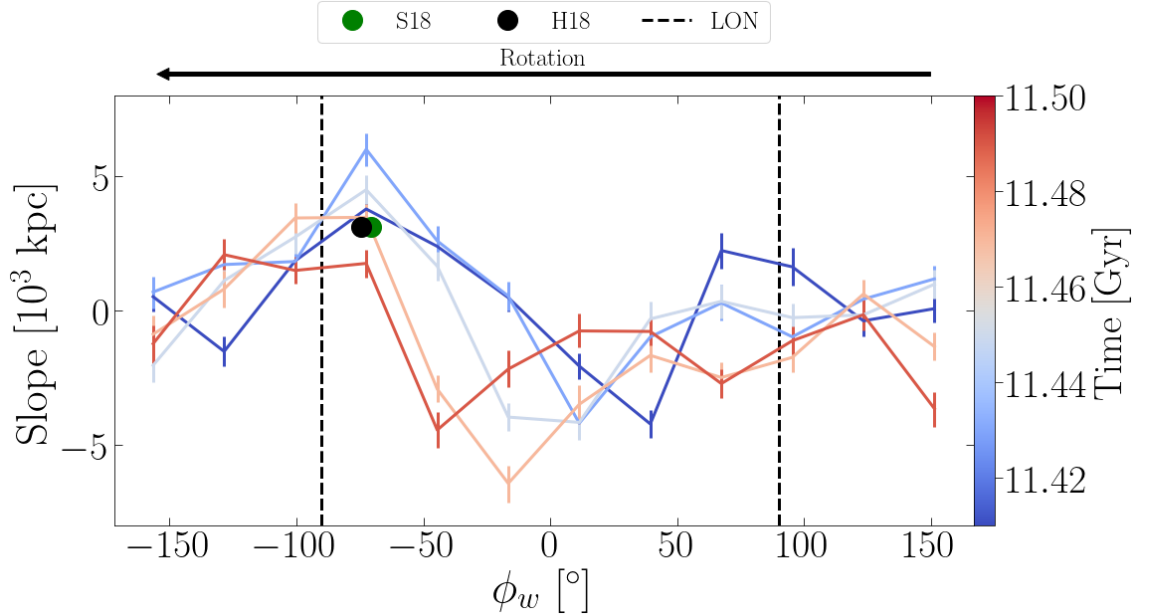
Figure 4.11: Variation of the slope of the $\langle v_z \rangle$-L_z relation with azimuth for samples at $R = 8.18\,\mathrm{kpc}$ in the warped model. The value $\phi_w = 0$ is defined as the azimuth on the warp's major axis with $z < 0$. Therefore the LON, indicated by the vertical dashed lines, is at $-90°$ and $90°$. The sense of rotation is indicated above the figure. In the Milky Way, the Sun is located $17.5°$ before the ascending node (Chen et al. 2019a), *i.e.* at $\phi_w = -72.5°$. The black and green dots represent the slope as measured by Schönrich & Dehnen (2018a) (S18) and Huang et al. (2018a) (H18), respectively (horizontally offset by $\pm 2°$ for clarity). The panel shows 5 snapshots separated by 20 Myr. A wave appears to propagate in the direction of rotation as a trough moves from $50°$ to $-50°$ in the span of ~ 80 Myr.

Fit	a $\times 10^3$ (kpc)	b (km s^{-1})	c (kpc km s^{-1})	d	A (km s^{-1})
linear (Eq. 4.12)	$3.11^{+0.59}_{-0.58}$	$2.72^{+0.24}_{-0.24}$	-	-	-
sinusoidal (Eq. 4.13)	$2.96^{+0.89}_{-1.4}$	$2.41^{+0.51}_{-5.6}$	$3443.59^{+33459.11}_{-3073.73}$	$0.73^{+1.10}_{-1.72}$	$1.24^{+6.89}_{-0.80}$
wrapping (Eq. 4.14)	$2.72^{+0.66}_{-0.66}$	$2.56^{+0.25}_{-0.25}$	$3601.17^{+151.99}_{-323.90}$	$-2.59^{+1.05}_{-0.42}$	$1.10^{+0.39}_{-0.42}$

Table 4.1: Best fit parameters for the fitting models of Eqns. 4.12 - 4.14 applied to the sample in Fig. 4.10.

slope varies in the range $[-5, 5] \times 10^3$ kpc; Schönrich & Dehnen (2018a) and Huang et al. (2018a) measure a slope of $\sim 3.11 \times 10^3$ kpc, which is within the range we find. The results of these snapshots happen to be instances when the slope at the Solar azimuth is very similar to that observed in the Milky Way. Note that a varies in a wave-like manner as the peaks and valleys shift with time. As the warp is fixed at each snapshot (see Chapter 2) the positive slope in the $\langle v_z \rangle$-L_z relation is not produced by the warp itself, but by a propagating bending wave, which suggests that the same may be happening in the MW. The phase of the wave moves in the direction of increasing ϕ_w, *i.e.* in the sense of rotation.

Fig. 4.12 plots the variation of $\langle v_z \rangle$ with L_z (top right), v_ϕ (bottom right), and R and R_g (bottom left) in the unwarped model. As the simulation is unwarped the simulated SN is arbitrary, so we perform our analysis at $R = 8.18$ kpc in 30 different azimuths and present the sample with the largest recent slope. The relation is significantly shallower than in the warped simulation. Fig. 4.13 shows the variation of the slope with azimuthal angle at different times (top panel), similar to Fig. 4.11. The variation of the slope with azimuth is less pronounced when compared to the warped model and barely reaches the Milky Way values throughout the 2 Gyr interval, with $|a| \lesssim 2 \times 10^3$ kpc. The bottom panel shows the effect of small artificial
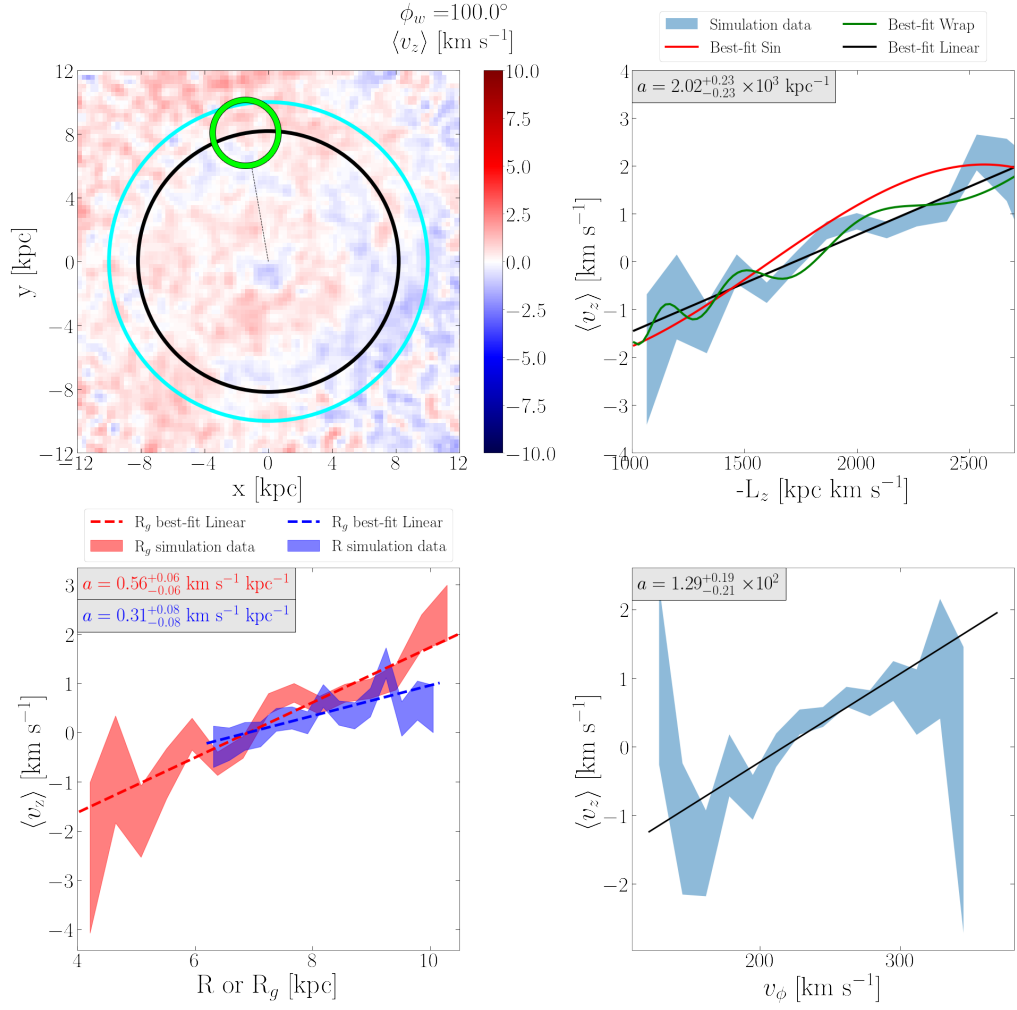
Figure 4.12: Same as Fig. 4.10 but for the unwarped model at 12 Gyr.
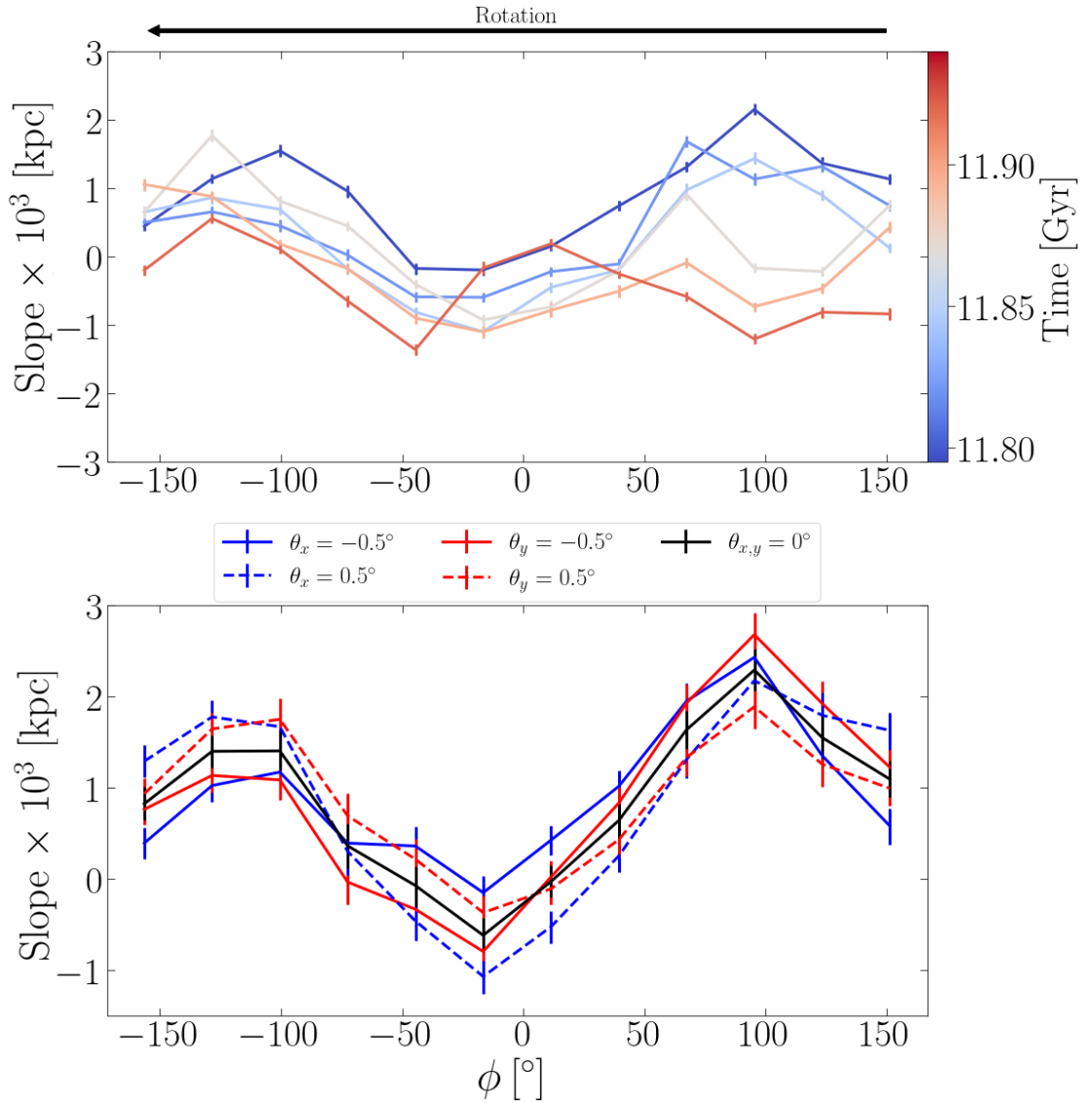
Figure 4.13: Variation of the slope of the $\langle v_z \rangle$-L_z relation with azimuth for SN samples in the unwarped model. Top panel: 5 times separated by 20 Myr (colours). Bottom panel: slope variation, for the unwarped model at different artificial tilts about the x-axis (red lines), about the y-axis (blue lines), and without any artificial tilt (black line). Note that the range of the y-axis for both panels is almost a third of that in Fig. 4.11. This shows that small unaccounted tilts do not produce the large slopes measured in the Milky Way or in the warped model.

tilts of the disc about the x (red) and y (blue) axes. These small (0.5°) tilts barely change the slope, indicating that the large slope observed in the Milky Way is not due to a mis-identified disc mid-plane.

Since the unwarped simulation lacks a line of nodes to simulate a SN sample, as in the analysis of Fig. 4.11, we measure the slope in 12 equally spaced in azimuth 2 kpc spheres. Fig. 4.14 plots the slope values for these 12 samples (white points) over a 2 Gyr interval starting from $t = 10$ Gyr with $\delta t = 10$ Myr. The slope values oscillate about $a = 0$ kpc without approaching the SN values. In contrast, the evolution of the slope in the warped model's SN sample (red solid line) shows strong oscillations about $a \sim 0.6 \times 10^3$ kpc with more than half of the values being positive. There are multiple time intervals ($\sim 15\%$ of time steps) where the slope reaches and surpasses the Schönrich & Dehnen (2018a) value.

The Sun is located behind the ascending node of the warp (Chen et al. 2019a), which could have an impact on the L_z vs v_z relation. In order to explore how the Sun's location relative to the line of nodes affect the measured slope, we measure the slope and its evolution in an "anti" Solar Neighbourhood (anti-SN) sample. The sample is located behind the descending node of the warp, *i.e.* $\phi_w = 252.5$ deg (blue solid line in Fig. 4.14). We observe that the slope at the anti-SN location oscillates about $a \sim -0.5 \times 10^3$ kpc. More than half of the slope values are now negative and the Schönrich & Dehnen (2018a) and Huang et al. (2018a) values are reached (or surpassed) in only a third of the time as the SN sample ($\leq 6\%$ of time steps). However, when considering the inverse of the slope in Huang et al. (2018a), the anti-SN sample reaches that value at the same rate as the SN sample reaches the real value.

We conclude that the bending waves produced by misaligned gas accretion along the warp in the simulation are able to produce similar trends observed by Schönrich & Dehnen (2018a) and Huang et al. (2018a) in the MW. The large positive values
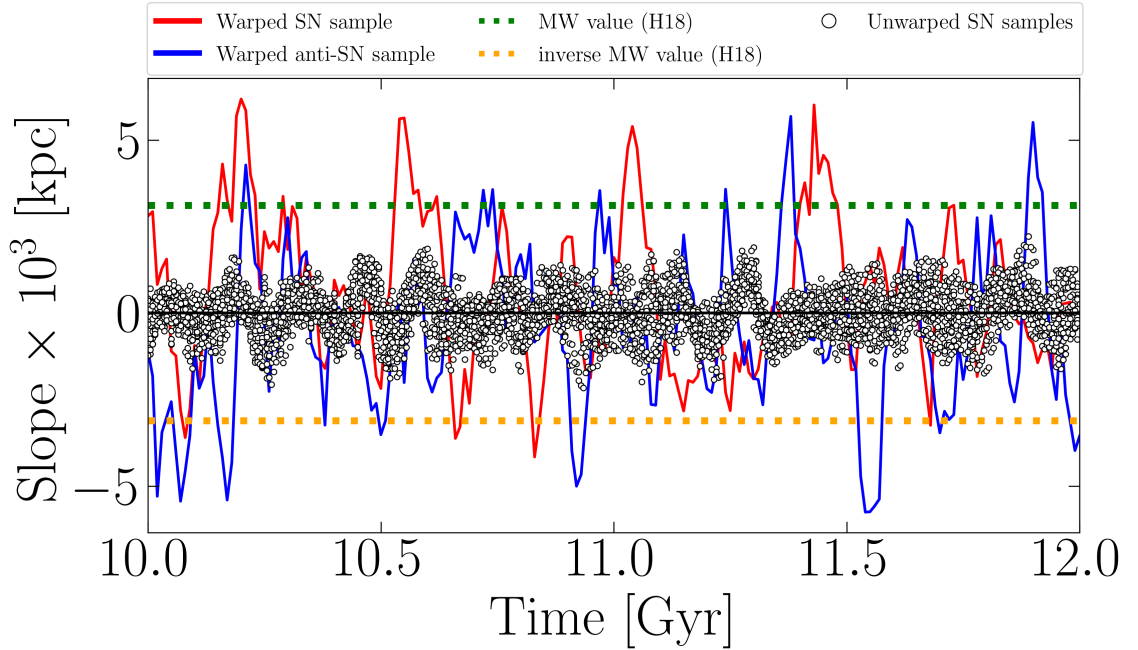
Figure 4.14: Evolution of the slope of the $\langle v_z \rangle$-L_z relation for all Solar Neighbour-hoods (SN) samples in the unwarped model (open circles) and SN samples in the warped model at $\phi_w = 72.5°$ (red) and $\phi_w = 252.5°$ (blue). The samples are spheres centred on $R = 8.18$ kpc and with $r = 2$ kpc. The green dotted line shows the SN slope value (Schönrich & Dehnen 2018a), while the orange dotted line is the negative of that value. In the unwarped model the mean and overall slope values do not generally exceed 2×10^3 kpc in the span of 2 Gyr and at any SN sample. In the warped model the slope regularly matches, or exceeds, the MW value.

of the slope found by Schönrich & Dehnen (2018a) and Huang et al. (2018a) are not unusual given the Sun's position relative to the line-of-nodes of the warp.

4.4.5 Propagation of the bending waves

In Sections 4.4.2 & 4.4.4 we established the presence of bending waves, their pattern speeds throughout the disc, and their consequences on vertical kinematics in a simulated SN. We now explore the time evolution of $\langle z \rangle$ and the surface density contrast, $\widetilde{\Sigma}$, distributions of stars in cylindrical sectors. We define the density contrast as:

$$\widetilde{\Sigma}(R, \phi) = \frac{\Sigma(R, \phi) - \Sigma(R)}{\Sigma(R)}, \tag{4.15}$$

where $\Sigma(R)$ is the mean surface density within a radial bin, and $\Sigma(R, \phi)$ is the surface density in an annular sector of the same radial bin. We use sectoral bins which are non-overlapping with $\Delta\phi_w = 12°$ in each ring. This analysis is a counterpart of the frequency analysis but in real space which aids in interpreting the consequences of the observed waves in Sec. 4.4.2.

For the warped simulation, Fig. 4.15 shows the evolution of $\widetilde{\Sigma}$ (left) and $\langle z \rangle$ (right) in 1 kpc wide rings from 5.5 kpc to 10.5 kpc (rows), starting at $t = 10$ Gyr with time steps $\delta t = 10$ Myr. The horizontal solid black lines show the location of the SN in the Milky Way (Chen et al. 2019a). The diagonal black lines are the most prominent frequencies of the prograde density $m = 2$ and bending $m = 1$ waves (dotted) and the retrograde $m = 1$ bending wave (dashed) taken from Fig. 4.8 (bottom-left and top-right, respectively) for this time interval. The values of the frequencies are indicated in the legend at the top of Fig. 4.15. The $\widetilde{\Sigma}$ distribution is dominated by an $m = 2$ angular dependence, *i.e.* at each annulus and time interval, $\widetilde{\Sigma}$ has two peaks (red) and troughs (blue). This $m = 2$ signal is prograde as the peaks and troughs propagate in the direction of increasing ϕ_w. We observe that the strongest density wave frequency matches the slope of the $m = 2$ signal in the $\widetilde{\Sigma}$
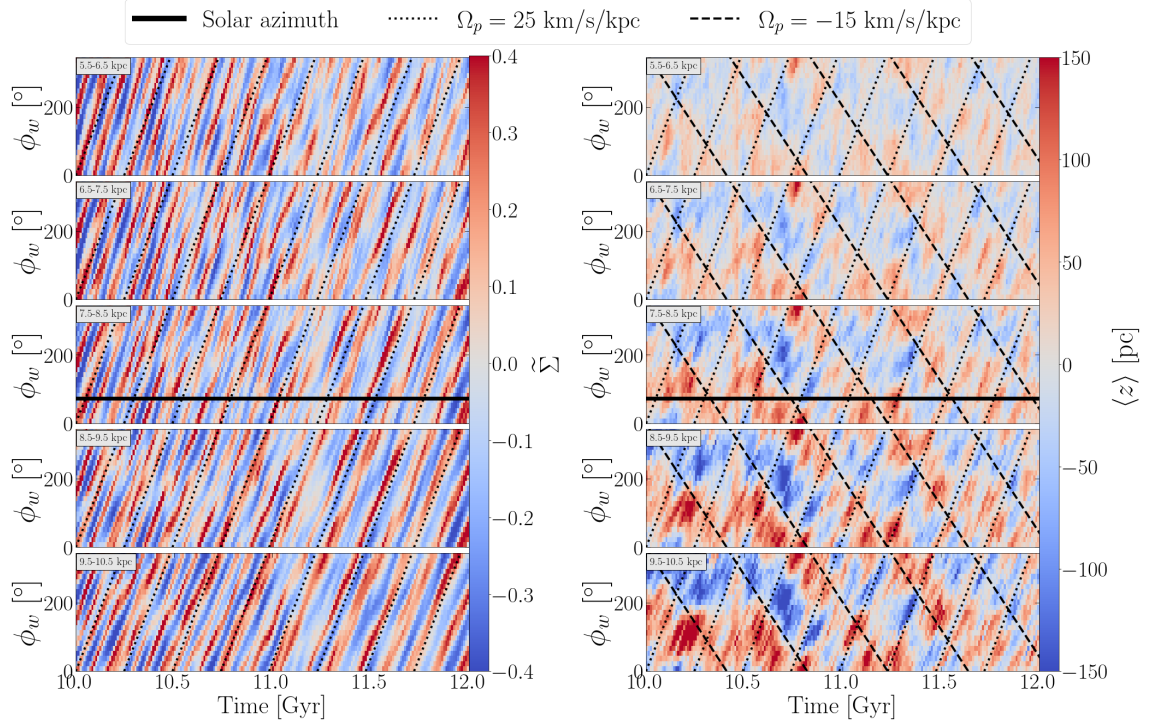
Figure 4.15: Evolution of the stellar surface density contrast, $\widetilde{\Sigma}$ (left) and mean height above the mid-plane, $\langle z \rangle$ (right) in the warped simulation. The horizontal solid black line represents the Solar azimuth relative to the warp's major axis (Chen et al. 2019a). The diagonal black lines correspond to the most prominent prograde density and bending (dotted) and retrograde bending (dashed) pattern speeds present in the $10 - 12$ Gyr interval (see Fig. 4.8).

distribution at $R \geq 8.5\,\mathrm{kpc}$. The coincidence of slopes is in some agreement with Fig. 4.7 as the $\Omega_p = 25\,\mathrm{km\,s^{-1}\,kpc^{-1}}$ peak is at $R \sim 9\,\mathrm{kpc}$.

The distributions of $\langle z \rangle$ at any time are dominated by an $m = 1$ angular dependence, *i.e.* at each annulus and time interval $\langle z \rangle$ has a single peak (red) and trough (blue). Over time the bend propagates in a retrograde direction, *i.e.* in the direction of decreasing ϕ_w. The bend amplitude increases with radius and is largely decoupled from the peak of the $m = 2$ spiral density wave (dotted lines, copied from the left panel). The bending wave pattern speed (dashed line) matches the slope of the $m = 1$ signal in the $\langle z \rangle$ distribution at all radii. This coincidence of slopes is in agreement with Fig. 4.7, which shows that the $\Omega_p \approx -15\,\mathrm{km\,s^{-1}\,kpc^{-1}}$ bending wave is spread across those radii.

Superposed on the overall $m = 1$ bending wave we can also see individual bending wave packets (which we loosely refer to as "ripples" to distinguish their particular behaviour) which propagate to *increasing* ϕ_w, *i.e.* in the direction of rotation, and have an angular frequency similar to that of the spirals. To confirm this apparent match in pattern speeds, we note that the slopes are similar to those of the spirals at $R \geq 7.5\,\mathrm{kpc}$. This suggests that even though ripples are emanating from the bending wave, they are modulated by the spirals, again hinting that there may be a coupling between the bending waves and the spirals.

We perform the same analysis on the unwarped model in Fig. 4.16 with an identical setup of cylindrical bins and time interval. The diagonal black lines are the most prominent frequencies of the $m = 2$ density (dotted) and $m = 1$ bending (dashed) waves taken from Fig. 4.6 (bottom-left and top-right, respectively) for the $10 - 12\,\mathrm{Gyr}$ time interval. The values of the frequencies are indicated in the legend at the top of Fig. 4.16. As in the warped model, the $\widetilde{\Sigma}$ distribution (left column) is dominated by a prograde $m = 2$ signal as the $\widetilde{\Sigma}$ distribution has two peaks (red) and troughs (blue) that propagate in the direction of increasing ϕ. Likewise, the
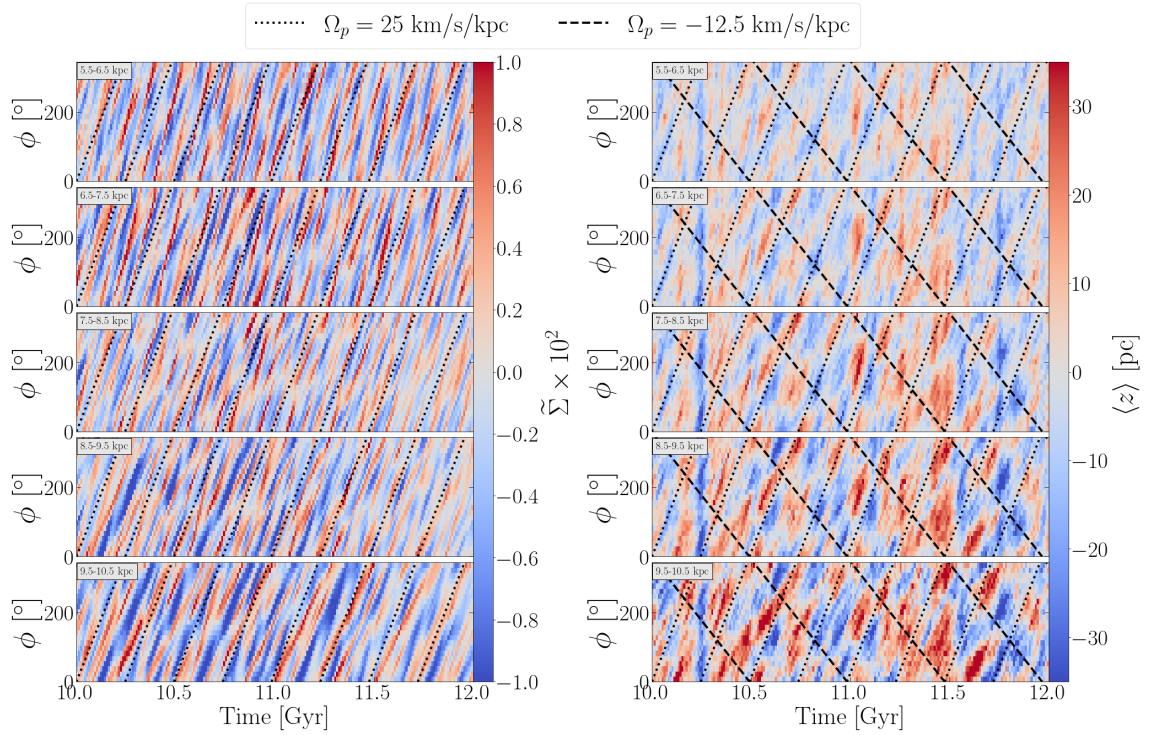
Figure 4.16: Similar to Fig 4.15 but for the unwarped model. The diagonal black lines correspond to the most prominent density (dotted) and bending (dashed) pattern speeds present in the $10 - 12$ Gyr interval (see Fig. 4.6).

most prominent density wave frequency also matches the slope of the $m = 2$ signal in the $\widetilde{\Sigma}$ distribution at $R \geq 8.5\,\mathrm{kpc}$ and we observe a superposition with a higher frequency density wave at $R \sim 7.5\,\mathrm{kpc}$.

The distributions of $\langle z \rangle$ in the right column of Fig. 4.16 show no dominant signal but a superposition of multiplicities with amplitudes that are weaker by a factor of 5 compared with the warped model. The most recognisable signals are a prograde $m = 2$ ($t = 10.5\,\mathrm{Gyr}$), a retrograde $m = 1$ ($11.0 \leq t/\,\mathrm{Gyr} \leq 11.5\,\mathrm{Gyr}$), and an $m = 0$ ($t = 10.25\,\mathrm{Gyr}$) signal. The retrograde bending (dashed) and prograde density and bending (dotted) wave pattern speeds seemingly match the slopes of the $m = 1$ and $m = 2$ signals in the $\langle z \rangle$ distribution at all radii. Some of the underlying signals in the $\langle z \rangle$ distributions can be interpreted as ripples though they are less coherent and of a lower amplitude than the distinct ripples emanating from the main bend in the warped model (see Fig 4.16). We also observe that some ripples (e.g. read peak at $t = 11\,\mathrm{Gyr}$ and $\phi_w = 200°$) have different shearing rates as they become decoupled from the prominent prograde bending wave (dotted) at $R \leq 8.5\,\mathrm{kpc}$.

4.4.6 The effect of stellar ages

The dispersion relation of Eq. 4.1 applies to cold discs, *i.e.* in the absence of in-plane velocity dispersion. In real discs, scattering at inner and outer Lindblad resonances and with giant molecular clouds increase the orbital eccentricity of stars, making populations kinematically hotter over time. This velocity dispersion at the galactic centre is the source of the buckling instability (Julian & Toomre 1966; Kulsrud et al. 1971). In the presence of an in-plane velocity dispersion σ_R, Eq. 4.1 is replaced by

$$m^2 \left[\Omega_p - \Omega(R) \right]^2 = \nu_h^2 + 2\pi G \Sigma(R) |k| - \sigma_R^2 k^2. \qquad (4.16)$$

Accordingly, for a given σ_R, small scale structures (large k) are more prone to instabilities. As σ_R rises with stellar age, it acts to damp the bending waves on
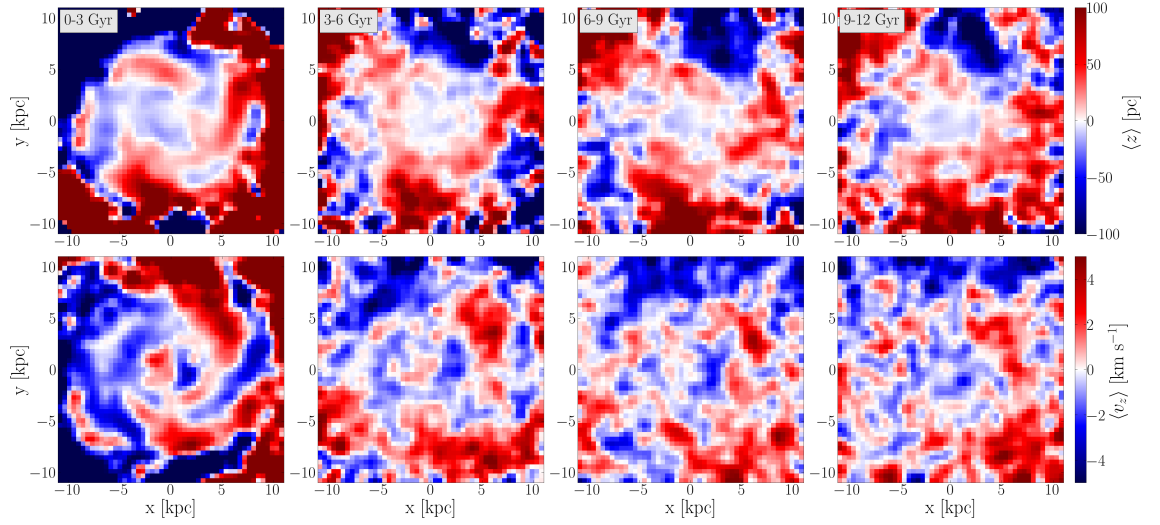
Figure 4.17: Face-on distributions of $\langle z \rangle$ (top), and of $\langle v_z \rangle$ (bottom) for different age populations (annotation at top right of each panel) in the warped model at 12 Gyr. A bending wave is visible in all populations but is strongest, and most clearly defined, in the youngest population. The solid black and cyan lines represent the Solar annulus, $R = 8.18\,\mathrm{kpc}$, and $R = 10\,\mathrm{kpc}$, respectively. A Gaussian filter has been applied to the colour distribution in each panel with a standard deviation of the Gaussian kernel set to $\sigma = 1\,\mathrm{pixel} = 570 \times 570\,\mathrm{pc}$.

small scales (large k, note the minus sign in the right-hand term). Therefore we now consider the effect of age on the bending waves in the warped model.

Fig. 4.17 presents the distributions of $\langle z \rangle$ (top row) and $\langle v_z \rangle$ (bottom row) separated by stellar age, in bins of 2 Gyr. The distributions are presented for stars formed in the main disc only, in order to avoid warp stars that can take up to ~ 6 Gyr to fully settle and phase mix into the disc (Khachaturyants et al. *submitted*). Besides the overall $m = 1$ bend, we observe strong bending waves, in the $\langle z \rangle$ and $\langle v_z \rangle$ distributions (coherent red and blue structures). These bending waves reach as far inside the disc as $R = 4$ kpc in the youngest population, with amplitudes of ~ 100 pc and ~ 5 km s^{-1} in the $\langle z \rangle$ and $\langle v_z \rangle$, respectively. More importantly, the bending waves, while strongest in the young populations, can be recognised in all populations. The bending waves in the youngest population are also the sharpest ones, whereas the waves in the older populations become increasingly dispersed at short wavelengths. This agrees with the idea that older populations are kinematically hotter, with this in-plane velocity dispersion damping the bending waves – see Eq. 4.16. Thus, in the old populations, Fig. 4.17 reveals a coherent large-scale signal but not so much the small scale patterns present in the young populations. According to the dispersion relation, for a given σ_R the large k become unstable earlier, so we see the fine structures (small scales, large k) disappear first.

In order to aid in comparing with observational data, for which stellar ages have high uncertainties (Sanders & Das 2018b), we split the stars formed in the main disc by their radial actions, J_R. The radial action of a star characterises the extent of radial oscillations of a star's orbit and is thus a proxy for the in-plane velocity dispersion. Fig. 4.18 presents the distributions of $\langle z \rangle$ (top row) and $\langle v_z \rangle$ (bottom row) separated by J_R in bins containing an equal number of stars. Bending waves become increasingly dispersed with increasing values of J_R, similar to the age cuts in Fig. 4.17.
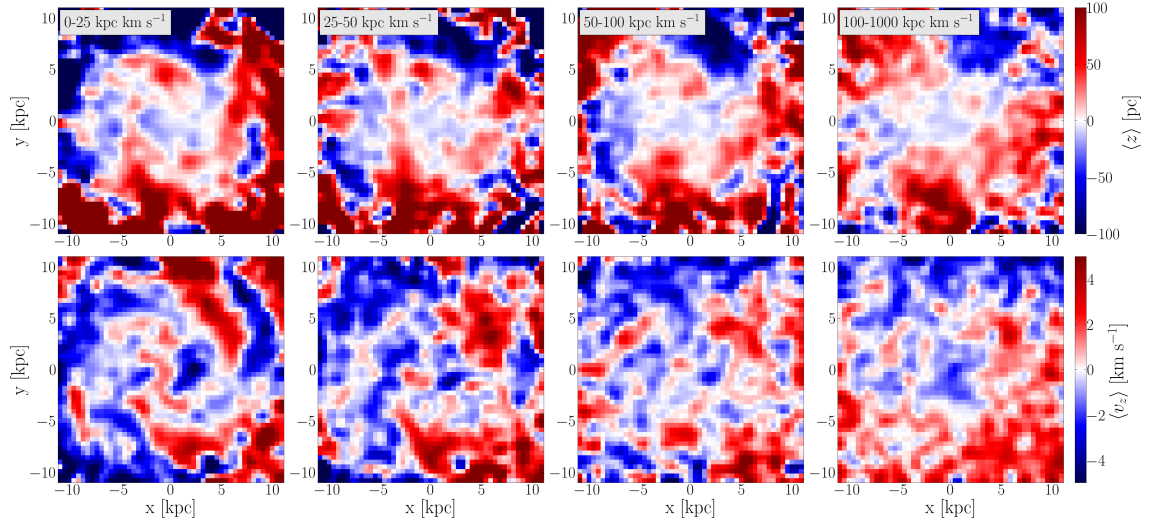
Figure 4.18: Face-on distributions of $\langle z \rangle$ (top), and of $\langle v_z \rangle$ (bottom) for populations with different radial action, J_R, ranges (annotation at top right of each panel) in warped model at 12 Gyr. A bending wave is visible in all populations. The solid black and cyan lines represent the Solar annulus, $R = 8.18$ kpc, and $R = 10$ kpc, respectively. A Gaussian filter has been applied to the colour distribution in each panel with a standard deviation of the Gaussian kernel set to $\sigma = 1$ pixel $= 570 \times 570$ pc.

4.5 Discussion

Vertical perturbations in the SN are generally attributed to satellite interactions (Ibata & Razoumov 1998b; Dehnen 1998b; Laporte et al. 2019b, 2018c,e). While the buckling of the bar can excite significant bending waves in the SN (Khoperskov et al. 2019), the likelihood that the bar buckled in the last few Gyr is very low given the observed distribution of stellar ages in the bulge (Debattista et al. 2019b). Unlike these scenarios, gas accretion along warps is ongoing throughout a galaxy's evolution. Because the gas flow along the warp is not perfectly smooth, it provides ample opportunity to excite bending waves in the stellar disc.

4.5.1 Spectral analysis

Our comparison of a warped and an unwarped N-body+SPH models highlights the role warped gas accretion has on vertically perturbing the disc. By means of a spectral analysis on the vertical distributions we observed bending waves in both simulations that were mostly in agreement with the WKB approximation. The spectral analysis also uncovered the presence of high-frequency prograde bending waves in the warped simulation that persist throughout the model's evolution. The frequencies of these bending waves are transient and change with time but preserve their relatively large amplitudes, indicating that the source of the waves is irregular but continuous. In the unwarped model the same prograde bending waves have less power than in the warped model, and dissipate in a span of $\sim 1\,\mathrm{Gyr}$ (Fig. 4.5). The continuous accretion of cold gas in the warped model injects power into the retrograde and, most significantly, prograde bending waves by continuously exciting the disc. The absence of such a perturbing force in the unwarped model leads to the prograde waves naturally decaying via differential rotation (winding). Of course, the slow retrograde bending waves observed in the unwarped simulation still require a source of vertical perturbation. In the pure N-body simulations of Chequers &

Widrow (2017), shot noise from an embedding dark matter halo was suggested as a probable excitation mechanism, and the same should happen in our simulations. Another possible source of vertical perturbation which, as far as we are aware has never been discussed, is supernovae feedback, which repeatedly expels gas from the disc. Investigating this mechanism is beyond the scope of this paper.

4.5.2 Bending wave propagation

An apparent coupling of $m = 2$ density and $m = 1$ bending waves, with a common "slow" prograde pattern speed at $\Omega_p \approx 25$ km/s/kpc, is suggested in Sec. 4.4.2 – see Figs. 4.5 and 4.7. While a perfectly symmetric two-armed spiral would produce a pure $m = 2$ density signal, and hence no correlation with an $m = 1$ bending wave, any asymmetry between the spiral arms will produce an $m = 1$ density signal, which might couple with an $m = 1$ bending wave. However, since the allowed regions for WKB density and bending waves are approximately complementary, a pattern speed in the allowed region for a WKB density wave generally lies in the forbidden region for a WKB bending wave – as seen in Figs. 4.5 and 4.7 – which would be expected to be short-lived. In the $\langle z \rangle$ distributions of the warped simulation, Fig. 4.15, the "slow" prograde bending waves seem to manifest as small wave packets that we refer to as ripples. We observe that the ripples are apparently coupled to the spiral density waves in that they closely follow the spiral propagation (dotted lines). The similar pattern speed $\Omega_p \approx 25 \, \mathrm{km\,s^{-1}\,kpc^{-1}}$ of the prograde bending and density wave frequencies in the spectral analysis reinforces the idea of a coupling between these waves, producing the observed ripples. In the unwarped model the ripples are less coherent, however, we still observe them on top of the superposed $m = 0$, retrograde $m = 1$, and prograde $m = 2$ signals. The distinguishable bending signals we do observe barely reach amplitudes 20% of those in the warped model. We interpret this as the effect of an irregular accretion of gas exciting the "slow"

waves to a larger extent than the weaker sources in an isolated disc, *i.e.* the halo noise and, possibly, supernovae feedback.

4.5.3   Bending waves in the SN

Bending waves can be detected in the slope of the $\langle v_z \rangle - L_z$ relation in the SN (Schönrich & Dehnen 2018a; Huang et al. 2018a). An analysis similar to that of Huang et al. (2018a) was performed on simulated SN in the warped and unwarped models. In the span of 2 Gyr the warped model was capable of reaching and surpassing the values of Huang et al. (2018a) roughly 15% of the time, while the unwarped model remained consistently below those values. We verified that the smaller values in the unwarped model are also unaffected by a mis-identified disc mid-plane as artificial tilts do not increase the measured slopes by a significant amount. The difference in bending wave amplitudes between the warped and unwarped models therefore must play a leading role in the difference between their slopes of the $\langle v_z \rangle - L_z$ relation. Additionally, the slope varies in a wave-like manner in the warped model as the peaks and troughs in the slope distribution shift in a prograde direction. Because we reorient to the warp frame, the wave-like pattern is a result of bending waves induced by the warp, rather than the warp's direct imprint on the SN.

The location of the SN sample in the warped model appears to also play a role in the L_z-$\langle v_z \rangle$ slope as the simulated anti-SN sample (at $\phi_w = 252.5°$) has more negative slope values and reaches the Schönrich & Dehnen (2018a) values only a third as often as the SN sample. However, the negative of the Schönrich & Dehnen (2018a) slope is reached at a similar rate as the regular slope in the SN sample. The location of the SN in the MW is currently estimated to be behind the ascending node of the Galactic warp (Chen et al. 2019a), which places the anti-SN sample behind the descending node. This could indicate that the bending waves depend on

the direction of infalling gas as the emerging waves produce different slopes in L_z vs $\langle v_z \rangle$. Further work is necessary to understand in which direction the waves we have identified propagate and whether this is related to the changing slope in the SN and anti-SN slopes.

4.6   Summary & Conclusions

1. In the warped model we are able to produce both retrograde and prograde bending waves; the latter would normally decay rapidly, but are re-excited throughout the model's evolution. The gas flux in the warped simulation varies strongly over time, and on a wide range of frequencies, which we interpret as the driving mechanism for these bending waves.

2. Bending waves are present in the unwarped model but are significantly weaker in amplitude when compared to the warped model. The prograde waves become more dispersed with time while the retrograde waves persist throughout; both results are in agreement with the WKB approximation.

3. A similar positive slope in the SN's L_z-$\langle v_z \rangle$ relation (Schönrich & Dehnen 2018a; Huang et al. 2018a) is observed in the simulated SN sample of the warped model. The slope shows a wave-like dependency in azimuth with the wave propagating in a prograde direction. Since the warp is fixed in our analysis, this indicates that the slope is a result of propagating bending waves and not a direct imprint of the warp. The location of the SN sample with respect to the line-of-nodes plays a role in the L_z vs $\langle v_z \rangle$ slope. A SN sample behind the descending node produces more negative slopes and reaches the Schönrich & Dehnen (2018a) and Huang et al. (2018a) slope values less frequently than in the SN sample, *i.e.* behind the ascending node. We also

observed positive slopes in the SN samples of the unwarped model, however, they do not reach the Schönrich & Dehnen (2018a) and Huang et al. (2018a) slope values.

4. In the warped simulation we detect bending waves with a similar morphology for stars younger than $8\,\mathrm{Gyr}$. The strongest and sharpest bending waves in $\langle z \rangle$ and $\langle v_z \rangle$ are in the youngest populations, while older populations are more dispersed. We also separated the stellar populations by the radial action, J_R, finding very similar trends in the strengths of the bending waves for all J_R populations.

5. By studying the evolution of the azimuthal $\widetilde{\Sigma}$ and $\langle z \rangle$ distributions in the warped model we have shown that the $m = 1$ bend has an amplitude which increases radially; it extends inwards to at least $R = 5\,\mathrm{kpc}$. This bend is retrograde with respect to the disc rotation and is decoupled from the spiral density waves. The $m = 1$ bending wave spawns localised bending waves, which we term ripples, which propagate with the spirals (and therefore are prograde) and may be coupled to them. The overlaid frequencies from the spectral analysis showed good agreement between the $m = 2$ spirals and the $m = 1$ prograde bending waves. The same analysis in the unwarped model has shown a superposition of $m = 0$, $m = 1$, and $m = 2$ bending waves. The amplitudes of these waves are significantly weaker than in the warped model.

As a result of our analysis we have further shown the importance of gas accretion and the resulting warp formation for galactoseismologic studies. With more advanced methods the uncovered bending waves can be further analysed on their direction of propagation and affect of the disc structure.

Chapter 5

Chemodynamics of warp stars

In Chapter 3 we examined mono-age warp star populations in the WM2 model and determined that warp stars can reach the Solar Neighbourhood after settling into the disc. The warp stars in our model populated the geometric thick disc, indicative of a vertically hot population. However, as the warp in our model formed via low metallicity accreting gas, warp stars can have a unique chemistry compared to in-situ stars. In this chapter we examine the chemical and dynamical properties of warp populations in three warped models to determine if warp stars can be distinguished as a separate population in the Solar annulus when applying cuts in chemical and action spaces. The models used in this chapter are the WM2-4 models.

5.1   Evolution of the warp

The top rows of Figures 5.1 - 5.3 present edge-on densities of stars (colour) and the cool ($T_g \leq 50,000$ K) gas (red contours) in the WM2-4 models at different time intervals. The time intervals are equally spaced and are based on the final timestep of each model with $t = 12$ Gyr and $t = 10$ Gyr for the WM2 and WM3-4 models, respectively. Due to our disc re-orientation procedure (see Chapter 2.3), the major axis of the warp is along the x-axis and reaches a peak negative value along the $x > 0$
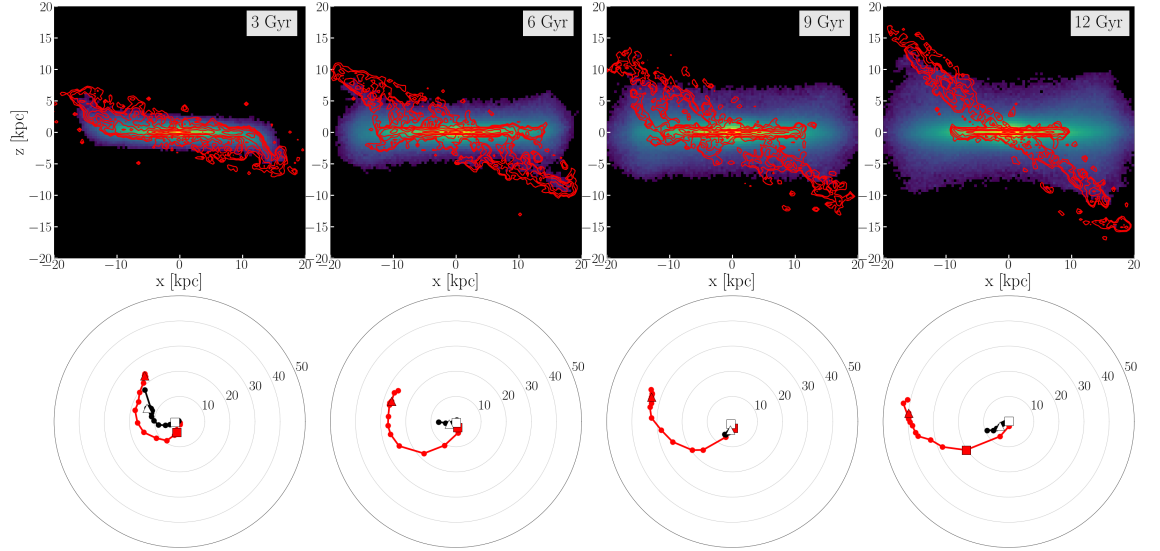
Figure 5.1: Top row: edge-on densities of the stellar and cold gas ($T \leq 50,000$K) distributions at four times in the evolution of the WM2 model. The colour represents the stellar surface density, while the red contours represent the cold gas column density. Time is labelled in the top right of each panel. A warp is present throughout the evolution of the warped model. Bottom row: Briggs figures for the warped model showing the evolution of the stellar (black) and cool gas (red) warps at the time referenced above. Markers represent annuli with $\Delta R = 1$ kpc, equally spaced from 5 to 20 kpc, with the square and triangle markers indicating annuli centred at 10 kpc and 20 kpc, respectively.
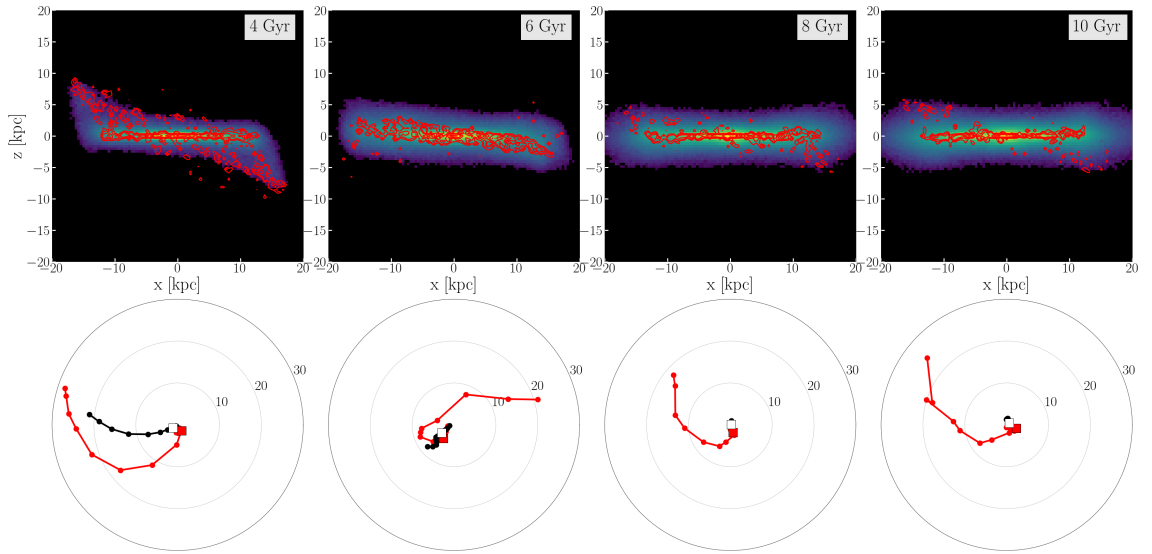
Figure 5.2: Same as Figure 5.1 but in the WM3 model.
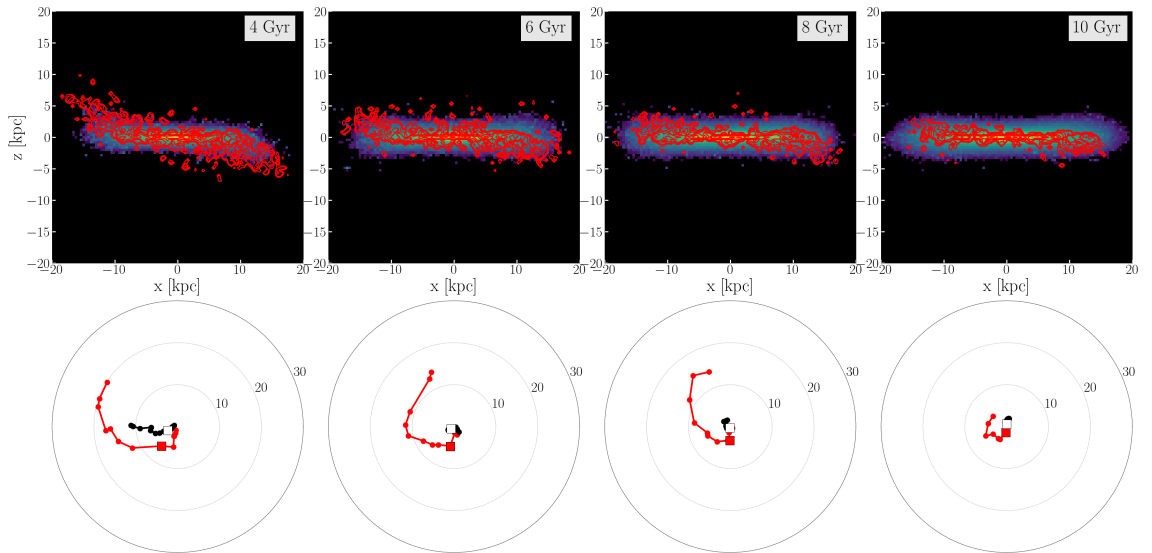
Figure 5.3: Same as Figure 5.1 but in the WM4 model.

side; when viewed from an inertial frame, the disc is tilting slowly and continuously during this time (Binney & May 1986; Ostriker & Binney 1989b; Debattista et al. 2015; Earp et al. 2017, 2019) but we subtract this tilting. Throughout the evolution of each warped model, gas is accreted onto the disc along an integral-shaped warp, however, the extent varies between models. Initially, the edge-on gas distribution presents clear and significant warping in each model with the vertical extent being $\sim 5\,\text{kpc}$, $\sim 10\,\text{kpc}$, and $\sim 2.5\,\text{kpc}$ from the midplane in the WM2, WM3, and WM4 models, respectively. However, the gas warp decreases in amplitude in all models, except in WM2 where the warp continues to grow and reaches $|z| \sim 15\,\text{kpc}$ by $t = 12\,\text{Gyr}$. The stellar disc in all the models starts off relatively thin and warped beyond $R \geq 10\,\text{kpc}$ but eventually becomes flatter and thicker. As discussed in Chapter 3, models with longer-lasting and higher warp amplitudes resulted in thicker discs which we observe in the three models.

The bottom row of Figures 5.1 - 5.3 show Briggs figures for the WM2-4 models at the same time intervals. The stellar (black) and gaseous (red) discs are divided into annuli of width $\Delta R = 1\,\text{kpc}$ where the total angular momentum of particles is calculated. The stellar disc shows distinct warping ($\theta_L \geq 10°$) at the early evolutionary stages in each model, however, in the span of $2 - 4\,\text{Gyr}$ the warping decreases significantly, and the disc appears flat up to $R \leq 12\,\text{kpc}$. The gaseous disc remains warped throughout the evolution of each model, but we observe a strong decrease of the warp amplitude in the WM4 model as its inclination does not surpass $\theta_L > 5°$ at $R \leq 12\,\text{kpc}$.

The evolution and magnitude of the galactic warp vary between the three models, which requires further analysis into the causes of the growth and dissipation of warps. Figure 5.4 shows the time evolution of the stellar disc (square markers) and surrounding gas (triangle markers) Briggs figures in the three models. The Briggs figures are computed in the inertial frame of each model. The stellar disc is defined
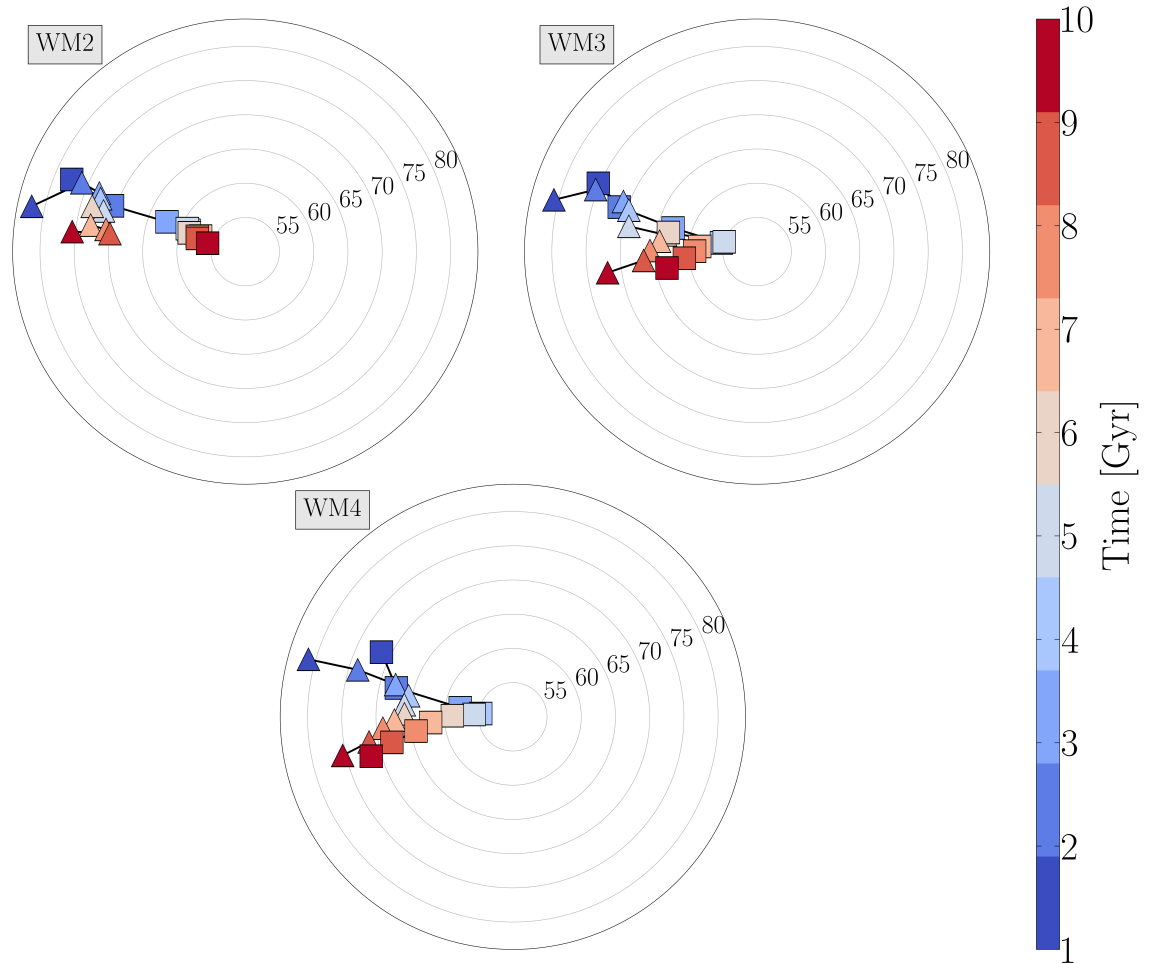
Figure 5.4: Time evolution of the stellar disc (squares) and surrounding gas (triangles) Briggs figures in the three models. The tilt of each component's angular momentum is computed within the inertial frame of each model. The stellar disc is defined as stars within $r \leq 10$ kpc, while the surrounding gas is defined by gas of all temperatures within $r \leq 20$ kpc.

as stars within $r \leq 10\,\mathrm{kpc}$, while the gaseous component is defined as gas of all temperatures located within $r \leq 20\,\mathrm{kpc}$. In the WM2 model we observe that the stellar disc is tilting throughout its evolution with a net tilt (changes in $|\theta_L|$ summed over time) of $\sim 20°$ at $t = 10\,\mathrm{Gyr}$. We also observe a growing misalignment between the stellar disc and surrounding gas as their angular momenta are seemingly aligned at $t \leq 3\,\mathrm{Gyr}$ but become significantly more misaligned, with a $\sim 20°$ separation between them at $t = 10\,\mathrm{Gyr}$.

Similarly to the WM2 model, the stellar discs in WM3 and WM4 tilt throughout their evolution with their net tilts both measuring at $\sim 25°$ at $t = 10\,\mathrm{Gyr}$. However, unlike in WM2, the stellar and gaseous components experience similar changes in θ_L and ϕ_L and appear to converge at $t = 10\,\mathrm{Gyr}$. The Briggs figures demonstrate a significant difference between the three models as WM2 is the only model where we observe a growing warp and an increasing misalignment between the stellar disc and surrounding gas.

A factor that could affect the structure and longevity of the warp in our models is the cooling of the coronal gas. Figure 5.5 shows the time evolution of the gas mass flux (black, left y-axis) and of the angle between the angular momenta of the stellar disc and surrounding gas, referred to as $\Delta\theta_L$ (blue, right y-axis). We compute the flux using inward moving ($v_r < 0\,\mathrm{kpc\,Gyr^{-1}}$) gas of all temperatures located between $15 \leq R/\,\mathrm{kpc} \leq 15.2$. We observe that the mass flux in WM2 (top) is overall decreasing with both its mean and total fluxes being $\sim 70\%$ of those in WM3 (middle) and WM4 (bottom). This difference in flux implies that the inflows are not a direct cause of the waning or growing warps in the three models. However, the increased gas inflows in WM3 and WM4 could instead be responsible for the increased tilting and resulting alignment between the disc and surrounding gas shown in Figure 5.4.

The time evolution of $\Delta\theta_L$ presents a gradual increase in the WM2 model from
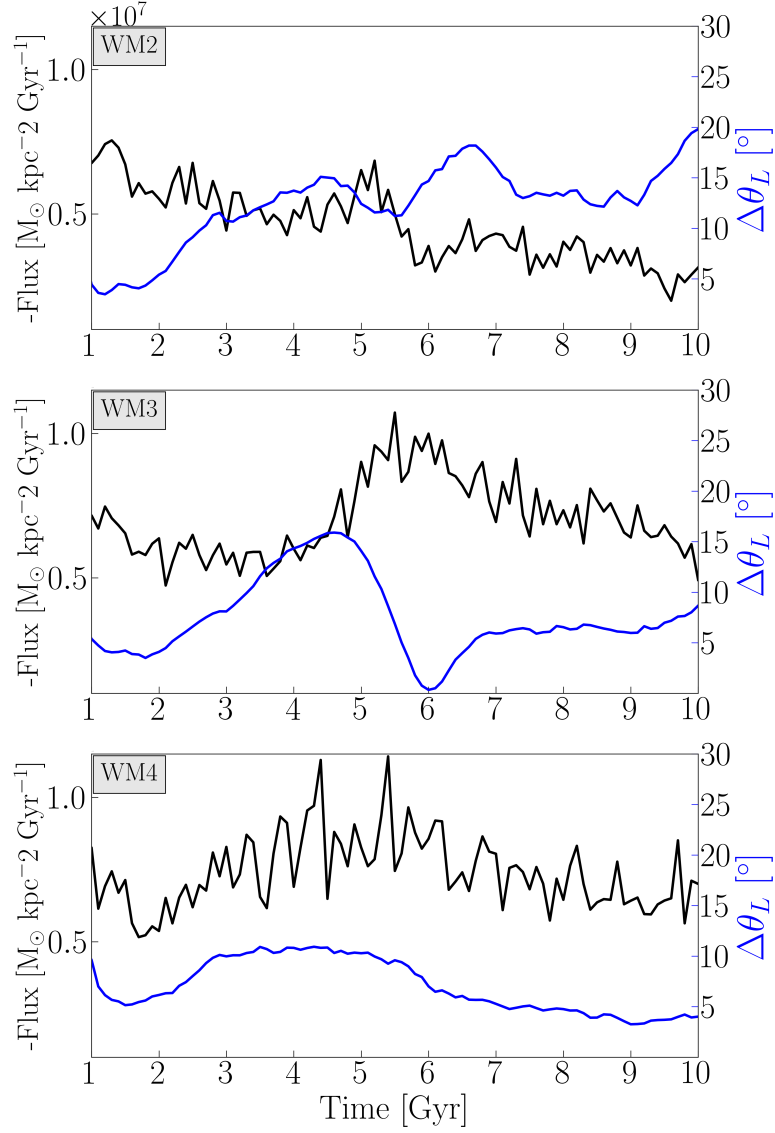
Figure 5.5: Time evolution of the mass flux of inflowing gas (black, left y-axis) and the angle between the angular momenta of the stellar disc and surrounding gas (blue, right y-axis) in the three models, indicated in the top left corner. The stellar disc and surrounding gas are defined in Figure 5.4. The inflowing gas is defined as the inward moving ($v_r < 0\,\mathrm{kpc}\,\mathrm{Gyr}^{-1}$) gas of all temperatures located within $15.0 \leq r/\,\mathrm{kpc} \leq 15.2$.

5° to 20° over the 9 Gyr interval. This increase is accompanied by the gradual drop of the mass flux, which by $t = 10\,\mathrm{Gyr}$ is only 40% of its initial flux. In WM3 we observe that $\Delta\theta_L$ is increasing up to $t \sim 5\,\mathrm{Gyr}$, which coincides with the lower flux. However, as the flux increases, $\Delta\theta_L$ drops to almost full alignment, after which it plateaus at $\sim 8°$. Lastly, in WM4 we observe relatively minor changes in $\Delta\theta_L$ as it first plateaus at 10° for 3 Gyr and then oscillates around 5° for the remaining 4 Gyr.

The increased gas inflows appear to drive the tilting of the stellar disc, which is in agreement with the results of Earp et al. (2019). We observe that the result of the stellar disc tilting is its increased alignment with the gas inflow, which results in the accreting gas reaching the disc more aligned. With a weaker misalignment between the disc and inflowing gas, the amplitude and longevity of the warp naturally decrease. In the WM2 model, both the tilting of the stellar disc and the magnitude of the gas inflow are relatively weak, which results in a stronger misalignment and, consequently, a growing and longer-lasting warp. However, in WM3 and WM4 the gas inflows are significant enough to continuously tilt and align the stellar discs with the surrounding gas, resulting in weaker and waning warps.

5.2 Warp populations

The continuous presence of a warp in the three models provides ample opportunity for star formation to take place in the warp and for the resulting warp populations to settle into the disc (Chapter 3). However, with the numerous differences between the three models, e.g. their star formation thresholds (Chapter 2) and warp amplitudes, the chemical and dynamical properties of the resulting warp populations can vary significantly. In the following sections, we study the warp populations of the three models to establish common trends in the chemical and action spaces.
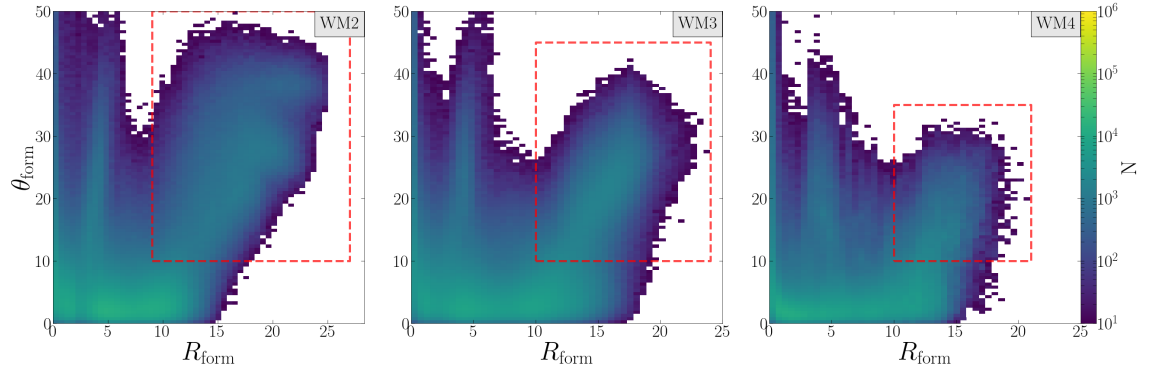
Figure 5.6: The number density distribution of all stars in the R_{form}–θ_{form} space (formation space) of three models, indicated in the top right corner. Stars that formed in the "tail-like" regions outlined by the red rectangles are defined as the main warp population. The populations of stars that formed in an early, transient warp at low radii ($R_{\text{form}} \leq 5\,\text{kpc}$) and high inclinations relative to the disc ($\theta_{\text{form}} \geq 10°$) are not included in our warp star populations.

5.2.1 Formation space

In Chapter 3 we recorded the phase-space coordinates and time of formation, t_{form}, for every star in the WM2 model in order to calculate their formation values. The main formation values of interest were the cylindrical radius of formation, R_{form}, and the inclination of a star's angular momentum relative to the disc at formation, θ_{form}. These formation values were then used to construct a *formation space* ($R_{\text{form}} - \theta_{\text{form}}$ plane) where warp stars were identified as a distinct population based on their R_{form} and θ_{form}. We now perform the same analysis on the stars in the WM3-4 models.

In Figure 5.6 we present the number density distribution of all stars in the formation space of models WM2-4. The "tail-like" regions at $R_{\text{form}} > 10\,\text{kpc}$ (outlined by red rectangles) are comprised of stars that were highly inclined ($\theta_{\text{form}} > 10°$) and on the outskirts of the disc ($R > 10\,\text{kpc}$) at formation; we define the warp populations in the three models as stars with $R_{\text{form}} \geq 10\,\text{kpc}$ and $\theta_{\text{form}} \geq 10°$. These

warp populations consist of $\sim 6 \times 10^5$, $\sim 5 \times 10^5$, and $\sim 2.5 \times 10^5$ warp stars in the WM2, WM3, and WM4 models, respectively. The warp populations make up a noticeable fraction of all stars formed throughout the models $(11-18\%)$, with model WM4 having the lowest fraction, which is in part due to its high star formation threshold. Other significant populations that we observe in the three models are the in-situ main disc population $(R_{\mathrm{form}} \leq 10 \, \mathrm{kpc}$ and $\theta_{\mathrm{form}} \leq 10°)$, and a "hump-like" region containing an old warp population $(2 \leq R_{\mathrm{form}}/\,\mathrm{kpc} \leq 5$ and $\theta_{\mathrm{form}} \geq 15°)$. This early warp population derives from a short-lived warp epoch when the models are still settling and does not relate to the warp described in Section 5.1, therefore we do not include it in the warp population. Similar to the analysis in Chapter 3, neglecting this population does not change any of the following results.

5.2.2 Chemical space

To determine if the chemical properties of the warp populations stand out from the in-situ populations, we analyse the chemical space in the three models. In Chapter 1, chemical space is defined as the relationship between the [Fe/H] and $[\alpha/\mathrm{Fe}]$ abundances. In our models, the α-element is represented by oxygen, [O/Fe]. However, this analysis aims to define general trends in chemical space that can be later applied to observational data so we will refer to the oxygen abundance as $[\alpha/\mathrm{Fe}]$.

Figure 5.7 presents chemical space distributions for all the stars in the three models. The top row of Figure 5.7 shows the number density distribution where we observe distinct branches that we identify as the thin and thick discs, however, they are difficult to discern in model WM4. The overall shapes of the chemical spaces show significant differences with models WM2-3 having a noticeable low-α population $([\alpha/\mathrm{Fe}] \leq -0.4)$. The bottom row of Figure 5.7 shows the distribution of fractions between the number of warp stars and the overall number of stars in each
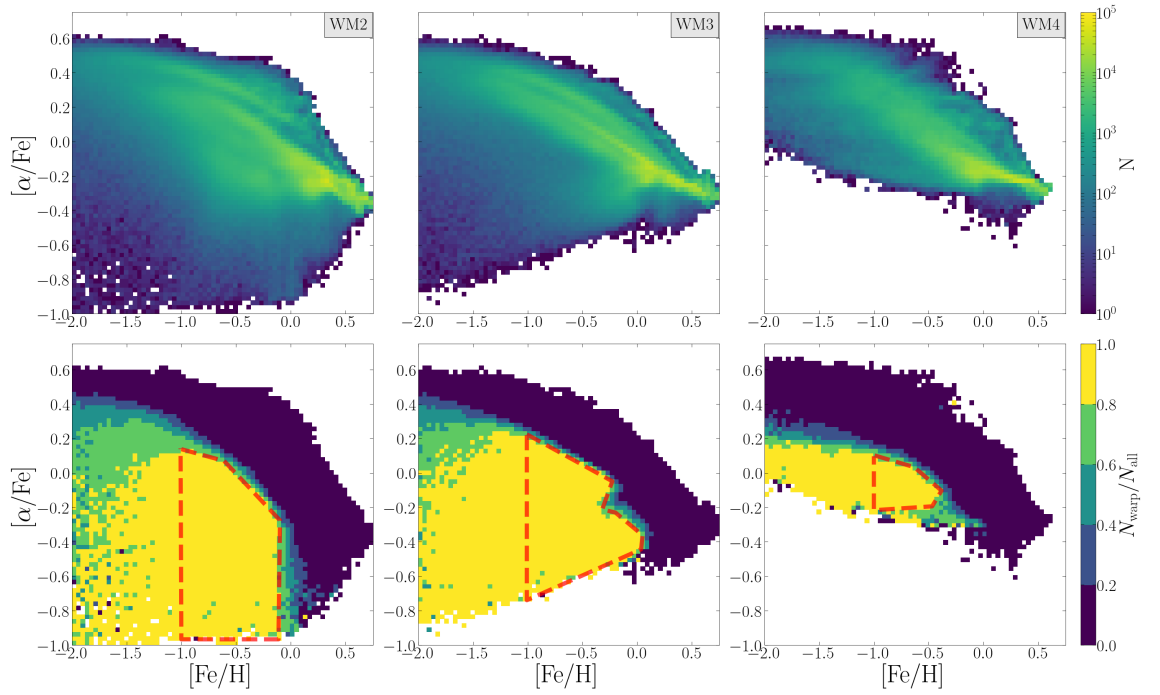
Figure 5.7: Distributions in [Fe/H]-[α/Fe] space (chemical space) for all the stars in the three models. The model is indicated in the top right corner of each column. Top: Number density distribution. Bottom: Distribution of the warp star purity, $N_{\text{warp}}/N_{\text{all}}$. The red dashed polygon outlines the area of chemical space where $N_{\text{warp}}/N_{\text{all}} \geq 0.8$ and [Fe/H] ≥ -1.

bin, $N_{\mathrm{warp}}/N_{\mathrm{all}}$, which we refer to as the warp star purity. In each model, we observe distinct regions where the warp star purity is ≥ 0.8 (yellow) and that the regions are located in very similar areas of chemical space. This area can be described as below the main distribution of the high-α region and at lower metallicities than the metal-poor end of the low-α region. We outline these regions of high warp star purity with dashed red polygons and define the resulting abundance limits as the chemical cut. We do not set any limits on the $[\alpha/\mathrm{Fe}]$ abundances when outlining the high-purity regions, however, we limit the lower range of the $[\mathrm{Fe/H}]$ values. The limit is applied to account for the absence of halo populations in our models as the $[\mathrm{Fe/H}] < -1$ region in the MW is considered to be dominated by halo stars (Das et al. 2020).

In our models, the chemistry of stellar particles is known with absolute certainty, which poses problems if the defined chemical cuts were applied to observational spectroscopic data which have varying degrees of uncertainty. In order to better represent real data, we first derive the mean abundance errors from the GALAHA DR2 (Buder et al. 2018) and APOGEE DR14 (Holtzman et al. 2018) spectroscopic surveys which are $\langle \delta[\mathrm{Fe/H}] \rangle \approx 0.05\,\mathrm{dex}$ and $\langle \delta[\mathrm{Mg/Fe}] \rangle \approx 0.06\,\mathrm{dex}$. and apply them to the stars in our models. We convolve the $[\mathrm{Fe/H}]$ and $[\alpha/\mathrm{Fe}]$ abundances in the three models with a Gaussian, with the respective mean observational uncertainties set as the standard deviation. The resulting chemical space distributions are presented in Figure 5.8 where we observe a strong blurring in the number density (top) and warp star purity (bottom) distributions. With artificial errors the separation between the thin and thick discs becomes harder to detect though we still observe different slopes in the low and high-α populations. The chemical cuts from Figure 5.8 (dashed red polygons) are overlaid on top of the warp star purity. We observe that the high purity regions have shifted towards lower $[\alpha/\mathrm{Fe}]$ values and the original chemical cuts are now contaminated by lower-purity regions, thus requiring
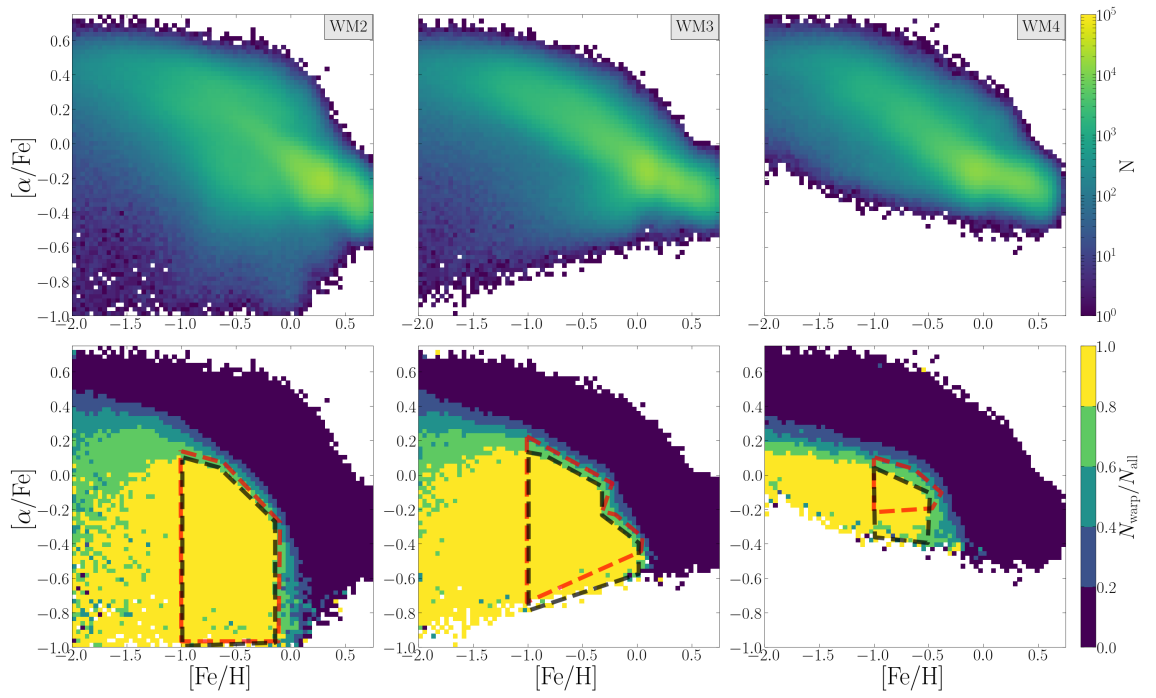
Figure 5.8: Same as Figure 5.7, but with artificial errors applied to the [Fe/H] and [α/Fe] values of each stellar particle. The dashed polygon indicates the chemical cut defined in Figure 5.7 (red) and the updated chemical cut that accounts for the abundance errors (black).

updated chemical cuts (dashed black polygons).

One of the key limitations in observational astronomy is the distance uncertainties. To more accurately apply the trends in the chemical space of our models onto current and upcoming observational data, we analyse the chemistry of stars located in a simulated Solar annulus. Similar to the analysis in Chapter 4, we simulate a Solar annulus sample using contemporary estimates of the Solar location relative to the MW warp. We define the Solar annulus as a cylindrical sector centred on $R = 8.2\,$kpc (Bland-Hawthorn & Gerhard 2016) and $\phi_w = -72.5°$ (Chen et al. 2019a), where ϕ_w is the angle between the peak of the warp's south side in the clockwise direction (see Chapter 2). The cylindrical sector has a width of $\Delta R = 4\,$kpc, maximum height of $|z_{max}| = 7\,$kpc, and azimuthal diameter of $\Delta\phi = 75°$.

In Figure 5.9 we present the chemical space for stars in the Solar annulus sample of the three models. Similarly to Figure 5.7, the top and bottom rows of Figure 5.9 show the number density and warp star purity distributions, respectively. We observe that the chemical thick disc becomes less recognisable in the WM3-4 models as the upper branch either becomes more diffuse or disappears altogether, while in WM2 model, the thick disc is still apparent. We also observe a change in the overall shape of the chemical space as the low-α and low-metallicity region in models WM2-3 becomes scarcely populated. The warp star purity distribution shows similar high-purity regions (yellow) as observed in Figure 5.7, however, there is a clear decrease of warp star purity in the low-metallicity regions ([Fe/H] < -1). An outline similar to the one in Figure 5.7 is applied to the regions of high warp star purity (dashed red polygons) while accounting for potential halo star contamination that will be present in the MW data.

Finally, Figure 5.10 shows the same chemical space distribution in the Solar annulus but with applied artificial errors in the elemental abundances (see Figure 5.8).
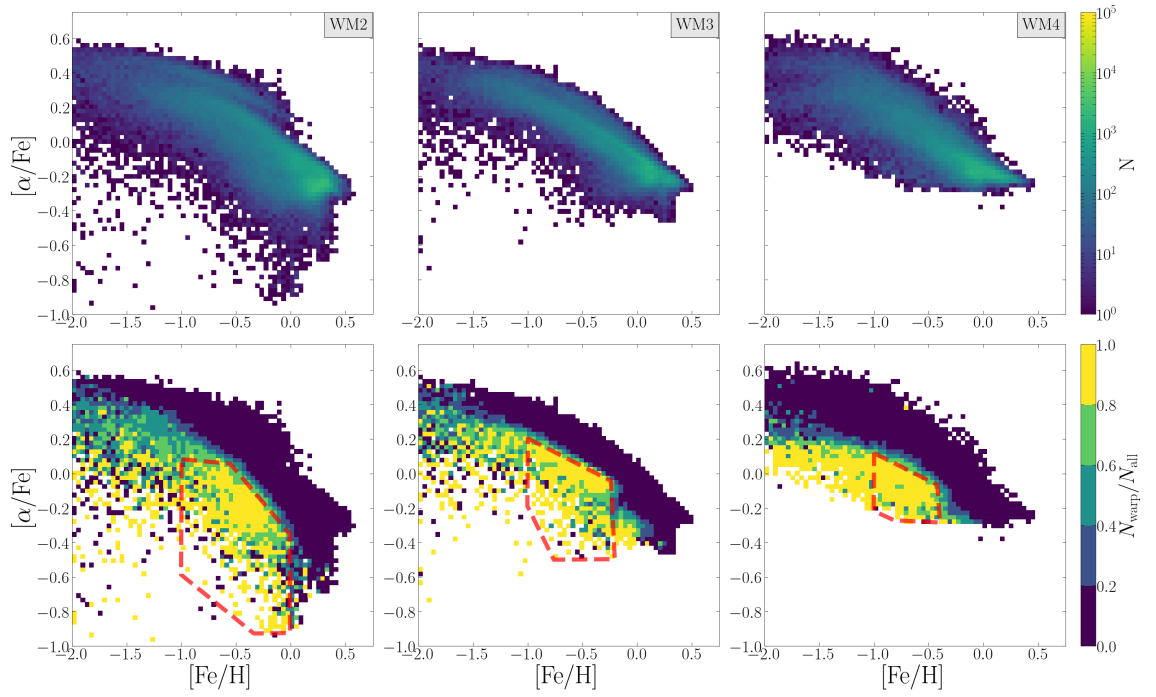
Figure 5.9: Chemical space distributions for stars in the Solar annulus of the three models. The model is indicated in the top right corner of each column. Top: Number density distribution. Bottom: Distribution of the warp star purity, $N_{\mathrm{warp}}/N_{\mathrm{all}}$. The dashed red polygon outlines the area of chemical space where $N_{\mathrm{warp}}/N_{\mathrm{all}} \geq 0.8$ and $[\mathrm{Fe/H}] \geq -1$.
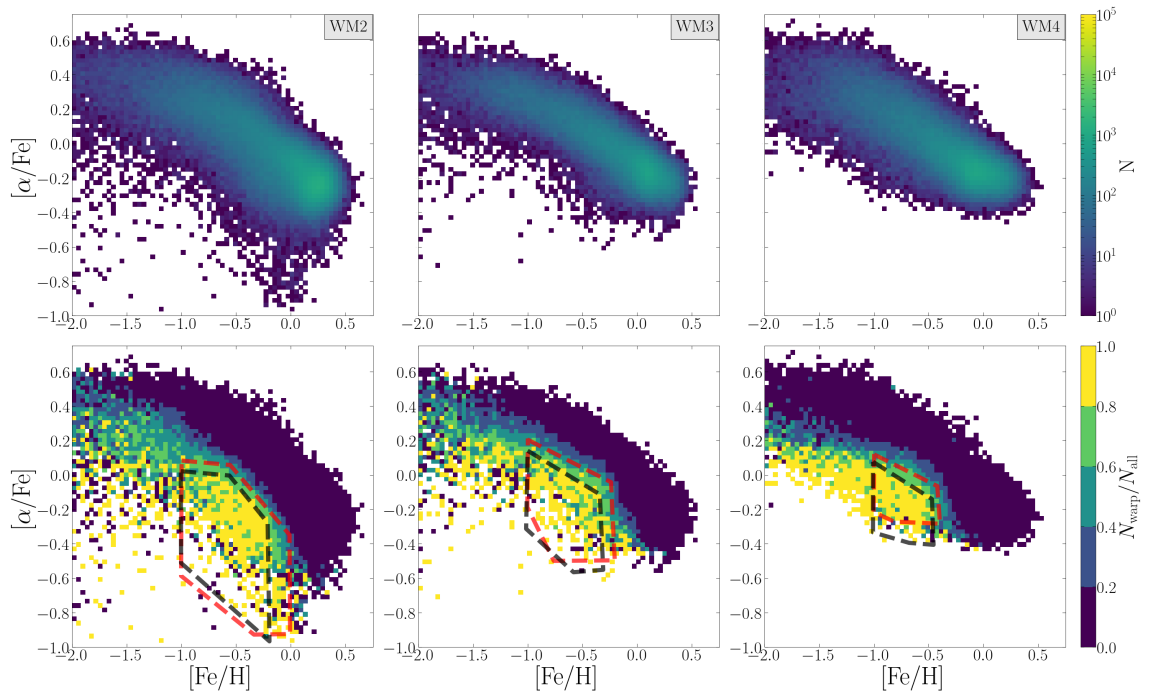
Figure 5.10: Same as Figure 5.9, but with artificial errors applied to the [Fe/H] and [α/Fe] values of each stellar particle. The dashed polygon indicates the chemical cut defined in Figure 5.9 (red) and the updated chemical cut that accounts for the abundance errors (black).

CHAPTER 5

We now cannot differentiate between the thin and thick discs in any of the models. Similar to Figure 5.8 we observe the high-purity regions shifting towards lower $[\alpha/\text{Fe}]$ and $[\text{Fe/H}]$ values out of the original chemical cut from (red polygons) defined in Figure 5.9. We, therefore, improve upon the chemical cut to only include the high-purity regions while accounting for potential halo star contamination (black polygons). The resulting abundance limits within the black polygons are defined as the definitive chemical cuts and are used throughout the rest of this and the following chapters.

Warp stars in the AMR

In a closed model, a galaxy is expected to have a negative age-metallicity relation (AMR) as younger stellar populations form in gas contaminated by the remnants of the older metal-poor populations (Spitoni et al. 2021; Chiappini et al. 1997). Observations in the MW present a flat and broad AMR even when accounting for errors in ages and metallicities (Casagrande et al. 2016). The flattening is likely due to radial migration as stars of different metallicities are brought into a region and pollute the inherent AMR. Observations in the warped outskirts of M31 have shown a clear negative trend in the AMR (Bernard et al. 2015), which can be interpreted as migration into the warp being inefficient. The results in Chapter 3 showed that migration occurs out of the warp as warp stars settle into the disc, which could similarly affect the resulting AMR. Other factors that can affect the AMR in our models include the strict definition of warp stars (formation space) and the potential contamination of the accreting gas by galactic outflows, however, this is beyond the scope of this thesis.

Figure 5.11 shows the number density (top) and warp star purity (bottom) distributions in the AMR for all the stars in the three models. In all three models, we observe an overall decreasing AMR as well as several branches of concentrated
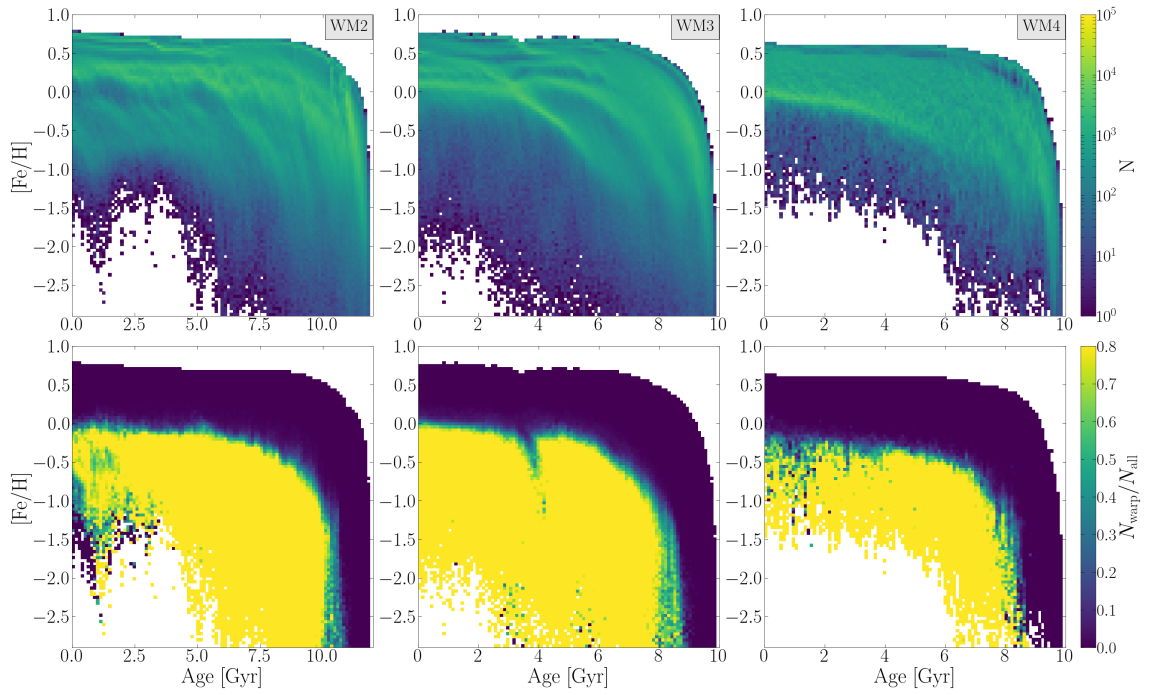
Figure 5.11: Distributions in the the age-metallicity relation (AMR) of the three models. The model is indicated in the top right corner of each column. Top: Number density distribution. Bottom: distributions of the warp star purity, $N_{\mathrm{warp}}/N_{\mathrm{all}}$.
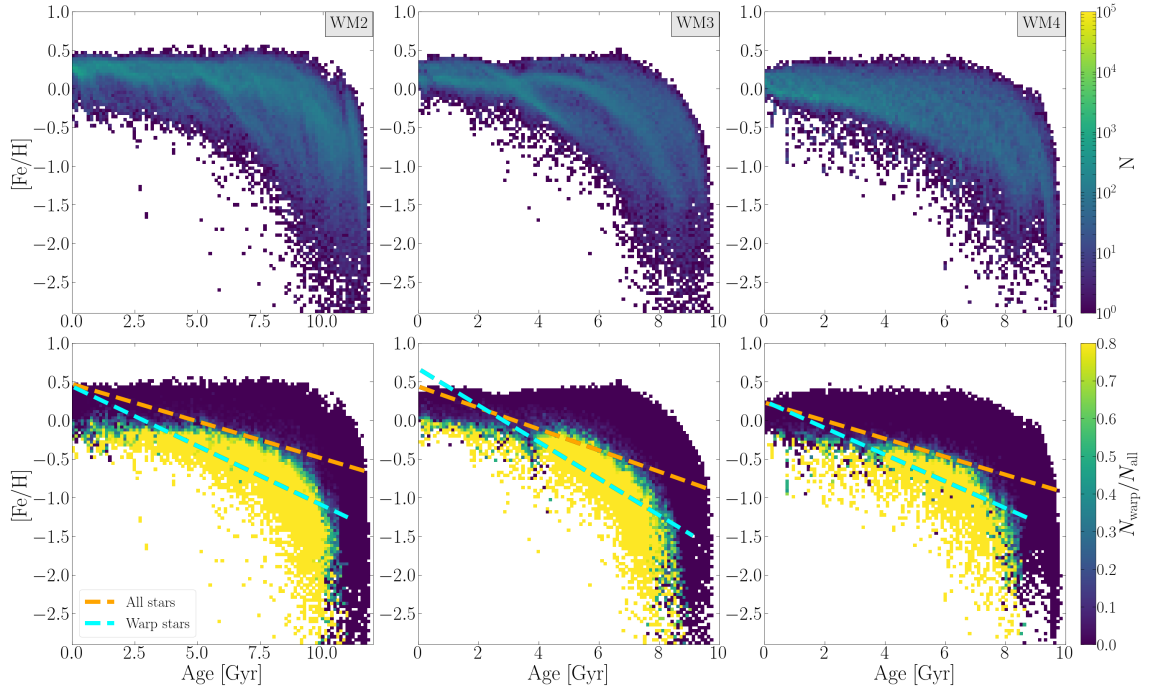
Figure 5.12: Same as Figure 5.11 but for stars in the Solar annulus of the three models. The dashed lines represents linear fits to the overall stellar distribution (orange) and to the warp population (cyan).

density with decreasing AMRs. The upper age limit in the high-purity region can indicate when the galactic warp starts to efficiently form stars, which appears to be $\sim 2\,\text{Gyr}$ from the beginning of each model. The warp star purity distribution shows that up to this age limit and below $[\text{Fe/H}] \leq 0$ the purity is above 80% with the warp population occupying the lower part of the AMR. In Figure 5.12 we present the same distributions in the AMR for stars in the Solar annulus of the three models. The number density distribution (top) shows a loss of the lower-metallicity population in the range $0 \leq \text{age/Gyr} \leq 7.5$, however, the warp star purity (bottom) still remains high below the main AMR. The dashed lines represent linear fits to the AMRs of the overall distribution (orange) and warp stars (cyan). We observe that the AMR is stronger in the warp stars when compared to the overall AMR in all models.
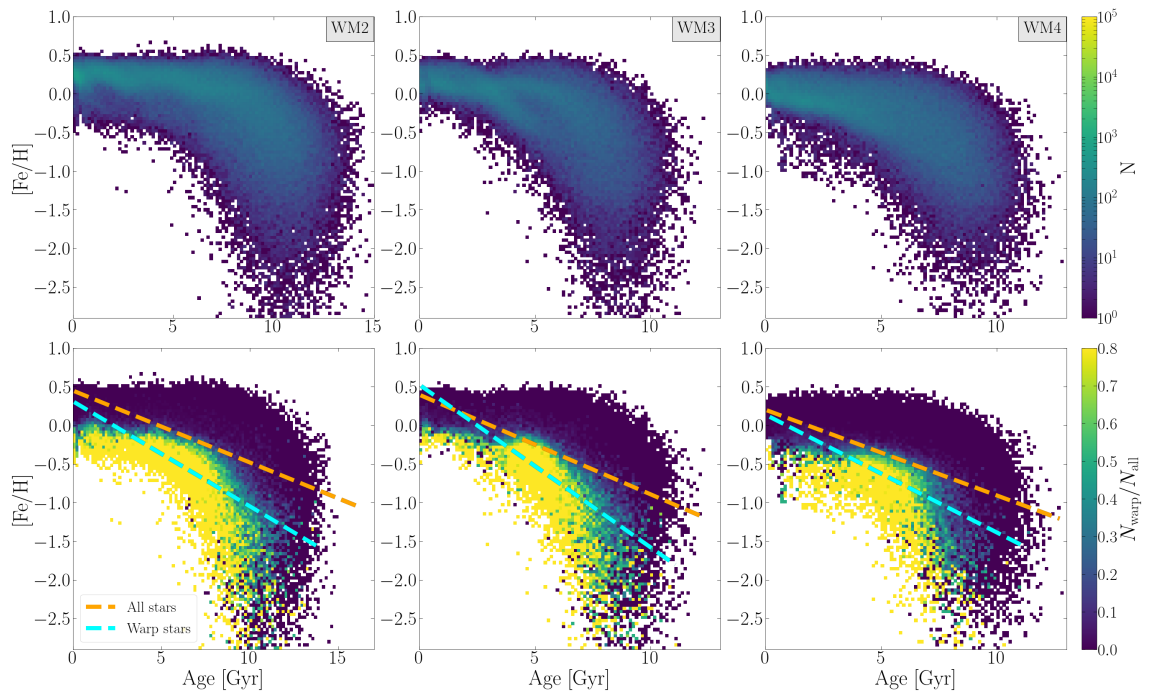
Figure 5.13: Same as Figure 5.12, but with artificial errors applied to the stellar ages and [Fe/H] values of each stellar particle.
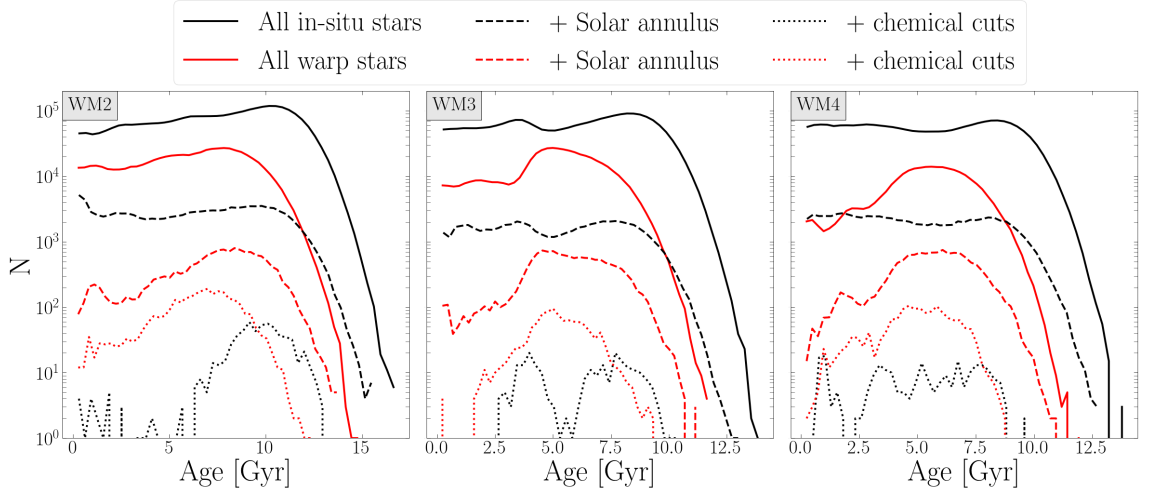
Figure 5.14: The age distribution for in-situ (disc, black) and warp (red) stars in the three models. The model is indicated in the top left corner. The line styles represent different cuts on the stellar populations that are: entire sample (solid), Solar annulus (dashed), and a chemical cut in the Solar annulus (dotted), the latter being defined for each model in Figure 5.14 with the red polygon.

The abundance uncertainties are estimated with the mean abundance errors from spectroscopic surveys, however, applying artificial errors to stellar ages is more challenging due to the naturally high uncertainties in age estimates. We settle on an optimistic 20% error in ages and apply them to the stars in our models by assuming that the age values are Gaussian. Figure 5.13 shows the AMR with artificial errors for stars in the Solar annulus of the three models. We observe similar differences between the linear fits to the overall and warp samples in the Solar annulus, with the warp population having a stronger AMR.

To interpret the sharp cutoff in warp star purity in Figures 5.11-5.13 we analyse the star formation history (SFH) in the three models. Figure 5.14 presents the distribution of ages, with applied artificial errors, for in-situ (black) and warp (red) stars in the WM2-4 models. The solid lines represent the unfiltered stellar sample

in each model, while the dashed and dotted lines indicate the Solar annulus sample and its definitive chemical cut for each model (Figure 5.10), respectively. The overall sample shows an expected dominance of in-situ stars over the warp population. The SFH of the in-situ stars remains relatively flat throughout, while the warp stars experience a decrease of different magnitudes depending on the model.

In WM2, the decline in the warp SFH is relatively slow and seemingly matches the slope of the in-situ SFH, indicating that misaligned gas is still being funnelled into the warp (Figure 5.1), fuelling further star formation. In WM3, the decline in the warp SFH occurs at $age \sim 5\,\mathrm{Gyr}$ after which it plateaus. This step-like change in the SFH is likely due to the increasing alignment between the angular momenta of the stellar disc and the surrounding gas, demonstrated in Figures 5.4-5.5. With the increased alignment, more stars forming within the inflowing gas will have smaller θ_{form} values and avoid our defined warp region in formation space (Figure 3.3), therefore decreasing the warp SFH. We observe a more significant and continuous decline in the warp SFH of WM4 at $age \leq 5\,\mathrm{Gyr}$, however, the cause of the decline is similar to the one described in WM3. With the alignment between the angular momenta being even stronger in WM4 (Figures 5.4-5.5), a larger population of stars will be outside of our defined warp region in formation space (Figure 3.3).

The Solar annulus sample does not change the shape of the in-situ SFH, however, in the warp population, the decline at $age \leq 5\,\mathrm{Gyr}$ becomes more pronounced. In Chapter 3 we demonstrated that the younger warp populations in WM2 settle to increasingly thicker discs and are less likely to be observed in the Solar neighbourhood; this explains the more pronounced decline in the SFH. Lastly, applying the definitive chemical cut to the Solar annulus sample causes the warp SFH to overtake that of the in-situ population at different age intervals depending on the model. This is expected as, by definition, the chemical cut contains the highest warp star purity.

5.2.3 Action space

The distinct chemical footprint of the warp population in the three models can aid in the detection of warp star candidates in the MW. However, the aim of our analysis is not to make a direct comparison between our models and observations as there are inherent limitations in simulated galaxies. An example of such limitations is the dissimilarity between the chemical spaces in our models and in the Solar neighbourhood. Therefore, the aim is to assess the overall trends in warp stars in relation to the in-situ population to create a blueprint for further analysis.

Roškar et al. (2010a) demonstrated that warp stars settling into the disc populate the geometric thick disc, indicating that they are on vertically "hot" orbits. We were able to recreate this result in Chapter 3 with model WM2 where, after settling, warp stars were found to be on near-circular orbits and populating the thick disc. A deeper analysis into the dynamical properties of warp stars can be achieved by studying their actions, which are constants of motion in an unperturbed potential field. Actions are defined as:

$$J_i \equiv \frac{1}{2\pi} \oint dq_i \, p_i \tag{5.1}$$

where q_i and p_i are the generalised coordinates and momenta along a star's orbit, respectively. Assuming that the potential in our models is approximately axisymmetric and slowly varying, the actions of a star are conserved (Binney & Tremaine 2008b). In order to further constrain the unique properties of warp stars, we compute the actions of all stars in the three models using the software library AGAMA (Vasiliev 2019).

To compute the stellar actions, we first interpolate the potential of each model using AGAMA. Spherical symmetry and a flattened axisymmetric distribution are assumed for the halo and disc, respectively. The rotation curve produced by the approximated total potential is presented in Chapter 2 for each model (red dashed

CHAPTER 5

lines in Figure 2.1). Finally, we compute the radial, vertical, and azimuthal actions (J_R, J_z, and J_φ, respectively) using the Stäckel fudge method (Binney 2012; Sanders & Binney 2016). In order to determine common trends across the action spaces of all three models, we normalise the computed actions:

$$\overline{J_i} = \frac{J_i}{J_{\text{tot}}} \tag{5.2}$$

where J_{tot} is the total action and defined as:

$$J_{\text{tot}} = \sqrt{J_R^2 + J_z^2 + J_\varphi^2} \tag{5.3}$$

We examine the relationships between the normalised stellar actions, referred to as *action space*, in the three models. Similar to our analysis in chemical space, we apply artificial errors using the mean action uncertainties in the Sanders & Das (2018a) dataset which are $\langle \delta J_R \rangle = 45\,\mathrm{kpc\,km\,s^{-1}}$, $\langle \delta J_z \rangle = 6\,\mathrm{kpc\,km\,s^{-1}}$, and $\langle \delta J_\varphi \rangle = 25\,\mathrm{kpc\,km\,s^{-1}}$.

In Figures 5.15 - 5.17 we present distributions in the $\overline{J_\varphi} - \overline{J_R}$, $\overline{J_\varphi} - \overline{J_z}$, and $\overline{J_z} - \overline{J_R}$ action spaces for stars in the Solar annulus (left) and in the definitive chemical cut of the Solar annulus (right) of the WM2 model. The top rows show the distribution of the warp star purity in the action spaces, while the middle and bottom rows show the distributions of the mean value and dispersion of stellar ages, $\langle \mathrm{age} \rangle$ and σ_{age}, respectively. In the Solar annulus, the purity distribution shows no distinct regions where warp stars are dominant, with low purity ($\leq 80\%$) values coloured in black. However, when applying the chemical cut, the warp star dominated regions become very distinct and provide the first cuts on the normalised actions. The $\langle \mathrm{age} \rangle$ distribution shows that the high-purity regions are composed of warp stars with $0 \leq \mathrm{age/\,Gyr} \leq 8$ which is in some agreement with Figure 5.14. The σ_{age} distributions show higher dispersions in the high-purity area than in the rest of the action space.
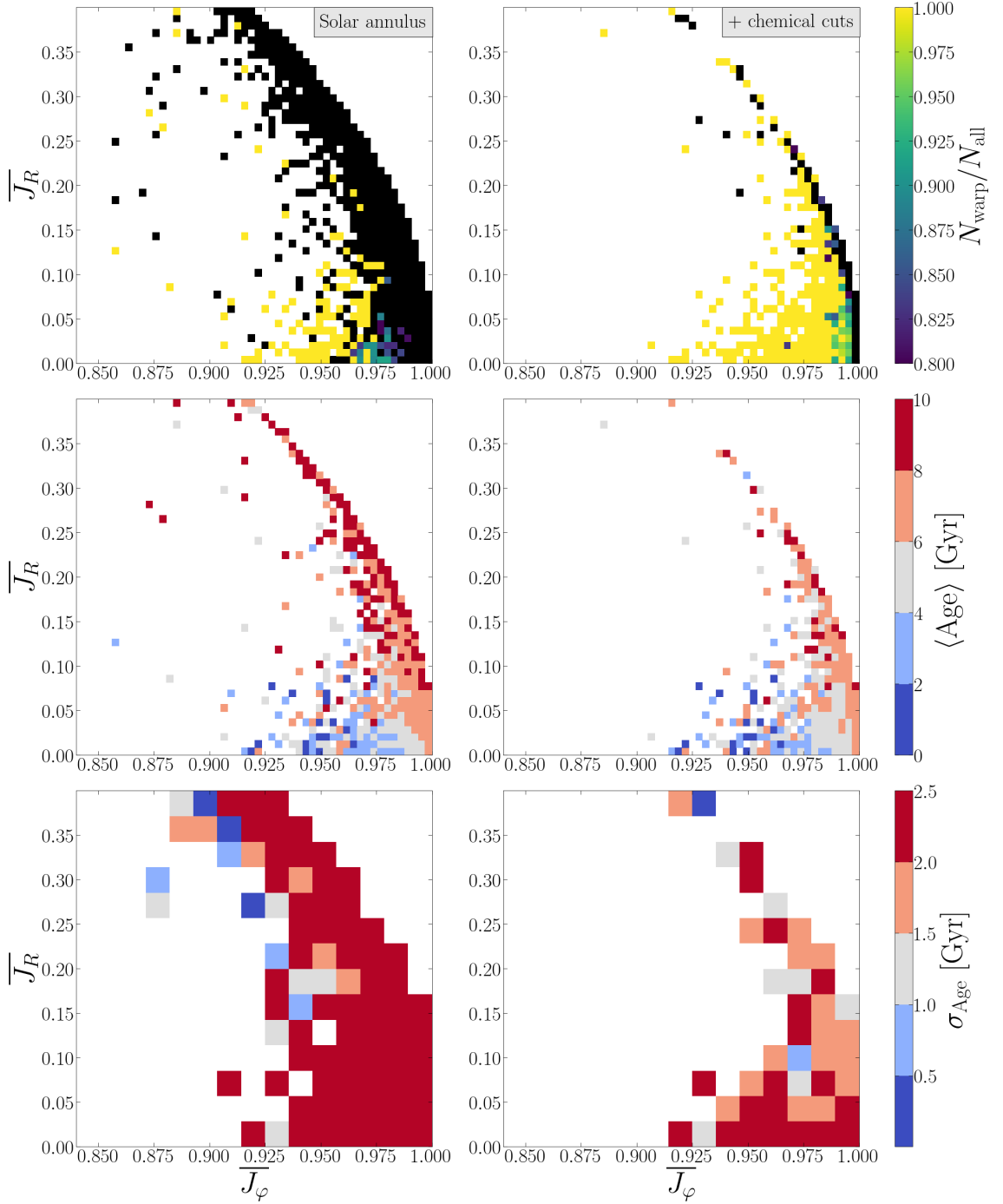
Figure 5.15: Distributions in $\overline{J_\varphi} - \overline{J_R}$ action space for stars in the Solar annulus (left) and in the chemical cut of the Solar annulus (right) of the WM2 model. The chemical cut is defined in Figure 5.9 with the red polygon. The distributions are of the warp star purity (top), the mean stellar age (middle), and the standard deviation of the age (bottom).
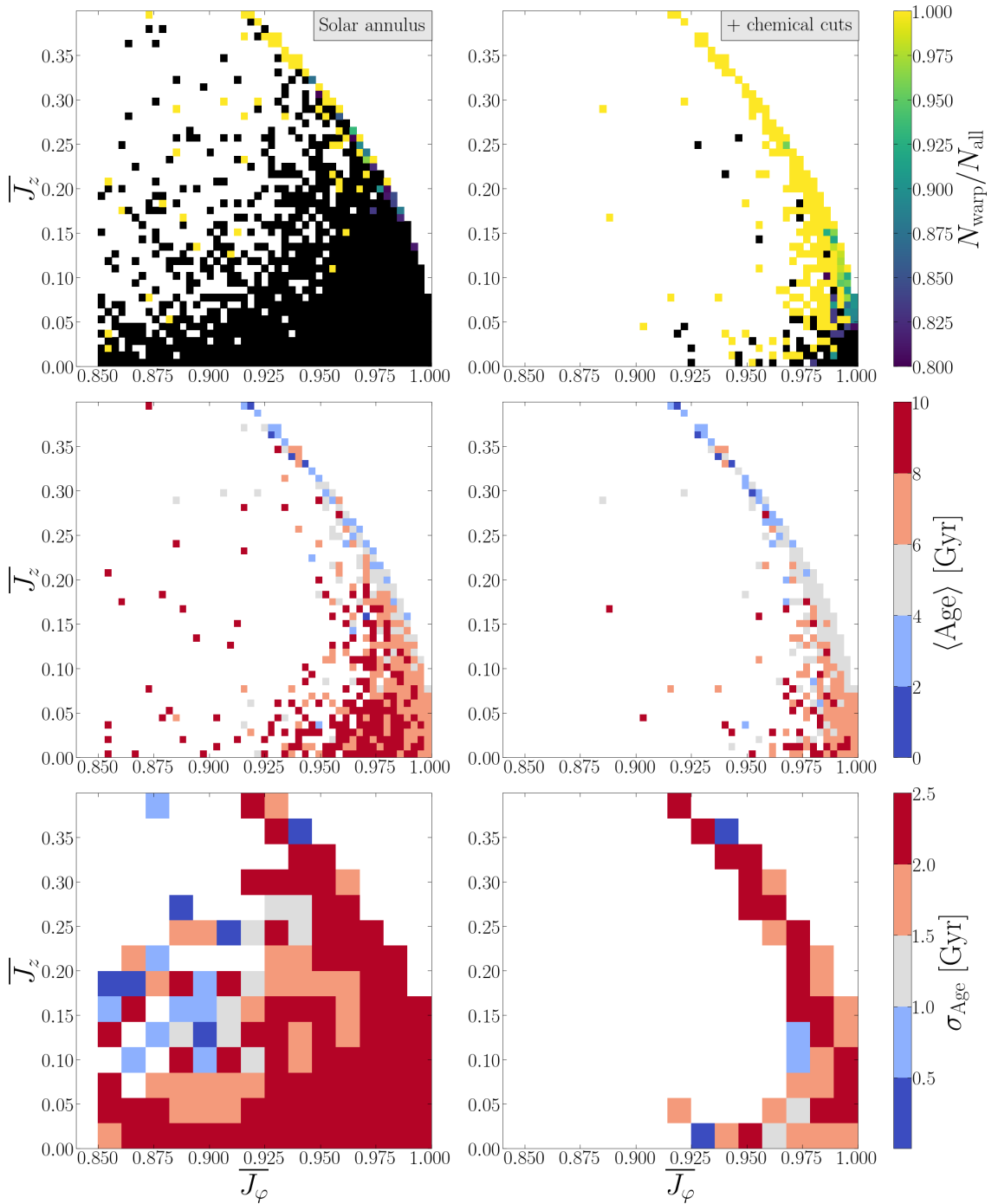
Figure 5.16: Same as Figure 5.15 but in the $\overline{J_\varphi} - \overline{J_z}$ action space of the WM2 model.
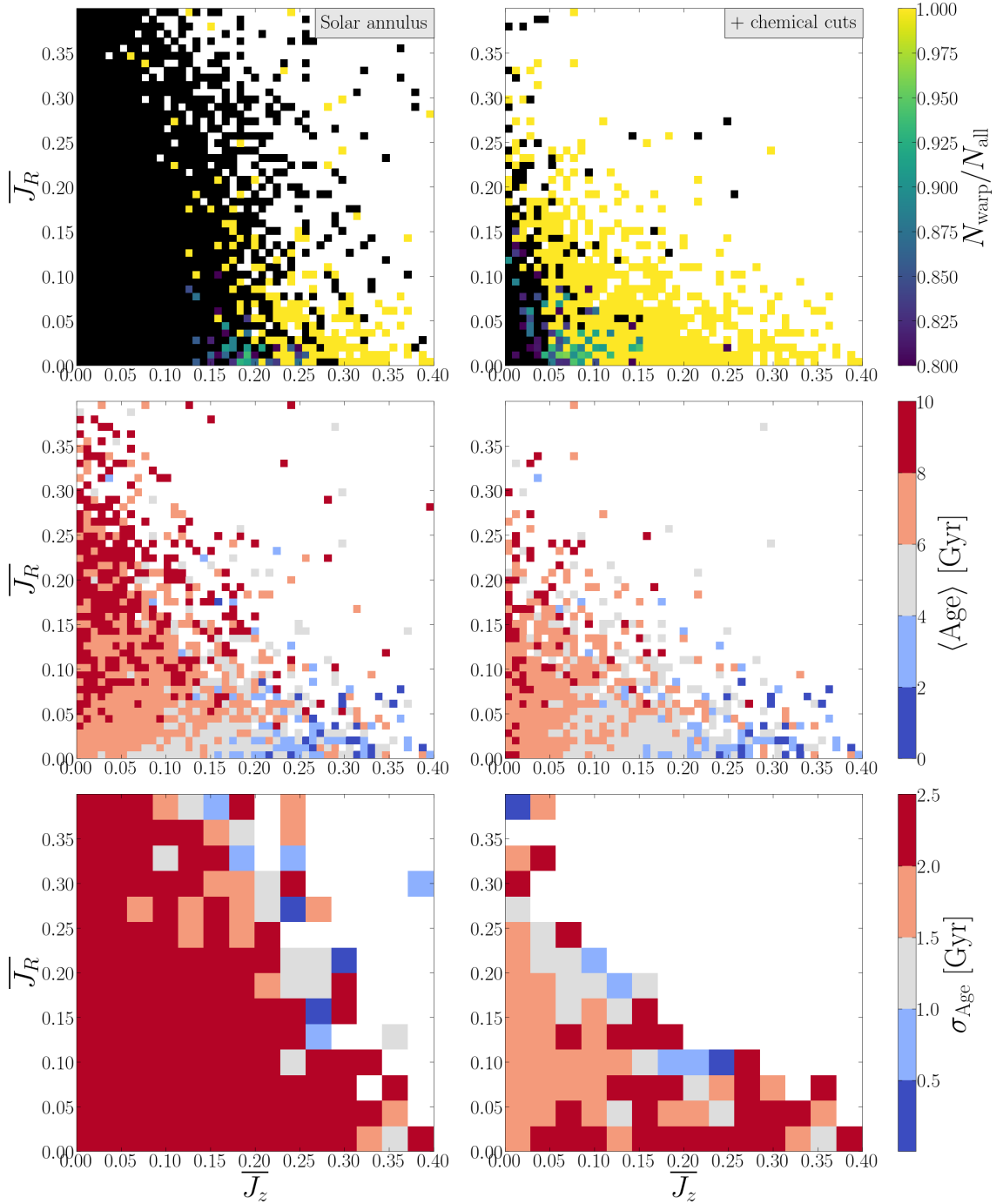
Figure 5.17: Same as Figure 5.15 but in the $\overline{J_z} - \overline{J_R}$ action space of the WM2 model.
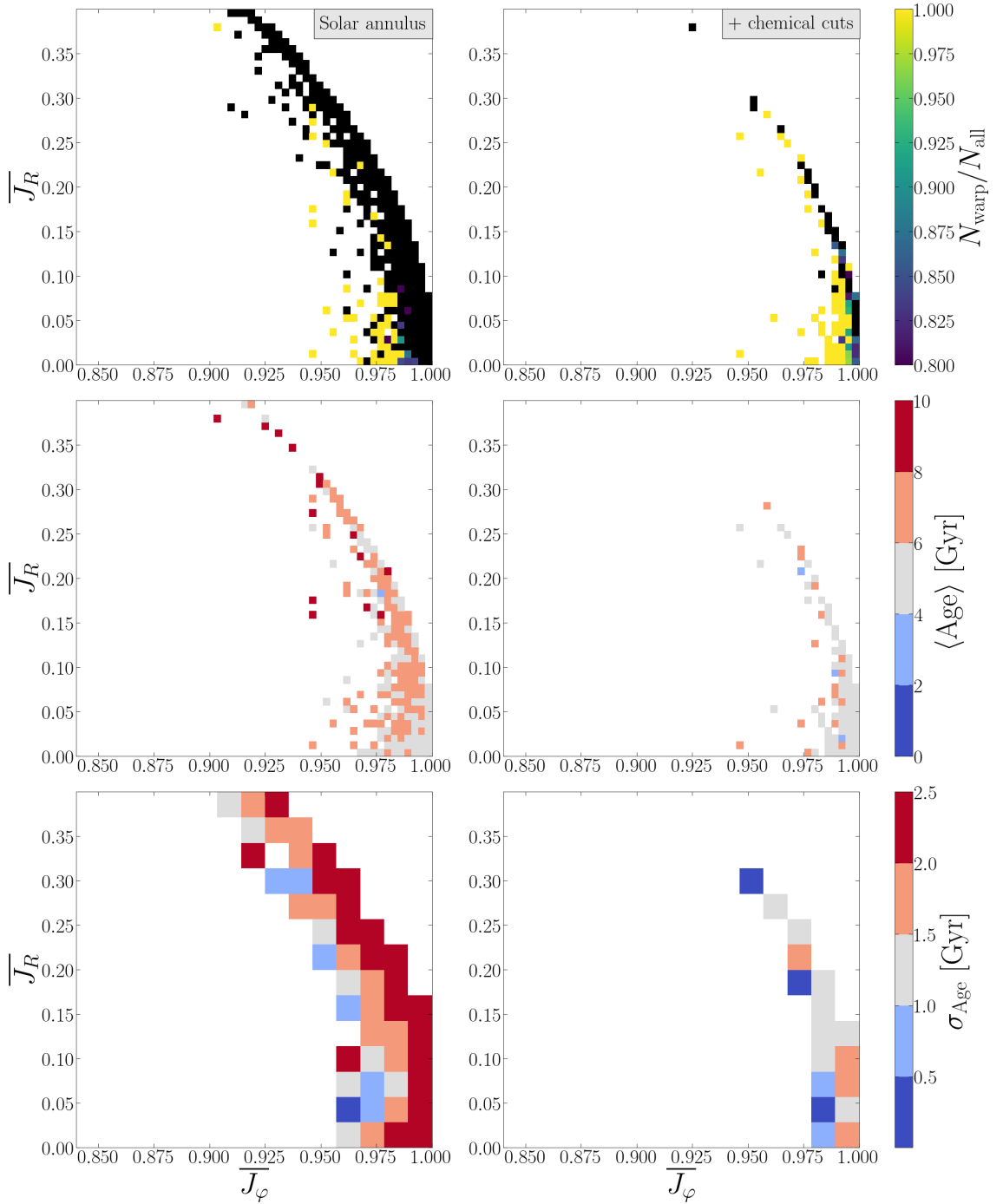
Figure 5.18: Same as Figure 5.15 but in the $\overline{J_\varphi} - \overline{J_R}$ action space of the WM3 model.
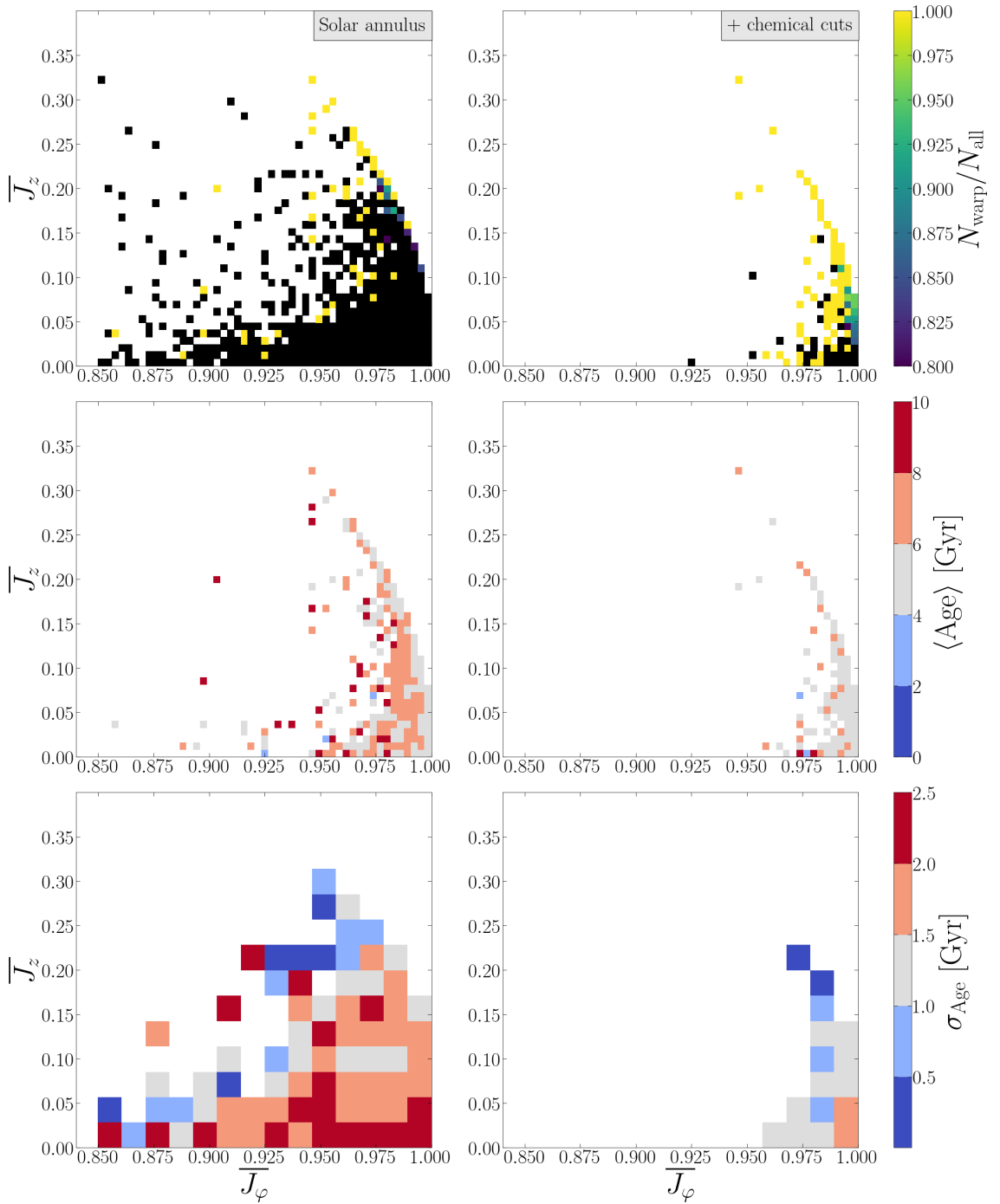
Figure 5.19: Same as Figure 5.15 but in the $\overline{J_\varphi} - \overline{J_R}$ action space of the WM3 model.
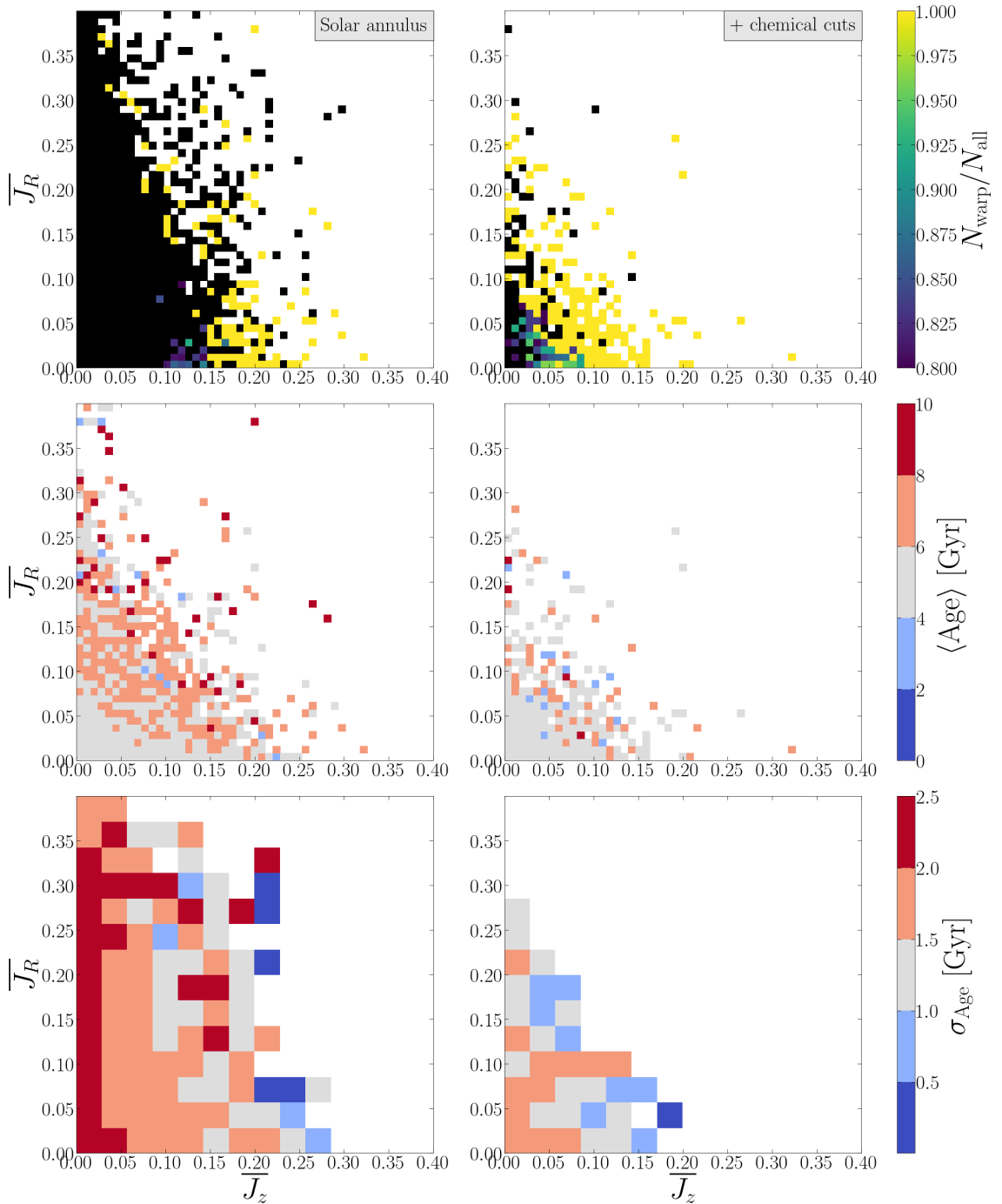
Figure 5.20: Same as Figure 5.15 but in the $\overline{J_z} - \overline{J_R}$ action space of the WM3 model.
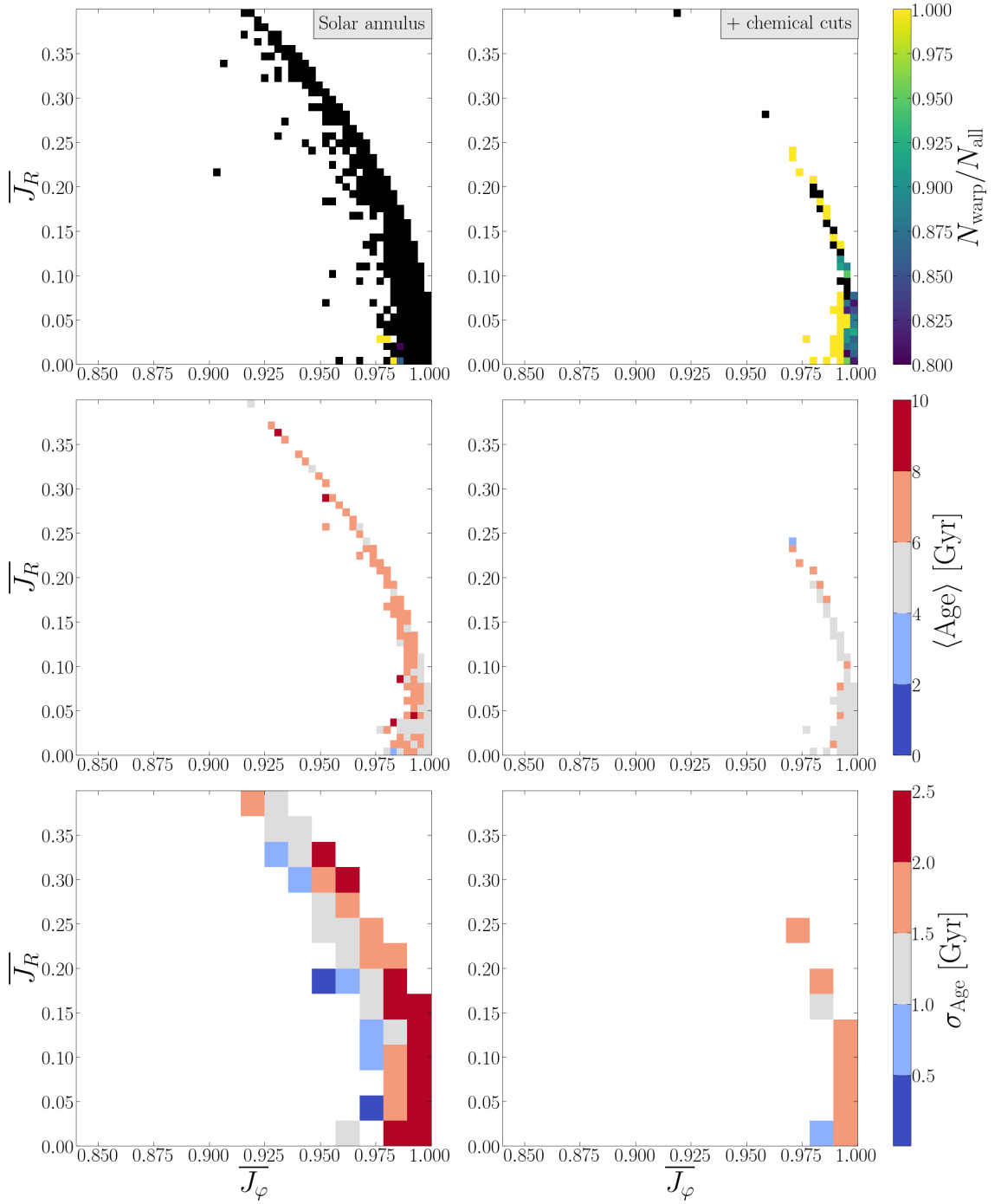
Figure 5.21: Same as Figure 5.15 but in the $\overline{J_\varphi} - \overline{J_R}$ action space of the WM4 model.
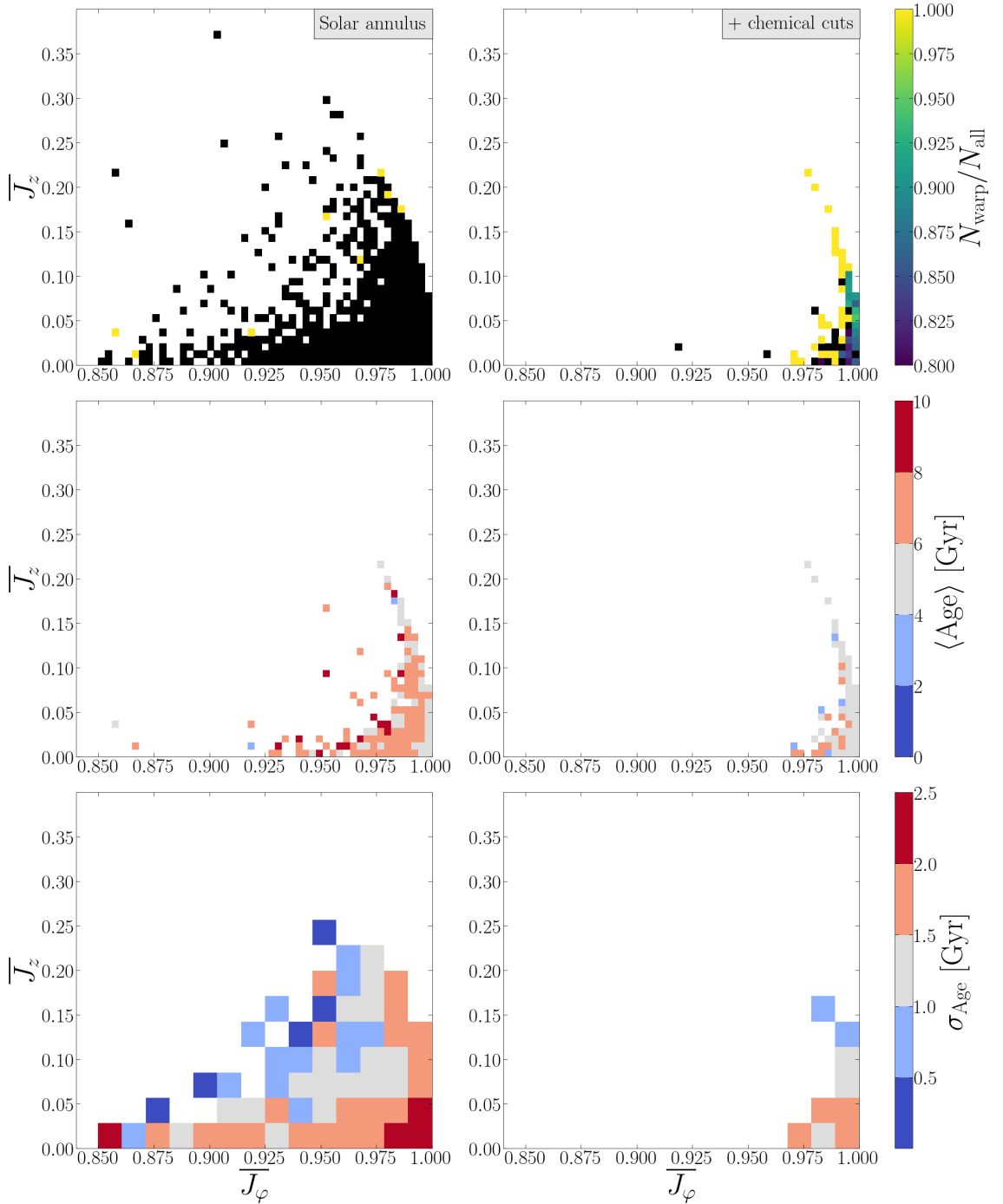
Figure 5.22: Same as Figure 5.15 but in the $\overline{J_\varphi} - \overline{J_z}$ action space of the WM4 model.
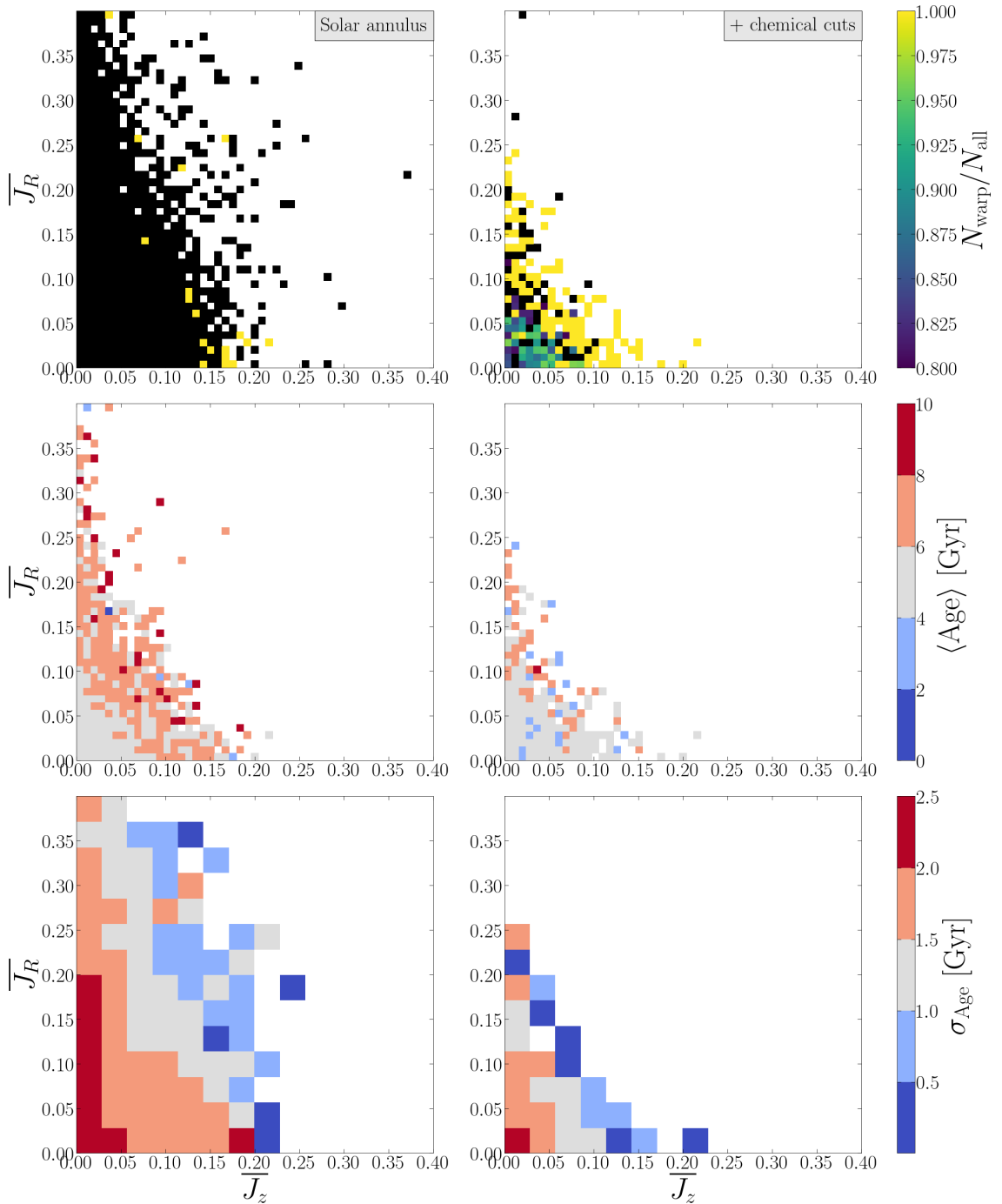
Figure 5.23: Same as Figure 5.15 but in the $\overline{J_z} - \overline{J_R}$ action space of the WM4 model.

Similar to Figures 5.15 - 5.17, we present the same action space distributions for the WM3 and WM4 models in Figures 5.18 - 5.20 and Figures 5.21 - 5.23, respectively. We observe the same trends in the warp star purity distributions as the definitive chemical cuts highlight the high-purity regions in similar areas of action space as in the WM2 model. The age distributions show that the high-purity regions are comprised of warp stars with $4 \leq$ age$/$ Gyr ≤ 6 which is in some agreement with Figure 5.14 for both WM3 and WM4. The σ_{age} distributions show a different result to WM2 as both high-purity regions in the WM3 and WM4 models have the lowest age dispersions in action space.

As a result of our action space analysis, we determined the action cuts that, in combination with the definitive chemical cut, produce warp star samples with the highest purity in each model. These actions cuts also account for potential halo star contamination (Posti et al. 2018) and thus can be applied to observational data. We use the following actions cuts in all three models : $\overline{J_R} \leq 0.2$, $\overline{J_z} \geq 0.9$, and $\overline{J_\varphi} \geq 0.9$. We refer to the combined action and chemical cuts in each model as the *warp filter*.

5.3   Warp stars at the Solar annulus

In this section, we apply the warp filters produced in the previous section to the simulated Solar annulus samples of the three models. We will demonstrate the effectiveness of the warp filter in each model by producing a sample of warp star candidates and comparing them to actual warp stars.

In Figure 5.24 we present the chemical (top), AMR (middle), and spatial (bottom) distributions of warp star candidates in the WM2-4 models. The warp star candidates were determined using the warp filters of each model. In the chemical space, we present the warp star candidates (green triangles) overlaid on top of the number density distribution (colour) of the Solar annulus sample in each model. The solid coloured polygons represent the definitive chemical cuts in each model.
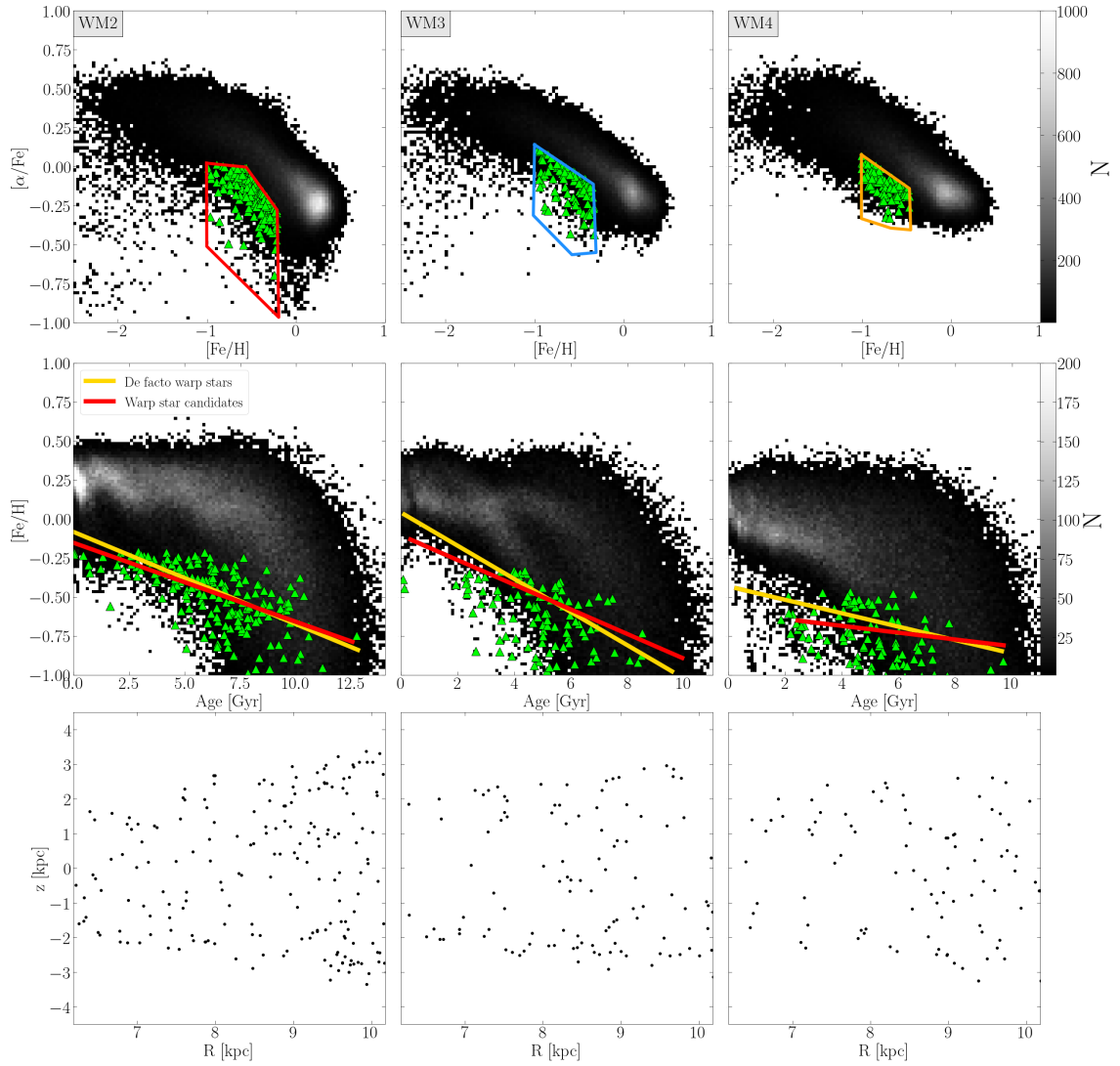
Figure 5.24: Distributions of warp star candidates in the WM2-4 models. Top: number density distribution of stars in the Solar annulus with overlaid warp star candidates (green triangles) in chemical space. The solid polygons represent the region of chemical space where the warp star purity is greater than 80% (Figure 5.10). Middle: number density distribution of stars in the Solar annulus with overlaid warp star candidates (green triangles) in the AMR. The solid lines represent the linear fits to the AMR of the warp star candidates (red) and the de facto warp stars identified in the models (yellow). Bottom: locations of the warp star candidates in the galactocentric $R - z$ plane.

The AMR similarly shows the warp star candidates (green triangles) overlaid on top of the number density distribution of the Solar annulus sample (colour). We observe a distinct negative AMR in the warp star candidates, which we confirm with a linear fit (solid red line). To assess the effectiveness of the warp filters, we examine the warp stars that were defined with R_{form} and θ_{form} in Section 5.2.1, referred to as *de facto* warp stars. We compute a linear fit to the AMR of the de facto warp stars located in the chemical cut of the Solar annulus (solid yellow line). Table 5.1 shows the parameters of the linear fits in each model. We observe a coincidence between the de facto and candidate warp stars in models WM2 and WM3, with a difference in slopes of $\sim 16\%$ and $\sim 35\%$, respectively. The WM4 model presents a much flatter AMR in the warp star candidates, which is most likely explained by the statistically smaller sample.

The spatial distribution of the warp star candidates is shown in the galacto-centric $R - z$ plane. We observe radial flaring in each of the three models as the $|z_{\mathrm{max}}|$ appears to symmetrically increase with R, which agrees with the results in Chapter 3. The relative accuracy of the warp filters can be estimated by determining the percentage of de facto warp stars that are contained within the sample of candidates. The resulting number (accuracy) of warp star candidates is 2500 (85%) in WM2, 1300 (93%) in WM3, and 250 (90%) in WM4.

5.4 Conclusions

Using three N-body+SPH models that experience continuous misaligned gas accretion, we have demonstrated that warp stars are unique in their elemental abundances and stand out in chemical space above other populations. The warp populations appear to occupy the α-poor and metal-poor regions immediately below the main chemical space distributions of the stellar disc. Further analysis of the chemical space regions of high warp star purity demonstrated that warp stars are equally

Model name	De facto warp stars		Warp star candidates	
	a×10 [Gyr^{-1}]	b×10	a×10 [Gyr^{-1}]	b×10
WM2	$-0.59^{+0.01}_{-0.01}$	$-0.82^{+0.05}_{-0.05}$	$-0.51^{+0.01}_{-0.01}$	$-1.52^{+0.07}_{-0.07}$
WM3	$-1.06^{+0.02}_{-0.02}$	$0.42^{+0.10}_{-0.11}$	$-0.79^{+0.05}_{-0.05}$	$-1.05^{+0.27}_{-0.28}$
WM4	$-0.43^{+0.02}_{-0.02}$	$-4.33^{+0.10}_{-0.10}$	$-0.22^{+0.07}_{-0.07}$	$-5.98^{+0.38}_{-0.37}$

Table 5.1: The slopes, a, and y-intercepts, b, of the linear fits to the AMRs of the de facto warp stars and warp star candidates in the Figure 5.13.

unique in action space. As a result, the combined constraints on the chemical and action spaces produced a warp sample of high purity ($\sim 90\%$).

The unique chemical and dynamical footprint that warp stars have is readily explained by the conditions under which warp stars form. The gas accreting onto the disc of our models is metal-poor, addressing the low-α and metal-poor properties of warp stars. The relatively low radial actions in the warp populations are in agreement with the results in Chapter 3 where settled warp stars are on near-circular orbits. We also speculate that the larger vertical actions in the warp populations result from them forming away from the midplane in the accreting gas. This coincides with warp stars populating the thick disc in WM2 (Chapter 3).

Finally, we can apply our warp filters to the Solar neighbourhood in search of warp star candidates. If the warp star candidates in the MW are identified with a degree of confidence and have relatively accurate age estimates, we can infer the SFH of the Galactic warp.

Chapter 6

Warp star candidates in the Milky Way

In this chapter, we apply the warp filters produced in Chapter 5 on an observational sample located in the Solar annulus with full 6D coordinates, elemental abundances, and age estimates. We analyse the action space distributions of the sample and observe trends similar to those in the WM2-4 models. Finally, after applying the warp filters, we produce a sample of warp star candidates and analyse their distributions in chemical space, the AMR, and the $R - z$ plane.

6.1   The GAIA sample

To apply the warp filters from the WM2-4 models, we require an observational sample with full 6D coordinates, elemental abundances, and age estimates. Sanders & Das (2018a) (hereafter SD18) constructed a value-add catalogue by cross-matching the *Gaia* DR2 with six spectroscopic ground-based surveys (APOGEE, GAIA-ESO, GALAH, LAMOST, RAVE, and SEGUE). The catalogue provides the distance, mass, and age estimates for $\sim 3 \times 10^6$ stars in *Gaia* DR2. The estimates

were calculated by SD18 using a Bayesian framework that characterised the probability density function of the three parameters using photometric, spectroscopic and astrometric data. The catalogue also provides the full 6D coordinates and actions which SD18 computed using the Stäckel fudge method (Binney 2012; Sanders & Binney 2016) and the McMillan (2017) potential. Although the catalogue contains cross-matches with multiple spectroscopic surveys, to reduce uncertainties when selecting our sample, only cross-matches with the GALAH DR2 (Buder et al. 2018) and APOGEE DR14 (Holtzman et al. 2018) high-resolution surveys are considered. The resulting catalogue contains $\sim 4.6 \times 10^5$ stars and is referred to as the SD18 dataset.

We prepare the Solar annulus sample by applying the necessary spatial and error cuts on the SD18 dataset. The SD18 dataset contains flags for each star to indicate if the data can be used with confidence. To simplify this process, we only select stars with one specific flag that encompasses all possible issues and uncertainties in SD18, which is the BEST flag. A flag value of BEST=1 implies that a star does not have duplicate entries in other spectroscopic surveys, has no issues in its observational values (astrometry, photometry, and spectroscopy), and that the output of the Bayesian framework in SD18 (mass and age) encountered no issues. In Table 6.1 we show the stellar counts and North-South asymmetries, *i.e.* $N_{z>0}/N_{z<0}$, in each catalogue and respective samples. Stars with BEST=1 comprise the primary sample referred to as "cross-match". In addition to the flags, we only select stars with action and distance uncertainties that are below 20%, referred to as the "+error" sample in Table 6.1, where "+" indicates that the sample is compounding on all previous samples.

Similar to the Solar annuli in Chapter 5, we select stars in a cylindrical sector centred on the Solar radius and azimuth, $R = 8.2\,\mathrm{kpc}$ and $\phi = 0°$ respectively. The sector has a radial range of $6.2 \leq R/\,\mathrm{kpc} \leq 10.2$, a maximum absolute height of
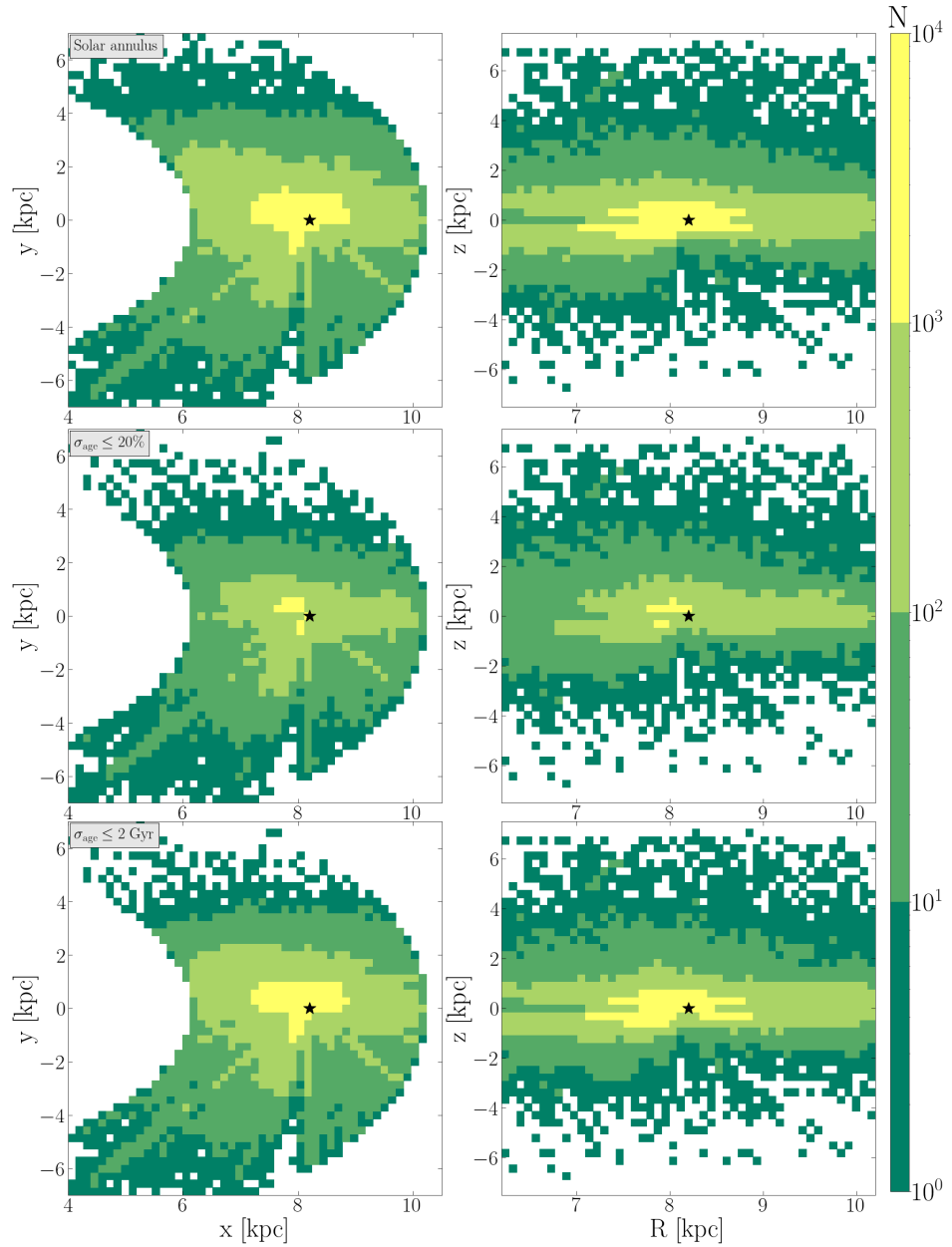
Figure 6.1: Spatial distributions of stars in our cross-match between the SD18 sample and spectroscopic surveys in Galactocentric coordinates in the $x - y$ (left) and $R - z$ (right) planes. The rows indicate different cuts applied to the considered sample. Top: stars in the "+Solar annulus" sample, referred to as the base sample. Middle: the base sample with a cut on the age percent errors, *i.e.* stars with $\sigma_{\mathrm{age}} \leq 20\%$. Bottom: the base cut with a cut on the age errors, *i.e.* stars with $\sigma_{\mathrm{age}} \leq 2\,\mathrm{Gyr}$.

$|z_{\mathrm{max}}| \leq 7\,\mathrm{kpc}$, and an azimuthal diameter of $\Delta\phi = 100°$. This sample is referred to as "+Solar annulus" in Table 6.1. In Figure 6.1 we present the number density distributions in Galactocentric coordinates in the $x-y$ (left) and $R-z$ (right) planes. The different rows indicate the cuts applied to the "+Solar annulus" sample, referred to as the base sample. The top row is for the base sample, while the middle and bottom rows are the compounding age cuts for stars with age errors $\sigma_{\mathrm{age}} \leq 20\%$ and $\sigma_{\mathrm{age}} \leq 2\,\mathrm{Gyr}$, respectively. The black star marker shows the Solar location. We observe north-south asymmetries in all versions of the "+Solar-annulus" sample, which is a consequence of the different observational footprints of each survey.

6.2 Chemical and action spaces

In this section we focus on the chemical space in the SD18 dataset samples. In SD18, the chemical abundances in GALAH are rescaled to match those in APOGEE. However, as our warp filters are based solely on the WM2-4 models we consider their application on the SD18 samples to be independent and not requiring of rescaling between the two surveys. Figure 6.2 shows the number density distribution of the "cross-match" sample in [Fe/H]-[α/Fe] chemical space, where we have chosen the magnesium abundance, [Mg/Fe], to represent the α-element. The spectroscopic surveys used in the SD18 dataset have multiple α-element abundances available, e.g. [O/Fe], however, [Mg/Fe] has overall smaller uncertainties. The mean uncertainties of the above-mentioned abundances in APOGEE (GALAH) are $\langle\delta[\mathrm{Fe/H}]\rangle \approx 0.01\ (0.08)$, $\langle\delta[\mathrm{Mg/Fe}]\rangle \approx 0.02\ (0.08)$, and $\langle\delta[\mathrm{O/Fe}]\rangle \approx 0.05\ (0.1)$. We observe faint signs of the chemical thin and thick discs in the chemical space of the SD18 sample. The definitive chemical cuts from the WM2-4 models (solid polygons in Figure 5.24) are overlaid and appear to be situated immediately below the main chemical space distributions of the stellar disc, mirroring the high-purity locations in the models.
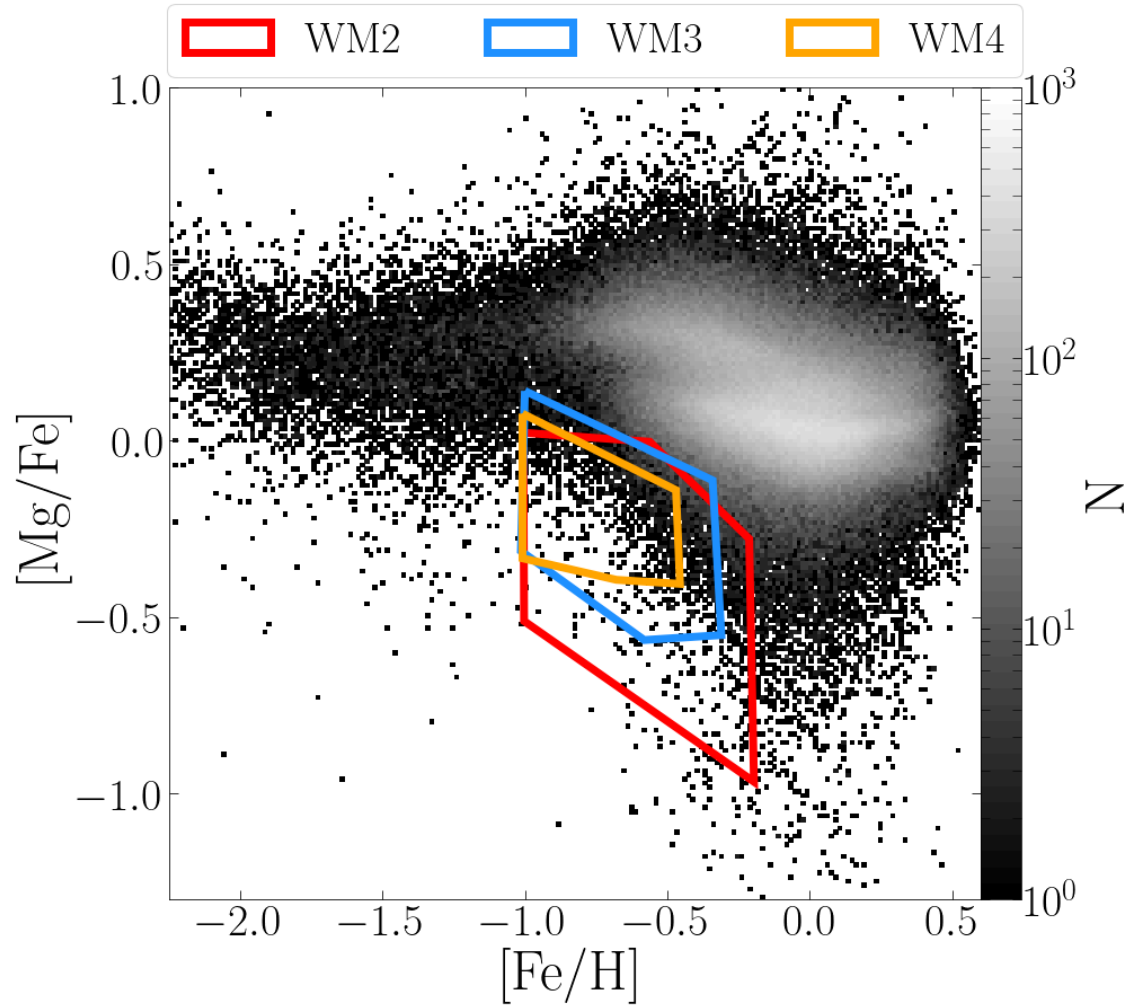
Figure 6.2: Number density distribution in chemical space of stars in the base sample (Figure 6.1). The solid polygons represent the chemical cuts from the WM2 (red), WM3 (blue), and WM4 (orange) models.
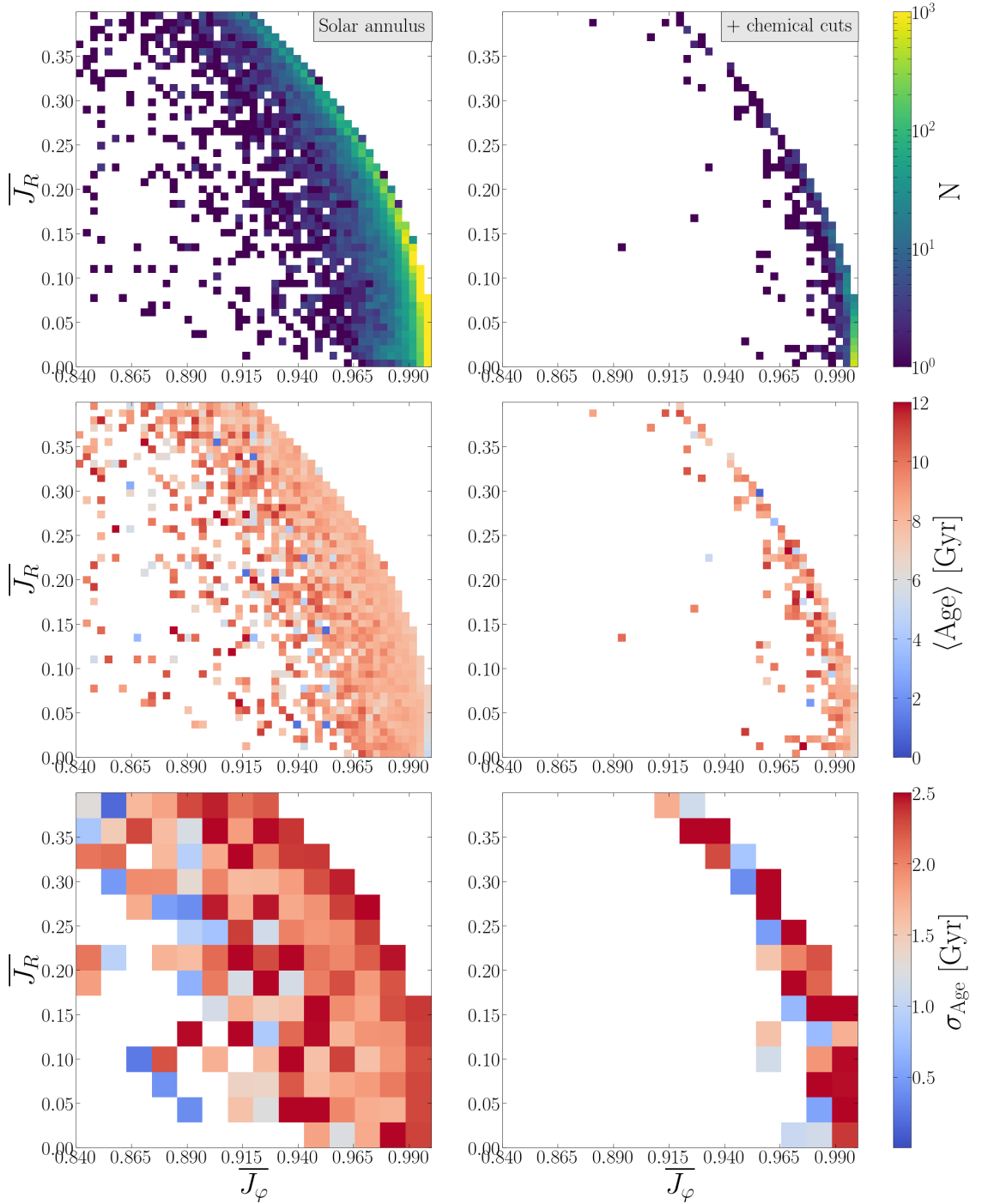
Figure 6.3: Distributions in $\overline{J_\varphi} - \overline{J_R}$ action space for stars in the "+Solar annulus" sample (left) and in the chemical cut of the "+Solar annulus" sample (right). The chemical cut is based on the WM2 model which we define in Figure 6.2 (solid red polygon). The distributions are of the stellar number density (top), the mean stellar age (middle), and the standard deviation of the age (bottom).
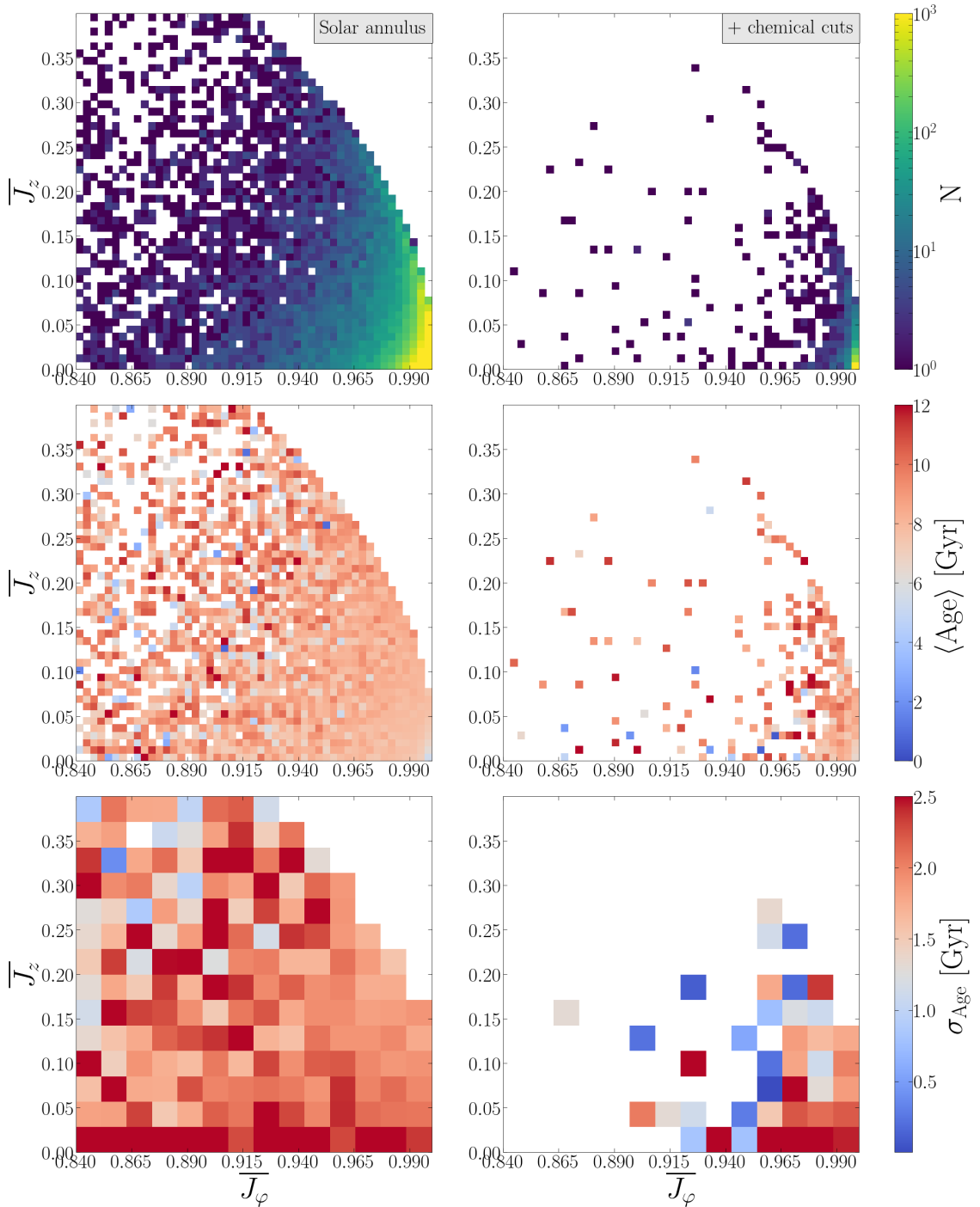
Figure 6.4: Same as Figure 6.3 but in the $\overline{J_\varphi} - \overline{J_z}$ action space.
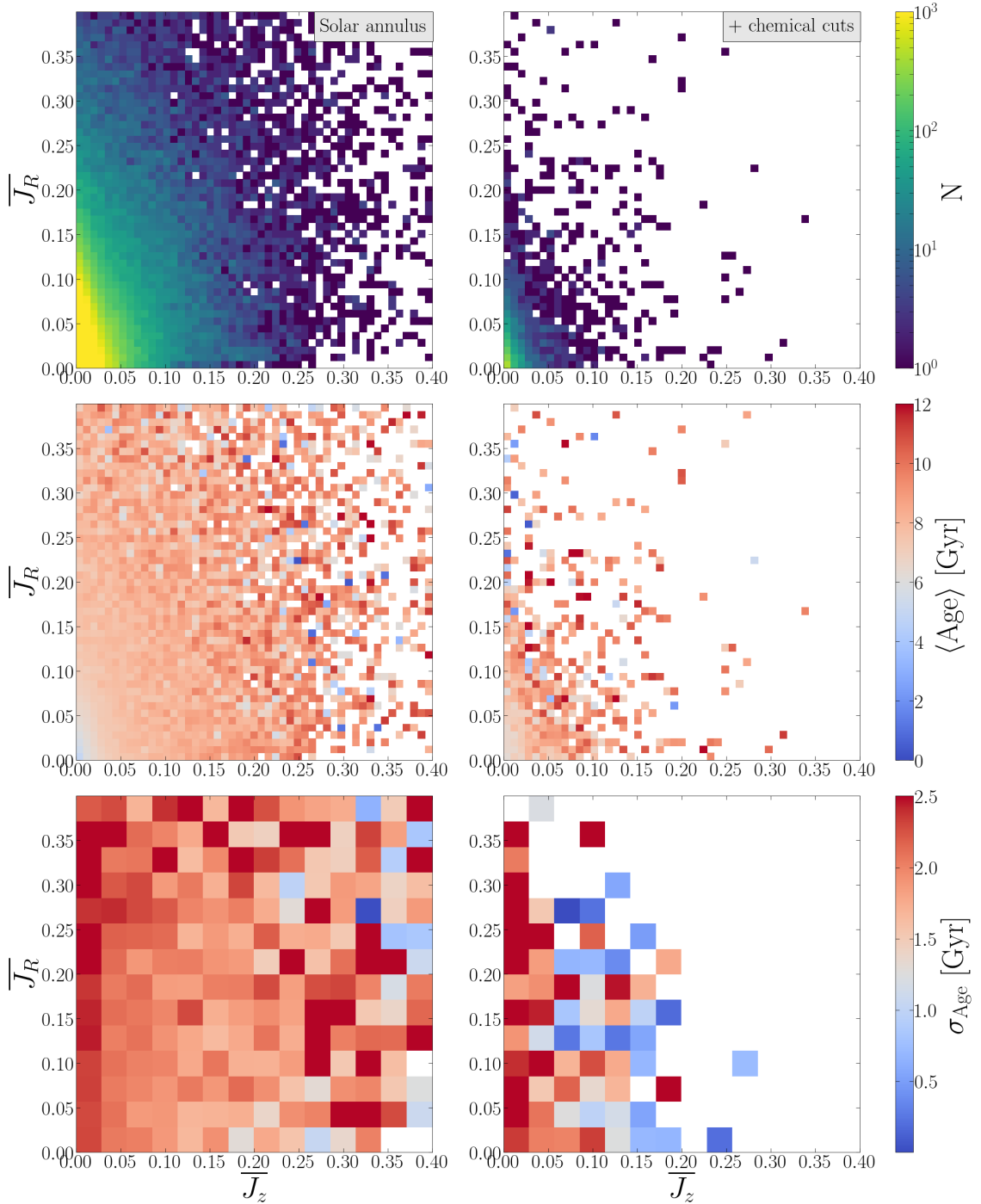
Figure 6.5: Same as Figure 6.3 but in the $\overline{J_z} - \overline{J_R}$ action space.
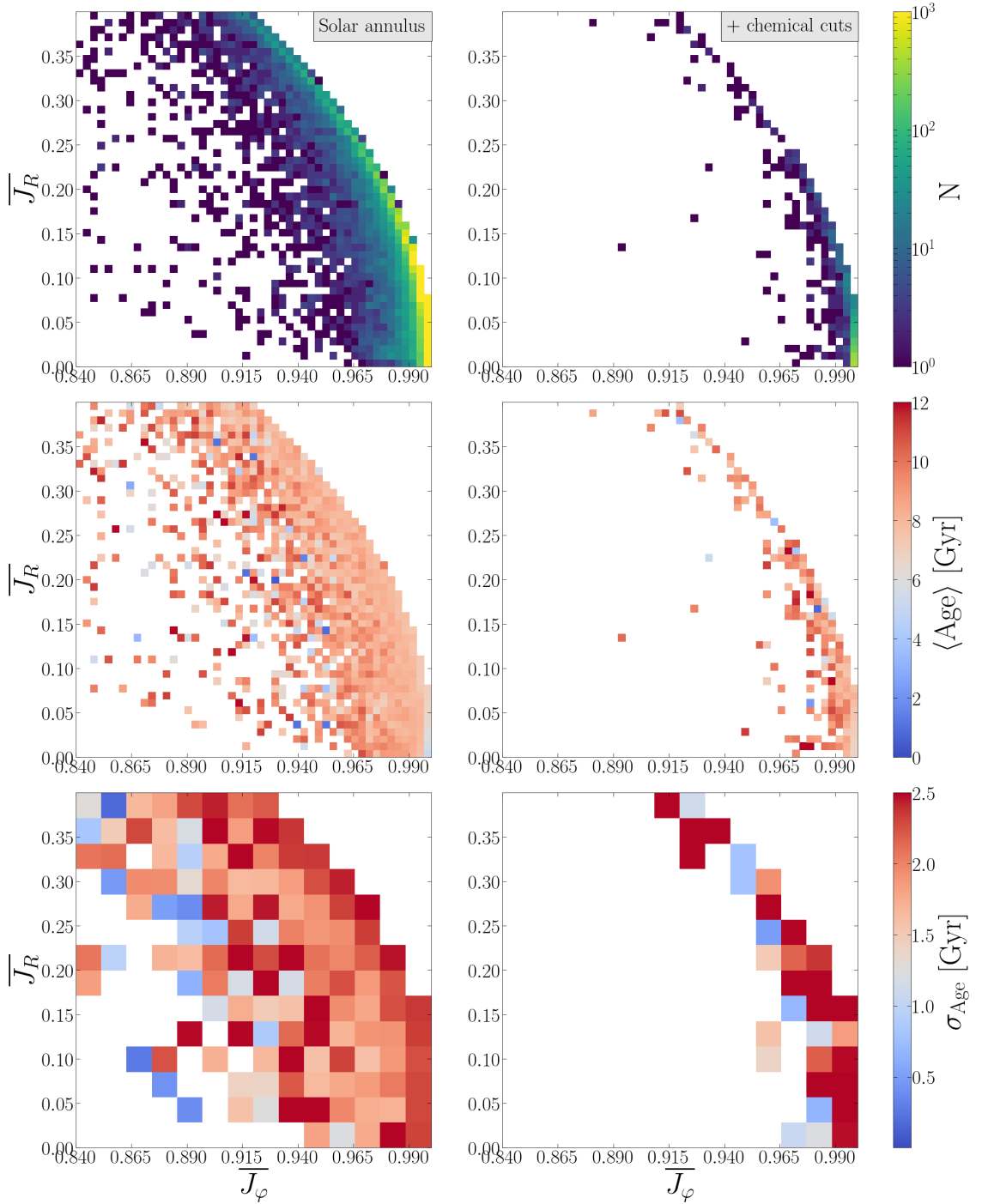
Figure 6.6: Distributions in $\overline{J_\varphi} - \overline{J_R}$ action space for stars in the "+Solar annulus" sample (left) and in the chemical cut of the "+Solar annulus" sample (right). The chemical cut is based on the WM3 model which we define in Figure 6.2 (solid blue polygon). The distributions are of the stellar number density (top), the mean stellar age (middle), and the standard deviation of the age (bottom).
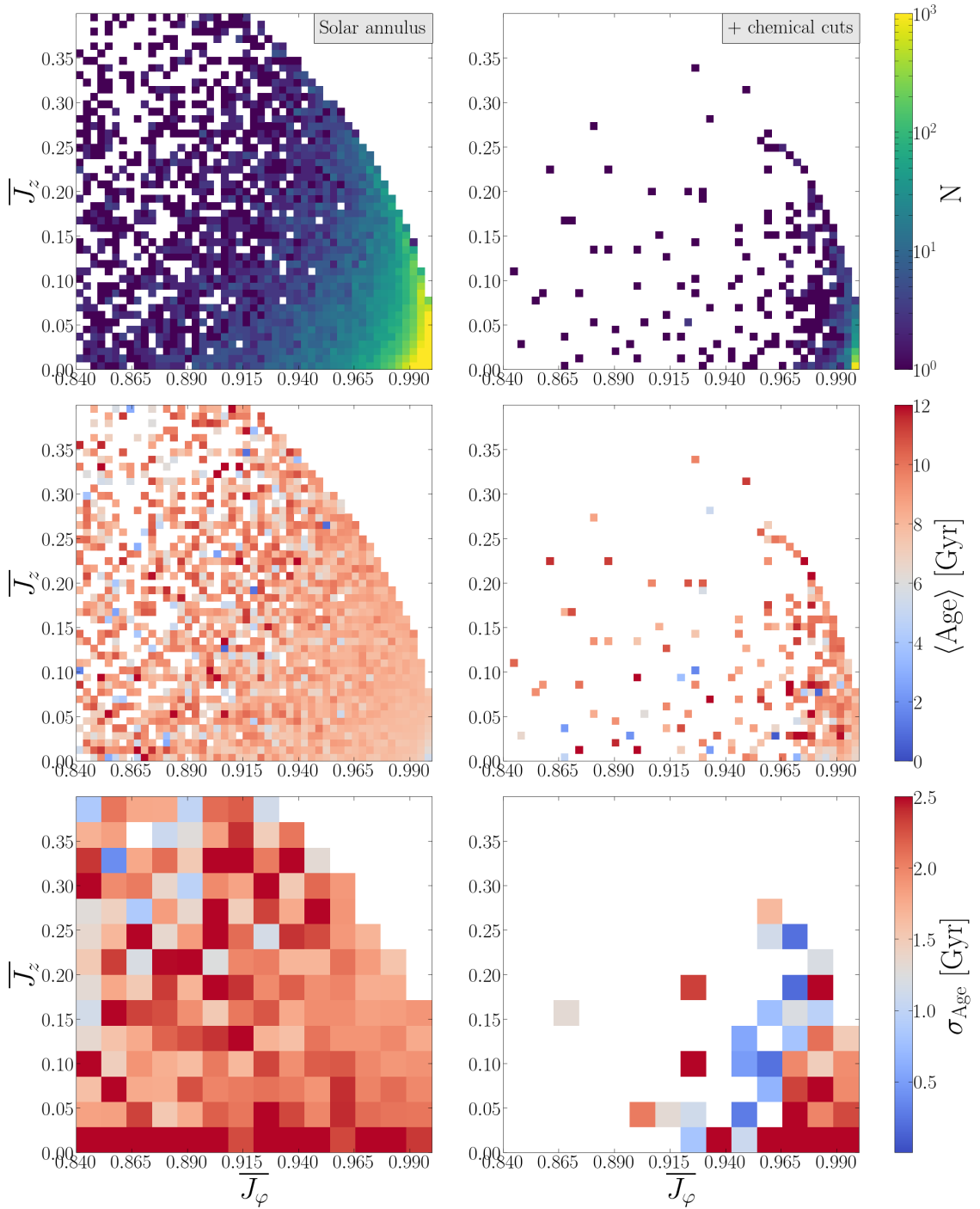
Figure 6.7: Same as Figure 6.6 but in the $\overline{J_\varphi} - \overline{J_z}$ action space.
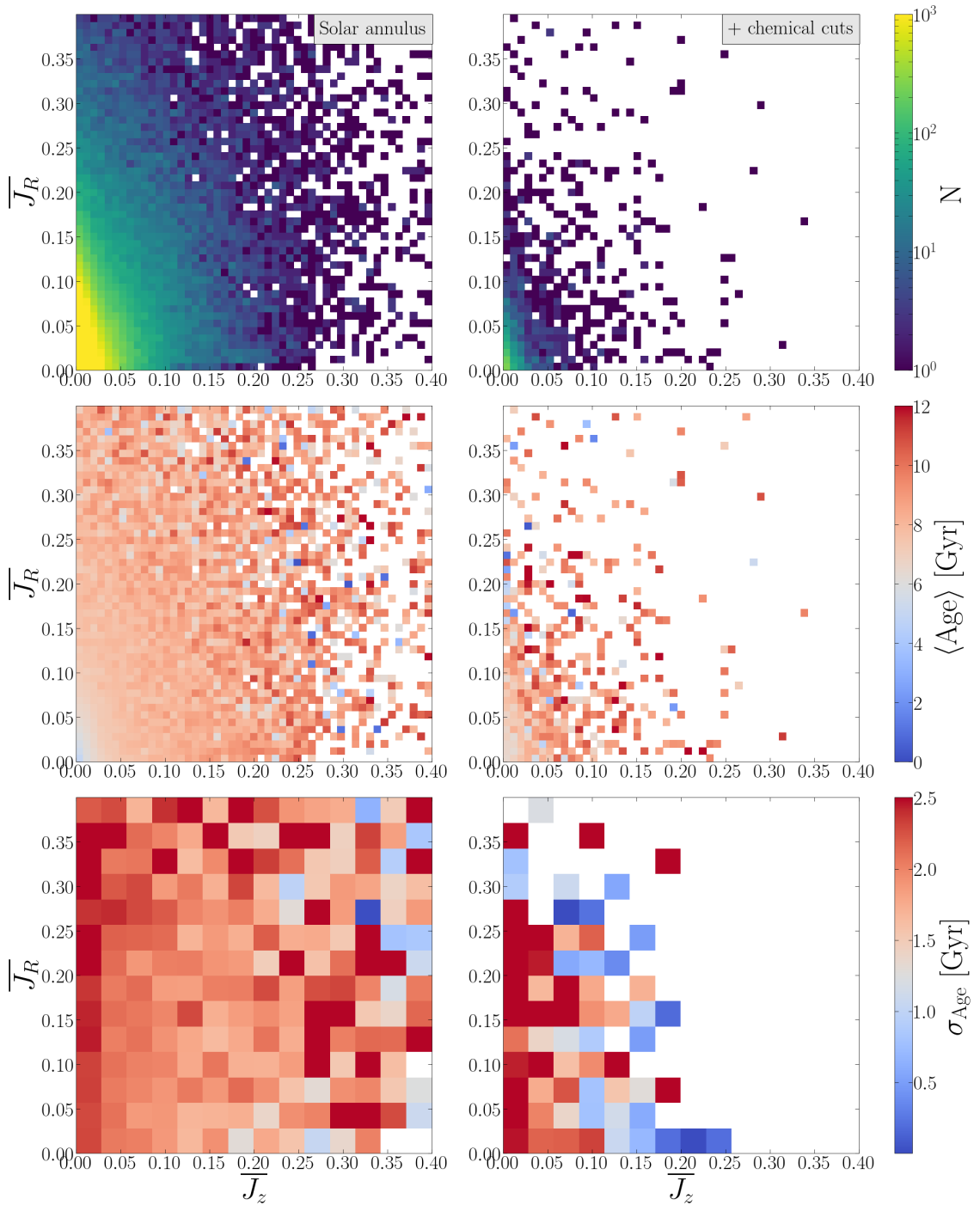
Figure 6.8: Same as Figure 6.6 but in the $\overline{J_z} - \overline{J_R}$ action space.
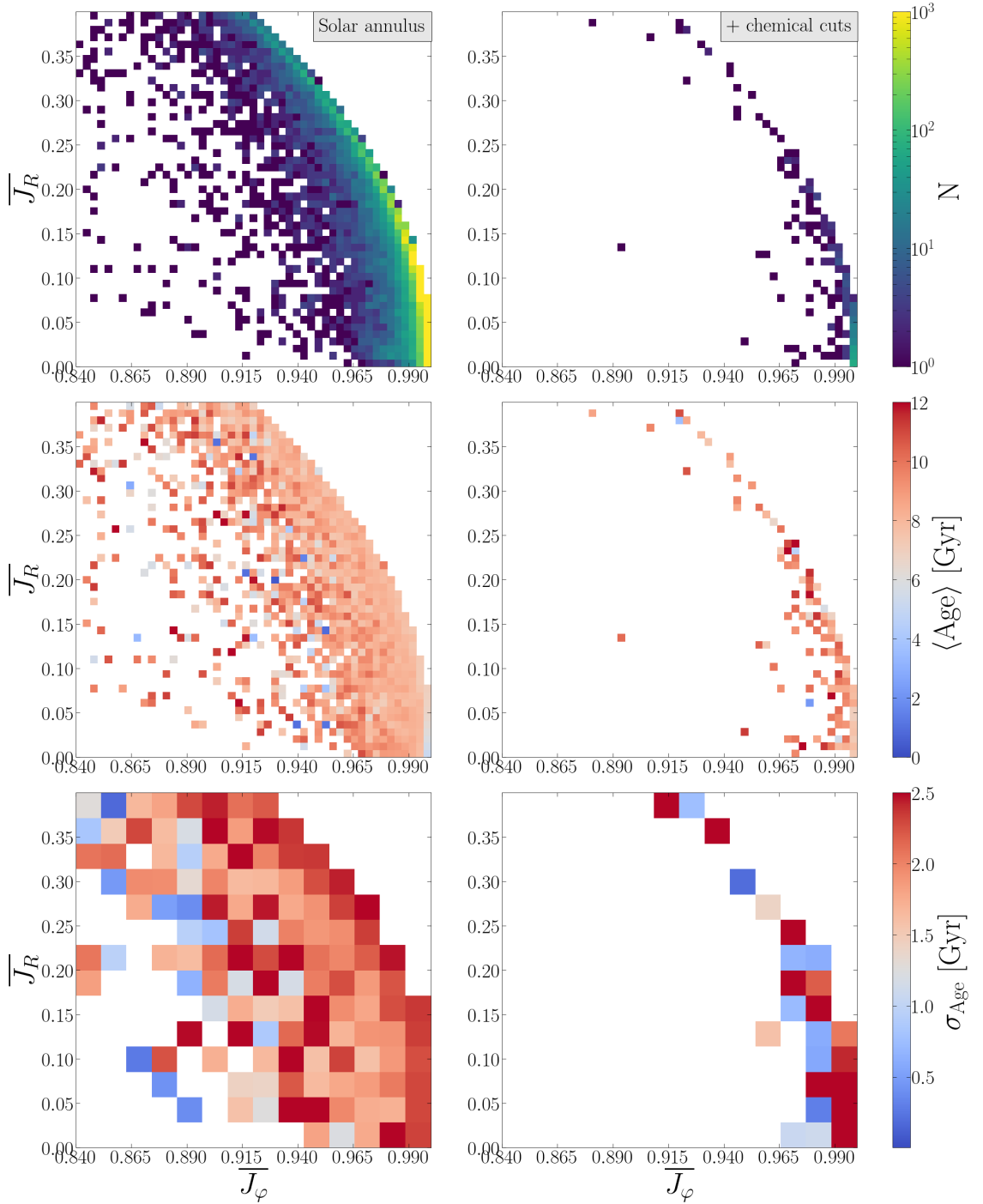
Figure 6.9: Distributions in $\overline{J_\varphi} - \overline{J_R}$ action space for stars in the "+Solar annulus" sample (left) and in the chemical cut of the "+Solar annulus" sample (right). The chemical cut is based on the WM4 model which we define in Figure 6.2 (solid orange polygon). The distributions are of the stellar number density (top), the mean stellar age (middle), and the standard deviation of the age (bottom).
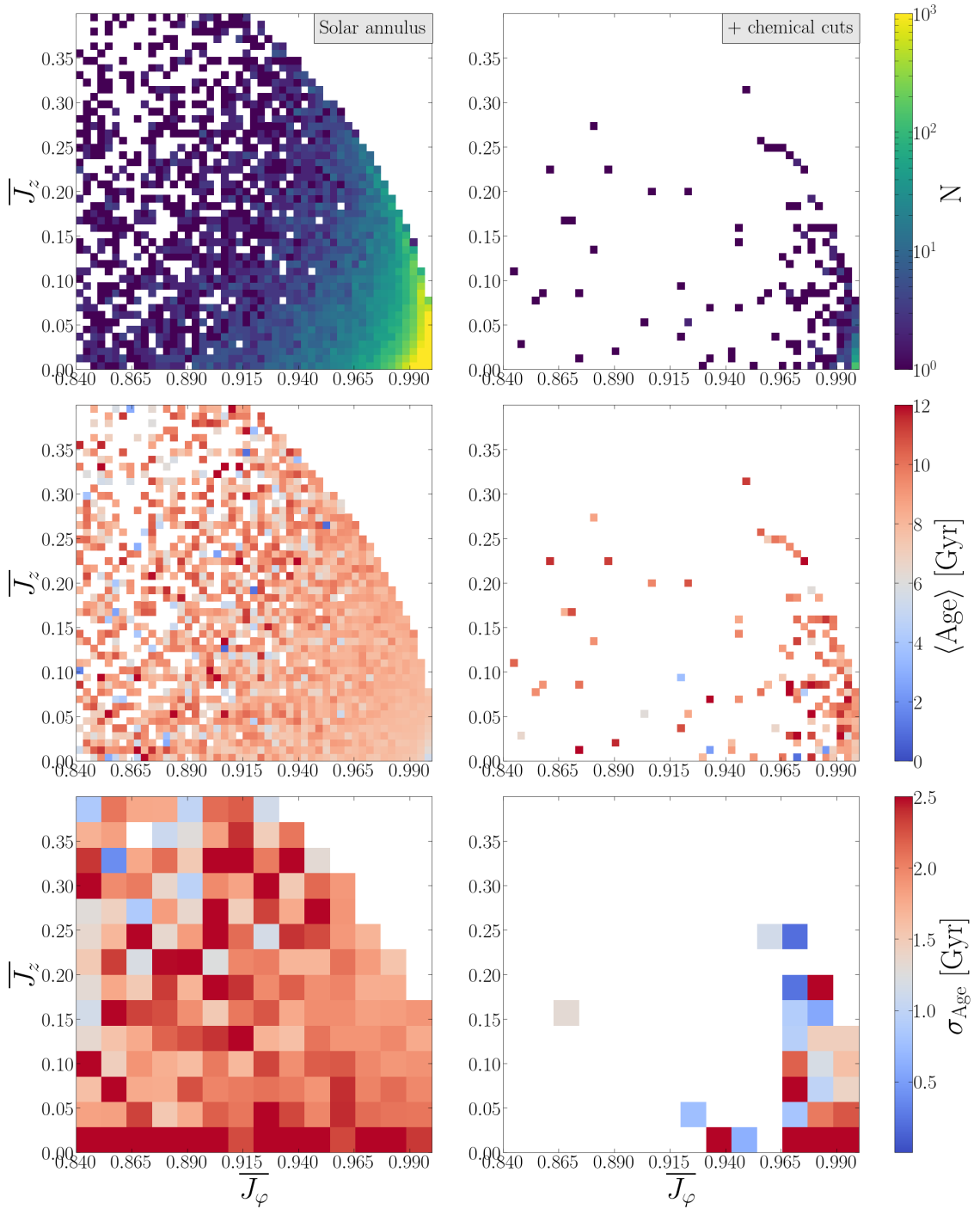
Figure 6.10: Same as Figure 6.9 but in the $\overline{J_\varphi} - \overline{J_z}$ action space.
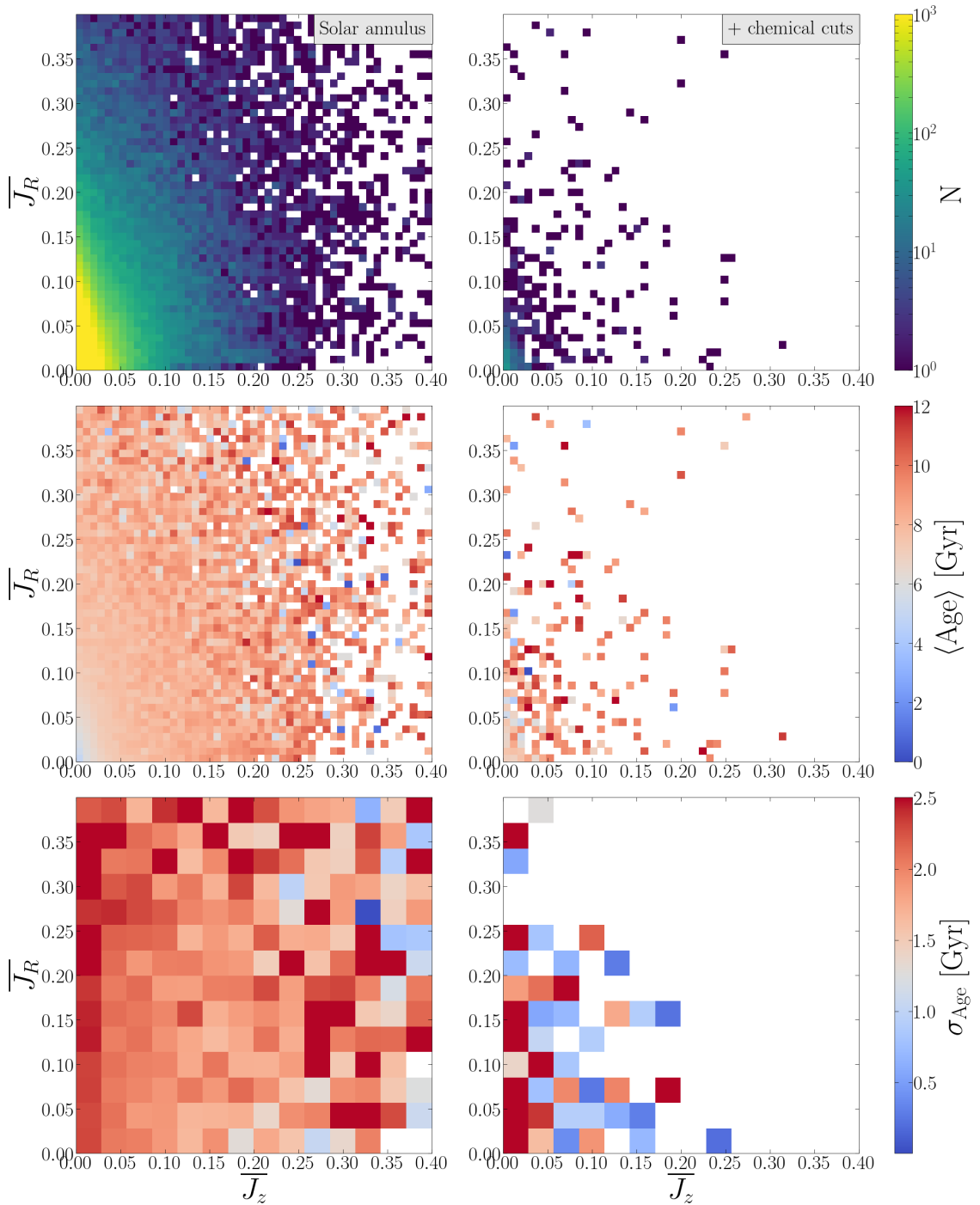
Figure 6.11: Same as Figure 6.9 but in the $\overline{J_z} - \overline{J_R}$ action space.

The WM2-4 chemical cuts are applied to the "+Solar annulus" sample and we examine the different action spaces in the SD18 dataset. Figures 6.3 - 6.11 are similar to the action space figures in Chapter 5 with the "+Solar annulus" and compounding chemical cuts in the left and right columns, respectively. The first rows in the figures show the number density distributions, and we observe similar structures in all action spaces, as seen in the WM2-4 models. However, the ⟨age⟩ distributions in the middle row show that our sample is mostly of old stars, i.e. age $\geq 7\,$Gyr. Finally, the σ_{age} distributions agree with the results shown in Chapter 5: the regions where we expect higher warp star purity have in general lower age dispersions compared to the rest of the distribution. We observed similar structures in the action spaces of the SD18 sample and will, therefore, apply the full warp filters in the following section.

6.3   Warp star candidates

In Figures 6.12 - 6.14 we present the warp star candidates in the SD18 dataset obtained via the warp filters of the WM2-4 models, respectively. Each column represents a different sample of the SD18 dataset onto which we apply the warp filters. The left column represents the "+Solar annulus" base sample, while the middle and right columns represent the base sample with cuts on the age uncertainties of $\sigma_{\mathrm{age}} \leq 20\%$ and $\sigma_{\mathrm{age}} \leq 2\,$Gyr, respectively. The first rows show the number density distributions of the samples with the overlaid warp star candidates (green triangles) in chemical space. The solid coloured polygons represent the definitive chemical cuts of the respective models. Prograde halo stars could be a significant contaminating factor in our warp filters as they are vertically hot and metal-poor (Posti et al. 2018). To account for this possible contamination we select retrograde ($\overline{J_\varphi} < 0$) stars, calculate their orbital eccentricities, e, in the McMillan (2017) MW potential using AGAMA, and select those on near-circular ($e \leq 0.4$) orbits. One
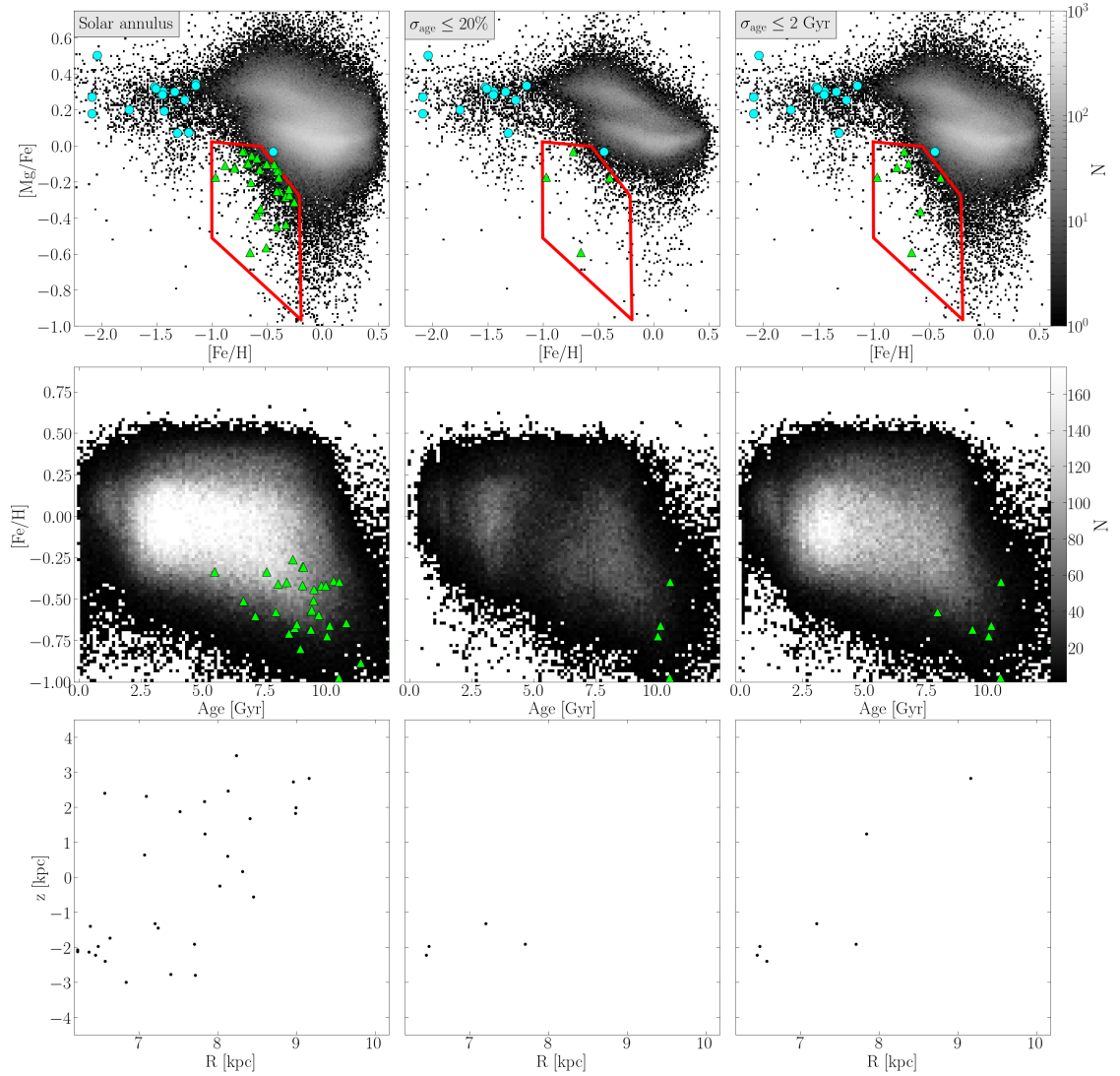
Figure 6.12: Distributions of warp star candidates in the base sample and subsequent quality cuts indicated in the top left corner (see Figure 6.1). Top: chemical space number density distribution (colour) with overlaid warp star candidates (green triangles). The cyan circles represent retrograde stars on near-circular orbits to account for possible contamination by halo stars. The solid polygon (red) represents the region of chemical space in the WM2 model where the warp star purity is greater than 80% (see Figures 5.10 and 6.2). Middle: number density distribution of stars in the Solar annulus in the age-metallicity distribution (AMR) with overlaid warp star candidates (green triangles). Bottom: locations of the warp star candidates in Galactocentric coordinates in the $R - z$ plane.
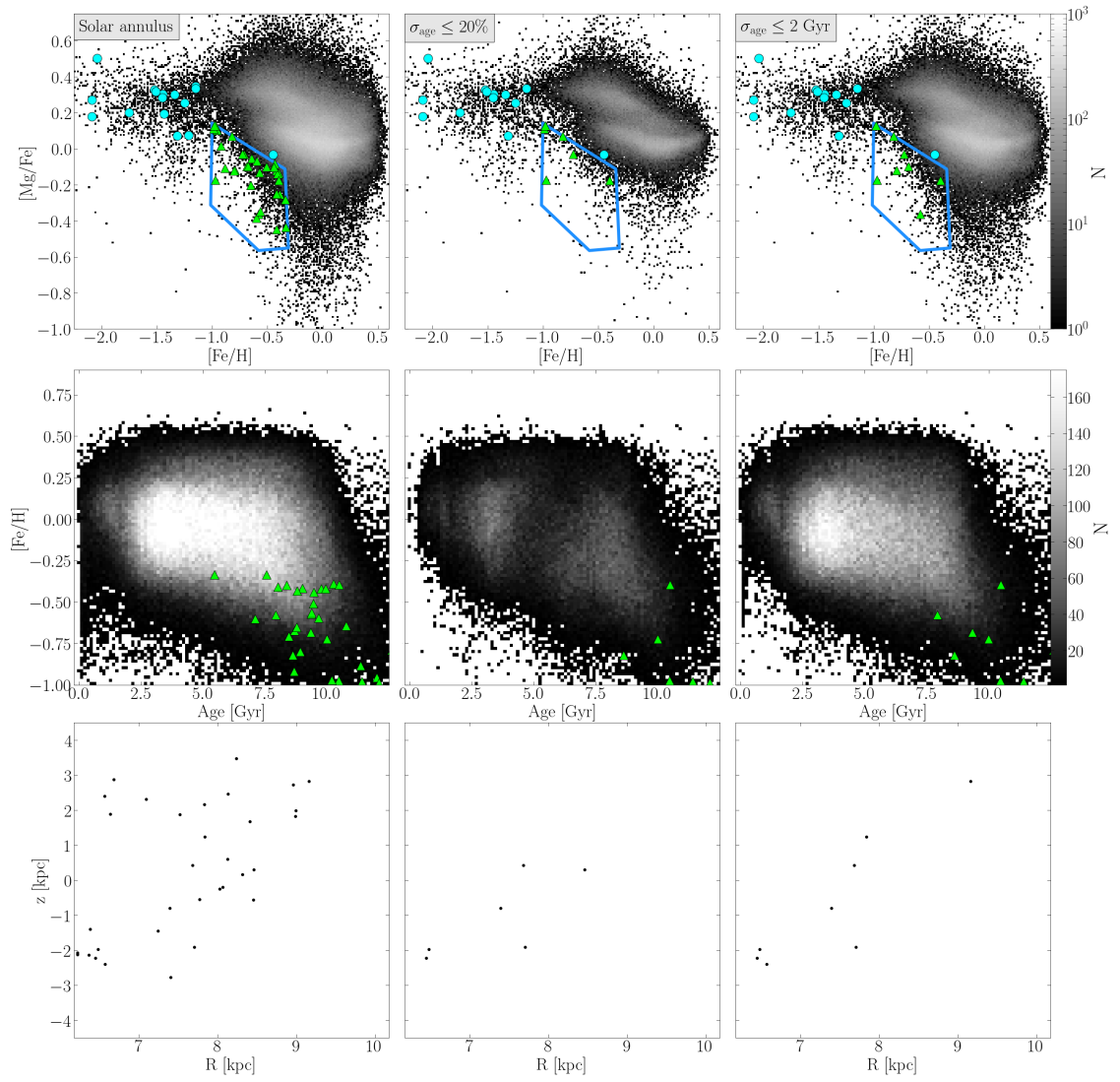
Figure 6.13: Same as Figure 6.12 but using the chemical cut from the WM3 model (blue solid polygon in Figure 6.2).
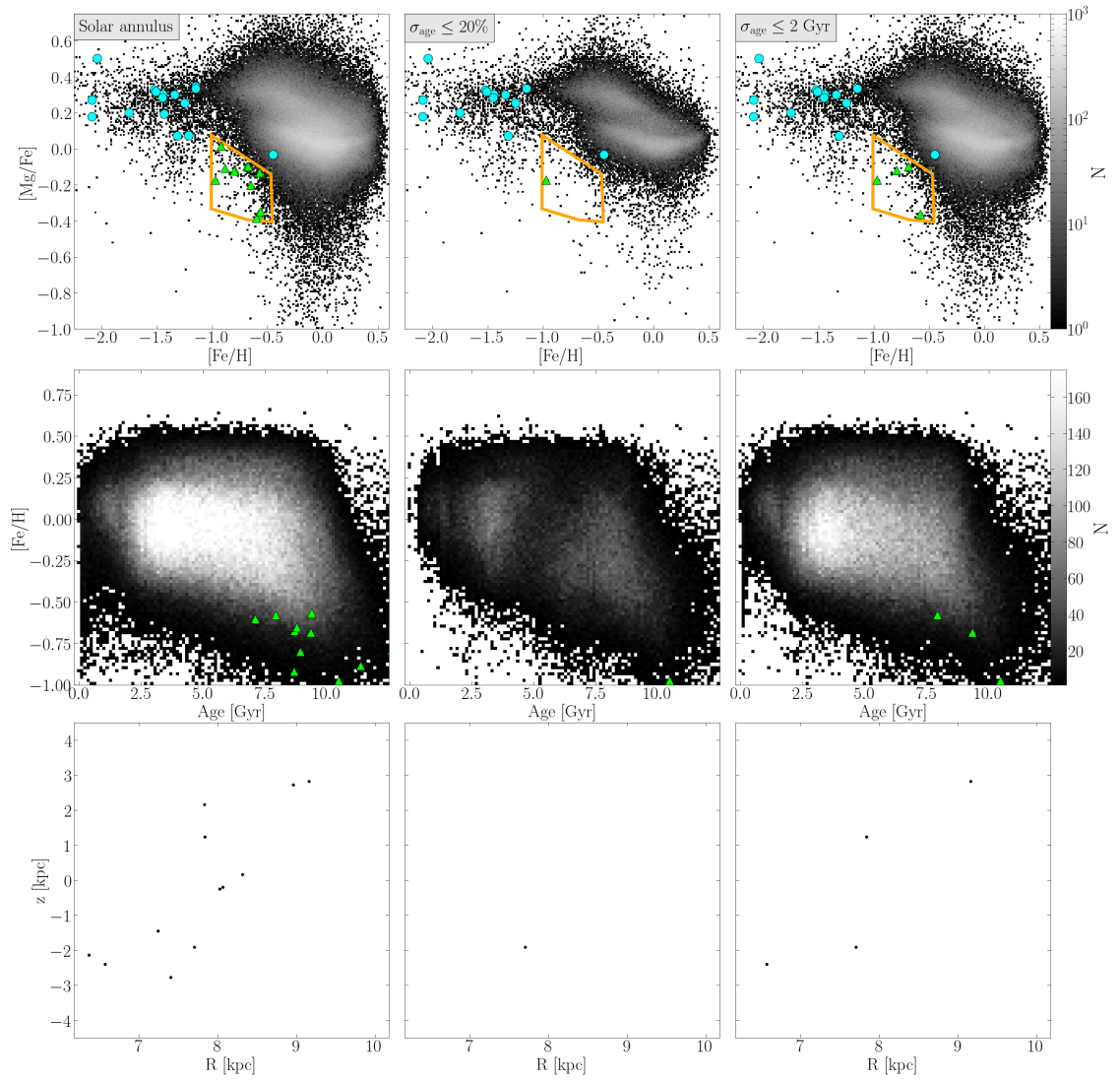
Figure 6.14: Same as Figure 6.12 but using the chemical cut from the WM4 model (orange solid polygon in Figure 6.2).

can assume that a similar amount of halo stars could be on prograde near-circular orbits. We overlay these contaminants in the chemical space (cyan points) and observe that they are outside of our chemical cuts, therefore they are unlikely to affect the purity of our sample.

The middle rows show the number density distribution of the samples in the AMR with the warp star candidates overlaid on top of them (green triangles). We observe a weak but negative AMR in the warp star candidates as they seemingly trace the metal-poor tail of the AMR. Finally, the bottom rows show the location of the warp star candidates in Galactocentric coordinates in the $R - z$ plane. We observe that our warp star candidates appear to be, on average, away from the midplane. In Table 6.1 we provide the full breakdown of the stellar counts and North-South asymmetries in our samples, including the applied warp filters. We consider the warp filters from the WM3 and WM4 models to be the least and most conservative in the detection of warp star candidates, respectively. When accounting for stars with $\sigma_{\mathrm{age}} \leq 2\,\mathrm{Gyr}$ we find 7, 8, and 4 warp star candidates in the WM2, WM3, and WM4 filters, respectively.

Within their dataset, SD18 defined two subsamples of stars with precise age estimates, turn-off and giant stars, which they estimate have uncertainties of $20\% - 30\%$ and $15\% - 20\%$, respectively. For turn-off stars, the precision comes from the combination of the parallaxes and spectroscopic metallicities breaking the metallicity-age degeneracy (Howes et al. 2019). In the giant stars, the precision is due to SD18's employed spectroscopic mass estimates combined with GAIA parallaxes which further constrained the luminosity and, therefore, the age estimates. Both of these subsamples compose $80 - 100\%$ of our warp star candidates, with giant stars being the majority. Turn-off stars only become prevalent when the WM3 warp filter is applied to the SD18 dataset and make up $20 - 50\%$ of the candidates.

Samples	Catalogue count			North/South asymmetry		
	APOGEE	GALAH	Total	APOGEE	GALAH	Total
Crossmatch	202904	258004	460908	2.2	0.8	1.2
+ Error cuts	153808	237478	391286	2.6	0.8	1.2
+ Solar annulus (base sample)	115490	224376	339866	3.3	0.8	1.2
+ Action filter	3162	3513	6675	6.7	0.5	1.5
+ Chemical filter (WM2)	3	28	31	-	0.7	1.9
$\sigma_t \leq 20\%$/	0	4	4	-	0.0	0.0
$\sigma_t \leq 2$ Gyr	1	6	7	-	0.2	0.4
+ Chemical filter (WM3)	3	30	33	-	1.0	1.2
$\sigma_t \leq 20\%$/	0	6	6	-	0.5	0.5
$\sigma_t \leq 2$ Gyr	1	7	8	-	0.4	0.6
+ Chemical filter (WM4)	1	11	12	-	0.6	0.7
$\sigma_t \leq 20\%$/	0	1	1	-	0.0	0.0
$\sigma_t \leq 2$ Gyr	1	3	4	-	0.5	1

Table 6.1: The stellar counts and North-South asymmetry values, *i.e.* $N_{z>0}/N_{z<0}$, in the spectroscopic surveys and their compounding cuts. Each warp filter from Chapter 5 is represented in a separate row with compounding cuts based on the age uncertainties.

CHAPTER 6

6.4 Conclusions

We examined the SD18 dataset and observed trends in the chemical and action spaces that hint at possible warp star contamination in the Solar annulus. In the chemical space of the SD18 dataset, we observe that the chemical cuts of the WM2-4 models appear to outline the region immediately below the main distribution. In action space, we observe lower than average σ_{age} distributions in the regions where a high warp star purity is expected.

We apply the warped filters of the WM2-4 models (Chapter 5) to the SD18 dataset and produce samples of warp star candidates. Depending on the warped filter, the samples that do not account for age uncertainties (raw samples) produce 12–33 warp star candidates, while those that do only produce 4–8 candidates. The smallest samples of candidates are produced when using the warp filter of WM4, a model which has a dissipating low-amplitude warp and the highest star formation threshold in our warped models. When the warp star candidates in the raw samples are overlaid on the AMR of the SD18 dataset, we observe a negative trend that is in partial agreement with the simulations. In the $R - z$ plane, the warp star candidates are concentrated away from the midplane, similarly to the warp stars in Chapters 3 and 5. However, the warp star candidates in the SD18 dataset are more concentrated in the $6 \leq R/\mathrm{kpc} \leq 8$ range due to the observational footprints of the spectroscopic surveys.

With the upcoming release of GAIA DR3 and larger-scale ground-based spectroscopic surveys, the detection of larger samples of warp star candidates could be possible. The larger samples of candidates could, in turn, provide further insight into the SFH of the Galactic warp. At the current state of our analysis, we can only detect what appears to be the earliest warp population that had enough time to settle into the disc and migrate into the Solar annulus 3.

Chapter 7

Conclusions and future prospects

Research concerning changes in the vertical structure of galactic discs, including the Milky Way (MW), is often focused on satellite mergers (Bailin 2003; Weinberg & Blitz 2006; Kalberla et al. 2007a; Purcell et al. 2011a; Gómez et al. 2013a; Laporte et al. 2018a,d; Petersen & Peñarrubia 2021). A mechanism that has not been researched as extensively is the warp formation via the accretion of cold misaligned gas. With the continuous accretion of cold gas, the warp is long-lasting, not episodic. Additionally, if star formation were taking place in the accreting gas, the dynamical properties and low-metallicity of the gas would be imprinted on the resulting stellar populations. Roškar et al. (2010a) studied warps in a cosmological simulation of a MW-like galaxy and observed stellar populations not only forming in the warp but also settling and populating the thick disc. These warp stars can serve as a tracer population from which we can infer the star formation history of the warp. This thesis has considered the impact galactic warps have on the vertical structure of discs via the accreting gas directly perturbing the disc and the settling and migration of stars born in the warp. The work in this thesis provides insight into the warp's role in the evolution of galaxies and a framework to study the Galactic warp's star formation history (SFH) and influence on the vertical structure of the disc.

CHAPTER 7

7.1 Bending waves

In Chapter 4 we investigated the bending waves that manifest in warped (WM1) and unwarped (UM) models and the differences between them. By performing spectral analysis on the density and vertical displacement, we extracted the dominant frequencies of the $m = 2$ density and $m = 1$ bending waves. We observe an overall agreement with the WKB approximation as both models have retrograde low-frequency bending waves throughout their evolution. The difference between the models manifests in the persistence of prograde bending waves in the warped model. In the WKB approximation, these waves are expected to weaken and disappear as a result of differential rotation. However, the presence of a continuous perturbing force in the form of accreting gas excites and injects significant power into both prograde and retrograde $m = 1$ waves. In WM1 the prograd e $m = 1$ bending waves appear to be modulated by the spiral density waves as we observe ripples emanating from the main retrograde $m = 1$ signal in the azimuthal $\langle z \rangle$ distributions. The prograde bending waves in the UM model are short-lived (~ 1 Gyr) and have smaller amplitudes, however, we still observe a coupling with the $m = 2$ spiral. The azimuthal $\langle z \rangle$ distributions in the UM present a superposition of different signals shifting from one to another, with the ripples being more dispersed and harder to distinguish. These discrepancies imply that the driving force behind the bending waves in isolated galaxies is not strong enough to support and amplify the prograde $m = 1$ bending waves, unlike the continuous inflow of misaligned gas.

The effect bending waves have on a disc's vertical structure was further investigated in simulated Solar neighbourhoods. In the warped model, we demonstrated that the positive slopes in the L_z vs v_z relation are not due to a direct imprint of the warp but are instead a consequence of bending waves. We confirmed this by orientating the disc in the warps inertial frame and observing a wave-like shift in the azimuthal distribution of the L_z vs v_z slope. If the warp were the direct cause of the

positive slopes, we would expect the change in the azimuthal slope distribution to occur similarly to a standing wave. The unwarped model presents noticeably flatter slopes with no distinct wave-like properties, however, a weak azimuthal variation is observed. The disparity in slope amplitudes is most likely due to the significant (factor of 4) difference in bending wave amplitudes between the warped and unwarped models. Lastly, when comparing the resulting slopes in the simulated Solar neighbourhood samples, we observed a strong similarity with the slope observed in the MW (Schönrich & Dehnen 2018a; Huang et al. 2018b).

7.2 Warp stars

7.2.1 Simulated warp stars

In Chapter 3 we considered the formation and settling of stellar populations that formed in the warp (warp stars) of WM2. We demonstrated that settling proceeds in two stages: reorientation (tilting) and phase mixing in angular momentum space. The reorientation stage is rapid and occurs within the first ~ 1 Gyr after a warp star forms. We performed this analysis on mono-age warp populations and discovered that the tilting time ranges from 0.25 to 1.75 Gyr. The phase mixing stage commences alongside the reorientation but is significantly slower. As warp stars form, they begin phase mixing in angular momentum space via differential precession and become fully phase-mixed after ~ 6 Gyr. The settling process is also accompanied by inward migration. We demonstrate that almost all settled warp stars are on near-circular orbits, therefore warp stars can reach the Solar annulus via radial migration. We find that warp stars are a possible tracer population that can be observed in the MW.

In Chapter 5, we investigated the dynamical and chemical properties of warp stars in three warped models (WM2-4). By comparing the distributions of warp

populations in chemical and normalised action spaces, we showed that warp stars stand out above all other stars. In chemical space, warp populations are distinctly lower in both α-element abundances and metallicity, occupying a chemical space region below the main thin and thick disc distributions in all models. This chemical distribution agrees with our initial hypothesis as warp stars form in low metallicity accreting gas, which experiences lower contamination via galactic outflows. The warp star purity distribution, *i.e.* ratio between the warp star and total star counts, in chemical space is mostly unchanged even with artificial abundance uncertainties. We based the uncertainties on the mean abundance errors in the GALAH and APOGEE spectroscopic surveys to simulate observations in the MW. As a result, we produced cuts in the chemical spaces of each model that maintain a warp star purity $\geq 80\%$.

The action space distributions did not produce any significant results, however, the application of the aforementioned chemical cuts uncovered regions of high warp star purity. We similarly produce cuts in action space based on the regions with high warp star purity. The actions cuts reflect the results from Chapter 3 as most warp stars are observed with high vertical action (thick disc) and relatively small radial action (near-circular orbits) values.

By examining the warp star distributions in the chemical and action spaces of WM2-4, we developed cuts in the respective spaces that can be applied to the Solar annulus in the MW. The different properties of each model provide a range of chemical space cuts that can account for different star formation thresholds and warp evolutionary histories (growing and waning warps).

7.2.2   Warp star candidates in the MW

In Chapter 6 we applied the warp filters produced in Chapter 5 to an observational sample in the Solar annulus. The sample consists of the Sanders & Das (2018a)

dataset cross-matched with the GALAH and APOGEE spectroscopic surveys, referred to as the SD18 dataset. The dataset contains 6D coordinates, elemental abundances, actions, and age estimates for $\sim 4.6 \times 10^5$ sources. By applying the warp filters from each warped model on the SD18 dataset, we produced samples of warp star candidates in the MW. The stellar counts in the these samples range from 33 (WM3) to 12 (WM4) without accounting for age uncertainties and from 8 (WM3) to 4 (WM4) for $\sigma_{\text{age}} \leq 2\,\text{Gyr}$. We observe that all warp star candidate samples are skewed towards older populations (age$\geq 5\,\text{Gyr}$), with the natural explanation being the large relative uncertainties in younger ages. However, the skew towards older ages could also result from a waning warp, demonstrated in our warped models. As a result, we produced the first samples of warp star candidates in the Solar annulus, which, while statistically small, could imply that the warp of the MW has been present throughout our Galaxy's evolution.

7.3 Future prospects

7.3.1 Phase-space spiral

One of the key limitations in contemporary N-body+SPH models, such as the ones used throughout this thesis, is resolution. Chapter 4 showed that bending waves of significant amplitude are generated by accreting cold gas. A logical continuation of our work, with the relatively recent discovery of the GAIA phase-space spiral, is determining if the bending waves produced by the warp can give rise to similar phase-space structures. At present resolution, the detection of such structures in our models is unlikely, so future work will aim to improve the mass resolution of N-body+SPH models.

More work must be carried out to understand the bending waves that emerge as a result of misaligned gas accretion, which includes isolating these waves in the

disc and determining their direction of propagation. By further investigating these bending waves, the role warps have in galactic evolution can be understood in greater detail.

7.3.2 Gaia DR3 and future surveys

In Chapters 3 and 5 we described the settling process and unique properties of warp stars, respectively. By determining the cuts in chemical and normalised action spaces, in Chapter 6 we were able to produce a small sample of warp star candidates in the Solar annulus of the MW. Our sample's limited size comes from multiple compounding issues that could be addressed in the future and produce a more statistically significant sample of warp star candidates. Firstly, current large-scale catalogues such as GAIA are limited to astrometric data within a small volume ($1/\pi \leq 3\,\mathrm{kpc}$) to avoid significant uncertainties (Ting & Rix 2019). Secondly, the latest data release of the GAIA mission (DR2) produced only $\sim 7 \times 10^6$ stars with radial velocities, which along with a lack of elemental abundance data significantly limited our chemodynamical analysis. The Sanders & Das (2018a) dataset partially alleviated these issues by providing age estimates for stars in a cross-match between GAIA DR2 and multiple spectroscopic surveys, however, the resulting sample produced a limited sample of $\sim 5 \times 10^5$ stars.

Further advances in the detection of warp star candidates can be achieved with the upcoming release of GAIA DR3, which is expected in early 2022. DR3 is expected to have a significantly larger sample of stars with full 6D coordinates. Furthermore, with the addition of cross-matches with current and upcoming ground-based spectroscopic surveys, we can obtain further insight into the star formation history of the Galactic warp. Lastly, the inclusion of machine learning algorithms in our analysis of warped simulations can improve the detection of warp star candidates by better defining their unique chemodynamical properties.

Bibliography

Aarseth, S. J. 1963, *Mon. Not. Roy. Astron. Soc.*, 126, 223

Abolfathi, B., Aguado, D. S., Aguilar, G., et al. 2018, *Astrophys. J. Supple.*, 235, 42

Adams, S. M., Kochanek, C. S., Beacom, J. F., Vagins, M. R., & Stanek, K. Z. 2013, *Astrophys. J.*, 778, 164

Adibekyan, V. Z., Delgado Mena, E., Sousa, S. G., et al. 2012, *Astron. Astrophys.*, 547, A36

Agertz, O., Teyssier, R., & Moore, B. 2009, *Mon. Not. Roy. Astron. Soc.*, 397, L64

Anders, F., Chiappini, C., Santiago, B. X., et al. 2014, *Astron. Astrophys.*, 564, A115

Anderson, M. E. & Bregman, J. N. 2010, *Astrophys. J.*, 714, 320

Ann, H. B. & Park, J. C. 2006, *New Astron.*, 11, 293

Antoja, T., Helmi, A., Romero-Gómez, M., et al. 2018, *Nature*, 561, 360

Antoja, T., Helmi, A., Romero-Gómez, M., et al. 2018, Nature, 561, 360

Appel, A. W. 1985, SIAM Journal on Scientific and Statistical Computing, 6, 85

Arp, H. 1964, *Astrophys. J.*, 139, 1045

Aumer, M. & White, S. D. M. 2013, *Mon. Not. Roy. Astron. Soc.*, 428, 1055

Aumer, M., White, S. D. M., Naab, T., & Scannapieco, C. 2013, *Mon. Not. Roy. Astron. Soc.*, 434, 3142

Azzalini, A. 1985, Scandinavian Journal of Statistics, 12, 171

Bailer-Jones, C. A. L., Rybizki, J., Fouesneau, M., Demleitner, M., & Andrae, R. 2020, arXiv e-prints, arXiv:2012.05220

Bailer-Jones, C. A. L., Rybizki, J., Fouesneau, M., Mantelet, G., & Andrae, R. 2018, *Astron. J.*, 156, 58

Bailin, J. 2003, *Astrophys. J. Letters*, 583, L79

Barnes, J. & Hut, P. 1986, *Nature*, 324, 446

Battaglia, G., Fraternali, F., Oosterloo, T., & Sancisi, R. 2006, *Astron. Astrophys.*, 447, 49

Bell, E. F. & de Jong, R. S. 2000, *Mon. Not. Roy. Astron. Soc.*, 312, 497

Bennett, M. & Bovy, J. 2021, *Mon. Not. Roy. Astron. Soc.*, 503, 376

Beraldo e Silva, L., de Siqueira Pedra, W., & Valluri, M. 2019a, *Astrophys. J.*, 872, 20

Beraldo e Silva, L., de Siqueira Pedra, W., Valluri, M., Sodré, L., & Bru, J.-B. 2019b, *Astrophys. J.*, 870, 128

Beraldo e Silva, L., Debattista, V. P., Khachaturyants, T., & Nidever, D. 2020a, *Mon. Not. Roy. Astron. Soc.*, 492, 4716

Beraldo e Silva, L., Debattista, V. P., Nidever, D., Amarante, J., & Garver, B. 2020b, arXiv e-prints, arXiv:2009.03346

Bernard, E. J., Ferguson, A. M. N., Chapman, S. C., et al. 2015, *Mon. Not. Roy. Astron. Soc.*, 453, L113

Biau, G. & Devroye, L. 2015, Lectures on the Nearest Neighbor Method, 1st edn. (Springer Publishing Company, Incorporated)

Binney, J. 1992, *Ann. Rev. Astron, Astrophys.*, 30, 51

Binney, J. 2012, *Mon. Not. Roy. Astron. Soc.*, 426, 1324

Binney, J., Dehnen, W., & Bertelli, G. 2000a, *Mon. Not. Roy. Astron. Soc.*, 318, 658

Binney, J., Dehnen, W., & Bertelli, G. 2000b, *Mon. Not. Roy. Astron. Soc.*, 318, 658

Binney, J., Gerhard, O., & Spergel, D. 1997, *Mon. Not. Roy. Astron. Soc.*, 288, 365

Binney, J. & May, A. 1986, *Mon. Not. Roy. Astron. Soc.*, 218, 743

Binney, J. & Schönrich, R. 2018, *Mon. Not. Roy. Astron. Soc.*, 481, 1501

Binney, J. & Tremaine, S. 2008a, Galactic Dynamics: Second Edition

Binney, J. & Tremaine, S. 2008b, Galactic Dynamics: Second Edition

Bland-Hawthorn, J. & Gerhard, O. 2016, *Ann. Rev. Astron, Astrophys.*, 54, 529

Bland-Hawthorn, J., Sharma, S., Tepper-Garcia, T., et al. 2019, *Mon. Not. Roy. Astron. Soc.*, 486, 1167

Bland-Hawthorn, J. & Tepper-García, T. 2021, *Mon. Not. Roy. Astron. Soc.*, 504, 3168

Block, D. L. & Wainscoat, R. J. 1991, *Nature*, 353, 48

Bosma, A. 1981a, *Astron. J.*, 86, 1791

Bosma, A. 1981b, *Astron. J.*, 86, 1825

Bosma, A. 1991, in Warped Disks and Inclined Rings around Galaxies, 181

Bovy, J., Rix, H.-W., & Hogg, D. W. 2012a, *Astrophys. J.*, 751, 131

Bovy, J., Rix, H.-W., Hogg, D. W., et al. 2012b, *Astrophys. J.*, 755, 115

Bovy, J., Rix, H.-W., Liu, C., et al. 2012c, *Astrophys. J.*, 753, 148

Bovy, J., Rix, H.-W., Schlafly, E. F., et al. 2016, *Astrophys. J.*, 823, 30

Bregman, J. N. & Lloyd-Davies, E. J. 2007, *Astrophys. J.*, 669, 990

Briggs, F. H. 1990a, *Astrophys. J.*, 352, 15

Briggs, F. H. 1990b, *Astrophys. J.*, 352, 15

Brown, A. G. A. 2021, arXiv e-prints, arXiv:2102.11712

Buder, S., Asplund, M., Duong, L., et al. 2018, *Mon. Not. Roy. Astron. Soc.*, 478, 4513

Buder, S., Sharma, S., Kos, J., et al. 2020, arXiv e-prints, arXiv:2011.02505

Bullock, J. S., Dekel, A., Kolatt, T. S., et al. 2001, *Astrophys. J.*, 555, 240

Burbidge, E. M., Burbidge, G. R., Fowler, W. A., & Hoyle, F. 1957, Reviews of Modern Physics, 29, 547

Burke, B. F. 1957, *Astron. J.*, 62, 90

Burton, W. B. 1988, The structure of our Galaxy derived from observations of neutral hydrogen., ed. K. I. Kellermann & G. L. Verschuur, 295–358

Buta, R. J., Byrd, G. G., & Freeman, T. 2003, *Astron. J.*, 125, 634

Buta, R. J., Sheth, K., Athanassoula, E., et al. 2015, *Astrophys. J. Supple.*, 217, 32

Cappellari, M., Emsellem, E., Krajnović, D., et al. 2011, *Mon. Not. Roy. Astron. Soc.*, 416, 1680

Casagrande, L., Silva Aguirre, V., Schlesinger, K. J., et al. 2016, *Mon. Not. Roy. Astron. Soc.*, 455, 987

Casey, A. R., Hawkins, K., Hogg, D. W., et al. 2017, *Astrophys. J.*, 840, 59

Casuso, E. & Beckman, J. E. 2004, *Astron. Astrophys.*, 419, 181

Chen, X., Wang, S., Deng, L., et al. 2019a, Nature Astronomy, 3, 320

Chen, X., Wang, S., Deng, L., et al. 2019b, Nature Astronomy, 3, 320

Chen, X., Wang, S., Deng, L., de Grijs, R., & Yang, M. 2018a, *Astrophys. J. Supple.*, 237, 28

Chen, X., Wang, S., Deng, L., de Grijs, R., & Yang, M. 2018b, *Astrophys. J. Supple.*, 237, 28

Cheng, J. Y., Rockosi, C. M., Morrison, H. L., et al. 2012, *Astrophys. J.*, 752, 51

Chequers, M. H. & Widrow, L. M. 2017, *Mon. Not. Roy. Astron. Soc.*, 472, 2751

Chequers, M. H., Widrow, L. M., & Darling, K. 2018, *Mon. Not. Roy. Astron. Soc.*, 480, 4244

Chevalier, R. A. 1974, *Astrophys. J.*, 188, 501

Chiappini, C., Matteucci, F., & Gratton, R. 1997, *Astrophys. J.*, 477, 765

Cioffi, D. F., McKee, C. F., & Bertschinger, E. 1988, *Astrophys. J.*, 334, 252

Cirasuolo, M., Afonso, J., Bender, R., et al. 2012, in Society of Photo-Optical Instrumentation Engineers (SPIE) Conference Series, Vol. 8446, Ground-based and Airborne Instrumentation for Astronomy IV, ed. I. S. McLean, S. K. Ramsay, & H. Takami, 84460S

Couch, W. J., Barger, A. J., Smail, I., Ellis, R. S., & Sharples, R. M. 1998, *Astrophys. J.*, 497, 188

Cropper, M., Katz, D., Sartoretti, P., et al. 2018, *Astron. Astrophys.*, 616, A5

Dale, D. A., Beltz-Mohrmann, G. D., Egan, A. A., et al. 2016, *Astron. J.*, 151, 4

Darling, K. & Widrow, L. M. 2019, *Mon. Not. Roy. Astron. Soc.*, 484, 1050

Das, P., Hawkins, K., & Jofré, P. 2020, *Mon. Not. Roy. Astron. Soc.*, 493, 5195

De Silva, G. M., Freeman, K. C., Bland-Hawthorn, J., et al. 2015, *Mon. Not. Roy. Astron. Soc.*, 449, 2604

de Vaucouleurs, G., de Vaucouleurs, A., Corwin, Herold G., J., et al. 1991, Third Reference Catalogue of Bright Galaxies

de Zeeuw, T. & Franx, M. 1991, *Ann. Rev. Astron, Astrophys.*, 29, 239

Debattista, V. P., Carollo, C. M., Mayer, L., & Moore, B. 2004, *Astrophys. J. Letters*, 604, L93

Debattista, V. P., Gonzalez, O. A., Sand erson, R. E., et al. 2019a, *Mon. Not. Roy. Astron. Soc.*, 485, 5073

Debattista, V. P., Gonzalez, O. A., Sanderson, R. E., et al. 2019b, *Mon. Not. Roy. Astron. Soc.*, 485, 5073

Debattista, V. P. & Sellwood, J. A. 1999, *Astrophys. J. Letters*, 513, L107

Debattista, V. P., van den Bosch, F. C., Roškar, R., et al. 2015, *Mon. Not. Roy. Astron. Soc.*, 452, 4094

Dehnen, W. 1998a, *Astron. J.*, 115, 2384

Dehnen, W. 1998b, *Astron. J.*, 115, 2384

Dekel, A. & Silk, J. 1986, *Astrophys. J.*, 303, 39

Dressler, A. 1980, *Astrophys. J.*, 236, 351

Dressler, A., Oemler, Augustus, J., Couch, W. J., et al. 1997, *Astrophys. J.*, 490, 577

Drimmel, R. & Spergel, D. N. 2001, *Astrophys. J.*, 556, 181

Earp, S. W. F., Debattista, V. P., Macciò, A. V., & Cole, D. R. 2017, *Mon. Not. Roy. Astron. Soc.*, 469, 4095

Earp, S. W. F., Debattista, V. P., Macciò, A. V., et al. 2019, *Mon. Not. Roy. Astron. Soc.*, 488, 5728

Efremov, Y. N., Ivanov, G. R., & Nikolov, N. S. 1981, *Astrophys. Space Sci.*, 75, 407

Elmegreen, B. G. 1990, *Astrophys. J. Letters*, 361, L77

Elmegreen, D. M. & Elmegreen, B. G. 1982, *Mon. Not. Roy. Astron. Soc.*, 201, 1021

Erwin, P. & Debattista, V. P. 2016, *Astrophys. J. Letters*, 825, L30

Erwin, P. & Debattista, V. P. 2017, *Mon. Not. Roy. Astron. Soc.*, 468, 2058

Escala, I., Kirby, E. N., Gilbert, K. M., et al. 2020, *Astrophys. J.*, 902, 51

Faber, S. M. & Gallagher, J. S. 1976, *Astrophys. J.*, 204, 365

Fabricius, C., Luri, X., Arenou, F., et al. 2020, arXiv e-prints, arXiv:2012.06242

Feldmann, R. & Spolyar, D. 2014, MNRAS, 446, 1000

Fiteni, K., Caruana, J., Amarante, J. A. S., Debattista, V. P., & Beraldo e Silva, L. 2021, *Mon. Not. Roy. Astron. Soc.*, 503, 1418

Fontanot, F., De Lucia, G., Hirschmann, M., et al. 2017, *Mon. Not. Roy. Astron. Soc.*, 464, 3812

Foreman-Mackey, D., Hogg, D. W., Lang, D., & Goodman, J. 2013, PASP, 125, 306

Fox, A. J., Richter, P., Ashley, T., et al. 2019, *Astrophys. J.*, 884, 53

Frankel, N., Sanders, J., Rix, H.-W., Ting, Y.-S., & Ness, M. 2019, *Astrophys. J.*, 884, 99

Frankel, N., Sanders, J., Ting, Y.-S., & Rix, H.-W. 2020, *Astrophys. J.*, 896, 15

Fraternali, F. & Binney, J. J. 2008, *Mon. Not. Roy. Astron. Soc.*, 386, 935

Friske, J. K. S. & Schönrich, R. 2019, *Mon. Not. Roy. Astron. Soc.*, 490, 5414

Gaia Collaboration, Brown, A. G. A., Vallenari, A., et al. 2018a, *Astron. Astrophys.*, 616, A1

Gaia Collaboration, Brown, A. G. A., Vallenari, A., et al. 2018b, *Astron. Astrophys.*, 616, A1

Gaia Collaboration, Brown, A. G. A., Vallenari, A., et al. 2020, arXiv e-prints, arXiv:2012.01533

Gaia Collaboration, Brown, A. G. A., Vallenari, A., et al. 2016a, *Astron. Astrophys.*, 595, A2

Gaia Collaboration, Brown, A. G. A., Vallenari, A., et al. 2016b, *Astron. Astrophys.*, 595, A2

Gaia Collaboration, Katz, D., Antoja, T., et al. 2018c, *Astron. Astrophys.*, 616, A11

Gaia Collaboration, Prusti, T., de Bruijne, J. H. J., et al. 2016c, *Astron. Astrophys.*, 595, A1

Gaia Collaboration, Prusti, T., de Bruijne, J. H. J., et al. 2016d, *Astron. Astrophys.*, 595, A1

Gallagher, John S., I. & Hunter, D. A. 1984, *Ann. Rev. Astron, Astrophys.*, 22, 37

García-Ruiz, I., Kuijken, K., & Dubinski, J. 2002a, *Mon. Not. Roy. Astron. Soc.*, 337, 459

García-Ruiz, I., Sancisi, R., & Kuijken, K. 2002b, *Astron. Astrophys.*, 394, 769

García-Ruiz, I., Sancisi, R., & Kuijken, K. 2002c, *Astron. Astrophys.*, 394, 769

George, K. 2017, *Astron. Astrophys.*, 598, A45

Gilmore, G., Randich, S., Asplund, M., et al. 2012, The Messenger, 147, 25

Gingold, R. A. & Monaghan, J. J. 1977, *Mon. Not. Roy. Astron. Soc.*, 181, 375

Gómez, F. A., Minchev, I., O'Shea, B. W., et al. 2013a, *Mon. Not. Roy. Astron. Soc.*, 429, 159

Gómez, F. A., Minchev, I., O'Shea, B. W., et al. 2013b, *Mon. Not. Roy. Astron. Soc.*, 429, 159

Gómez, F. A., White, S. D. M., Grand, R. J. J., et al. 2017, *Mon. Not. Roy. Astron. Soc.*, 465, 3446

González-García, A. C., Oñorbe, J., Domínguez-Tenreiro, R., & Gómez-Flechoso, M. Á. 2009, *Astron. Astrophys.*, 497, 35

Graham, A. W. 2019, *Mon. Not. Roy. Astron. Soc.*, 487, 4995

Grand, R. J. J., Kawata, D., Belokurov, V., et al. 2020, *Mon. Not. Roy. Astron. Soc.*, 497, 1603

Grosbøl, P., Patsis, P. A., & Pompei, E. 2004, *Astron. Astrophys.*, 423, 849

Hartwick, F. D. A. 1976, *Astrophys. J.*, 209, 418

Hayden, M. R., Bovy, J., Holtzman, J. A., et al. 2015, *Astrophys. J.*, 808, 132

Hayden, M. R., Recio-Blanco, A., de Laverny, P., Mikolaitis, S., & Worley, C. C. 2017, *Astron. Astrophys.*, 608, L1

Haywood, M. 2001, *Mon. Not. Roy. Astron. Soc.*, 325, 1365

Helmi, A. 2020, *Ann. Rev. Astron, Astrophys.*, 58, 205

Helmi, A., Babusiaux, C., Koppelman, H. H., et al. 2018, *Nature*, 563, 85

Herbert-Fort, S., Zaritsky, D., Christlein, D., & Kannappan, S. J. 2010a, *Astrophys. J.*, 715, 902

Herbert-Fort, S., Zaritsky, D., Christlein, D., & Kannappan, S. J. 2010b, *Astrophys. J.*, 715, 902

Holmberg, E. 1941, *Astrophys. J.*, 94, 385

Holmberg, J., Nordström, B., & Andersen, J. 2009, *Astron. Astrophys.*, 501, 941

Holtzman, J. A., Hasselquist, S., Shetrone, M., et al. 2018, *Astron. J.*, 156, 125

Howes, L. M., Lindegren, L., Feltzing, S., Church, R. P., & Bensby, T. 2019, *Astron. Astrophys.*, 622, A27

Huang, Y., Schönrich, R., Liu, X. W., et al. 2018a, *Astrophys. J.*, 864, 129

Huang, Y., Schönrich, R., Liu, X. W., et al. 2018b, *Astrophys. J.*, 864, 129

Hubble, E. P. 1926, *Astrophys. J.*, 64, 321

Hunter, C. & Toomre, A. 1969a, *Astrophys. J.*, 155, 747

Hunter, C. & Toomre, A. 1969b, *Astrophys. J.*, 155, 747

Ibata, R., Chapman, S., Ferguson, A. M. N., et al. 2005, *Astrophys. J.*, 634, 287

Ibata, R. A. & Razoumov, A. O. 1998a, *Astron. Astrophys.*, 336, 130

Ibata, R. A. & Razoumov, A. O. 1998b, *Astron. Astrophys.*, 336, 130

Ibata, R. A., Wyse, R. F. G., Gilmore, G., Irwin, M. J., & Suntzeff, N. B. 1997, *Astron. J.*, 113, 634

Ideta, M., Hozumi, S., Tsuchiya, T., & Takizawa, M. 2000, *Mon. Not. Roy. Astron. Soc.*, 311, 733

Jeon, M., Kim, S. S., & Ann, H. B. 2009, *Astrophys. J.*, 696, 1899

Jiang, I.-G. & Binney, J. 1999, *Mon. Not. Roy. Astron. Soc.*, 303, L7

Jørgensen, B. R. & Lindegren, L. 2005, *Astron. Astrophys.*, 436, 127

Julian, W. H. & Toomre, A. 1966, *Astrophys. J.*, 146, 810

Jurić, M., Ivezić, Ž., Brooks, A., et al. 2008, *Astrophys. J.*, 673, 864

Kalberla, P. M. W., Dedes, L., Kerp, J., & Haud, U. 2007a, *Astron. Astrophys.*, 469, 511

Kalberla, P. M. W., Dedes, L., Kerp, J., & Haud, U. 2007b, *Astron. Astrophys.*, 469, 511

Kazantzidis, S., Zentner, A. R., Kravtsov, A. V., Bullock, J. S., & Debattista, V. P. 2009, *Astrophys. J.*, 700, 1896

Kennicutt, Robert C., J. 1998, *Astrophys. J.*, 498, 541

Kepner, J. V. 1999, *Astrophys. J.*, 520, 59

Kerr, F. J. 1957a, *Astron. J.*, 62, 93

Kerr, F. J. 1957b, *Astron. J.*, 62, 93

Khoperskov, S., Di Matteo, P., Gerhard, O., et al. 2019, *Astron. Astrophys.*, 622, L6

Kollatschny, W. & Dietrich, M. 1990, *Astron. Astrophys.*, 233, 333

Kollmeier, J. A., Zasowski, G., Rix, H.-W., et al. 2017, arXiv e-prints, arXiv:1711.03234

Kormendy, J. & Kennicutt, Robert C., J. 2004, *Ann. Rev. Astron, Astrophys.*, 42, 603

Kuijken, K. & Garcia-Ruiz, I. 2001, in Astronomical Society of the Pacific Conference Series, Vol. 230, Galaxy Disks and Disk Galaxies, ed. J. G. Funes & E. M. Corsini, 401–408

Kulsrud, R. M., Mark, J. W. K., & Caruso, A. 1971, *Astrophys. Space Sci.*, 14, 52

Kunder, A., Kordopatis, G., Steinmetz, M., et al. 2017, *Astron. J.*, 153, 75

Laporte, C. F. P., Gómez, F. A., Besla, G., Johnston, K. V., & Garavito-Camargo, N. 2018a, *Mon. Not. Roy. Astron. Soc.*, 473, 1218

Laporte, C. F. P., Gómez, F. A., Besla, G., Johnston, K. V., & Garavito-Camargo, N. 2018b, *Mon. Not. Roy. Astron. Soc.*, 473, 1218

Laporte, C. F. P., Gómez, F. A., Besla, G., Johnston, K. V., & Garavito-Camargo, N. 2018c, *Mon. Not. Roy. Astron. Soc.*, 473, 1218

Laporte, C. F. P., Johnston, K. V., Gómez, F. A., Garavito-Camargo, N., & Besla, G. 2018d, *Mon. Not. Roy. Astron. Soc.*, 481, 286

Laporte, C. F. P., Johnston, K. V., Gómez, F. A., Garavito-Camargo, N., & Besla, G. 2018e, *Mon. Not. Roy. Astron. Soc.*, 481, 286

Laporte, C. F. P., Minchev, I., Johnston, K. V., & Gómez, F. A. 2019a, *Mon. Not. Roy. Astron. Soc.*, 485, 3134

Laporte, C. F. P., Minchev, I., Johnston, K. V., & Gómez, F. A. 2019b, *Mon. Not. Roy. Astron. Soc.*, 485, 3134

Levine, E. S., Blitz, L., & Heiles, C. 2006a, *Astrophys. J.*, 643, 881

Levine, E. S., Blitz, L., & Heiles, C. 2006b, *Astrophys. J.*, 643, 881

Levine, E. S., Blitz, L., & Heiles, C. 2006c, *Astrophys. J.*, 643, 881

Li, Z.-Y. & Shen, J. 2020, *Astrophys. J.*, 890, 85

Lin, C. C. & Shu, F. H. 1964, *Astrophys. J.*, 140, 646

Lin, C. C. & Shu, F. H. 1966, Proceedings of the National Academy of Science, 55, 229

Lindegren, L., Hernández, J., Bombrun, A., et al. 2018, *Astron. Astrophys.*, 616, A2

Lindegren, L., Lammers, U., Bastian, U., et al. 2016, *Astron. Astrophys.*, 595, A4

López-Corredoira, M., Abedi, H., Garzón, F., & Figueras, F. 2014, *Astron. Astrophys.*, 572, A101

López-Corredoira, M., Cabrera-Lavers, A., Garzón, F., & Hammersley, P. L. 2002a, *Astron. Astrophys.*, 394, 883

López-Corredoira, M., Cabrera-Lavers, A., Garzón, F., & Hammersley, P. L. 2002b, *Astron. Astrophys.*, 394, 883

López-Corredoira, M., Cabrera-Lavers, A., & Gerhard, O. E. 2005, *Astron. Astrophys.*, 439, 107

Loveday, J. 1996, *Mon. Not. Roy. Astron. Soc.*, 278, 1025

Lu, Z., Mo, H. J., & Lu, Y. 2015, *Mon. Not. Roy. Astron. Soc.*, 450, 606

Lucy, L. B. 1977, *Astron. J.*, 82, 1013

MacArthur, L. A., Courteau, S., Bell, E., & Holtzman, J. A. 2004, *Astrophys. J. Supple.*, 152, 175

Majewski, S. R., Schiavon, R. P., Frinchaboy, P. M., et al. 2017, *Astron. J.*, 154, 94

Martinez-Valpuesta, I. & Athanassoula, E. 2008, in Formation and Evolution of Galaxy Bulges, ed. M. Bureau, E. Athanassoula, & B. Barbuy, Vol. 245, 103–106

McKee, C. F. & Ostriker, J. P. 1977, *Astrophys. J.*, 218, 148

McMillan, P. J. 2017, *Mon. Not. Roy. Astron. Soc.*, 465, 76

Merritt, D. & Sellwood, J. A. 1994, *Astrophys. J.*, 425, 551

Mikkola, D., McMillan, P. J., & Hobbs, D. 2020, *Mon. Not. Roy. Astron. Soc.*, 495, 3295

Miller, G. E. & Scalo, J. M. 1979, *Astrophys. J. Supple.*, 41, 513

Monaghan, J. J. 1992, *Ann. Rev. Astron, Astrophys.*, 30, 543

Monaghan, J. J. 1997, Journal of Computational Physics, 136, 298

Monaghan, J. J. 2005, Reports on Progress in Physics, 68, 1703

Mondal, C., Subramaniam, A., & George, K. 2019, Journal of Astrophysics and Astronomy, 40, 35

Nadarajah, S. 2005, Journal of Applied Statistics, 32, 685

Nandakumar, G., Hayden, M. R., Sharma, S., et al. 2020, arXiv e-prints, arXiv:2011.02783

Navarro, J. F., Frenk, C. S., & White, S. D. M. 1996, *Astrophys. J.*, 462, 563

Nelson, E. J., van Dokkum, P. G., Brammer, G., et al. 2012, *Astrophys. J. Letters*, 747, L28

Nelson, R. W. & Tremaine, S. 1995, MNRAS, 275, 897

Newton, K. & Emerson, D. T. 1977, *Mon. Not. Roy. Astron. Soc.*, 181, 573

Nidever, D. L., Bovy, J., Bird, J. C., et al. 2014, *Astrophys. J.*, 796, 38

Ostriker, E. C. & Binney, J. J. 1989a, *Mon. Not. Roy. Astron. Soc.*, 237, 785

Ostriker, E. C. & Binney, J. J. 1989b, *Mon. Not. Roy. Astron. Soc.*, 237, 785

Ostriker, E. C. & Binney, J. J. 1989c, *Mon. Not. Roy. Astron. Soc.*, 237, 785

Padmanabhan, T. 2001, Theoretical Astrophysics - Volume 2, Stars and Stellar Systems, Vol. 2

Pagel, B. E. J. & Patchett, B. E. 1975, *Mon. Not. Roy. Astron. Soc.*, 172, 13

Patel, S. G., van Dokkum, P. G., Franx, M., et al. 2013, *Astrophys. J.*, 766, 15

Peñarrubia, J., Gómez, F. A., Besla, G., Erkal, D., & Ma, Y.-Z. 2016, *Mon. Not. Roy. Astron. Soc.*, 456, L54

Peebles, P. J. E. 1970, *Astron. J.*, 75, 13

Petersen, M. S. & Peñarrubia, J. 2021, Nature Astronomy, 5, 251

Posti, L., Helmi, A., Veljanoski, J., & Breddels, M. A. 2018, *Astron. Astrophys.*, 615, A70

Postman, M., Franx, M., Cross, N. J. G., et al. 2005, *Astrophys. J.*, 623, 721

Potter, D., Stadel, J., & Teyssier, R. 2017, Computational Astrophysics and Cosmology, 4, 2

Powell, M. J. D. 1964, The Computer Journal, 7, 155

Press, W. H., Teukolsky, S. A., Vetterling, W. T., & Flannery, B. P. 1992, Numerical Recipes in C, 2nd edn. (Cambridge, USA: Cambridge University Press)

Prochaska, J. X., Werk, J. K., Worseck, G., et al. 2017, *Astrophys. J.*, 837, 169

Purcell, C. W., Bullock, J. S., Tollerud, E. J., Rocha, M., & Chakrabarti, S. 2011a, *Nature*, 477, 301

Purcell, C. W., Bullock, J. S., Tollerud, E. J., Rocha, M., & Chakrabarti, S. 2011b, *Nature*, 477, 301

Putman, M. E., Peek, J. E. G., & Joung, M. R. 2012, *Ann. Rev. Astron, Astrophys.*, 50, 491

Qu, Z., Bregman, J. N., Hodges-Kluck, E., Li, J.-T., & Lindley, R. 2020, *Astrophys. J.*, 894, 142

Radburn-Smith, D. J., Roškar, R., Debattista, V. P., et al. 2012, *Astrophys. J.*, 753, 138

Raha, N., Sellwood, J. A., James, R. A., & Kahn, F. D. 1991a, *Nature*, 352, 411

Raha, N., Sellwood, J. A., James, R. A., & Kahn, F. D. 1991b, *Nature*, 352, 411

Reddy, B. E., Lambert, D. L., & Allende Prieto, C. 2006, *Mon. Not. Roy. Astron. Soc.*, 367, 1329

Reed, B. C. 1996, *Astron. J.*, 111, 804

Renzini, A. 1999, in The Formation of Galactic Bulges, ed. C. M. Carollo, H. C. Ferguson, & R. F. G. Wyse, 9

Reshetnikov, V., Battaner, E., Combes, F., & Jiménez-Vicente, J. 2002, *Astron. Astrophys.*, 382, 513

Richter, P. 2017, Gas Accretion onto the Milky Way, ed. A. Fox & R. Davé, Vol. 430, 15

Robin, A. C., Luri, X., Reylé, C., et al. 2012, *Astron. Astrophys.*, 543, A100

Rogstad, D. H., Lockhart, I. A., & Wright, M. C. H. 1974, *Astrophys. J.*, 193, 309

Rosswog, S. 2009, *New Astronomy Review*, 53, 78

Roškar, R., Debattista, V. P., Brooks, A. M., et al. 2010a, *Mon. Not. Roy. Astron. Soc.*, 408, 783

Roškar, R., Debattista, V. P., Brooks, A. M., et al. 2010b, *Mon. Not. Roy. Astron. Soc.*, 408, 783

Roškar, R., Debattista, V. P., Quinn, T. R., Stinson, G. S., & Wadsley, J. 2008a, *Astrophys. J. Letters*, 684, L79

Roškar, R., Debattista, V. P., Quinn, T. R., Stinson, G. S., & Wadsley, J. 2008b, *Astrophys. J. Letters*, 684, L79

Roškar, R., Debattista, V. P., Quinn, T. R., & Wadsley, J. 2012, *Mon. Not. Roy. Astron. Soc.*, 426, 2089

Sanchez-Saavedra, M. L., Battaner, E., Guijarro, A., Lopez-Corredoira, M., & Castro-Rodriguez, N. 2003, VizieR Online Data Catalog, J/A+A/399/457

Sancisi, R. 1976, *Astron. Astrophys.*, 53, 159

Sancisi, R., Fraternali, F., Oosterloo, T., & van der Hulst, T. 2008a, *Astron. Astrophys. Rev.*, 15, 189

Sancisi, R., Fraternali, F., Oosterloo, T., & van der Hulst, T. 2008b, *Astron. Astrophys. Rev.*, 15, 189

Sandage, A. & Bedke, J. 1994, The Carnegie atlas of galaxies, Vol. 638

Sanders, J. L. & Binney, J. 2016, *Mon. Not. Roy. Astron. Soc.*, 457, 2107

Sanders, J. L. & Das, P. 2018a, *Mon. Not. Roy. Astron. Soc.*, 481, 4093

Sanders, J. L. & Das, P. 2018b, *Mon. Not. Roy. Astron. Soc.*, 481, 4093

Sartoretti, P., Katz, D., Cropper, M., et al. 2018, *Astron. Astrophys.*, 616, A6

Schmidt, M. 1963, *Astrophys. J.*, 137, 758

Schommer, R. A., Suntzeff, N. B., Olszewski, E. W., & Harris, H. C. 1992, *Astron. J.*, 103, 447

Schönrich, R., Binney, J., & Asplund, M. 2012, *Mon. Not. Roy. Astron. Soc.*, 420, 1281

Schönrich, R. & Dehnen, W. 2018a, *Mon. Not. Roy. Astron. Soc.*, 478, 3809

Schönrich, R. & Dehnen, W. 2018b, *Mon. Not. Roy. Astron. Soc.*, 478, 3809

Schönrich, R., McMillan, P., & Eyer, L. 2019, *Mon. Not. Roy. Astron. Soc.*, 487, 3568

Schweizer, F. 1976, *Astrophys. J. Supple.*, 31, 313

Searle, L. & Sargent, W. L. W. 1972, *Astrophys. J.*, 173, 25

Sellwood, J. A. 1996, *Astrophys. J.*, 473, 733

Sellwood, J. A. 2013, Dynamics of Disks and Warps, ed. T. D. Oswalt & G. Gilmore, Vol. 5, 923

Sellwood, J. A. 2013, Dynamics of Disks and Warps (Dordrecht: Springer Netherlands), 923–983

Sellwood, J. A. & Athanassoula, E. 1986, *Mon. Not. Roy. Astron. Soc.*, 221, 195

Sellwood, J. A. & Binney, J. J. 2002a, *Mon. Not. Roy. Astron. Soc.*, 336, 785

Sellwood, J. A. & Binney, J. J. 2002b, *Mon. Not. Roy. Astron. Soc.*, 336, 785

Sellwood, J. A. & Carlberg, R. G. 1984, *Astrophys. J.*, 282, 61

Sellwood, J. A. & Lin, D. N. C. 1989, *Mon. Not. Roy. Astron. Soc.*, 240, 991

Sellwood, J. A. & Merritt, D. 1994, in American Astronomical Society Meeting Abstracts, Vol. 184, American Astronomical Society Meeting Abstracts #184, 36.01

Sellwood, J. A., Nelson, R. W., & Tremaine, S. 1998, *Astrophys. J.*, 506, 590

Shen, S., Wadsley, J., & Stinson, G. 2010, *Mon. Not. Roy. Astron. Soc.*, 407, 1581

Shostak, G. S. & van der Kruit, P. C. 1984, *Astron. Astrophys.*, 132, 20

Silk, J. 2003, *Mon. Not. Roy. Astron. Soc.*, 343, 249

Snaith, O., Haywood, M., Di Matteo, P., et al. 2015, *Astron. Astrophys.*, 578, A87

Soderblom, D. R. 2010, *Ann. Rev. Astron, Astrophys.*, 48, 581

Solway, M., Sellwood, J. A., & Schönrich, R. 2012, *Mon. Not. Roy. Astron. Soc.*, 422, 1363

Soubiran, C., Jasniewicz, G., Chemin, L., et al. 2018, *Astron. Astrophys.*, 616, A7

Sparke, L. S. & Casertano, S. 1988, MNRAS, 234, 873

Spitoni, E., Verma, K., Silva Aguirre, V., et al. 2021, *Astron. Astrophys.*, 647, A73

Spitzer, Lyman, J. 1956, *Astrophys. J.*, 124, 20

Springel, V. 2005, *Mon. Not. Roy. Astron. Soc.*, 364, 1105

Steinmetz, M., Zwitter, T., Siebert, A., et al. 2006, *Astron. J.*, 132, 1645

Stevens, A. R. H., Lagos, C. d. P., Contreras, S., et al. 2017, *Mon. Not. Roy. Astron. Soc.*, 467, 2066

Stinson, G., Seth, A., Katz, N., et al. 2006a, *Mon. Not. Roy. Astron. Soc.*, 373, 1074

Stinson, G., Seth, A., Katz, N., et al. 2006b, *Mon. Not. Roy. Astron. Soc.*, 373, 1074

Thilker, D. A., Bianchi, L., Boissier, S., et al. 2005a, *Astrophys. J. Letters*, 619, L79

Thilker, D. A., Bianchi, L., Boissier, S., et al. 2005b, *Astrophys. J. Letters*, 619, L79

Thornley, M. D. & Mundy, L. G. 1997, *Astrophys. J.*, 484, 202

Ting, Y.-S., Hawkins, K., & Rix, H.-W. 2018, *Astrophys. J. Letters*, 858, L7

Ting, Y.-S. & Rix, H.-W. 2019, *Astrophys. J.*, 878, 21

Tinsley, B. M. 1975, *Astrophys. J.*, 197, 159

Tinsley, B. M. 1977, *Astrophys. J.*, 216, 548

Tinsley, B. M. 1980, *Fundamentals of Cosmic Physic*, 5, 287

Toomre, A. 1964, *Astrophys. J.*, 139, 1217

Toomre, A. 1981, in Structure and Evolution of Normal Galaxies, ed. S. M. Fall & D. Lynden-Bell, 111–136

Tumlinson, J., Peeples, M. S., & Werk, J. K. 2017, *Ann. Rev. Astron, Astrophys.*, 55, 389

Tumlinson, J., Thom, C., Werk, J. K., et al. 2011, Science, 334, 948

Twarog, B. A. 1980a, *Astrophys. J.*, 242, 242

Twarog, B. A. 1980b, *Astrophys. J.*, 242, 242

van den Bergh, S. 1962, *Astron. J.*, 67, 486

van den Bosch, F. C., Abel, T., Croft, R. A. C., Hernquist, L., & White, S. D. M. 2002a, *Astrophys. J.*, 576, 21

van den Bosch, F. C., Abel, T., Croft, R. A. C., Hernquist, L., & White, S. D. M. 2002b, *Astrophys. J.*, 576, 21

van den Bosch, F. C., Burkert, A., & Swaters, R. A. 2001, *Mon. Not. Roy. Astron. Soc.*, 326, 1205

Vasiliev, E. 2019, *Mon. Not. Roy. Astron. Soc.*, 482, 1525

Velliscig, M., Cacciato, M., Schaye, J., et al. 2015, *Mon. Not. Roy. Astron. Soc.*, 453, 721

von Hoerner, S. 1960, *Zeitschrift fuer Astrophysik*, 50, 184

Wadsley, J. W., Stadel, J., & Quinn, T. 2004, *New Astron.*, 9, 137

Weaver, H. & Williams, D. R. W. 1974, *Astron. Astrophys. Suppl.*, 17, 251

Wegg, C., Gerhard, O., & Portail, M. 2015, *Mon. Not. Roy. Astron. Soc.*, 450, 4050

Weiland, J. L., Arendt, R. G., Berriman, G. B., et al. 1994, *Astrophys. J. Letters*, 425, L81

Weinberg, M. D. 1995, *Astrophys. J. Letters*, 455, L31

Weinberg, M. D. 1998, *Mon. Not. Roy. Astron. Soc.*, 297, 101

Weinberg, M. D. & Blitz, L. 2006, *Astrophys. J. Letters*, 641, L33

Westmeier, T., Braun, R., & Koribalski, B. S. 2011, *Mon. Not. Roy. Astron. Soc.*, 410, 2217

White, S. D. M. 1979, *Mon. Not. Roy. Astron. Soc.*, 189, 831

Widrow, L. M., Gardner, S., Yanny, B., Dodelson, S., & Chen, H.-Y. 2012, The Astrophysical Journal, 750, L41

Wilczynski, E. J. 1896, *Astrophys. J.*, 4, 97

Willett, K. W., Lintott, C. J., Bamford, S. P., et al. 2013, *Mon. Not. Roy. Astron. Soc.*, 435, 2835

Williams, B. F., Dalcanton, J. J., Dolphin, A. E., Holtzman, J., & Sarajedini, A. 2009, *Astrophys. J. Letters*, 695, L15

Woolf, V. M. & West, A. A. 2012, *Mon. Not. Roy. Astron. Soc.*, 422, 1489

Wyse, R. F. G., Gilmore, G., & Franx, M. 1997, *Ann. Rev. Astron, Astrophys.*, 35, 637

Yoachim, P., Roškar, R., & Debattista, V. P. 2010, *Astrophys. J. Letters*, 716, L4

York, D. G., Adelman, J., Anderson, John E., J., et al. 2000, *Astron. J.*, 120, 1579

Yusifov, I. 2004, in The Magnetized Interstellar Medium, ed. B. Uyaniker, W. Reich, & R. Wielebinski, 165–169

Zaritsky, D. & Christlein, D. 2007a, *Astron. J.*, 134, 135

Zaritsky, D. & Christlein, D. 2007b, *Astron. J.*, 134, 135

Zschaechner, L. K. & Rand, R. J. 2015, *Astrophys. J.*, 808, 153

Zschaechner, L. K., Rand, R. J., & Walterbos, R. 2015, *Astrophys. J.*, 799, 61